

RETINAL PLASTICITY IN AGEING AND GLAUCOMA

**Thesis submitted for the degree of Doctor of Philosophy
Cardiff University**

Jan 2008

Yuan Lei

School of Optometry and Vision Sciences

Cardiff University

UMI Number: U585097

All rights reserved

INFORMATION TO ALL USERS

The quality of this reproduction is dependent upon the quality of the copy submitted.

In the unlikely event that the author did not send a complete manuscript and there are missing pages, these will be noted. Also, if material had to be removed, a note will indicate the deletion.



UMI U585097

Published by ProQuest LLC 2013. Copyright in the Dissertation held by the Author.
Microform Edition © ProQuest LLC.

All rights reserved. This work is protected against
unauthorized copying under Title 17, United States Code.



ProQuest LLC
789 East Eisenhower Parkway
P.O. Box 1346
Ann Arbor, MI 48106-1346

CONTENTS

	Page
Contents	I
Acknowledgements	V
Abbreviation	VI
List of figures	VII
List of Tables	XVIII
Summary	IX
CHAPTER 1 INTRODUCTION	1
1.1. Retina	2
1.1.1. Gross anatomy	2
1.1.2. Retinal ganglion cells (RGCs)	4
1.2. Optic nerve	6
1.2.1. Structure and molecular composition of the lamina cribosa	6
1.2.2. Size distribution of axons in the optic nerve	8
1.3. Glaucoma	10
1.3.1. Clinical features	10
1.3.2. Classification of glaucoma	13
1.3.3. Aetiology	16
1.3.4. Risk factors	19
1.3.5. RGC shrinkage prior to cell death	20
1.3.6. Ageing and glaucoma	21
1.4. RGC death and glaucoma	23
1.5. RGC death and ageing	24
1.6. Retinal plasticity	24
1.6.1. Central nerve system / retinal remodelling	25
1.6.2. Developmental plasticity	25
1.6.3. Plasticity in the mature retina	26
1.6.4. Corrupted networks	27
1.6.5. Regulation of dendritic remodelling	28
1.7. Perineuronal net	29
1.8. Background of the imaging techniques	32
1.8.1. Normarski Differential Interference (NDIC)	32
1.8.2. Multiphoton confocal microscopy	33
1.9. Hypothesis	35
1.10. Aim and objectives	35
CHAPTER 2 MATERIALS AND METHODS	37
2.1. Tissue source	37
2.2. Retinal preparation	38
2.2.1. Dissection of retina	38
2.2.2. Preparation of retinal whole mounts	39
2.2.3. Preparation of paraffin sections	39
2.3. Histology	40

2.3.1. Haematoxylin and Eosin	40
2.3.2. Immunofluorescence	40
2.3.3. Fast red	42
2.4. Dendritic labelling	42
2.4.1. Intracellular injection of dyes	42
2.4.2. DiOlistic delivery	44
2.5. Microscopy	45
2.5.1. Nomarski Differential Interference Contrast (NDIC) microscopy	45
2.5.2. Confocal microscopy	45
2.6. A novel approach to quantify retinal transneuronal degeneration	46
2.6.1. Image acquisition	46
2.6.2. Data collection	47
2.6.3. Automated detection of cell nuclei	47
2.6.4. Method validation	49
2.6.5. Statistics	49
2.7. Topography of retinal neuron degeneration in the rgcl	49
2.7.1. Image acquisition	49
2.7.2. Morphometric data collection	50
2.7.3. Nearest neighbour analysis	53
CHAPTER 3 DEVELOPMENT AND VALIDATION OF MULTIPHOTON- DAPI METHOD	55
Objectives	55
3.1. Introduction	55
3.2. Results	56
3.2.1. Comparisons of retinal staining methods	56
3.2.2. Nomarski imaging of retinal whole mounts	57
3.2.3. Single-photon confocal imaging of the retinal whole mount	61
3.2.4. Multi-photon confocal microscopy	64
3.2.5. Method validation	66
3.3. Discussion	69
3.3.1. Retinal transverse sections and retinal whole mounts	69
3.3.2. DMSO cleared retinal whole mounts	69
3.3.3. Immunofluorescent and fast red labelling	69
3.3.4. Nomarski and confocal microscopy	70
3.3.5. Single photon and multi-photon confocal microscopy	71
3.3.6. Automatic quantification	71
3.3.7. Validation of multiphoton-DAPI method	72
3.4. Conclusions	72
CHAPTER 4 RETINAL TRANSNEURONAL DEGENERATION IN HUMAN GLAUCOMA	74
Objectives	74
4.1. Introduction	74
4.2. Results	75
4.2.1. Multiphoton imaging of neurons	75

4.2.2. Neuron quantification in the RGCL, INL and ONL	78
4.2.3. Correlation of neuron densities	82
4.3. Discussion	84
CHAPTER 5 RETINAL TRANSNEURONAL DEGENERATION IN AGEING	87
Objectives	87
5.1. Introduction	87
5.2. Results	89
5.2.1. Multiphoton imaging	91
5.2.2. Neuron quantification in the RGCL, INL and ONL	91
5.2.3. Correlation of neurons densities	96
5.3. Discussion	96
5.3.1. Reduction of neuron densities	96
5.3.2. Correlated neuronal loss	96
5.3.3. A complex of age related retinal degenerations	97
5.3.4. Transneuronal degeneration in ageing and glaucoma	98
5.4. Conclusion	99
CHAPTER 6 TOPOGRAPHY OF NEURONAL LOSS IN THE RETINAL GANGLION CELL LAYER OF HUMAN GLAUCOMA	100
Objectives	100
6.1. Introduction	100
6.2. Results	101
6.2.1. Method validation	101
6.2.2. Neuron densities and nearest neighbour distances (NNDs)	102
6.2.3. Distribution of nearest neighbour distances (NNDs)	105
6.2.4. Regularity and the degree of dispersion	109
6.2.5. Graphical evidence of the patterns of neuronal loss	109
6.3. Discussion	111
6.3.1. Method validation	111
6.3.2. Altered NNDs in glaucoma	111
6.3.3. The underlying mechanism of two patterns of neuronal death	112
6.4. Conclusions	113
CHAPTER 7 DENDRITIC MORPHOLOGY OF RGCS	114
Objectives	114
7.1. Introduction	114
7.2. Results	115
7.2.1. Gene gun technique and intracellular injection	115
7.2.2. Immunofluorescent staining of neuron dendrites	116
7.2.3. Golgi impregnation	118
7.2.4. Human tissue quality evaluation	120
7.3. Discussion	130
7.3.1. The failure of dendritic labelling in the human retinas	130

7.3.2. Tissue quality evaluation	130
7.4. Conclusions	131
CHAPTER 8 THE EXPRESSION OF CHONDROITIN SULPHATE GLYCOSAMINOGLYCANS AND AGGREGAN CORE PROTEIN EPITOPES IN YOUNG, AGED, AND GLAUCOMATOUS HUMAN RETINAS	132
Objective	132
8.1. Introduction	132
8.2. Results	133
8.2.1. Controls	134
8.2.2. The expression of CS-GAG 1B5	135
8.2.3. The expression of CS-GAG 2B6	136
8.2.4. The expression of CS-GAG 3B3	137
8.2.5. The expression of aggrecan core protein 6B4	138
8.2.6. The expression of aggrecan core protein 7D1	139
8.2.7. Negative results	140
8.3. Discussion	141
CHAPTER 9 GENERAL DISCUSSION	143
9.1. Summary	143
9.2. Future work	147
9.2.1. Transneuronal degeneration in ageing and glaucoma	147
9.2.2. The topographical changes of RGC distribution in ageing eyes	147
9.2.3. The expression of proteoglycans in the human retinas	147
Appendix I Statistical raw data	148
Appendix II Constituents and preparation of buffer solutions	162
References	165

Acknowledgement

The completion of the project would not have been possible without the help and support from many people I met during my PhD training. I would like to acknowledge the supervision and support of Dr JE Morgan and Professor ME Boulton in the School of Optometry, Cardiff University. The technical help from Mr Nigel Garahan, Mr Chris Von Ruhland, Dr Boris Hermann, Dr Gill Smith, Dr Jon Errichson, Dr Julie Albon from Cardiff University, Dr David Becker, Dr ChrisThrasivoulou and Mr Daniel Ciantar from UCL and statistical support from Mr Paul McGeoghan in Cardiff University are much appreciated. I am also grateful for the love, kindness and support of my husband Yen Chang Huang, my parents, my grandparents, Mr and Mrs Higham, Miss Rachel Oslar, Mr Matthew Davey and Mr Garath Clees, especially during the writing up of the manuscript.

Abbreviations

4'-6-Diamidino-2-phenylindole (DAPI)

Central nerve system (CNS)

Differential interference contrast (NDIC)

Dimethyl sulfoxide (DMSO)

Inner nucleus layer (INL)

Inner plexiform layer (IPL)

Intraocular pressure (IOP)

Lateral geniculate nucleus (LGN)

Lucifer yellow (LY)

Monoclonal antibody (mAb)

Nearest neighbour analysis (NNA)

Nearest neighbour distance (NND)

Nearest neighbour index (NNI)

Outer nucleus layer (ONL)

Outer plexiform layer (OPL)

Photoreceptor layer (PRL)

Photoreceptors (PRs)

Polyvinylpyrrolidone (PVP)

Primary angle closure glaucoma (PACG).

Primary open angle glaucoma (POAG)

Regularity index (RI)

Retinal ganglion cell layer (RGCL)

Retinal ganglion cells (RGCs)

LIST OF FIGURES

	Page
Figure 1-1 Eye is a spherical hollow globe filled with aqueous humour. The outer layer including sclera and cornea is fibrous and protective. The middle layer including choroid, ciliary body and iris is vascular. The innermost layer is the retina.	3
Figure 1-2 The earliest Arabic drawing of the structure of the eye (left) and a simple diagram of the organization of the retina (right, adopted from www.webvision.com with permission).	3
Figure 1-3 Distribution of nerve fibre diameter in normal monkey nerve. The mean fibre diameter is highest in the inferior-temporal region and highest in the superior nasal region. S, superior; I inferior; N, nasal and T, temporal.	9
Figure 1-4 A view of the fundus of the eye in normal (A) and glaucoma patients (B). C and D are schematic diagrams of the features of normal and glaucomatous disks, respectively. There are cupping and excavation in glaucomatous optic disk.	11
Figure 1-5 Notching of the inferior optic rim tissue.	12
Figure 1-6 Splinter haemorrhage in the superior temporal quadrant.	12
Figure 1-7 Peripapillary atrophy on the temporal side of the disc in a patient with glaucoma.	13
Figure 1-8 Models of axonal degeneration. (A) Wallerian degeneration: the transaction of the axon leads to degeneration of the distal segment. (B) Retrograde degeneration or 'dying-back' type of axonal degeneration. It starts at the distal end and slowly degenerates toward the soma. (C) When the distal part of an axon of a sympathetic neuron is locally deprived of nerve growth factor (NGF), the deprived axon segment degenerates, whereas the rest of the axon and the cell survive. (D) During normal development, inappropriate axonal branches are frequently eliminated; in some cases, at least, this seems to occur by branch elimination.	18
Figure 1-9 Prevalence of glaucoma in white (A) and black and Hispanic (B) subjects. BES=Baltimore Eye Survey; BDES=Beaver Dam Eye Study; BMES=Blue Mountains Eye Study; Melbourne VIP=Melbourne Visual Impairment Project; RS=Rotterdam Study; Barbados=Barbados Eye Study; KEP=Kongwa Eye Project; Proyecto VER=Vision Evaluation Research.	22

Figure 1-10 Plasticity of retinal ganglion cells in development. In each hull, the dot represents the soma and the line indicates the direction and length of the most distant filled dendrite. Scale: 250 μm . 26

Figure 1-11 Anti-neurofilament (NF) labelling from normal (A), and 7 day detached (B-D) retinas. In the detached retinas anti-NF labelling was much more intense in retinal ganglion cells (B-D) and sometimes these cells show unusual processes that appeared to be growing from their cell bodies (C,D). (OS, outer segments; ONL, outer nuclear layer; INL, inner nuclear layer; GCL, ganglion cell layer.) Scale bar 25 μm . Adopted from Coblentz et al. 2003). 27

Figure 1-12 Schematic of mechanisms that might mediate calcium-dependent dendritic growth. a. In cortical neurons, calcium influx through voltage-sensitive calcium channels (VGCCs) leads to the activation of calcium/calmodulin-dependent protein kinase IV (CaMKIV). CaMKIV activates cyclic-AMP-responsive-element-binding protein (CREB) and other transcription factors, which regulate the expression of proteins that regulate dendritic growth. b. Calcium signalling pathways in dendrites that regulate branch stability. α -AMPA, α -amino-3-hydroxy-5-methyl-4-isoxazole propionic acid receptor; BDNF, brain-derived neurotrophic factor; ER, endoplasmic reticulum; NMDAR, N-methyl-D-aspartate receptor (Wong and Ghosh 2002). 29

Figure 1-13 The structure of proteoglycan. 31

Figure 1-14 Illustration of DIC microscope. 1) Polarizer; 2) Nomarski prism; 3) Condenser; 4) Specimen; 5) Objective; 6) Objective Nomarski prism; 7) Analyzer; 8) Eyepiece. A plane-polarised wave front created by the action of the condenser 3) and polarizer 1) passes through the specimen 4). Wave front is collected by the objective 5) and is "sheared" into two offset wave fronts by the upper Wollaston prism 6). Because the optical paths are different between the ray-pairs, the specimen image is duplicated laterally and longitudinally. When the wave fronts pass through the analyzer 7), they are recombined into one vibration plane. This is where the constructive or destructive wave interference takes place. The differences in optic path are manifested as light or dark areas in the image. If there is no difference in the phase of the ray, it is showed as a uniform gray background. 33

Figure 1-15 Structure of a confocal microscope (A) and multiphoton microscope (B). (A) The laser light is focused onto a small pinhole, which is split and directed by the beam splitter towards the sample. The fluorescent light emitted by the sample passes through the beam splitter and is focused onto the detection pinhole. Only light that passes the aperture finally reaches the detector. (B) Multiphoton excitation occurs at a tiny diffraction limited focal volume. Therefore, a confocal pinhole is not necessary. In fact, all photons, including those photons scattered when passing through the sample 34

contribute to the image. A and B are adopted from http://fb6www.uni-paderborn.de/ag/ag-sol/fgruppe/mainframe/microscope_e.htm and Svoboda and Yasuda 2006, respectively.

Figure 2-1 Retinal dissection for whole mount. Retinal directions (S = superior, N = nasal, I = inferior, T = temporal) are indicated. '+' and 'o' represent the fovea and optic disk, respectively. 39

Figure 2-2 Experimental set ups of intracellular cell filling rigs (A&B, Becker's lab, department of anatomy and developmental biology, UCL, UK); gene gun shooting arrangement (C), and the structure of gene gun system (D). 44

Figure 2-3 Multiphoton-ultraviolet (MPUV) confocal microscope system. MPUV consists of a Leica upright microscope with motorised xyz stage. Multi- and single- photon lasers are available, including ultraviolet, blue-argon, green-krypton, and green-helium etc. The wavelength of mutliphoton laser ranges from about 700nm - 1000nm, which excite fluorophores from ultraviolet to Cy5 range. 46

Figure 2-4 The sampling grid used to quantify retinal cells. The position of fovea (F) and optic disc are used as reference points. Each point on the grid is 1.7 mm apart (equivalent to 6 degrees eccentricity). 28 red points are sampling positions. 47

Figure 2-5 Nuclei detection design. Original image (A) is converted to a grey level image (B), then a binary image (C), finally the result image (D) and the nuclei identified are labelled by red dots. 48

Figure 2-6 Morphometric processing of the images to calculate NNDs. In ImageJ, the original images (A) were converted to grey level (B) to identify the cell nuclei (ITCN, C). The centre of each nucleus is labelled by a single 'red dot' the size of 1 pixel (C). The green and blue channels of the image were then turned off by colour threshold function, leaving only 'dots' to represent cell nuclei centres (D). After Kodaith transform in NeuroLucida, the NND of each neuron was calculated. 51

Figure 2-7 Multiphoton images of DAPI labelled cell nuclei in the retinal ganglion cell layer. A-H is individual series images of cells at different z planes of the retina whole mount. I is the projection image of A-I. 3D nearest neighbour analysis was based on image A-H. 52

Figure 2-8 Nearest neighbour index (NNI) indicates the degree of spatial dispersion and/or clustering. The values of NNI range between two theoretical extremes: 0 and 2.1491. $NNI=1$, the data is randomly distributed; $NNI>1$, dispersed points; $NNI<1$, clustering. 54

Figure 3-1 Haematoxylin and eosin staining of a retinal paraffin transverse section from the inferior mid-peripheral retina (as indicated by *). The retina is from a normal Caucasian male donor of 63 years old. GCL, ganglion cell layer; IPL, inner plexiform layer; INL, inner nucleus layer; OPL, out plexiform layer; ONL, outer nucleus layer. + represents the position of the fovea, and o is the optic nerve. The scale bar of A is 40 μ m and B is 5 mm. 56

Figure 3-2 TUJ-1 labelling of neurons in the retinal ganglion cell layer of the retinal whole mounts. (A) is the negative control. (B) and (C) show staining with fluorescein and fast red respectively. The sample was taken from the peripheral inferior retina (as indicated by *). + represents the position of the fovea, and o is the optic nerve. The scale bar of A-C is 100 μ m and D is 5 mm. 57

Figure 3-3 Nomarski differential interference contrast (NDIC) imaging of cells in the retinal ganglion cell layer. Changing the position of the objective Nomarski prism produces a corresponding spectrum of interference colours in the specimen image (A-D), i.e. optical staining. The retina is from a normal Caucasian male donor of 63 years old. The sample was taken from the nasal retina (as indicated by *). + represents the position of the fovea, and o is the optic nerve. The donor is a The scale bar of A-D is 100 μ m and E is 5 mm. 58

Figure 3-4 NDIC images of the retinal ganglion cell layer. Focusing down meant cells in difference planes of the RGCL gradually appeared in sharp focus (A-E). F is the end of the RGCL and the beginning of inner plexiform layer (IPL), beyond which point no cell body could be observed in sharp focus. The retina is from a normal Caucasian male donor of 63 years old. The sample was taken from the nasal retina (as indicated by *). + represents the position of the fovea, and o is the optic nerve. The scale bar of A-F is 40 μ m and G is 5 mm. 59

Figure 3-5 Nomarski differential interference contrast microscopy images of cells in the RGCL from central (A) to mid-peripheral (BC) retina. The retina is from a normal Caucasian male donor of 63 years old. The 'flower petal' on the right of each image represents the retina whole mount: * indicates where the sample was taken, + represents the position of the fovea, and o is the optic nerve. The scale bars of the microscopic images are 10 μ m and the flower petal are 5 mm. 60

Figure 3-6 A series of confocal images of TUJ-1 labelling (green, A-C) and DAPI labelling (blue, D-F); (G) and (H) are projection images of (A-C) and (D-F) respectively; I is the overlay image of G&H. A-C and D-F are images taken at an z interval of 2 μ m focusing from the retinal ganglion cell layer towards the inner plexiform layer (C and F are the end of retinal ganglion cells layer and the beginning of the inner plexiform layer). The retina is from a normal Caucasian male donor of 73 years old. The 'flower petal' (J) represents the retina whole mount: * indicates where the sample was taken, + 62

represents the position of the fovea, and o is the optic nerve. Scale bar for A-I is 50 μ m and for J is 5 mm.

Figure 3-7 Confocal image of DAPI labelling (blue, A) and TUJ-1 labelling (green, B) in the inner nucleus layer of a human retinal whole mount. C is an overlay picture of A and B. In addition to retinal ganglion cells, B-C show that TUJ-1 stains cells in the inner nucleus layer. The ‘flower petal’ (D) represents the retina whole mount: * indicates where the sample was taken, + represents the position of the fovea, and o is the optic nerve. The retina is from a normal Caucasian male donor of 73 years old. Scale bar for A-C is 50 μ m and D is 5 mm.

63

Figure 3-8 Single photon and multi-photon images of cells in the outer nucleus layer which was imaged with the retinal ganglion cell layer upper most. The ‘flower petal’ (D) represents the retina whole mount: * indicates where the sample was taken, + represents the position of the fovea, and o is the optic nerve. The retina is from a normal Caucasian male donor of 73 years old. Scale bar for A-C is 20 μ m and D is 5 mm.

64

Figure 3-9 Multiphoton images of DAPI stained cell nuclei in the retinal ganglion cell layer (RGCL), inner nucleus layer (INL) and outer nucleus layer (ONL) of the human retinal whole mounts. These were sequentially imaged with the RGCL upper most and focusing from the RGCL to the ONL. An example of 3D models of the layers imaged was built by Imaris software. The ‘flower petal’ represents the retina whole mount: * indicates where the sample was taken, + represents the position of the fovea, and o is the optic nerve. The retina is from a normal Caucasian male donor of 73 years old. Scale bar for RGCL, INL and ONL is 20 μ m and ‘flower petal’ is 5 mm.

65

Figure 3-10 The distribution of retinal ganglion cells (RGCs) in the human retinal whole mounts. Samples are taken at the positions of the sampling grid in Figure 2-4. Our results from NDIC (n=3) and multiphoton-DAPI methods (n=6) were comparable to literature values (n=5, Cucio et al, 1990). The direction superior and inferior refer to the appropriate sides of the horizontal meridian, a line that passes through the fovea and the optic disk; nasal and temporal refer to the parts of the vertical meridian that was perpendicular to the horizontal meridian.

66

Figure 3-11 Validation of the automated computer counts by manual counts. In multiphoton-DAPI images, the automated counts were compared with manual counts. The results were analysed by linear regression (A, n=3, r²=0.991) and Bland-Altman plot (B, n=3, most of the points fall within mean \pm 2SD), both of which suggest a good correlation of the two counting techniques. SD, standard deviation.

68

Figure 3-12 Validation of multiphoton-DAPI method by Nomarski differential contrast microscopy (NDIC). Retinal whole mounts were stained by DAPI

68

solution (3 mg/mL) overnight, and imaged by multiphoton microscopy as described in Chapter 2 (2.6.). The same samples were then imaged by NDIC method. The counting results of neurons in the retinal ganglion cell layer were compared with NDIC counts. The results were analysed by linear regression (A, $n=3$, $r^2=0.984$) and Bland-Altman plot (B, $n=3$, most of the points fall within mean $\pm 2SD$), both of which shows good correlations of the counting results measured by multiphoton-DAPI method and NDIC method. SD, standard deviation.

Figure 4-1 Multiphoton images of DAPI stained cell nuclei in the RGCL, INL and ONL in normal ($n=6$) and glaucomatous ($n=6$) retinas. Here an example from one retina of each group was given. These imaged were sequentially taken with the RGCL upper most and focusing from the RGCL to the ONL. Two 3D models of the retinal layers for normal and glaucomatous retinas were built by Imaris software. The images shown were taken from the temporal retina at 2.7 mm eccentricity (as indicated by * in the 'flower petal' below the multiphoton images and point 5 on the grid). There is + represents the position of the fovea, and o is the optic nerve. The scale bar of multiphoton images is 20 μm and the 'flower petal' is 5 mm. RGCL, retinal ganglion cell layer; INL, inner nucleus cell layer; outer nucleus layer (ONL).

77

Figure 4-2 Colour coded mean neuron density maps and correlation maps in control ($n=6$) and glaucomatous ($n=6$) retinas. Colour gradient was assigned to values of densities, e.g. for RGCL, the colours from red to blue represent densities values range between 0 and 18 ($\times 1000$ per mm^{-2}), with each colour represents a particular density value. Ratios of neuron densities were shown on the right of each contour plot. The contour map spatially correlates with the sampling grid. xy axis show eccentricities (mm), (0,0) is the fovea. RGCL, retinal ganglion cell layer; INL, inner nucleus cell layer; outer nucleus layer (ONL).

79

Figure 4-3 Comparisons of neuron densities in the RGCL (A), INL (B) and ONL (C) of glaucomatous ($n=6$) and control ($n=6$) retinas. Lines show means of neuron densities at each eccentricity, and bars show means within 4mm eccentricity. In the RGCL, the neuron density was significantly reduced between 0.5 and 4 mm eccentricity. In the INL and ONL, this was significant between 2-4 and 2-3 mm eccentricity. From the RGCL to ONL, the region of density reductions was narrowed down. Error bars show mean ± 1 SD. RGCL, retinal ganglion cell layer; INL, inner nucleus cell layer; outer nucleus layer (ONL).

81

Figure 4-4 The neuron density ratios of INL/RGCL (A), ONL/RGCL (B) and ONL/INL (C) in glaucomatous ($n=6$) and control ($n=6$) retinas. Lines show means of neuron density ratios at each eccentricity. In the two groups of comparison, there is significant difference of INL/RGCL and ONL/RGCL between 3 and 4 mm eccentricity, but no significant difference of ONL/INL at any eccentricity tested. Error bars show mean ± 1 SD. RGCL, retinal

83

ganglion cell layer; INL, inner nucleus cell layer; outer nucleus layer (ONL).

Figure 5-1 Multi-photon images of DAPI stained cell nuclei in RGCL, INL and ONL of young (n=6) and aged (n=6) human retinas. Here an example from one retina of each group is shown. These images were sequentially taken with the RGCL upper most and focusing from the RGCL to the ONL. Two 3D models of the retinal layers for young and aged retinas were built by Imaris software. The images shown were taken from the temporal retina at 6 mm eccentricity (as indicated by * in the 'flower petal' below the multiphoton images and point 9 on the grid). There is + represents the position of the fovea, and o is the optic nerve. The scale bar of multiphoton images is 10 μm and the 'flower petal' is 5 mm. RGCL, retinal ganglion cell layer; INL, inner nucleus cell layer; outer nucleus layer (ONL). 89

Figure 5-2 Colour coded neuron density maps and correlation maps in young (A, n=6) and aged (B, n=6) retinas. Colour gradient was assigned to values of densities, e.g. for RGCL, the colours from red to blue represent density values range between 0 and 18 ($\times 1000$ per mm^{-2}), with each colour representing a particular density value. Ratios of neuron densities were shown on the right of each contour plot. The contour map spatially correlates with the sampling grid. xy axis show eccentricities (mm), (0,0) is the fovea. RGCL, retinal ganglion cell layer; INL, inner nucleus cell layer; outer nucleus layer (ONL). 92

Figure 5-3 Comparisons of RGC quantities measured by multiphoton-DAPI method in young adults (n=6) and literature values (n=5) (Curcio and Allen 1990). The measurements were taken at nasal, temporal, superior and inferior regions of the retina. There was a close correlation between neuron density results from multiphoton-DAPI method and literature values. 93

Figure 5-4 Comparisons of neuron densities in the RGCL, INL and ONL of young (n=6) and ageing (n=6) retinas. Lines show means of neuron densities at each eccentricity, and bars show means within 4mm eccentricity. Error bars show mean \pm 1 SD. Compared to young retinas, ageing retinas showed significant reduction of neuron densities in central retina. * $p < 0.05$, ** $p < 0.01$. RGCL, retinal ganglion cell layer; INL, inner nucleus cell layer; outer nucleus layer (ONL). 95

Figure 6-1 Correlation of the nearest neighbour distances (NNDs) counted by manual (n=6) and automated method (n=6). 20 frames of 0.96 mm^2 each were selected from 12 retinas to cover the full density range. Best-fit linear regression has a correlation coefficient (R^2) of 0.999. This is confirmed by Bland-Altman plot (in the sub-window), i.e. most of the points fall within the range of mean \pm SD, and there is no trend as x value increases. 102

Figure 6-2 Colour coded maps of mean nearest neighbour distances (NNDs) distribution in control (A, n=6) and glaucomatous retinas (B, n=6). Colour gradient is assigned to values of NNDs (μm), e.g. in A the colours from red to blue represent NND values range between 5 and 25 ($\times 1000$ per mm^2), with each colour represents a particular density value. The contour map spatially correlates with the sampling grid in C. xy axis show eccentricities (mm), (0,0) is the fovea. 104

Figure 6-3 Correlation of neuron densities and the average nearest neighbour distances (NNDs). Best-fit linear regression equation and corresponding correlation coefficient (R2) are indicated. Neuron density and average NND is inversely correlated. 105

Figure 6-4 Nearest neighbour distances (NNDs) distribution in glaucomatous (n=6) and age-matched control retinas (n=6). Compared with controls, NNDs in glaucomatous retinas are shifted to the right (A), and the densities of neurons reduced (A, bar chart). The skewness and kurtosis of NND distribution in glaucomatous retinas is 2.57 and 16.347, compared with 1.765 10.611 in normal retinas respectively (A). The higher positive skewness in glaucoma indicate that the peak of NND distribution is shifted to the higher NND values and has a longer tail than control. The higher kurtosis in glaucoma NND distribution indicate that the peak is more flat than control. The NNDs $\geq 20 \mu\text{m}$ (in A) is re-plotted (in B); in glaucoma group, the percentage of NNDs within this range increases 4.5 fold compared with controls. 106

Figure 6-5 Histogram showing the distribution of nearest neighbour distances (NNDs) with and without the correction for the presence of displaced amacrine cells in the RGCL (10%) in normal (A) and glaucomatous retinas (B). There is less than 3% difference in the mean NNDs between the inclusion and the exclusion of amacrine cells in both groups. 108

Figure 6-6 Typical images of diffuse pattern (B) and focal pattern (C) of neuronal loss in glaucoma group (n=6) compared with normal (A, n=6). The imaging position is indicated by * in the 'flower petal' on the right of the microscopic images. + represents the position of the fovea, and o is the optic nerve. Arrows in C indicate areas of clustered neuronal loss. The image size is 1600x1200 pixels, i.e. 1.98 pixels/ mm^2 resolution. The scale bar of microscopic images is 100 μm and the 'flower petal' is 5 mm. 110

Figure 7-1 Dye labelling of retinal neurons. A and B show DiI labelled RGCs in the fresh chick retina (A) and the fixed human retina (B, Caucasian male of 79 years old) using the gene gun technique, respectively; C shows a lucifer yellow labelled retinal ganglion cell in the porcine retina by intracellular injection. The 'flower petal' a-c corresponds to the sampling position of A-C on the retinal whole mounts. Scale bar of A-C 50 μm . and a-c 5 mm. 116

Figure 7-2 Immunofluorescence labelling of retinal ganglion cells (n=3). Green, SMI 32 antibody; red, DAPI staining. Here an example from one retina of each group is shown. SMI32 partially labelled the dendrites of neurons in the retinal ganglion cell layer. The 'flower petal' represents the retina whole mount: * indicates where the sample was taken, + represents the position of the fovea, and o is the optic nerve. The retina is from a normal Caucasian male donor of 79 years old. Scale bar for AB is 50 μ m, C is 10 μ m and D is 5 mm.

117

Figure 7-3 Retinal ganglion cell layer stained by Golgi impregnation in human retinas (n=3). Here an example from one retina of each group is shown. No dendritic structure could be identified. The 'flower petal' on the right of the image shows where the sample is taken on the retina whole mount. * indicates where the sample was taken, + represents the position of the fovea, and o is the optic nerve. The retina is from a normal Caucasian male donor of 74 years old. Scale bar for AB is 50 μ m, C is 10 μ m and D is 5 mm.

119

Figure 7-4 Immunofluorescent labelling of RGCs with TUJ-1 (green) and DAPI (blue) in human retinas: A-C, 24h 'Bristol retinas'; D-F, 48h 'Bristol retinas'; G-I, normal 'US retinas'; J-L, glaucomatous 'US retinas'. The 'flower petal' (a-c) represents the retina whole mounts: * indicates where the sample was taken, + represents the position of the fovea, and o is the optic nerve, and a-c corresponds to A-C, D-F, G-I and J-L. TUJ-1 labelling was significantly reduced in the 48h group (D-F) compared with the 24h group (A-C). The percentage of the RGCs labelled in the 24h 'Bristol retina' (A-C) was comparable to the normal 'U.S. retina' (G-I). Glaucomatous retinas (J-L) showed a significantly lower percentage of TUJ-1 labelling than normal retinas from the same source (G-I). RGCs were completely depleted in some areas of the retina (K) which is indicated by the white squares. Scale bar 50 μ m for confocal microscopic images and 5 mm for the 'flower petals'.

124

Figure 7-5 Immunofluorescent labelling of neurons in the retinal ganglion cell layers of rat retinas that were immediately fixed (A-C), and after 48h in PBS at 4oC (D-F). C and F are the overlay image of A&B and D&E, respectively. Red, TUJ-1; blue, DAPI. The 'flower petal' a and b represents the retina whole mounts A-C and D-F respectively: * indicates where the sample was taken, + represents the position of the fovea, and o is the optic nerve. Rat retinas fixed 48h after death (D-F) showed a significant lower percentage of TUJ-1 labelling than those fixed immediately (A-C), and the loss of cell soma and axons. Scale bar 50 μ m for confocal images and 5 mm for 'flower petals'.

127

Figure 7-6 Colour coded confocal images of DiI labelled neurons. A) shows a fully labelled retinal ganglion cell in the rat retina fixed immediately in 4% paraformaldehyde; B) shows the same labelling but in a rat retina fixed after 48h from enucleation. The 'flower petal' shows the sampling position on the retina whole mounts A-C and D-F respectively: * indicates where the sample

129

was taken, + represents the position of the fovea, and o is the optic nerve. The dendrites of rat retinas fixed immediately were completely labelled (A), but not those fixed 48h later (B). Scale bar for microscopic images 50 μ m and flower petal 5 mm.

Figure 8-1 The negative and positive controls of different isotopes of GAGs. A) shows the immunostaining when the primary antibodies were eliminated; B) shows the immunostaining of CS-GAG 1B5, 2B6 and 3B3 when the chondroitinase ABC digestion was eliminated; C) shows the positive control staining of bovine cartilage sections. 134

Figure 8-2 1B5 expression in the young (18-33 yr, n=4), aged (58-90 yr, n=4) and glaucomatous (77-89 yr, n=4) retinas. Here an example from one retina of each group is shown. A-C are 1B5, DAPI and overlay images of young retinas; D-F and G-I are those of aged and glaucomatous retinas respectively. Scale bar 50 μ m. 135

Figure 8-3 2B6 expression in the young (18-33 yr, n=4), aged (58-90 yr, n=4) and glaucomatous (77-89 yr, n=4) retinas. Here an example from one retina of each group is shown. A-C are 2B6, DAPI and overlay images of young retinas; D-F and G-I are those of aged and glaucomatous retinas respectively. Scale bar 50 μ m. 136

Figure 8-4 3B3 expression in the young (18-33 yr, n=4), aged (58-90 yr, n=4) and glaucomatous (77-89 yr, n=4) retinas. Here an example from one retina of each group is shown. A-C are 3B3, DAPI and overlay images of young retinas; D-F and G-I are those of aged and glaucomatous retinas respectively. Scale bar 50 μ m. 137

Figure 8-5 6B4 expression in the young (18-33 yr, n=4), aged (58-90 yr, n=4) and glaucomatous (77-89 yr, n=4) retinas. Here an example from one retina of each group is shown. A-C are 6B4, DAPI and overlay images of young retinas; D-F and G-I are those of aged and glaucomatous retinas respectively. Scale bar 50 μ m. 138

Figure 8-6 7D1 expression in the young (18-33 yr, n=4), aged (58-90 yr, n=4) and glaucomatous (77-89 yr, n=4) retinas. Here an example from one retina of each group is shown. A-C are 6B4, DAPI and overlay images of young retinas; D-F and G-I are those of aged and glaucomatous retinas respectively. Scale bar 50 μ m. 139

Figure 8-7 There was no expression of keratocan, lumican, versican, 5D4 or decorin in the human retinas. 140

Figure 9-1 An illustration of the 3D structure of the human retina (Adopted from Webvision with permission).	143
Figure 9-2 A) 3D reconstruction of the multiphoton-DAPI images; B) orthogonal view the 3D reconstruction model; C) a single xy scan within a z stack of multiphoton-DAPI images, in which a z slice is shown vertically (right) and the other horizontally (bottom). Scale bar 20 μm .	144

LIST OF TABLES

Table 1-1 The diagnosis of glaucoma.	14
Table 1-2 Identified primary open-angle glaucoma loci	20
Table 2-1 Details of eye donors used in this project.	37
Table 2-2 Antibodies used to label retinal ganglion cells.	41
Table 2-3 Antibodies against various proteoglycans used to identify their expression in the human retina.	42
Table 2-4 Excitation lines and laser types used in the current project.	46
Table 3-1 Mean peak densities of RGCs measured by NDIC and multiphoton-DAPI methods.	67
Table 3-2 Methods for automated detection and analysis of cell nuclei.	72
Table 7-1 The ratio of TUJ-1 and DAPI labelling in four groups of human retinas (n=3 in each group)	125

fSummary

This project is to investigate retinal plasticity at the cellular level, i.e. changes of the cell density, cell pattern, cell morphology and the perineuronal net, in the aged and glaucomatous retinas.

A multiphoton-DAPI method was developed to study retinal transneuronal degeneration. In glaucoma, the neurodegeneration at the retinal ganglion cell layer (RGCL) initiates a cascade of transneuronal degeneration in the inner nucleus layer (INL) and the outer nucleus layer (ONL). On the other hand, in ageing, neurons in both the RGCL and ONL are markedly affected; the neuronal loss in the INL correlates with both layers. This suggests other mechanisms in addition to transneuronal degeneration that contribute to the retinal degeneration in ageing.

In glaucoma, the pattern of the neuronal loss in the RGCL was analysed. Supported by the microscopic observation, nearest neighbour analysis (NNA) reveals a combination of diffuse and clustered patterns of neuronal loss. In particular, the diffuse pattern was more common in the central retina whereas the clustered loss was prominent in the mid-peripheral retina. It is very likely that these two patterns of neuronal loss were produced by two different pathologic mechanisms leading to RGC depletion.

There appear to be differences between the chondroitin glycosaminoglycan (CS-GAG) staining and the aggrecan core protein staining in the RGCL, INL and the inner plexiform layer. This suggests that some of the GAG attachment regions of aggrecan have been removed in these domains. The major source of CS-GAG staining appears to be from aggrecan because only negative staining for decorin, biglycan, lumican, keratocan and versican was found. Also, negative 5D4 staining suggests that this aggrecan is not or minimally substituted with keratocan sulphate. This study emphasises the importance of the perineuronal net in potentially restricting the recovery and regeneration of neurons in the adult retina.

CHAPTER 1 INTRODUCTION

Throughout history, people have been intrigued by the mechanism of vision formation. Most elderly people experience some loss of vision, even in the absence of any identifiable eye disease. Vision loss dramatically reduces the life quality of people, especially in the elderly, where even moderate reductions in visual field can have a substantial impact on the mobility (Nelson et al., 2003; Noe et al., 2003). Approximately 2% of the population overall has glaucoma, rising to over 4% in those over 75 years of age (Quigley, 1996). It accounts for 13% of blind registration in the UK (Evans, 1991). Since age is a major risk factor in glaucoma, the proportion of the population affected by this disease is set to increase as the mean age of the population rises.

Glaucoma firstly causes the loss of peripheral vision, which if unchecked will progress to complete loss of vision. This results from the losses of optic nerve fibres and retinal ganglion cells (RGCs), i.e. the output neurons of the retina. In most cases, glaucoma is associated with increased intraocular pressure (IOP). Although notable advances have been made in the surgical and medical reduction of IOP, many sufferers continue to lose vision even when the IOP has been brought under control. If we are to identify and target those retinal areas that are at risk of progressive RGC loss, it is important to understand the processes leading to cell death. Various experimental glaucoma models have provided pathological evidence of the disease, and currently much effort has been devoted to the understanding of the molecular mechanisms of RGC apoptosis. However, at the cellular level, surprisingly little is known of the damage in the human retina.

Evidence of retinal plasticity in human glaucoma would be particularly exciting since it would raise the possibility that these changes could be reversed, with possible recovery in visual function. Retinal plasticity has been elegantly demonstrated in the developing retina in which RGCs can compensate for the loss of surrounding cells by expanding their dendritic trees (Linden and Perry, 1982; Troilo et al., 1996). In end stage glaucoma, surviving RGCs show dendritic pruning, and the reduction in the overall area is similar

to that seen in experimental glaucoma (Morgan et al., 2000; Pavlidis et al., 2003), but as yet we do not know whether these changes occur in human glaucoma.

This chapter aims to provide a comprehensive background of a) the anatomy and physiology of human retina, b) aetiology of glaucoma, c) the mechanism of RGC death, and d) cell plasticity changes associated with ageing and glaucoma.

1.1. Retina

1.1.1. Gross anatomy

The formation of vision starts in the retina. It is a thin sheet of neural tissue approximately 0.5 mm thick, lining the back of the eye (Figure 1-1). It was the Greek philosophers (Hippocrates, Aristotle, Plato) who provided the first known theories concerning the function and anatomy of the eye (Figure 1-2, left) (Polyak, 1957). Figure 1-2 is a radial section of a portion of the retina: the RGCs lie innermost in the retina; the photoreceptors (rods and cones) lie outermost in the retina against the retinal pigment epithelium (RPE) and choroid. Light travels through the cornea, pupil, lens, vitreous humour and the thickness of the retina to activate photoreceptors. Subsequently, the visual pigment translates the light stimuli first into a biochemical message, and then an electrical message that stimulates all the succeeding neurons of the retina. The photic input and some preliminary organization of the visual image are transformed to spiking discharge patterns of the RGCs. Millions of axons in the optic nerve then transfer the retinal messages to the lateral geniculate nucleus (LGN) and the primary visual cortex in the brain. The blood supply to photoreceptors is indirectly from the choriocapillaries. The inner retinal layers are directly nourished by branches of the central retinal artery (Osborne et al., 2004).

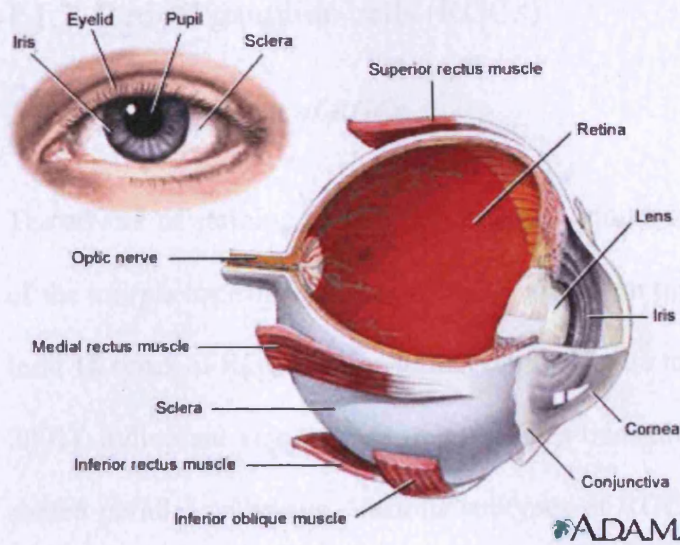


Figure 1-1 Eye is a spherical hollow globe filled with aqueous humour. The outer layer including sclera and cornea is fibrous and protective. The middle layer including choroid, ciliary body and iris is vascular. The innermost layer is the retina.

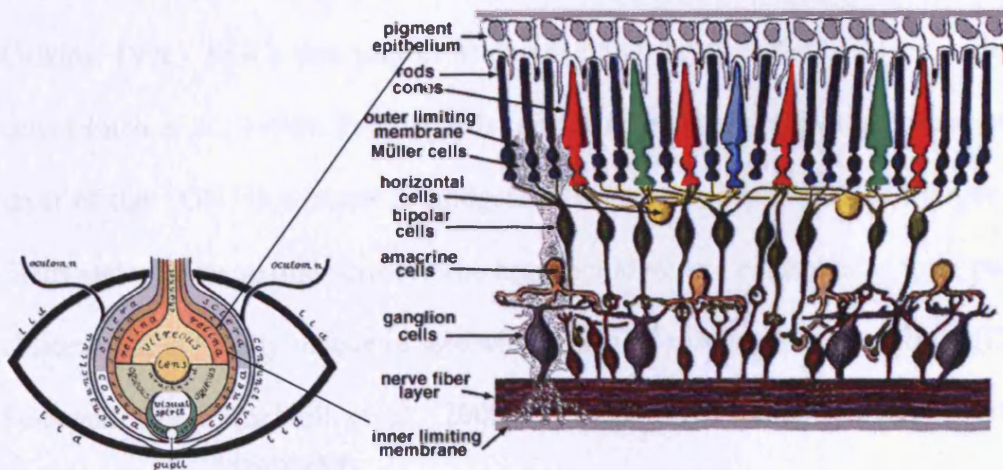


Figure 1-2 The earliest Arabic drawing of the structure of the eye (left, Polyak 1957) and a simple diagram of the organization of the retina (right, adopted from www.webvision.com with permission).

1.1.2. Retinal ganglion cells (RGCs)

1.1.2.1. Classification of RGCs

The advent of staining techniques on whole mount retinas allowed the characterisation of the morphological features of RGCs. Based on the morphology of RGC, there are at least 18 types of RGCs in the human retina that are morphologically different (Masland, 2001). Individual signals from many RGCs transmit visual information to the brain in shared parallel pathways. Various subtypes of RGCs with specific morphological and functional features (Dacey, 1996; Helga Kolb, 1992; Perry et al., 1984) all exit the eye globe in the optic nerve, converge upon the chiasm, form the optic tract and terminate in the LGN (Yucel et al., 2003). The LGN is separated into three functionally distinct layers: the magnocellular, parvocellular and koniocellular pathways, which are responsible for motion, red–green and blue-ON channels, respectively (Hendry and Calkins, 1998). RGCs that project to parvocellular layer of the LGN are called midget cells (Shieh et al., 1998). Parasol cells, on the other hand, project to the magnocellular layer of the LGN. Compared to midget cells, parasol cells have much larger dendritic fields and a lower spatial density. The human midget and parasol cells form two distinct clusters that gradually reduce in size with decreased distance from the fovea (Dacey and Petersen, 1992; Rockhill et al., 2000; Watanabe and Rodieck, 1989). Midget cells comprise the great majority of the RGC population, and reach a high density in the central retina (Dacey, 1994). RGCs can also be divided based on the spatial summation properties of their receptive field, e.g. in cat, X-cells is linear and Y-cells non-linear. The linear cells sum photoreceptor signals linearly across their receptive fields, whereas

the non-linear cells showed distinct non-linearities of spatial summation (Enroth-Cugell and Robson, 1966).

1.1.2.2. Spatial distribution

The advent of staining techniques on whole mount retinas allowed the characterisation of the morphological features of RGCs. There are at least 18 types of RGCs in the human retina that are morphologically different (Masland, 2001). RGCs that project to parvocellular layer of the LGN are called midget cells (Shieh et al., 1998). Parasol cells, on the other hand, project to the magnocellular layer of the LGN. Compared to midget cells, parasol cells have much larger dendritic fields and a lower spatial density. The human midget and parasol cells form two distinct clusters that gradually reduce in size with decreased distance from the fovea (Dacey and Petersen, 1992; Rockhill et al., 2000; Watanabe and Rodieck, 1989). Midget cells comprise the great majority of the RGC population, and reach a high density in the central retina (Dacey, 1994).

The arrangement of RGCs on the retinal surface is not spatially random, but distributed in an ordered mosaic. The ultimate spatial pattern of RGCs is determined not only by the regularity of the soma spacing but also by the overlap among dendrites. Receptive and dendritic fields of cells within a mosaic partially overlap: characteristically, the nearest neighbour distances are greater than would be expected in a random distribution. RGCs of different types may be independently and closely spaced; however, the individual RGCs of the same type maintain the maximal spacing (Lin et al., 2004; Wassle and Riemann, 1978). In the human retina, the ratio of parasol to midget dendritic field diameter changes dramatically as a function of eccentricity. Parasol cell density increases more slowly as it approaches the central retina than does midget cell density, and the dendritic overlap (dendritic field area \times cell density) remains constant (Dacey and Petersen, 1992).

1.1.2.3. Projections to the central nerve system (CNS)

Individual signals from many RGCs transmit visual information to the brain in shared parallel pathways. Various subtypes of RGCs with specific morphological and

functional features (Dacey, 1996; Helga Kolb, 1992; Perry et al., 1984) all exit the eye globe in the optic nerve, converge upon the chiasm, form the optic tract and terminate in the LGN (Yucel et al., 2003). The LGN is separated into three functionally distinct layers: the magnocellular, parvocellular and koniocellular pathways, which are responsible for motion, red–green and blue-ON channels, respectively (Hendry and Calkins, 1998).

1.1.2.4. Retinal circuitry

The response properties of RGCs result from transformations of photoreceptor responses, which are mediated by interactions in the outer plexiform layer (OPL) and inner plexiform layers (IPL) of the retina. In the IPL, synchronous chemical synaptic signals from individual amacrine cells and bipolar cells interact with different varieties of functionally specialised RGCs. Such signals may spread among these presynaptic elements through mutual interconnections by electrical junctions (Brivanlou et al., 1998). RGCs themselves also intercommunicate through electrical junctions. In the OPL, the dendrites of bipolar cells reach up to rod spherules and cone pedicles. Horizontal cells laterally inhibit cones through GABAergic feedback upon contact with cone pedicles. Hyperpolarized rods depolarise rod bipolar cells, which synapse with AII amacrine cells. In addition, signals from rods can reach RGCs via chemical synapses input from the AII amacrine cells. Rod circuitry is piggy-backed onto the cone pathways; this occurs largely via synapses (chemical or gap junctions) by AII amacrine cells, and onto the axon terminals of cone bipolar cells, which then excite RGCs.

1.2. Optic nerve

1.2.1. Structure and molecular composition of the lamina cribrosa

The lamina cribrosa (LC) is a lattice-like structure which consists of successive perforated cribriform plates. The plates are lined by basement membranes and were

made up of a core of elastin fibers with a sparse, patchy distribution of collagen type III. By 1990, the basic collagen composition of the extracellular matrix (ECM) of the LC had been characterized. In the connective tissue components of the LC, types I, III, IV, V, and VI collagen and elastin were identified (Goldbaum et al., 1989; Hernandez et al., 1987; Tengroth et al., 1985), and collagen types I & III being the major structural fibrillar components of stromal extracellular matrices (Albon et al., 1995). This was followed by the characterization of other components such as proteoglycans and glycoproteins (Caparas et al., 1991; Morrison et al., 1994). The cellular component of the LC was studied in tissue explanted and two cell types grown from this tissue were characterized, which were glial cells and fibroblastic cells (Hernandez et al., 1988). Astrocytes, which are the major glial cell type in the nonmyelinated optic nerve head in most mammalian species, provide cellular support to the axons and synthesize ECM macromolecules (Anderson, 1969; Hernandez, 2000). In the human optic nerve head, there are two sub-populations of astrocyte type 1: type 1A expresses glial fibrillary acidic protein (GFAP), a cytoskeletal marker of astrocytes, but do not express neural cell adhesion molecule (NCAM); type 1B express both GFAP and NCAM (Hernandez, 2000). Lamina cribrosa cells are different from astrocytes as they do not express GFAP nor vascular specific markers or microglial markers (Hernandez et al., 1988). The activation of glial cells is a significant component of the response to injury in the CNS and in the retina. Human glaucomatous optic neuropathy and animal models have demonstrated synthesis of inducible nitric oxide synthase by reactive astrocytes in the optic nerve head which led to cell death (Neufeld, 1999; Yang et al., 2004).

1.2.2. Size distribution of axons in the optic nerve

The size distribution of axons in the optic nerve follows a certain pattern. In monkey optic nerves, the smallest mean diameter axons were in the central infero-temporal quadrant, and the largest mean fibre diameter was the superior nasal periphery (Figure 1-10) (Sanchez et al., 1986). Furthermore, the region of smallest axon diameter correlates with the highest density of fibres within nerve bundles, and the region of largest axon diameter had lowest fibre density. In cat, the distribution of axon diameter, as estimated from measurements of axonal cross-sectional area was clearly bimodal: the group of finest axons had a mode at approximately 1 micrometer, and the mode of the group of intermediate size axons was approximately 2 micrometers, fibres diameters larger than 3.5 micrometers formed the extensive tail of the distribution (Williams and Chalupa, 1983). These groups probably correspond to the alpha, beta, and gamma classes of retinal ganglion cells. It confirmed that the mean fibre diameter varied inversely with the density of axon packing.

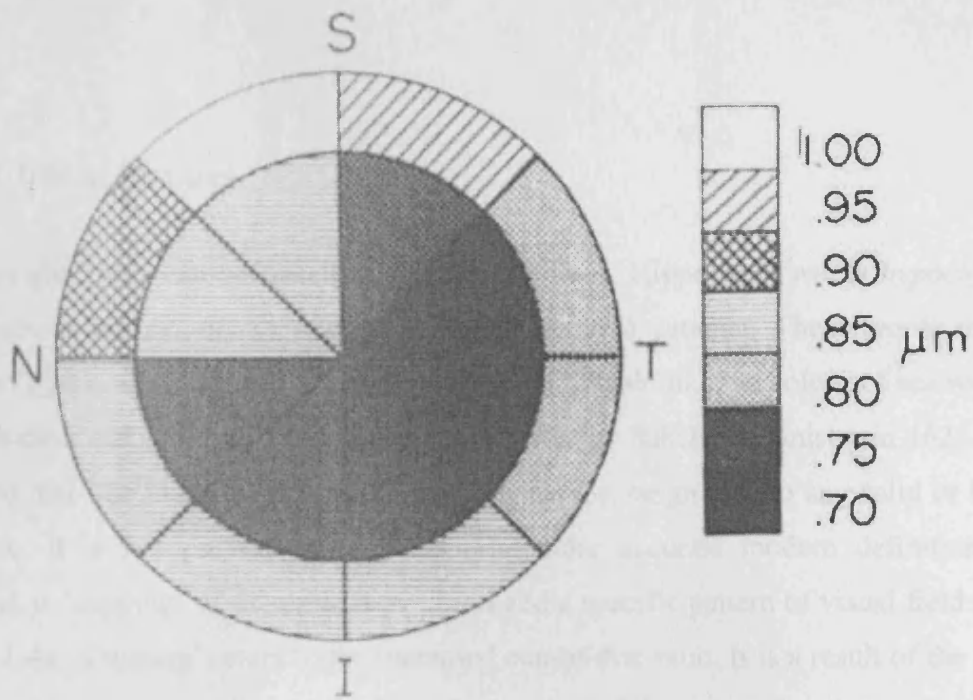


Figure 1-3 Distribution of nerve fibre diameter in normal monkey nerve. The mean fibre diameter is highest in the inferior-temporal region and highest in the superior nasal region. S, superior; I inferior; N, nasal and T, temporal (Sanchez et al., 1986).

1.3. Glaucoma

1.3.1. Clinical features

The term glaucoma can be traced to Hippocratic times. Hippocratic words *hypochyma* and *glaucosis* are synonyms, and both vaguely refer to cataract. These words mean ‘disputed’; generally accepted to signify greenish or bluish, like the colour of sea water. The first clear recognition of absolute glaucoma was by Rikchard Banister in 1622. He described that ‘the humour settled in the hollow nerves, be growne to any solid or hard substance, it is not possible to cured...’ The more accurate modern definition of glaucoma is ‘cupping’ of the optic nerve head and a specific pattern of visual field loss (Figure 1-4). ‘Cupping’ refers to the increased cup-to-disc ratio. It is a result of the loss of RGC axons and the collapse and posterior bowing of the connective tissue sheets of lamina cribrosa (Morrison et al., 2005). Therefore, a change in the degree of cupping is a more important sign of the glaucomatous damage than the actual size of the cup. The most common visual field defect in glaucoma is arcuate scotoma, i.e. an arcuate defect emanating from the blind spot (Morrison et al., 2005). The arcuate scotoma follows the pathways of the axon bundles originated at the superior and inferior poles of the optic nerve (Tielsch et al., 1991; Tuulonen and Airaksinen, 1991), passes through the fovea but do not anatomically cross a horizontal midline, producing ‘nasal steps’.

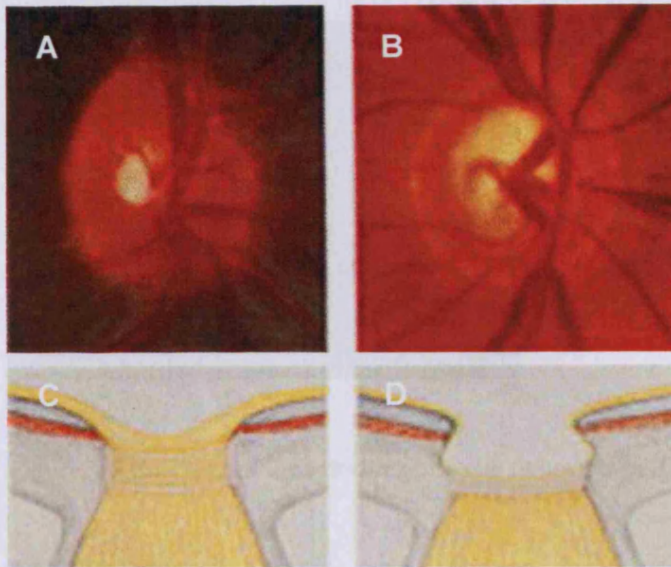


Figure 1-4 A view of the fundus of the eye in normal (A) and glaucoma patients (B). C and D are schematic diagrams of the features of normal and glaucomatous disks, respectively. There are cupping and excavation in glaucomatous optic disk. Adopted from (Quigley, 1993).

Another important indication of axon damage is the appearance and configuration of the neural rim, which is the area between the cup and the edge of the disc. The rim tissue is often the first area to show changes in glaucoma. In a normal eye, the neural rim is uniformly pink in colour because of the good vascular perfusion. The rim tissue will decrease its width as the axons are lost. Figure 1-5 shows a generalised atrophy of the rim and cup that is typical in moderate to advanced glaucoma, with corresponding visual field loss. In early glaucoma, the inferior rim usually shows the first sign of damage, followed by superior rim damage, and the nasal rim is last affected. The thinning of a focal area of the disc can lead to the development of a 'notch' in the rim tissue, especially in the superior and inferior regions (Figure 1-4) (Nada J. Lingel and Smith, 2006).

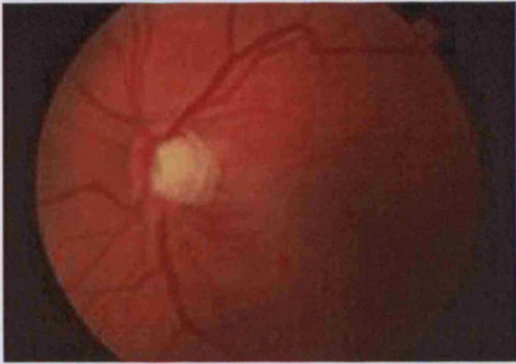


Figure 1-5 Notching of the inferior optic rim tissue (Nada J. Lingel and Smith, 2006).

Another important optic nerve change in glaucoma is haemorrhage on or approximate to the optic disc (Figure 1-6) (Nada J. Lingel and Smith, 2006). A small disc haemorrhage (also called splinter haemorrhage) is commonly associated with normal tension glaucoma.

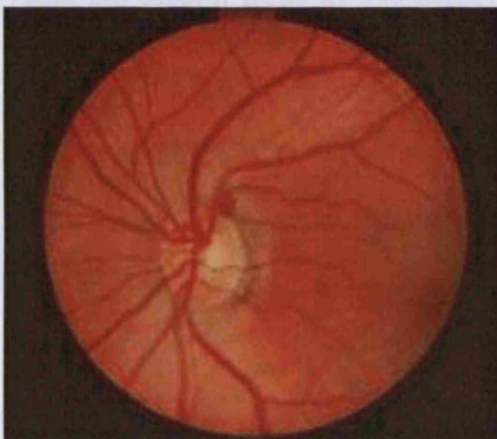


Figure 1-6 Splinter haemorrhage in the superior temporal quadrant.

Patients with peripapillary atrophy are sometimes suspicious of glaucoma (Kornzweig et al., 1968). In these cases, large choroidal vessels and sclera are visible around the ONH, and hyper or hypo-pigmentation (Figure 1-7).

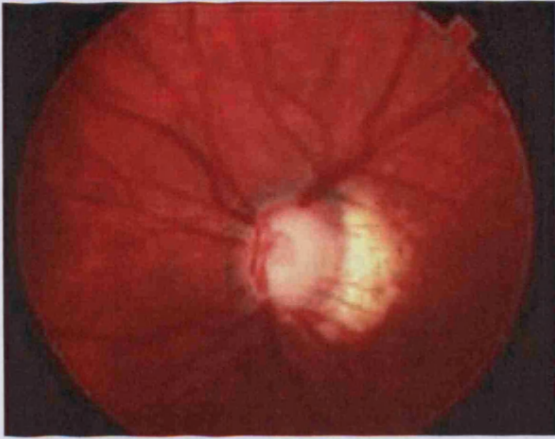


Figure 1-7 Peripapillary atrophy on the temporal side of the disc in a patient with glaucoma.

1.3.2. Classification of glaucoma

1.3.2.1. Primary open angle glaucoma and angle closure glaucoma

There are several types of glaucoma; the most common ones are primary open angle glaucoma (POAG) and primary angle closure glaucoma (PACG). Asia accounts for a disproportionate number of PACG cases, whereas the prevalence of POAG is more evenly distributed throughout the world. Although PACG and POAG are both characterised by the damage to the optic nerve and the visual field loss, they differ in terms of whether the trabecular meshwork is obstructed by the peripheral iris, i.e. in PACG the iris obstructs the trabecular meshwork, whereas in POAG the trabecular meshwork seems to be open. This difference affects the medical and surgical managements of the two diseases. A procedure known as gonioscopy is used to differentiate between the two types of glaucoma. Gonioscopy involves examination of the anterior chamber with a lens that enables the observer to see the angle between the cornea-sclera and iris, i.e. the

iridocorneal angle. The angle is graded depending on the amount of the trabecular meshwork that can be seen.

POAG has conventionally been characterised as a disease of raised eye pressures. The changes in the optic nerve head, retinal nerve fibre layer and visual-field are associated with raised IOP (Weinreb and Khaw, 2004), but they can also occur in individuals whose eye pressures are below the population mean of 15.5 mm Hg. The diagnosis of POAG can be made if the optic nerve damage meeting any of the three categories of evidence listed in Table 1-1.

Table 1-1 The diagnosis of glaucoma (Foster et al., 2002)

Category 1 diagnosis (structural and functional evidence)

Eyes with a cup to disc ratio (CDR) or CDR asymmetry ≥ 97.5 th percentile for the normal population, or a neuroretinal rim width reduced to ≤ 0.1 CDR (between 11 to 1 o'clock or 5 to 7 o'clock) that also showed a definite visual field defect consistent with glaucoma.

Category 2 diagnosis (advanced structural damage with unproved field loss)

If the subject could not satisfactorily complete visual field testing but had a CDR or CDR asymmetry ≥ 99.5 th percentile for the normal population, glaucoma was diagnosed solely on the structural evidence.

In diagnosing category 1 or 2 glaucoma, there should be no alternative explanation for CDR findings (dysplastic disc or marked anisometropia) or the visual field defect (retinal vascular disease, macular degeneration, or cerebrovascular disease).

Category 3 diagnosis (Optic disc not seen. Field test impossible)

If it is not possible to examine the optic disc, glaucoma is diagnosed if: (A) The visual acuity $< 3/60$ and the IOP > 99.5 th percentile, *or* (B) The visual acuity $< 3/60$ and the eye shows evidence of glaucoma filtering surgery, or medical records were available confirming glaucomatous visual morbidity.

Patients with PACG may present with acutely raised IOP, a mid-dilated pupil, a red eye, nausea and vomiting; whereas in other cases, they may have mild complaints such as a non-specific headache, eye pain and halos around lights. In PACG, one of the mechanisms for the obstruction of the trabecular meshwork is by pupillary block, i.e. the aqueous humour can not leave the posterior chamber behind the iris, because of the apposition of the iris to the lens of the eye. Consequently, there is a pressure gradient between the posterior and anterior chambers of the eye, which causes a forward bowing of the peripheral iris and further obstructs the trabecular meshwork.

1.3.2.2. Glaucoma with secondary ocular pathology

Secondary glaucoma represents those eyes in which a second form of ocular pathology, e.g. neovascularisation, uveitic, trauma etc. has caused IOP above the normal range, leading to optic nerve damage.

1.3.2.3. Normal tension glaucoma

Some people have normal or low IOP but maybe considered as a glaucoma suspect based on other criteria, e.g. patients with high cup to disc ratio but no visual field defect, those with definite field defects but disc is normal, those with optic disc margin haemorrhage, those with an narrow angle but normal disc, visual field, IOP and no peripheral iris obstruction of the angle.

1.3.3. Aetiology

The biological basis of the progression of POAG is not yet fully understood. The debate continues about whether the damage to the optic nerve is caused by high IOP, vascular insufficiency in the optic nerve head, or both factors. There appears to be a correlation between visual field loss, optic nerve atrophy, loss of RGC axons and RGCs themselves (Kerrigan-Baumrind et al., 2000; Morrison et al., 2005; Repka and Quigley, 1989). Some, but not all investigators have also noted changes in the outer retina (Nork et al., 2000; Panda and Jonas, 1992; Quigley, 2001). Several alternations in the cellular and molecular components of the ONH have been noted, including the abnormalities in the extracellular matrix (Hernandez et al., 1990; Hernandez and Ye, 1993), the deposition of collagen IV and other molecules within the lamellar pores, alterations of elastin (Hernandez, 1992) and astrocyte expression of collagen IV, tropoelastin, hyaluronic acid, glial fibrillary acidic protein, tenascin, and nitric oxide synthase etc (Hernandez, 2000).

Pressure-induced changes in lamina cribrosa may be the initial site of glaucomatous damage, which lead to the blockade of both retrograde and anterograde axonal transport with subsequent failure of axonal transport and growth factor deprivation (Nickells, 2007). Consistent with this, anatomical evidence in DBA mice showed that the death of neurons occurred in a fan-shaped focal sector extending from the optic nerve head (Jakobs et al., 2005). 'DBA mice' is a genetic model for studying glaucoma. In these mice, the genetic defects in the iris cause obstructions in the trabecular meshwork. As a result, by 8–9 months of age, DBA mice have developed an elevated IOP; by 10–12 months they exhibit an optic neuropathy that shares similarities with human glaucoma (John et al., 1998; Libby et al., 2005). Moreover, IOP-independent mechanisms may also be responsible for the development and progression of glaucomatous neuropathy.

Up to one-sixth of patients with glaucoma develop it despite normal IOP (Liesegang, 1996). Therefore, the high IOP is merely a risk factor for the development of glaucoma.

The nature of the initial damage in lamina cribrosa is not clear. It has been suspected to be a 'mechanical model', but conflicting evidence exists in normal tension glaucoma (Tezel et al., 1996; Wax et al., 1998). Clinical (Flammer et al., 2002) and pathological (Osborne et al., 2004) evidence suggests that tissue ischemia stress, i.e. inadequacy blood flow to a tissue that fails to meet cellular energy demands, is associated with the pathogenic mechanisms underlying the damage/death of axons and neurons. At cellular level, the activation of glial cells plays an important role in neuron remodelling and further degeneration in the way that glial cells can cause TNF- α facilitated RGC death (Tezel and Wax, 2000). From the astrocytes isolated from glaucomatous optic nerve heads, a microarray analysis showed an up-regulation of genes responsible for cell proliferation, cell adhesion, and the synthesis of new extracellular matrix (Hernandez et al., 2002). This further suggested an association between gene expression and glia activation as part of the events occurred in glial scar formation.

Although the degeneration of neurons in glaucoma seems compartmentalised (Whitmore et al., 2005), optic nerve degeneration seems to be one of the most important and earliest sign of glaucomatous damage. In general, severely damaged axons normally die rapidly by anterograde degeneration or Wallerian degeneration (Figure 1-8). The axons affected by less severe insult die slowly in a retrograde fashion, which starts at the synaptic end of the axons and extend towards the neuron soma. It is not clear if both types of axon death are present in glaucoma. However, the axonal damage may cause the degeneration of cell bodies of RGCs (Raff et al., 2002).

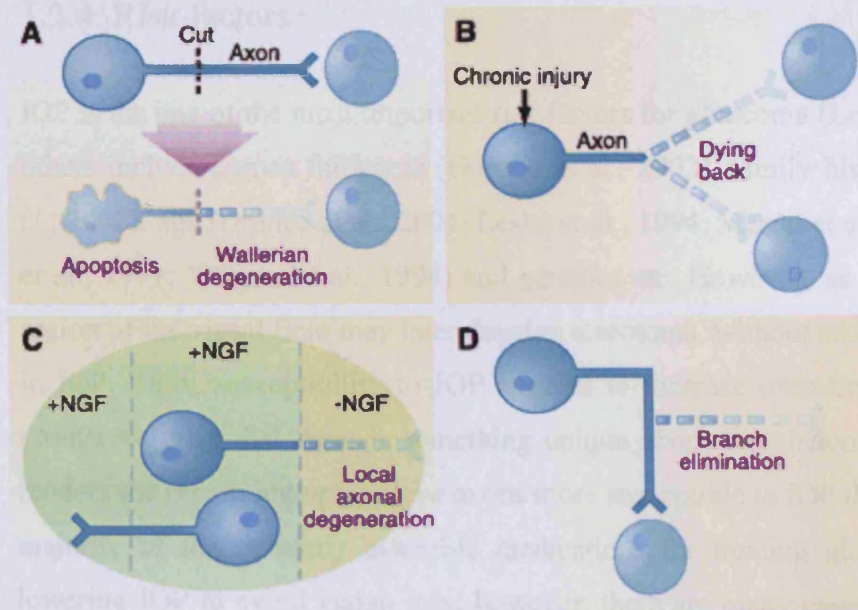


Figure 1-8 Models of axonal degeneration. (A) Wallerian degeneration: the transaction of the axon leads to degeneration of the distal segment. **(B) Retrograde degeneration or ‘dying-back’ type of axonal degeneration.** It starts at the distal end and slowly degenerates toward the soma. **(C) When the distal part of an axon of a sympathetic neuron is locally deprived of nerve growth factor (NGF),** the deprived axon segment degenerates, whereas the rest of the axon and the cell survive. **(D) During normal development, inappropriate axonal branches are frequently eliminated; in some cases, at least, this seems to occur by branch elimination (Raff et al., 2002).**

Glaucomatous damage is not restricted to the retina, but extends to the LGN (Weber et al., 2000; Yucel et al., 2000; Yucel et al., 2001; Yucel et al., 2003) and visual cortex (Crawford et al., 2001). Injuries spread from diseased neurons to connected neurons is a well known phenomenon of neurodegenerative disorders (Su et al.1997). As we know that in the visual pathway, RGCs conveyed visual information from the retina to the LGN. In glaucoma, since there is an active and regulated program of axonal self-destruction that is molecularly distinct from somal apoptosis (Raff et al., 2002; Whitmore et al., 2003), the death of RGCs and/or their axons might lead to synaptic degeneration of neurons in the LGN. Paradoxically, LGN might provide growth factors for the survival of RGCs, therefore, RGCs death might be aggravated by the degeneration of LGN neurons through the deprivation of neurotrophic factors (Gupta and Yucel, 2001; Johnson and Cowey, 2000).

1.3.4. Risk factors

IOP is the one of the most important risk factors for glaucoma (Leske et al., 2003); others include cornea thickness (Gordon et al., 2002), family history (Gordon et al., 2002), age (Drance et al., 2001; Leske et al., 1994; Mason et al., 1989; Tielsch et al., 1991; Wensor et al., 1998) and genetics etc. However, an initially normal region of the visual field may later develop a scotoma, without an apparent change in IOP. Thus, susceptibility to IOP appears to increase over time. AGIS study (2000) suggests that there is something unique about the glaucomatous eye that renders the remaining optic nerve axons more susceptible to IOP than normal. The majority of the currently available medications for treating glaucoma aim for lowering IOP to avoid vision loss; however, there are many cases of progressive glaucoma despite apparently successful pressure lowering. Therefore, understanding the nature of the increased susceptibility to IOP might provide key information for the aetiology and pathology of the disease. It will also be important for developing specific treatments designed to reverse or stabilize these conditions to reverse, or avoid vision loss.

Recent advances have identified a number of specific mutations in the genetic code of glaucoma patients that are linked with specific glaucomatous phenotypes. Transgenic animal models for these genes were developed to understand their biological function, and the interaction with genetic and environmental factors. The genetic evidence of hereditary POAG includes cases of familial POAG, i.e. the higher incidence of POAG in relatives (especially twins) of POAG patients. According to Human Genome Organisation (HUGO) Genome Database Nomenclature Committee, GLC1 is the symbol for POAG (letters A, B, C, and so forth applied to each new locus identified). Mutation of myocilin gene (MYOC) at the GLC1A locus is thought to be associated with Juvenile-onset POAG and adult-onset POAG (Stone et al., 1997). POAG, however, is a heterogeneous

disease with a complex of genetic trait (Table 1-2). Moreover, some of the genes may display incomplete penetrance or variable expressivity (Hewitt et al., 2006). In the human genome, sequence variation includes single nucleotide polymorphisms, insertions or deletions of a few nucleotides and variation in the repeat number of a motif. The sequence variations have been shown to occur in exons (gene coding regions) as well as introns (intervening promoting regions) (Andolfatto, 2005), which added to the complexity of glaucoma genetics.

Table 1-2 Identified primary open-angle glaucoma loci (Adopted from (Hewitt et al., 2006)).

Loci	OMIM	Gene	Location	Reference study	Typical phenotype
GLC1A	601652	<i>Myocilin</i>	1q23-q25	(Stone, Fingert et al. 1997)	JOAG/HTG
GLC1B	606689		2cen-q13	(Stoilova et al., 1996)	NTG/HTG
GLC1C	601682		3q21-q24	(Wirtz et al., 1997)	HTG
GLC1D	602429		8q23	(Trifan et al., 1998)	NTG/HTG
GLC1E	602432	<i>Optineurin</i>	10p15-p14	(Rezaie et al., 2002)	NTG
GLC1F	603383		7q35-q36	(Wirtz et al., 1999)	HTG
GLC1G	609887	<i>WDR36</i>	5q33-q35	(Monemi et al., 2005)	NTG/HTG
GLC1H	609745		15q11-q13	(Allingham et al., 2005)	NTG/HTG
GLC1J	608695		9q22	(Wiggs et al., 2004)	JOAG
GLC1K	608696		20p12	(Wiggs et al., 2004)	JOAG

HTG, high-tension glaucoma; NTG, normal tension glaucoma; JOAG, juvenile onset glaucoma; NS, not specified; NTG, normal-tension glaucoma.

1.3.5. RGC shrinkage prior to cell death

Neuron shrinkage is a well-known cellular response to pathological injury (Cook et al., 1951; Morgan et al., 2000). The decrease in cell body size and dendritic arborisation corresponds to a decrease in function (Eysel and Wolfhard, 1984).

Weber has noted that in experimental primate glaucoma RGCs undergo reductions in the size of their dendritic arborisation, followed by the reduction in the size of the cell bodies and axons (Weber et al., 1998). A similar decrease, well in advance of the loss of RGCs, has also been observed for Thy-1 message production, i.e. an axonal marker for RGCs (Schlamp et al., 2001). Neuron atrophy also occurs in the LGN in experimental primate glaucoma. This process was significant in the surviving neurons of both M and P pathways (Yucel et al., 2001). The degree of shrinkage in M and P pathways showed a linear relationship to RGC loss (Yucel et al., 2001). From these findings, it appears that RGCs undergo specific cellular changes in glaucoma. While these changes likely precede the death of the RGCs, it is not currently clear whether or not they can be reversed by simply lowering the eye pressure. If not, such reductions in cellular activity could contribute significantly to the progressive nature of the vision loss in glaucoma. This would suggest an opportunity for rescuing these cells that are undergoing injury but possibly not yet committed to die, and for maintenance of the integrity of healthy cells by providing resilience to a variety of hostile factors or agents.

1.3.6. Ageing and glaucoma

Glaucoma is a common problem in the elderly. Statistic reviews showed that POAG is an age-related disease (Friedman, 2004; Repka and Quigley, 1989) (Figure 1-7). Morphological studies in both ageing and glaucoma eyes have shown an increased accumulation of extracellular material in both the trabecular meshwork (Gottanka et al., 1997; Rohen and Witmer, 1972) and uveoscleral outflow pathway (Lutjen-Drecoll et al., 1986), which may potentially cause a reduction in the aqueous humour outflow. Consequently, the elevation of IOP might initiate a vicious cycle leading to further reductions in the outflow and pressure elevation. Therefore, it is likely that the normal ageing processes could shift the balance towards the initiation of glaucoma and its progression by various mechanisms (Gabelt and Kaufman, 2005).

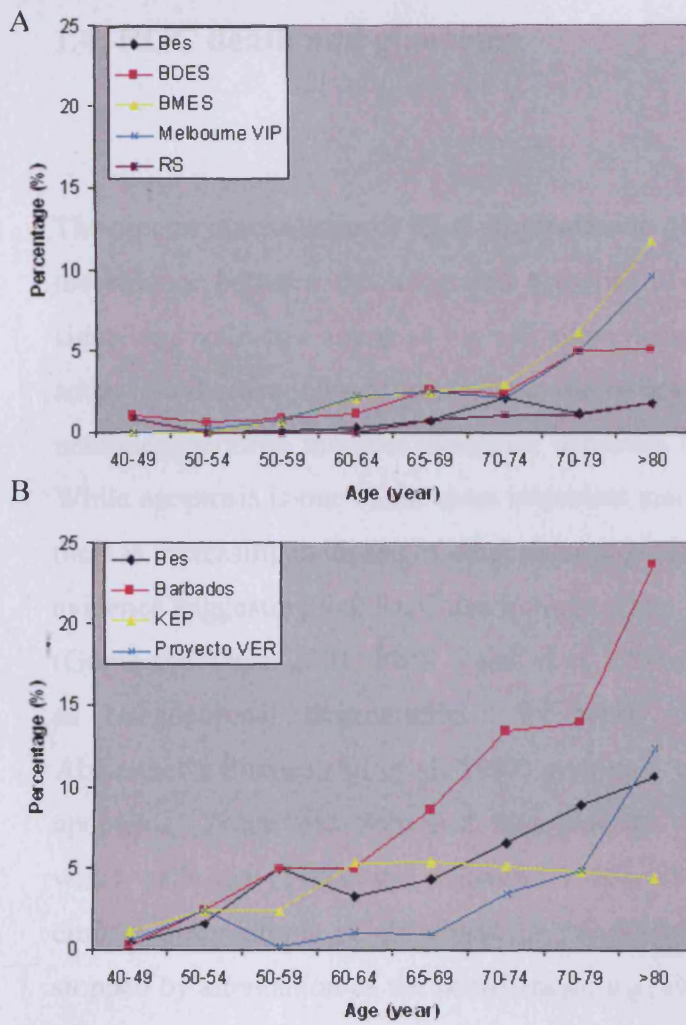


Figure 1-9 Prevalence of glaucoma in white (A) and black and Hispanic (B) subjects. BES=Baltimore Eye Survey; BDES=Beaver Dam Eye Study; BMES=Blue Mountains Eye Study; Melbourne VIP=Melbourne Visual Impairment Project; RS=Rotterdam Study; Barbados=Barbados Eye Study; KEP=Kongwa Eye Project; Proyecto VER=Vision Evaluation Research (Gabelt and Kaufman 2005).

1.4. RGC death and glaucoma

The precise mechanisms of RGC elimination in glaucoma remain obscure. In general, the balance between the integrated activities of multiple trophic and degenerative signalling pathways acting at the cell soma decides the fate of the cell: whether to adapt to a disease-induced stress, or to die by apoptosis. In glaucoma, the process of neurodegeneration involves synapses, dendrites and axons (Whitmore et al. 2005). While apoptosis is one of the most important mechanisms of cell death in glaucoma, there is increasing evidence of other non-apoptotic components. For instance, there is evidence suggesting that RGC death in glaucoma is disseminated in the same manner (Gupta and Yucel 2001, 2003; Yucel et al. 2000; Yucel et al. 2001; Yucel et al. 2003) as transneuronal degeneration in many other neurological disorders, e.g. Alzheimer's disease (Su et al. 1997) and brain trauma (Conti et al. 1998). Besides apoptosis, Yoles and Schwartz hypothesised 'final common pathways' through which cells die (Yoles and Schwartz 1998). This concept explains two important clinical observations in glaucoma: a) the progression of the disease could not be stopped by attenuation of the initial insult, e.g. high IOP, and b) patients with severe pre-existing damage are more likely to deteriorate than those who has equal or higher IOP but do not have visual field loss at the time of diagnosis (Kaushik et al. 2003). Thus, the damaged neurons in glaucoma could be in various conditions ranging from normal, sick, degenerating and dead (Neufeld 1998). The fate of these neurons can be a function of their proximity to the original site of damage coupled with individual susceptibility.

1.5. RGC death and ageing

RGCs are the first cells produced in the mammalian retina. During development, many more RGCs are produced than will ultimately survive in the adult visual system. In different species, between 50% and 80% of the total RGCs produced die (Finlay and Pallas 1989). In humans, this figure approximates 70%. Correlation of the extent of RGC loss as a function of normal ageing has been found to be remarkably difficult. This is because of the inter- and intra- individual variations of the quantities of RGCs. However, there are studies that have successfully examined the numbers of RGCs and their axons. In humans, the number of foveal RGCs reduces by 16-25% between the second and sixth decades (i.e. this translates to about 1/3 loss during a 70-year life span) (Curcio and Drucker 1993; Gao and Hollyfield 1992); the loss of optic nerve fibres was about 4,000 to 6,000 per year (Balazsi et al. 1984; Jonas et al. 1990; Mikelberg et al. 1989); on the contrary, Repka and Quigley found an insignificant decline in optic nerve fibre number with age (Repka and Quigley 1989). Choplin and co-workers found little correlation of nerve fibre layer thickness with age (Choplin et al. 1998), whereas Poinoosawmy and colleagues found a decrease of 0.5% of the retinal nerve fibre layer thickness per year, or nearly one-third of the total thickness over a lifetime (Poinoosawmy et al. 1997).

1.6. Retinal plasticity

Plasticity involves the transformations of neurons and neural networks as part of their normal functions. It is clearly reversible in many of its manifestations. Remodelling, on the other hand, may invoke normal plastic mechanisms, or represent the removal of inhibitory mechanisms that maintain structural homeostasis (Marc et al. 2003). Remodelling can potentially corrupt spatial processing and prevent the retina from providing signals throughout the visual circuits.

1.6.1. Central nerve system / retinal remodelling

The mammalian CNS remodels during development and learning, as well as in response to injury and disease. CNS actively impairs after losing sensory drive, with neurochemical/molecular reorganizations, functional and morphological alterations, and sprouting of new connections (Marc et al. 2003; Wall et al. 2002). For example, CNS neurons show plasticity in changing the number of dendritic spines in association with learning and memory (Sorra and Harris 2000). Furthermore, altered visual experience can induce compensatory axonal sprouting associated with functional remodelling (DeBello et al. 2001). Retina is also expected to show plasticity and/or to remodel in response to pathological stimuli since it is a prototypical CNS assembly that developed from the embryonic forebrain. In fact, in response to deafferentation, neurons in both retina and CNS display a range of degenerative changes, including apoptosis, reshaping of neurites, revision of synaptic connectivity, modulation of gene expression and glial transformations, which in turn alter the signal processing in the entire visual pathway (Marc et al. 2003).

1.6.2. Developmental plasticity

Developmental plasticity has been demonstrated in circuit maturation in the mammalian retina. It involves significant post-natal refinement, including improved high spatial frequency cut-offs of RGCs at about post-natal day 30 in cats (Dubin 1977). Intrinsic processes may participate in shaping the retina and RGC arbours, in particular. It has long been suspected that RGC arbour pruning is a key process in the refinement of function (Dubin 1977; Perry and Linden 1982; Rusoff and Dubin 1978). After synaptogenesis, retinal circuits appear to guide synaptic refinement (Sernagor et al. 2001) first via cholinergic transmission (Bansal et al. 2000) and there-after via glutamatergic transmission (Stacy et al. 2005). When axotomy of the optic nerve was induced at birth, the dendrites of the surviving RGCs around the depleted area were preferentially directed towards this depopulated region, whereas normal RGCs had a roughly elliptical dendritic convex hull, centred around the soma (Linden and Perry 1982) (Figure 1-10). The author concludes that the orientation of RGC dendrites is strongly influenced by neighbouring cells; during normal

development, dendrites compete for their afferents. This shows that the alteration of appropriate stimuli and cellular neighbourhoods invokes neuronal plasticity in the retina.



Figure 1-10 Plasticity of retinal ganglion cells during development. In each hull, the dot represents the soma and the line indicates the direction and length of the dendrite. Scale bar 250 μm . Adopted from Marc et al. 2003.

1.6.3. Plasticity in the mature retina

Plasticity in the mature retinas is not well defined. It may be delicately concealed as subtle changes in the expression of key synaptic proteins, changes in local wiring, and refinement of dendritic form (Marc et al. 2003). Light adaptation is a type of plasticity that reflects a functional transition from scotopic to photopic vision. It was shown that dopamine and retinoic acid reduced the coupling between horizontal cells under light-adapted conditions (Weiler et al. 2000). Dopamine could modulate RGC spike generation to produce retinal network adaptation, i.e. the ability of the retinal network to remain sensitive to small differences in light intensity with respect to the background, regardless of its absolute intensity (Page-McCaw et al. 2004; Vaquero et al. 2001). The adult mammalian retina activates dendrite sprouting and structural

remodelling of Muller cells, photoreceptor synapses, second and even third order neurons (e.g. bipolar cells, horizontal cells and RGCs etc.) when challenged by retinal detachment (Coblentz et al. 2003; Fisher and Lewis 2003; Lewis et al. 1998) and injection of kainic acid (Peichl and Bolz 1984). Figure 1-11 shows the upregulation of growth associated protein 43, which is associated with axon growth and synaptogenesis, as well as synaptic remodelling in experimental retinal detachment.

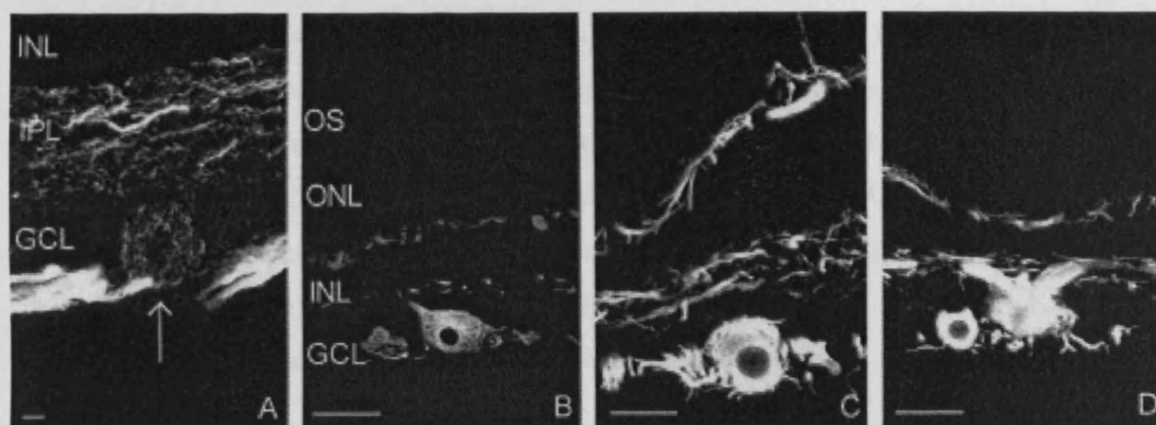


Figure 1-11 Anti-neurofilament (NF) labelling from normal (A), and 7 day detached (B-D) retinas. In the detached retinas anti-NF labelling was much more intense in retinal ganglion cells (B-D) and sometimes these cells show unusual processes that appeared to be growing from their cell bodies (C,D). (OS, outer segments; ONL, outer nuclear layer; INL, inner nuclear layer; GCL, ganglion cell layer.) Scale bar 25 μ m. Adopted from Coblentz et al. 2003.

1.6.4. Corrupted networks

In addition to structural and functional changes of RGCs, connectivity in the visual pathway may also begin to alter in response to glaucoma and ageing. As mentioned before, cell shrinkage was speculated to occur prior to RGC death, which may in turn promote the dendritic pruning and axon extension of the neighbouring RGCs. In late stage glaucoma, if cell death is restricted to the RGC layer, vision restoration might potentially be achieved by stopping cell shrinkage or promoting the dendritic extension of the remnant RGCs. However, if the cell death spreads to other layers, e.g. in INL and ONL, to restore vision loss means to rewire the corrupted networks.

1.6.5. Regulation of dendritic remodelling

There is a well-defined relationship between the dendritic morphology of a neuron and its function. Dendrites integrate information from an array of synaptic inputs; the branching pattern of dendrites determines the number and type of inputs that a neuron can receive. Previous studies indicate a key role for calcium signalling in dendritic growth and patterning. Calcium influx through voltage-gated calcium channels (VGCC) activate a transcriptional programme that regulates overall dendritic growth (Redmond et al. 2002; Wong and Ghosh 2002) (Figure 1-8). The effect of VGCC activation on dendritic growth was suppressed by pharmacological inhibitors of calcium/calmodulin-dependent protein kinases (CaM kinases), and mimicked by transfection of an activated form of CaM kinase IV (CaMKIV), but not CaMKII (Redmond et al. 2002). The best-characterized nuclear target of CaMKIV is the transcription factor cyclic-AMP-responsive-element-binding protein (CREB). One of the targets of CREB is the neurotrophin BDNF (Shieh et al. 1998).

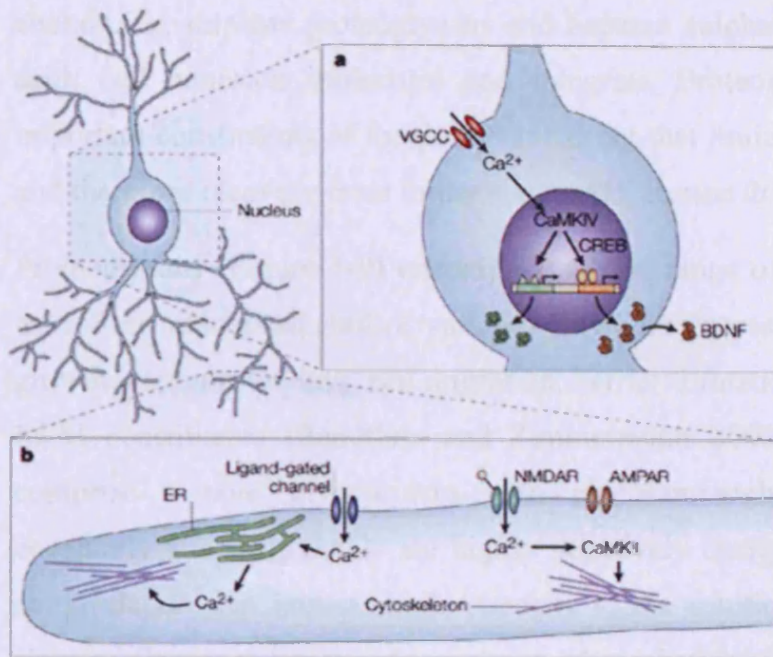


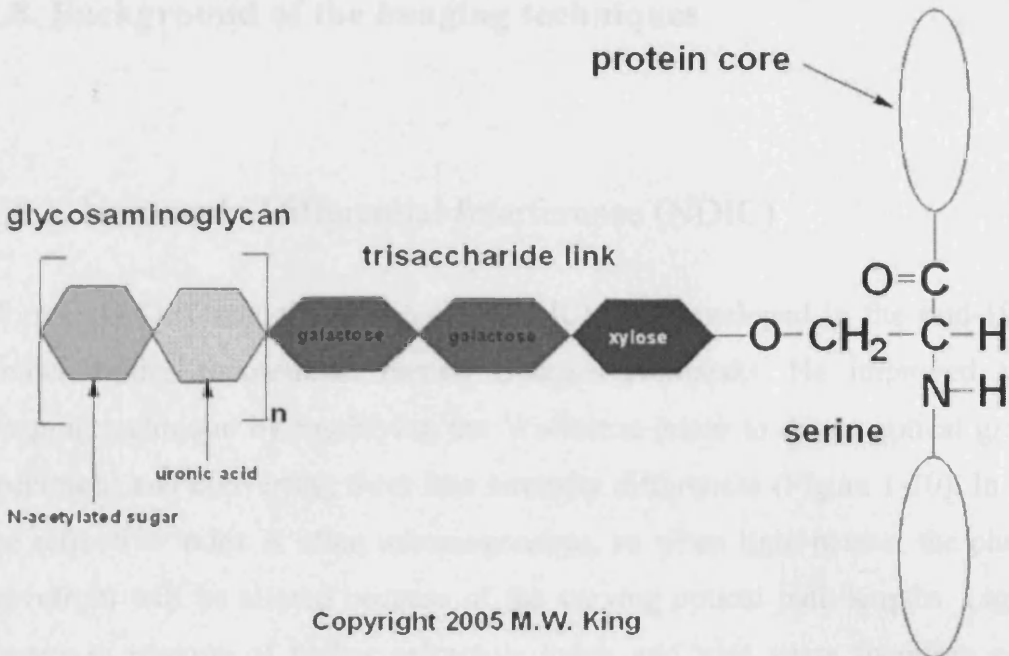
Figure 1-12 Schematic of mechanisms that might mediate calcium-dependent dendritic growth. **a.** In cortical neurons, calcium influx through voltage-sensitive calcium channels (VGCCs) leads to the activation of calcium/calmodulin-dependent protein kinase IV (CaMKIV). CaMKIV activates cyclic-AMP-responsive-element-binding protein (CREB) and other transcription factors, which regulate the expression of proteins that regulate dendritic growth. **b.** Calcium signalling pathways in dendrites that regulate branch stability. AMPAR, α -amino-3-hydroxy-5-methyl-4-isoxazole propionic acid receptor; BDNF, brain-derived neurotrophic factor; ER, endoplasmic reticulum; NMDAR, N-methyl-D-aspartate receptor. Adopted from Wong and Ghosh 2002.

1.7. Perineuronal net

Golgi and Cajal in the 1890s described a reticular system that was present on the surface of neuronal bodies and proximal dendrites. This is later on known as the perineuronal net, which is formed by extracellular matrix (ECM) materials that deposits on the cell surface around synaptic endings, as well as in the space between neurons and astrocytic processes. ECM is composed of glycoproteins, proteoglycans, hyaluronan, collagens; glycoproteins, particularly tenascin-C and tenascin-R;

chondroitin sulphate proteoglycans and heparan sulphate proteoglycans; hyaluronic acid; cell adhesion molecules and integrins. Proteoglycan is one of the most important constituents of the perineuronal net that limits the CNS from remodelling and therefore recovery from injury (Fox and Caterson 2002; Morgenstern et al. 2002).

Proteoglycans (Figure 1-9) encompass a wide range of complex molecules, which have been associated with a variety of cellular processes including cell adhesion, growth, receptor binding, cell migration, barrier formation and interaction with other ECM constituents (Bandtlow and Zimmermann 2000). These diverse molecules comprise a core glycoprotein with glycosaminoglycan (GAG) sugar chains covalently attached. GAGs are highly negatively charged molecules with extended conformation that imparts high viscosity to the solution. Each GAG consists of a simple, linear polymer of repeating disaccharide units, composed from two alternating monosaccharides: usually one sugar is an uronic acid and the other is either *N*-acetylglucosamine or *N*-acetylgalactosamine. Different types of GAG may be created as a result of sulphation and epimerization modifications that are carried out on the sugars themselves following polymerization. The length of GAG chains may also vary, from a polypeptide chain of just 10 kDa to 400 000 kDa; the core protein itself may have varying numbers of GAG chains attached, from one to well over 100. These result in a diverse array of PGs with a range of functional complexities. Many of the functional properties of PGs are attributed to the attached side chains; much of the interaction between PGs and cell-surface receptors or ECM proteins is thought to occur via binding sites on the GAG chains, although the core protein is also able to bind substrates (Bandtlow and Zimmermann 2000). The GAGs have high viscosity and low compressibility, which makes them ideal for a lubricating fluid in the joints. At the same time, their rigidity provides structural integrity to cells and provides passageways between cells, allowing for cell migration.



Copyright 2005 M.W. King

Figure 1-13 The structure of proteoglycan.

1.8. Background of the imaging techniques

1.8.1. Normarski Differential Interference (NDIC)

Normarski Differential Interference (NDIC) was developed in the mid-1950s by a French optics theoretician named Georges Nomarski. He improved the phase imaging technique by modifying the Wollaston prism to detect optical gradients in specimens and converting them into intensity differences (Figure 1-10). In a sample, the refractive index is often inhomogeneous, so when light passes, the phase of the wavefront will be altered because of the varying optical path lengths. Light travels slower in regions of higher refractive index and vice versa therefore contrast is obtained by converting these phase changes into amplitude changes. This technique emphasises edges and lines, rejects out-of-focus interference. If the refractive index changes are out of focus, it will be blurred and have a shallow spatial gradient in the focal plane, which will not contribute much to the contrast of the image. NDIC is well suited for studying the internal structures of un-stained samples.

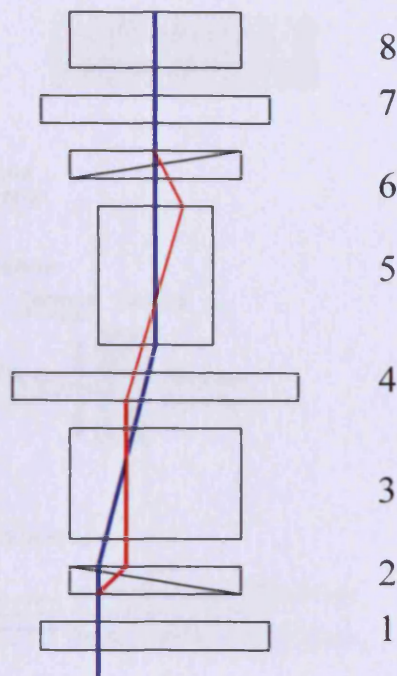


Figure 1-14 Illustration of DIC microscope. 1) Polarizer; 2) Nomarski prism; 3) Condenser; 4) Specimen; 5) Objective; 6) Objective Nomarski prism; 7) Analyzer; 8) Eyepiece. A plane-polarised wave front created by the action of the condenser 3) and polarizer 1) passes through the specimen 4). Wave front is collected by the objective 5) and is "sheared" into two offset wave fronts by the upper Wollaston prism 6). Because the optical paths are different between the ray-pairs, the specimen image is duplicated laterally and longitudinally. When the wave fronts pass through the analyzer 7), they are recombined into one vibration plane. This is where the constructive or destructive wave interference takes place. The differences in optic path are manifested as light or dark areas in the image. If there is no difference in the phase of the ray, it is showed as a uniform gray background.

1.8.2. Multiphoton confocal microscopy

The basic characteristic of confocal microscopy is that it eliminates all the out of focus information by a detection pinhole (Figure 1-11A). When a fluorescent molecule absorbs a single photon of light of a particular wavelength, the energy causes an electron to be excited to a higher energy level, and soon decay back to the ground state by emitting a photon of light, i.e. the fluorescence light one sees. In two-photon excitation, instead of absorbing a single photon, the fluorophore is excited by the near-simultaneous absorption of two photons, therefore emitting more energy and therefore a longer wave length light (Figure 1-11 B).

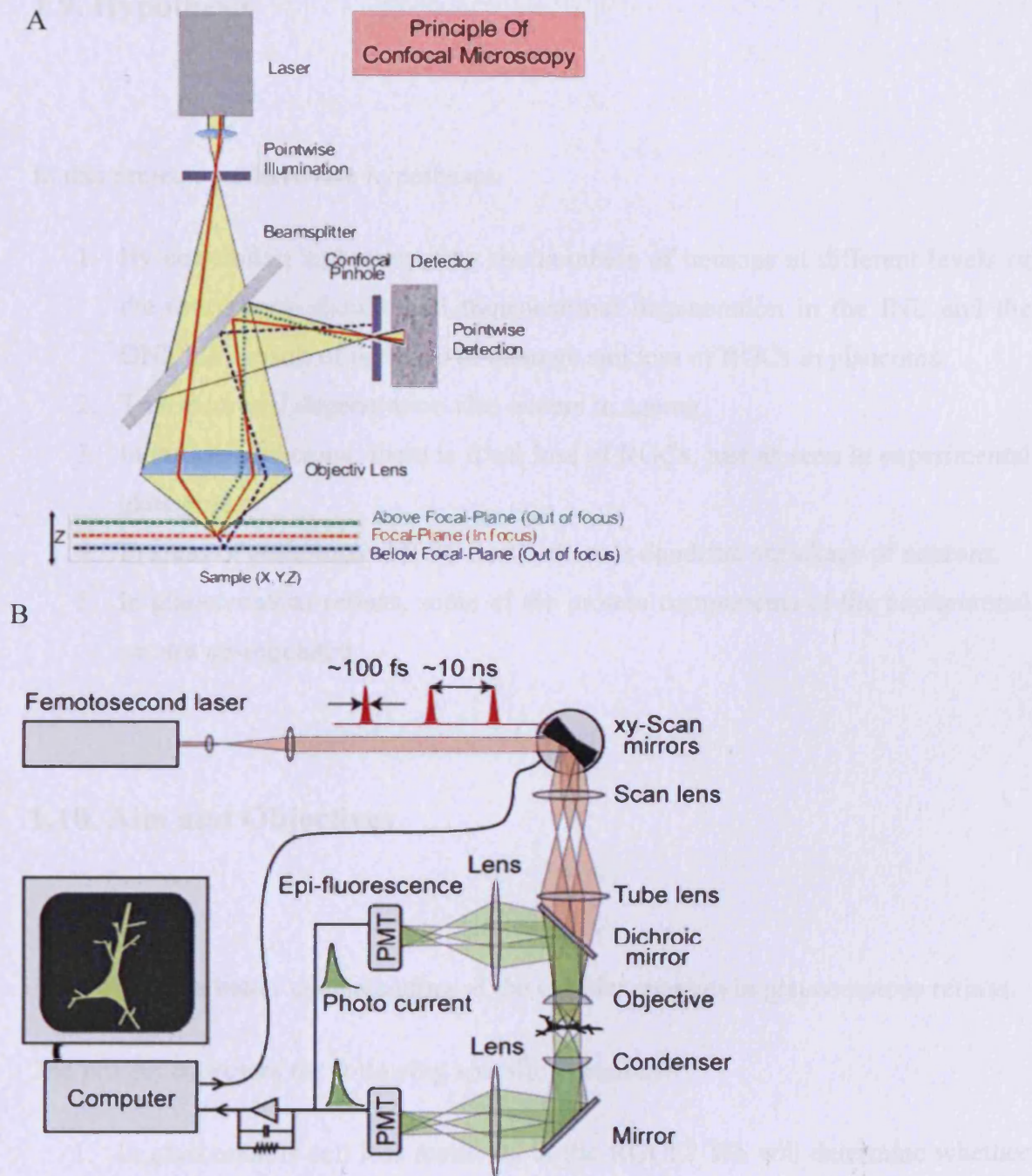


Figure 1-15 Structure of a confocal microscope (A) and multiphoton microscope (B). (A) The laser light is focused onto a small pinhole, which is split and directed by the beam splitter towards the sample. The fluorescent light emitted by the sample passes through the beam splitter and is focused onto the detection pinhole. Only light that passes the aperture finally reaches the detector. (B) Multiphoton excitation occurs at a tiny diffraction limited focal volume. Therefore, a confocal pinhole is not necessary. In fact, all photons, including those photons scattered when passing through the sample contribute to the image. PMT, photomultiplier tubes. A and B are adopted from http://fb6www.uni-paderborn.de/ag/ag-sol/fgruppe/mainframe/microscope_e.htm and Svoboda and Yasuda 2006, respectively.

1.9. Hypothesis

In this project, we have five hypotheses:

1. By correlating and comparing the numbers of neurons at different levels of the retina, one should find transneuronal degeneration in the INL and the ONL, as a result of optic nerve damage and loss of RGCs in glaucoma.
2. Transneuronal degeneration also occurs in ageing.
3. In human glaucoma, there is focal loss of RGCs, just as seen in experimental glaucoma.
4. In areas of pathological RGC death, there is dendritic shrinkage of neurons.
5. In glaucomatous retinas, some of the protein components of the perineuronal net are up-regulated.

1.10. Aim and Objectives

Aim: To gain a better understanding of the cellular changes in glaucomatous retinas.

The project addresses the following specific questions:

1. In glaucoma, is cell loss restricted to the RGCL? We will determine whether changes in other neuron populations occur as a result of RGC loss or whether outer retinal structure is preserved.
2. In ageing eyes, which population of neurons are most vulnerable? How does this compare with glaucomatous neuron loss? We will quantify trans-retinal degeneration of neurons in aged eyes by comparison with young eyes.
3. What is the topography of neuronal death in the RGCL in human glaucoma? We will determine the pattern of neuron loss by nearest neighbour analysis.

4. Do retinal ganglion cells remodel in response to surrounding cell loss? Do the dendritic trees of surviving cells expand to fill areas vacated by dead RGCs?
5. As part of the perineuronal net, which type(s) of proteoglycan was/were expressed in the human retina? We will analyse the expression of chondroitin-GAGs (CS-GAGs), keratan sulphated-GAGs (KS-GAGs) and aggrecan, versican, decorin, lumican and keratocan core proteins using monoclonal antibodies (mAbs) by immunohistochemistry.

CHAPTER 2 MATERIALS AND METHODS

2.1. Tissue source

Normal and glaucomatous human eyes were retrieved according to the ethical approval of Lions Eye Bank at the University of Washington, Mayo Clinic (MN, US) and Corneal Transplant Service at Bristol Eye Hospital, UK. The details of donors are listed in Table 2-1. All eyes were collected within 24 hours of cadaver time. All the glaucomatous eyes from Mayo Clinic were diagnosed as POAG, with last recorded IOP ranging from 15-30 mm Hg. Detailed clinical history for the rest of the eyes is not available except age, gender, ethnic origin (only for eyes from Lions Eye Bank) and the cause of death. All post-mortem human retinas were fixed in 4% paraformaldehyde within 24 hours of death. Eyes were kept in the fixative for at least three weeks before dissection.

Table 2-1 Details of eye donors used in this project.

Control eyes

Age (y)	Sex	Cause of death	Fixation
85	F	Ca. Pancreas	Within 24h
59	M	PM	Within 24h
74	F	PM	Within 24h
63	M	Glyoblastoma	Within 24h
73	M	PM	Within 24h
63	M	PM	Within 24h
79	F	PM	Within 24h
89	F	PM	Within 24h
23	M	PM	Within 24h
18	M	Overdose	Within 24h
33	F	PM	Within 24h

Glaucoma eyes

	Donor	164	172	173	177	178	179
	Date	2005	2006	2006	2006	2006	2006
	Age	77	67	81	84	77	83
	sex	F	M	F	M	M	M
	Year of death	1989	2002				2006
*Stage	R	1	3				3
*Stage	L	1	0				3
Max IOP	R	22	27				15
	L	28	16				16
Average IOP	R	17					12
	L	19					13
	Duration	16 years					1 month
	Eyedrops	xalatan OS	Xalatan,Cosopt,alp ha-OD	Lumigan;OD-Tru	timolol	cosopt, xal	xalatan OU
cup	R	0.4	0.5				0.9
cup	L	0.5	0.3				0.85
	VF R	normal					sup nasal
	VF L	normal					step
	Method	SITA **					sup arc
	Date	2005					SITA
							2006

*visual fields stage: stage 1, IOP only, no medication; stage 2, more than two medication, no damage; stage 3, mild field loss; stage 4, severe field loss; stage 5, filter

** SITA is short for Swedish interactive thresholding algorithm

2.2. Retinal preparation

2.2.1. Dissection of retina

After removing the anterior segment and vitreous humour, retina was freed from the pigmented epithelium. Four equal cuts were made on the retina, yielding 4 quadrants approximately 60° wide (Figure 2-1). The retina was flattened as much as possible, except for a few ripples at the ocular equator.

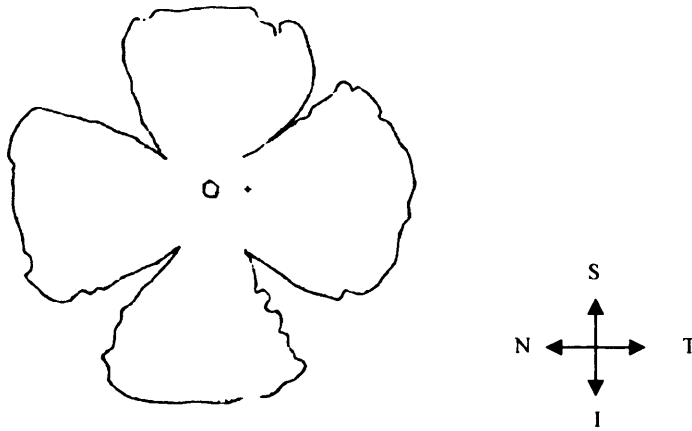


Figure 2-1 Retinal dissection for whole mount. Retinal directions (S = superior, N = nasal, I = inferior, T = temporal) are indicated. '+' and 'o' represent the fovea and optic disk, respectively.

2.2.2. Preparation of retinal whole mounts

We compared clearing retinal whole mounts by 100% DMSO (Sigma-Aldrich, UK) with dehydrating tissue by raised concentration of alcohol and xylene for NDIC imaging. A retinal whole mount was placed on a glass microscopic slide, cleared by 100% DMSO and mounted. The preparation was kept in the fridge overnight and rinsed in distilled water and re-mounted in glycerol (Sigma-Aldrich, UK) before imaging. For comparison, retinal whole mounts were also dehydrated sequentially in 2 changes of 50%, 70%, 90%, 100% alcohol and xylene for 5 minutes each.

2.2.3. Preparation of paraffin sections

Fixed human retinas were washed in distilled water for 30 min, then dehydrated in 50%, 70% and 90% ethanol (2 hours each), three changes of absolute ethanol (1 hour each), and three changes of xylene (2 hours each). After incubation in paraffin for 3 hours at 60°C (Thermo Shandon Citadel 2000, UK), retinal samples were transferred to plastic moulds filled with hot paraffin and allow to cool at room temperature. Finally, retinal transverse sections were cut at 7 µm thickness with a Surgipath rotary microtome, Germany. The sections were floated on water and picked up on glycerine-albumen coated glass microscope slides (RA Lamb, USA).

2.3. Histology

2.3.1. Haematoxylin and Eosin

First, retina cross sections were deparaffinized in 2 changes of xylene (5 minutes each), two changes of absolute alcohol, 95% alcohol and 70% alcohol and washed with tap water (2 minutes each). Second, sections were placed in haematoxylin solution for 5 minutes and washed with running tap water for 2 minutes. Third, sections were dipped in 1% acidic alcohol for 1 minute and washed with running tap water for 2 minutes. Fourth, sections were counterstained in eosin solution for 1 minute, washed and dehydrated through 95% alcohol, absolute alcohol and xylene (2 minutes each). Finally, sections were mounted with xylene based DPX mounting medium (Lamb, USA).

2.3.2. Immunofluorescence

2.3.2.1. RGCs labelling

Retinal whole mounts were labelled using TUJ-1 antibody (anti- β III tubulin; Molecular Probes, Invitrogen, UK) and SMI32 (Neurofilament Heavy antibody, Convence, UK). After PBS washes, retina whole mounts were incubated in the normal blocking solution containing 10% normal goat serum (Sigma-Aldridge, UK), 1% bovine serum albumin (Sigma-Aldridge, UK), and 0.2% Triton X-100 (Sigma-Aldridge, UK) for 1 hour. Then, the retinal whole mounts were incubated in the same medium with the primary antibodies (Table 2-2). After further washes, retinas were incubated in Alexa Fluor conjugated goat anti-mouse IgG solution (1:500 in PBS; Molecular Probes, Invitrogen, UK) and counterstained with 4'-6-Diamidino-2-phenylindole solution (DAPI solution, 0.1 μ g/mL in distilled water, Molecular Probes, Invitrogen, UK). Retinas were flat-mounted with the hardset mounting medium for fluorescence (VECTASHIELD®, Vector Laboratories, UK).

Table 2-2 Antibodies used to label retinal ganglion cells.

Primary Antibody	Host	Dilution	Incubation
TUJ-1	Mouse	1:500	Primary/secondary: over night at 4 °C
SMI32	Mouse	1:100	*Primary: 2 days at room temperature Secondary: 3 days at 4 °C

*The incubation time had to be prolonged to optimise the quality of the staining.

2.3.2.2. *Proteoglycans labelling*

12 human retinas were used in the study: young (18-33 yr, n=4), aged (60-85 yr, n=4) and glaucoma (67-89 yr, n=4). Retinal transverse sections were labelled using a range of monoclonal antibodies (mAbs) against CS-GAGs, keratan sulphated-GAGs (KS-GAGs), and aggrecan, decorin, biglycan, lumican, keratocan and versican core proteins (Table 2-2). All the mAbs in Table 2-2 were kindly donated by Prof Bruce Caterson, Cardiff University, UK. Positive and negative controls were included in the experiment: positive controls were paraffin sections of bovine cartilage; negative controls were retinal sections either without chondroitinase ABC treatment (1B5, 3B3 & 2B6) or without primary antibodies. For 1B5, 3B3 and 2B6, retinal sections were initially treated with 25 mU/ml chondroitinase in 0.1 M Tris Acetate (pH 6.8) to generate 'CS-stubs'. After 1 hour blocking in 5% bovine serum albumin in PBS (Sigma-Aldridge, UK), sections were incubated in Alex 488 conjugated goat anti-mouse IgG solution (1:400 in PBS; Molecular Probes, Invitrogen, UK), and counter stained with DAPI solution (0.1 µg/mL in distilled water). Sections were incubated in 50 mM CuSO₄ solution (pH 5) for 30 minutes to reduce autofluorescence (Schnell et al., 1999). Finally, sections were mounted with ProLong Gold anti-fade reagent (Molecular Probes, Invitrogen, UK).

Table 2-3 Antibodies against various proteoglycans used to identify their expression in the human retina.

Primary antibody	Host	Dilution
1B5	Mouse	1:100
1C6	Mouse	1:50
2B6	Mouse	1:100
3B3	Mouse	1:100
6B4	Mouse	1:50
7D1	Mouse	1:50
5D4	Mouse	1:50
Decrin	Mouse	1:50
Keratocan	Mouse	1:50
Lumican	Mouse	1:50
Vercican	Mouse	1:50
PR8A4	Mouse	1:20
8A4 (link protein)	Mouse	1:10

2.3.3. Fast red

Alkaline phosphatase chromogen kit (Fast Red, Dako, UK) was used as an alternative to the fluorescein staining. After TBS (tris-buffered saline) washes, retinal whole mounts were incubated with primary antibody TUJ-1 overnight at 4 °C. After further washes in TBS, the retina was incubated with biotinylated antibody (Dako, UK) at 4°C overnight. On the third day, the retina was incubated in alkaline biotin complex and alkaline phosphate substrate solution (Dako, UK) for 3 hours and 30 minutes, respectively, at room temperature. Finally, the samples were washed in distilled water and observed under a light microscope.

2.4. Dendritic labelling

2.4.1. Intracellular injection of dyes

The intracellular injection rig is illustrated in Figure 2-2AB. The retina was placed in a tissue chamber containing PBS with the RGCL uppermost. The retina was held in place by a nylon net. The tissue chamber was positioned on a fixed stage epifluorescence

microscope (MicroInstruments, Oxford, UK). Micropipettes were pulled from filament containing capillary glass (Clark Electromedical Instruments, Reading, U.K.; GC120-FIO). Micropipettes were backfilled with 15% lucifer yellow (M395, Sigma, UK) in 0.1 M lithium chloride. The process of injection was observed through a water immersion long working distance objective (x40/0.75 NA, Zeiss, Germany). The micropipette was advanced at an angle of ca. 35° to the retinal surface; cell bodies were impaled under direct visual control and filled with lucifer yellow by applying small oscillating hyperpolarising currents across the electrode tip (1-2 nA, 500 milliseconds, 1 Hz). The molecular weight of this dye is sufficiently low that it rapidly diffused away from the field of view, even when the tip was in the extracellular matrix of the retina. As soon as the tip penetrated a cell, its soma and proximal dendrites were rapidly filled with lucifer yellow, indicating that the tip was intracellular. Cells were judged to be completely labelled when a sufficient extent of axon and the finest dendritic processes were clearly visible.

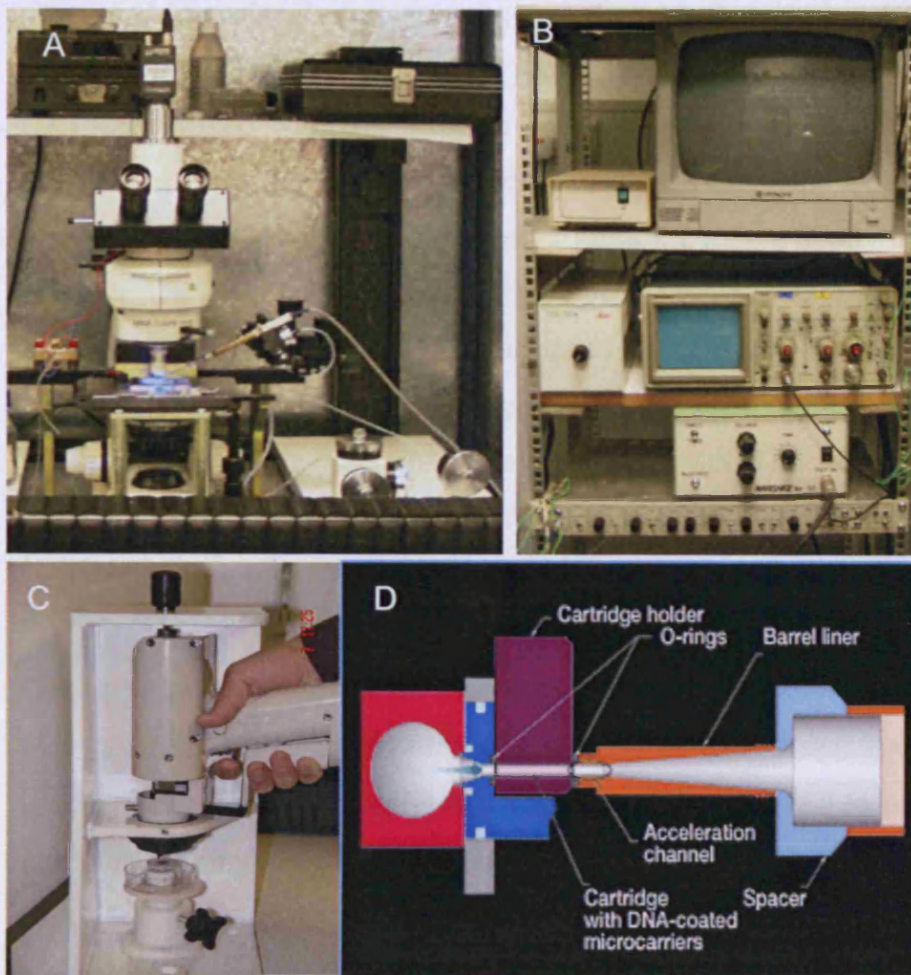


Figure 2-2 Experimental set ups of intracellular cell filling rigs (A&B, Becker's lab, department of anatomy and developmental biology, UCL, UK); gene gun shooting arrangement (C), and the structure of gene gun system (D).

2.4.2. DiOlistic delivery

2.4.2.1. Preparation of gene gun 'bullets'

Although intracellular dye-filling remains an effective approach in revealing the dendritic morphologies of retinal neurons, it is labour intensive especially when a large number of cells need to be labelled. Ballistic labelling, which was initially used for introducing plasmid into plant cells, was developed to transfect neurons with lipid soluble dye particle (reviewed by Grutzendler et al., 2003). Detailed protocol of preparing gene gun 'bullets' can be found at <http://thalamus.wustl.edu/wonglab/genegun.html>. In brief, 3 mg of DiI, DiO and DiD

mixture (Molecular Probes, Invitrogen, UK) were dissolved in 600 μ l dichloromethane (Sigma-Aldrich, UK). A total of 40 mg of tungsten particles (1 μ m diameter; Bio-Rad, UK) were mixed with dye solution and spread onto a glass slide. The lipophilic dye precipitates onto the tungsten particles as dichloromethane evaporated. A razor blade was used to sweep off the dye coated particles into a 1 mL eppendorf. Tefzel tube (Adtech, UK) had been pre-coated by injecting polyvinylpyrrolidone (PVP, 10 mg/mL in ethanol; Sigma-Aldrich, UK) before tungsten particles were introduced. The tube was then inserted into a tubing preparation station (Bio-Rad, Catalog No. 165-2420, UK) to allow particle precipitation onto the tube wall. The nitrogen gas dried tubing was cut into 13 mm 'bullets', and stored in the dark at 4°C.

2.4.2.2. Bullet delivery

Gene gun bullets were expelled from the Bio-Rad gene gun system at pressures ranging from 80 and 110 psi. A Millipore nitrocellulose filter insert (pore size 0.22 μ m) was placed between the gun barrel and the tissue (Figure 2-2C) to prevent large clumps of particles landing on the tissue and to reduce the shock wave. This method labelled RGCs of live and fixed tissue. However, fixation time and temperature should be controlled; otherwise, the carbocyanine dyes tend to leak out.

2.5. Microscopy

2.5.1. Nomarski Differential Interference Contrast (NDIC) microscopy

Retinal whole mounts cleared by DMSO (Sigma-Aldrich, UK) were imaged using the NDIC mode of the microscope (Leica DMRA2; objective: HCS PLAN APO 40x/0.75 PH2).

2.5.2. Confocal microscopy

Immunofluorescent staining of retinal whole mounts was imaged by confocal microscopy (Leica TCS SP2 confocal system equipped with a Leica DMRE microscope,

Milton Keynes, UK; Figure 2-3). Fluorescent profiles were first located using epifluorescence illumination before taking a series of *xy* optical sections throughout the depth of the retina. The laser and excitation lines used in the current project are listed in Table 2-3.

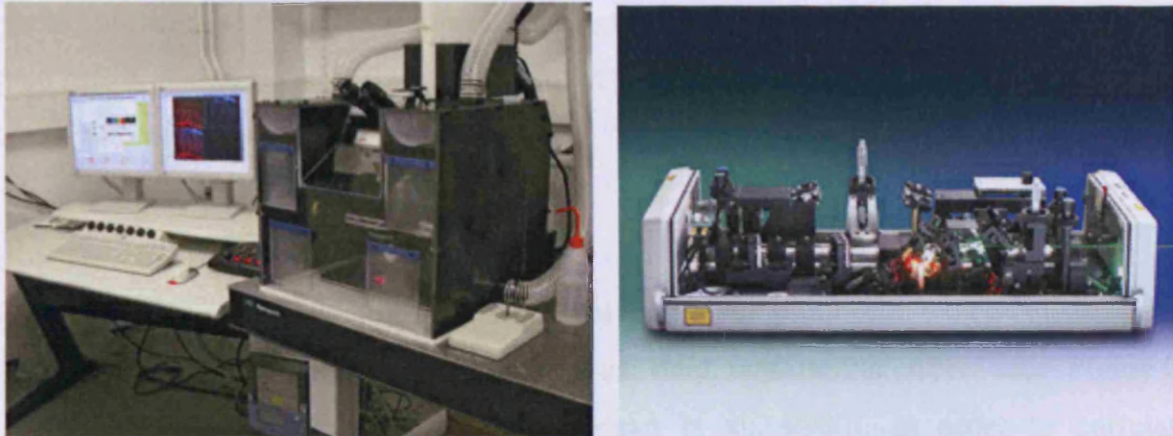


Figure 2-3 Multiphoton-ultraviolet (MPUV) confocal microscope system. MPUV consists of a Leica upright microscope with motorised xyz stage. Multi- and single- photon lasers are available, including ultraviolet, blue-argon, green-krypton, and green-helium etc. The wavelength of mutliphoton laser ranges from about 700nm - 1000nm, which excite fluorophores from ultraviolet to Cy5 range.

Table 2-4 Excitation lines and laser types used in the current project.

	Excitation (nm)	Laser
FITC/Alex 488	488	Argon
Lucifer yellow	488	Argon
DAPI	351 & 364	Ultraviolet
Dil	543	Argon

2.6. A novel approach to quantify retinal transneuronal degeneration

2.6.1. Image acquisition

Retinas were stained by DAPI solution (3 $\mu\text{g}/\text{mL}$ in PBS) overnight at 4°C and whole mounted with RGCL uppermost in a hard set mounting medium for fluorescence (VECTASHIELD[®] Mounting Medium). The specimen was placed on a motorised

microscope stage that allowed the selection of any retinal location to an accuracy of 1 μm . DAPI molecules were excited by the 843 nm line of the Ti-Sapphire Tsunami multiphoton laser (SpectraPhysics, UK). Images were acquired by the confocal system mentioned above (HCX PL Apo 40/1.25 NA oil CS objective lens). Individual xy scans were built into a xyz stack or a projected image. Standard settings of laser power, gain and offset, pinhole size of the confocal microscope were kept constant at each session to facilitate comparisons between retinas.

2.6.2. Data collection

In order to relate retinal pathology to clinical data, a sampling grid, which corresponded to the test locations in a Humphrey 30-2 visual field, was used to collect data (Figure 2-4) (Kerrigan-Baumrind et al., 2000; Morgan et al., 2000). In order to correlate anatomical positions on the retina to the visual field, the distance (mm) was converted to degrees of visual angle according to a nonlinear conversion of retinal magnification factor (Drasdo and Fowler, 1974) ($y = 0.035x^2 + 3.4x + 0.1$, where y is the eccentricity in arc degrees, and x is in millimetres).

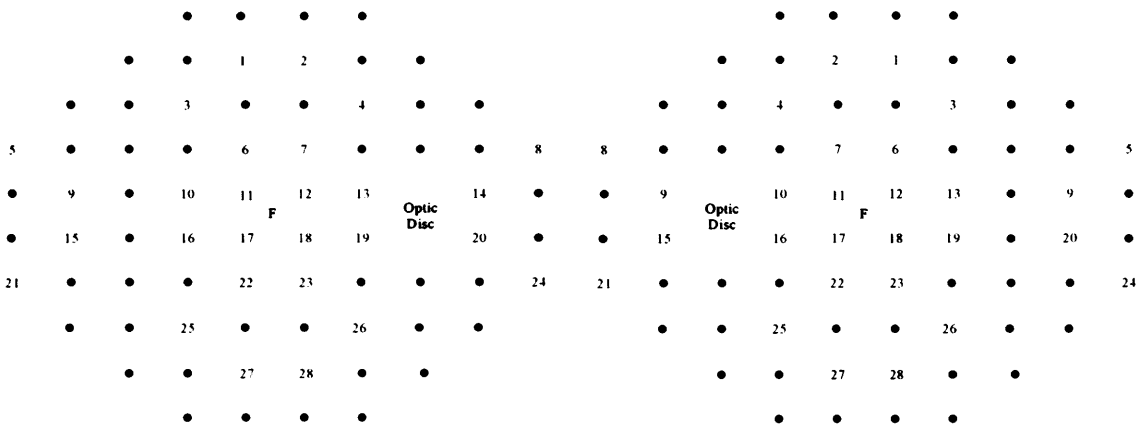


Figure 2-4 The sampling grid used to quantify retinal cells. The position of fovea (F) and optic disc are used as reference points. Each point on the grid is 1.7 mm apart (equivalent to 6 degrees eccentricity). 28 red points are sampling positions.

2.6.3. Automated detection of cell nuclei

Neuron nuclei were detected and counted using an established method (Byun et al., 2006), which has been implemented as a plug-in in the public domain of ImageJ (version 1.34, US National Institutes of Health). In this model, nuclei were considered as a class of ‘blob-like’ structures (Byun et al., 2006). Macros were developed to

convert the projected images in each layer of the retina firstly to grey level images (Figure 2-5); after an appropriate amount of Gaussian blurring, the resultant image was duplicated, and one of them was converted to a binary image and served as a mask to extract nuclei from the background. In each image, the average nuclei diameter was determined to give the width threshold in pixels. Endothelial cells (elongated nuclei), astrocytes (Ogden, 1978) and glia cells (Ramirez et al., 1996) could be distinguished from neurons by their laminar location, small size, and nuclear morphology. In addition, 'forbidden lines' were applied that objects touching two out of four edges of a measuring field were excluded from the analysis, because failure to do so often results in overestimation or under estimation of cell numbers, i.e. all objects/none touching the edge objects are included will result in over-/under- estimations.

The number of neurons in RGCL was corrected for the presence of displaced amacrine cells in RGCL to give RGC counts, i.e. there were 0.3% to 24% amacrine cells between 0.5 to 4 mm eccentricity in the human retina (Curcio and Allen, 1990; Curcio and Drucker, 1993).

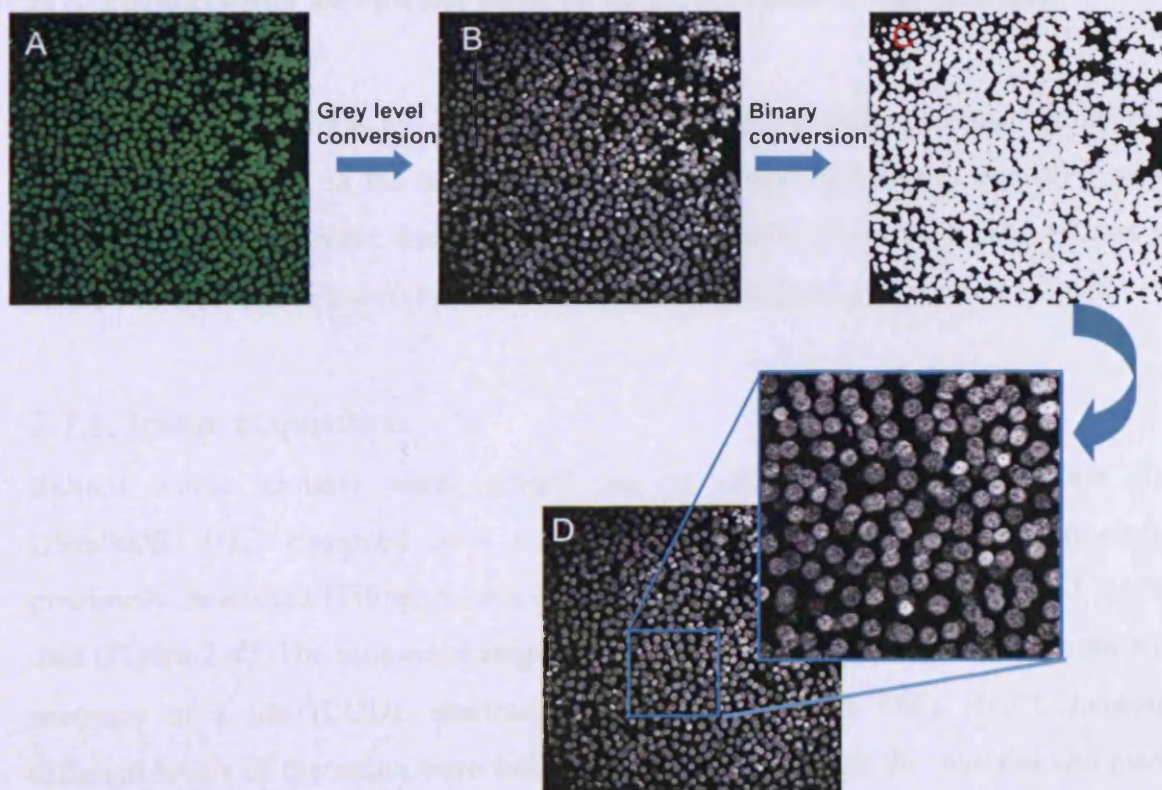


Figure 2-5 Nuclei detection design. Original image (A) is converted to a grey level image (B), then a binary image (C), finally the result image (D) and the nuclei identified are labelled by red dots.

2.6.4. Method validation

The automated quantification of DAPI stained nuclei was compared with the manual count of the same image; false positives and negatives were recorded. The multiphoton-DAPI method was also validated against the conventional NDIC method (Curcio and Allen, 1990; Curcio and Drucker, 1993) by comparing RGC counts for the same specimen.

2.6.5. Statistics

Statistical analysis was performed in SPSS 14.0 for Windows. A general linear model was used to compare neuron densities and ratios at different eccentricities of the retina in control and glaucoma groups. For each retina, given that measurements were taken at six different eccentricity levels, 'repeated measures' analysis was performed with Bonferroni correction. Differences were considered significant at the 95% level of confidence or higher.

2.7. Topography of retinal neuron degeneration in the RGCL

Six glaucomatous retinas (67-83 years old) and six age-matched control retinas (61-89 years old) were used in the study. Although the clinical histories of control eyes were not available, none were from patients receiving ophthalmic care. The retinas were stained by DAPI solution (0.1 µg/mL in PBS) for 20 minutes and whole mounted.

2.7.1. Image acquisition

Retinal whole mounts were imaged on an epifluorescence microscope (Leica DM6000B, UK) equipped with a digital camera (MBF CX9000, Germany), as previously described (Filippopoulos et al., 2006). A sampling grid was used to collect data (Figure 2-4). The motorised stage allowed the selection of any retinal location to an accuracy of 1 µm (LUDL electronics encoder, Mac5000, UK). RGCL neurons at different levels of the retina were imaged by focusing through the material and marking the centre of all cells. 22 frames were taken per retina using x10 objective (HC PL APO

NA 10x/0.40, Leica, UK) to cover 30% of the area corresponding to the central 15 deg of vision (4 mm eccentricity).

2.7.2. Morphometric data collection

The morphometric analysis is similar to section 2.6.3 except that the minimum width for searching nuclei centres was set to 10 pixels and threshold level was 0.3 pixels. The images were further processed by particle counting function in NeuroLucida (MicroBrightField, Inc) and NNDs calculated by NeuroLucida Explorer (Figure 2-5, MicroBrightField, Inc). The NNDs of automated quantification was validated against manual method. Endothelial cells (elongated nuclei), astrocytes (Ogden, 1978) and glia cells (Ramirez et al., 1996) were filtered and excluded on the basis of their shape, size and laminar organisation. Images were further processed using a particle counting function in NeuroLucida (MicroBrightField, Inc) and the NNDs determined by NeuroLucida Explorer (MicroBrightField, Inc). The NNDs of automated quantification were validated against manual method. In the central retina where there were several layers of the cells, the results from 2D NNA was validated by 3D NNA based on multiphoton images of DAPI staining acquired by Leica TCS SP2 confocal system equipped with a Leica DMRE microscope (HCX PL Apo 40/1.25 NA oil CS objective lens; Leica, Milton Keynes, UK) (n=6). In the 3D image stacks, the centre of each nuclei was marked by cell counter plug-in of ImageJ and the xyz coordinates were determined (Figure 2-6); the NNDs were calculated by a macro written in ImageJ (
$$\text{NND} = \sqrt{(x_1 - x_2)^2 + (y_1 - y_2)^2 + (z_1 - z_2)^2}$$
, where (x_1, y_1, z_1) and (x_2, y_2, z_2) are the xyz coordinates of the two nearest neighbour cells.

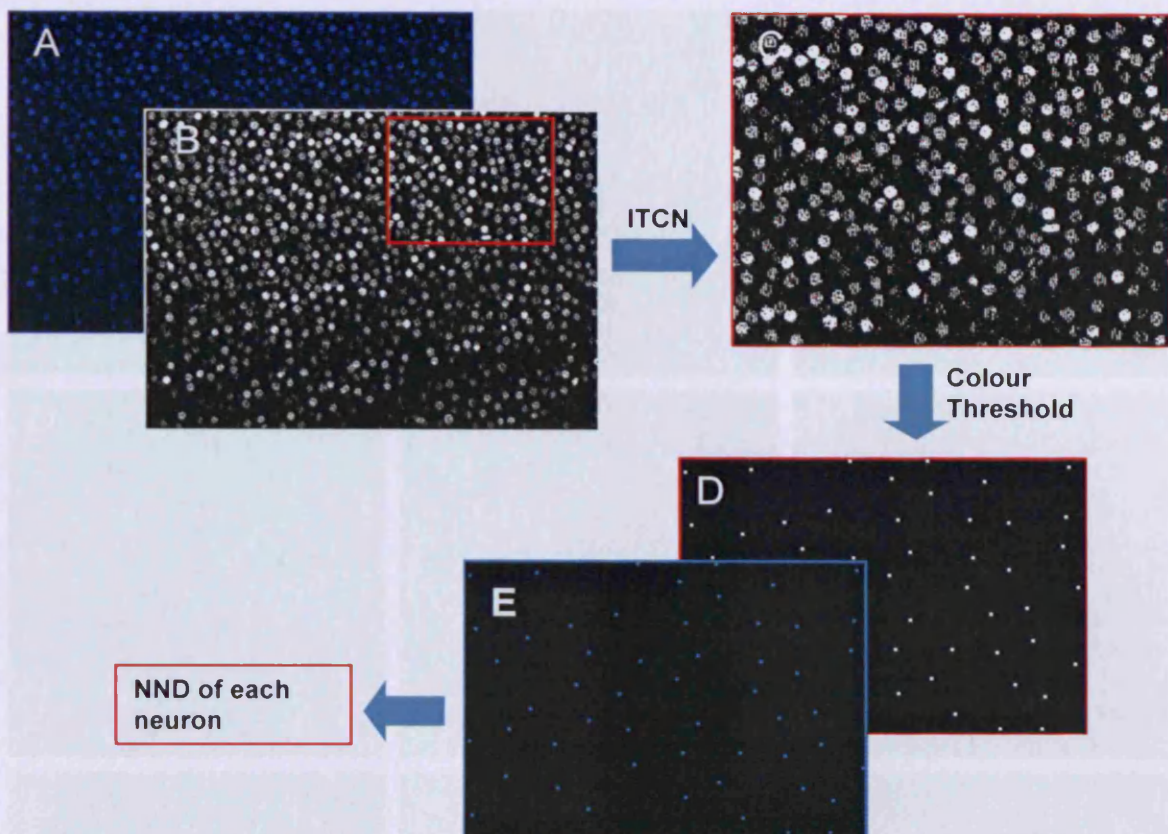


Figure 2-6 Morphometric processing of the images to calculate NNDs. In ImageJ, the original images (A) were converted to grey level (B) to identify the cell nuclei (ITCN, C). The centre of each nucleus is labelled by a single 'red dot' the size of 1 pixel (C). The green and blue channels of the image were then turned off by colour threshold function, leaving only 'dots' to represent cell nuclei centres (D). After Kodaith transform in NeuroLucida, the NND of each neuron was calculated.

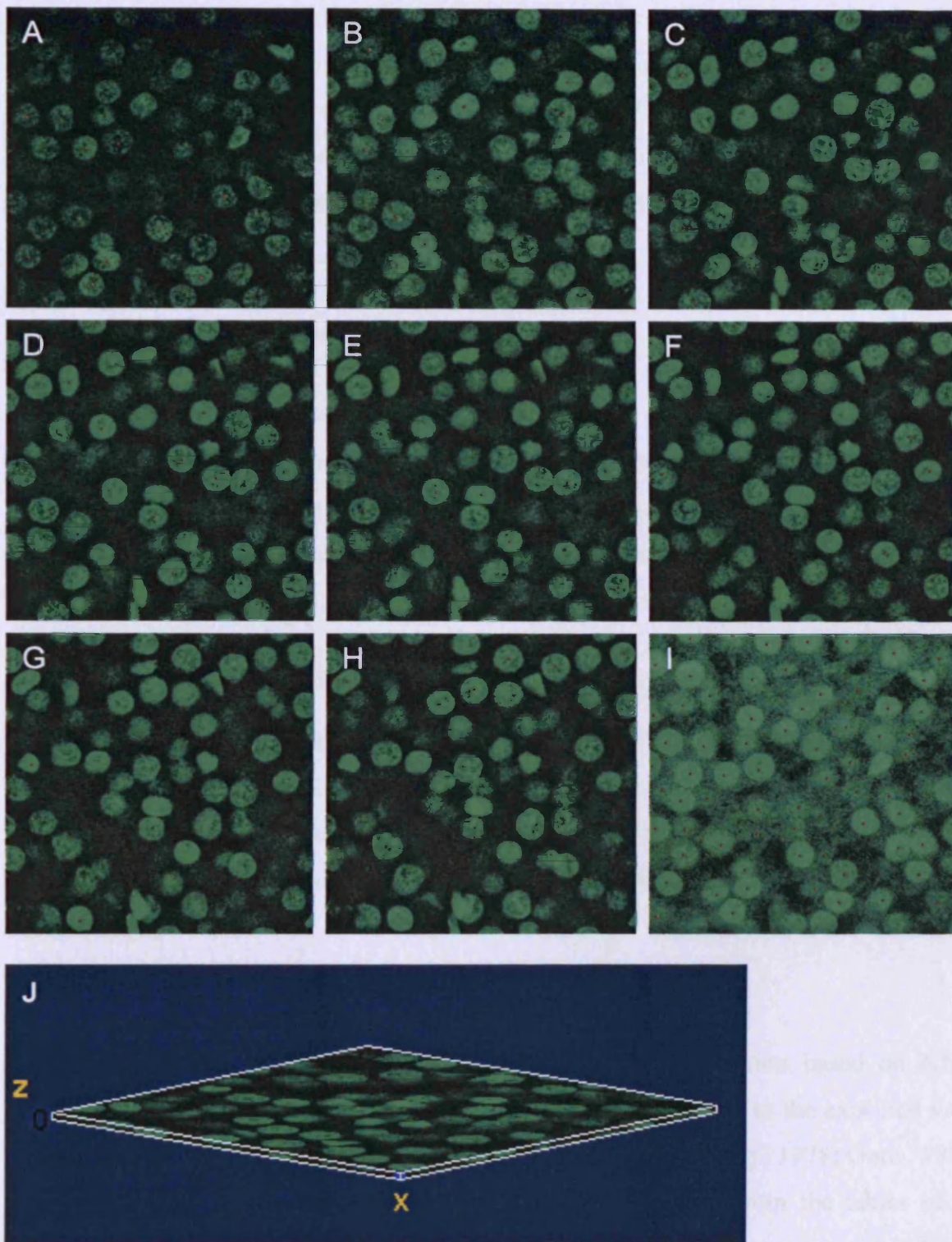


Figure 2-7 Multiphoton images of DAPI labelled cell nuclei in the retinal ganglion cell layer. A-H is individual series images of cells at different z planes of the retina whole mount. I is the projection image of A-I. 3D nearest neighbour analysis was based on image A-H.

A computer simulation model was designed in Image Pro Plus 4.0 to test the deviation of RGC NNDs caused by displaced amacrine cells. Ten images were selected from each group to cover the whole range of neuron densities. Assuming that there were 10% displaced amacrine cells within the retinal area examined (Curcio and Allen, 1990), NNDs were compared before and after the random removal 10% of the points (n=6).

2.7.3. Nearest neighbour analysis

2.7.3.1. Nearest neighbour distances (NNDs)

The average NNDs in glaucomatous retinas (n=6) were compared with that of age-matched control retinas (n=6). Since the data was not normally distributed, a nonparametric test for two independent samples (Mann-Whitney U) was applied in SPSS 14.0 for Windows. Differences were considered significant at the 95% level of confidence or higher.

2.7.3.2. The regularity index (RI)

RI was calculated to quantify the regularity level of the neuronal spatial patterns. RI is the ratio of average NNDs to the standard deviation (SD) of NNDs within a sample. For a random pattern, RI significantly above 2 may indicate a degree of regular spacing (Cook, 1996).

2.7.3.3. Nearest neighbour index (NNI)

NNI measures the degree of spatial dispersion in the distribution based on NNDs (Figure 2-7). NNI is calculated as the ratio of the average NNDs to the expected value of NNDs in a random pattern of the same mean density (Donnerlly, 1978; Getis, 1998). z-statistic indicates if a NNI value is significant, i.e. z-score from the tables of the normal distribution for $\alpha = 0.05$ (2-tail) is ± 1.96 . A negative z-score indicates clustering; a positive score means dispersion.

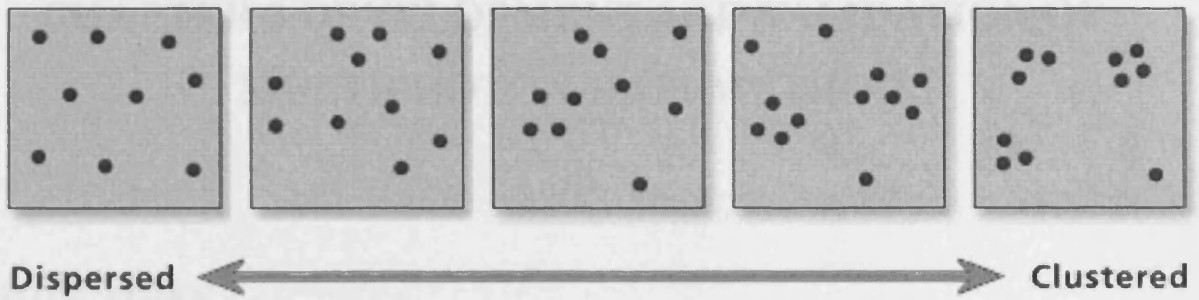


Figure 2-8 Nearest neighbour index (NNI) indicates the degree of spatial dispersion and/or clustering. The values of NNI range between two theoretical extremes: 0 and 2.1491. $NNI=1$, the data is randomly distributed; $NNI>1$, dispersed points; $NNI<1$, clustering.

3.4. Introduction

It was recognized that advances in the RC/L and the ONL would be required to improve histological contrast (NDR) microscopy in determining the overall tissue quality in the early stages of diagnosis, to the upper retina (Curcio 2001; Curcio and Allen 1990). The development of RC/L would be supported by TUB-7 labelling. However, the conventional imaging techniques including NDR and single plane fluorescence were hindered by their depth of field requirements which overexposed the middle layers of the retina.

Here I report the development of a novel approach using multiplexed confocal microscopy to image DAPI labelled nuclei at defined layers of the retina (multiplexed-DAPI method). This technique optically dissects retinal structures and provides high resolution, high contrast images. It not only avoids background saturation but also allows correlation of in vivo quantitative at different layers of the retina.

CHAPTER 3 DEVELOPMENT AND VALIDATION OF MULTIPHOTON-DAPI METHOD

OBJECTIVES

- To develop a method to quantify and correlate neuron densities in the RGCL, INL and ONL of human retinal whole mounts
- To evaluate the accuracy of the method developed

3.1. Introduction

It was proposed that neurons in the RGCL and the ONL would be counted by Nomarski Interference Contrast (NDIC) microscopy to determine the correlated neuron loss in the outer retina in relation to the inner retina (Curcio 2001; Curcio and Allen 1990). The presence of RGCs would be confirmed by TUJ-1 labelling. However, the conventional imaging techniques, including NDIC and single photon microscopy were restricted by their depth of field in detecting subtle changes in the middle layers of the retina.

Here I report the development of a novel approach using multiphoton confocal microscopy to image DAPI labelled nuclei at defined levels of the retina (multiphoton-DAPI method). This technique optically dissects retinal whole mounts, and provides high resolution, high contrast images. It not only avoids tissue dehydration but also allows correlation of neuron quantities at different layers of the retina.

3.2. Results

3.2.1. Comparisons of retinal staining methods

The retinal transverse sections were stained by haematoxylin and eosin (H&E), which showed nuclei at different layers of the retina (Figure 3-1). However, this method is predisposed to tissue shrinkage, and is limited by the number of neurons presented at any given location.

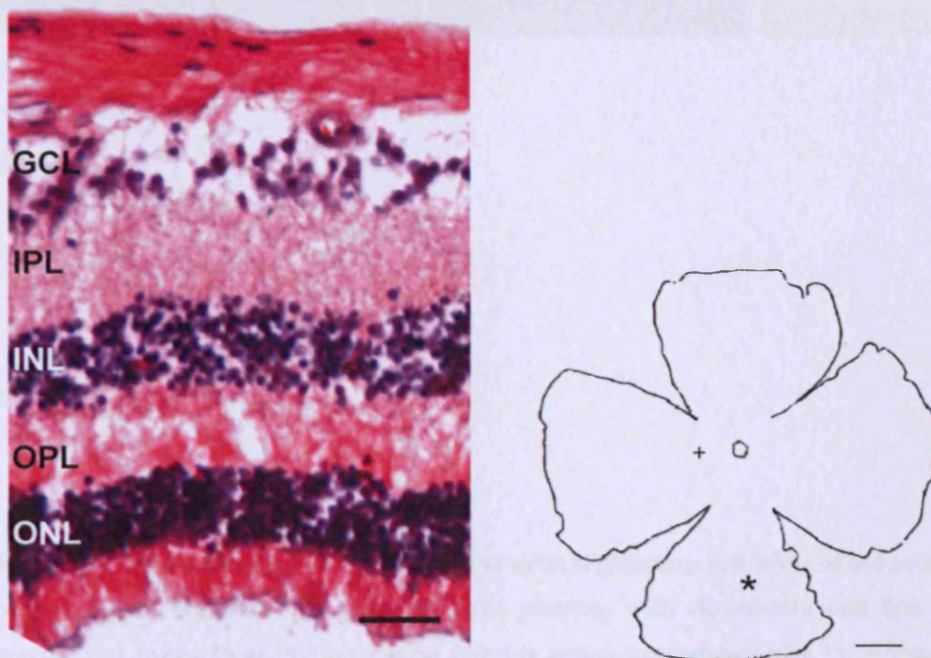


Figure 3-1 Haematoxylin and eosin staining of a retinal paraffin transverse section from the inferior mid-peripheral retina (as indicated by *). The retina is from a normal Caucasian male donor of 63 years old. GCL, ganglion cell layer; IPL, inner plexiform layer; INL, inner nucleus layer; OPL, out plexiform layer; ONL, outer nucleus layer. + represents the position of the fovea, and o is the optic nerve. The scale bar of A is 40 μm and B is 5 mm.

In the retinal whole mounts, cells labelled by fluorescein were much clearer than those labelled by fast red (Figure 3-2).

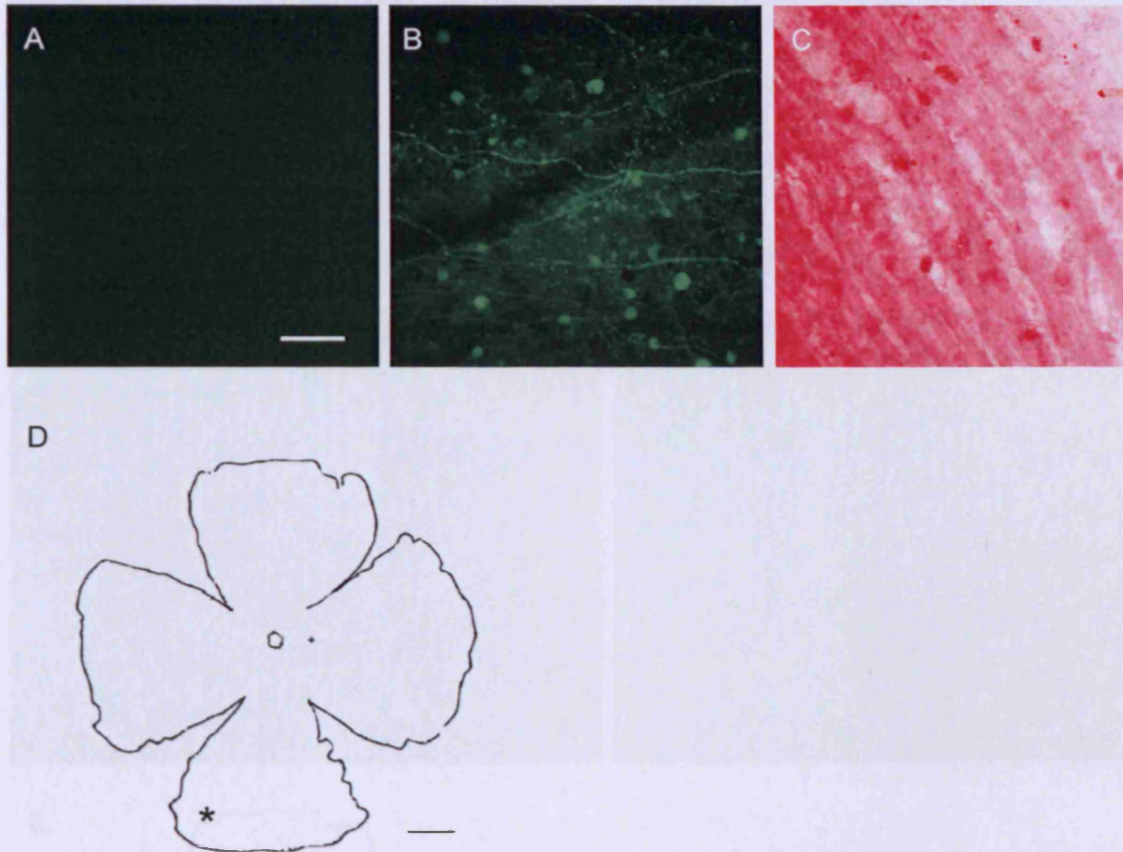


Figure 3-2 TUJ-1 labelling of neurons in the retinal ganglion cell layer of the retinal whole mounts. (A) is the negative control. (B) and (C) show staining with fluorescein and fast red respectively. The sample was taken from the peripheral inferior retina (as indicated by *). + represents the position of the fovea, and o is the optic nerve. The scale bar of A-C is 100 μ m and D is 5 mm.

3.2.2. Nomarski imaging of retinal whole mounts

DMSO cleared tissue yielded good quality sample preparations for NDIC imaging in less time compared with the tissue dehydration method by alcohol and xylene. NDIC was used to image neurons in the RGCL in the unstained retinal whole mounts (Figure 3-3).

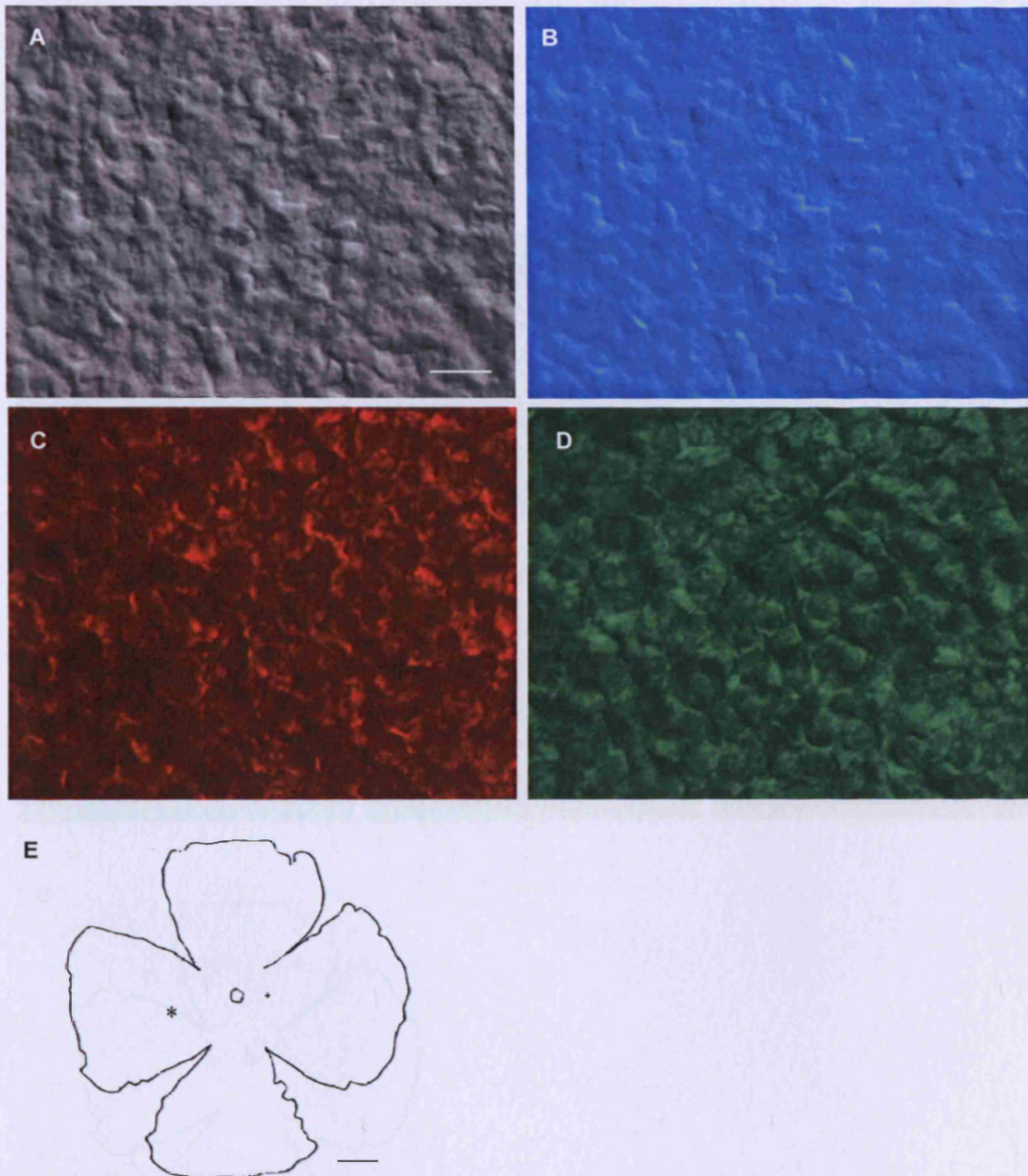


Figure 3-3 Nomarski differential interference contrast (NDIC) imaging of cells in the retinal ganglion cell layer. Changing the position of the objective Nomarski prism produces a corresponding spectrum of interference colours in the specimen image (A-D), i.e. optical staining. The retina is from a normal Caucasian male donor of 63 years old. The sample was taken from the nasal retina (as indicated by *). + represents the position of the fovea, and o is the optic nerve. The donor is a The scale bar of A-D is 100 μm and E is 5 mm.

On focusing down, neurons in the RGCL and the INL appeared sequentially (Figure 3-4). However, with NDIC method, no cell body could be clearly seen beyond Figure 3-4 F as it was focused from the RGCL to the INL. This is due to the short depth of field of Nomarski microscopy. Figure 3-5 shows typical images of RGCL neurons in the central and mid-peripheral retina.

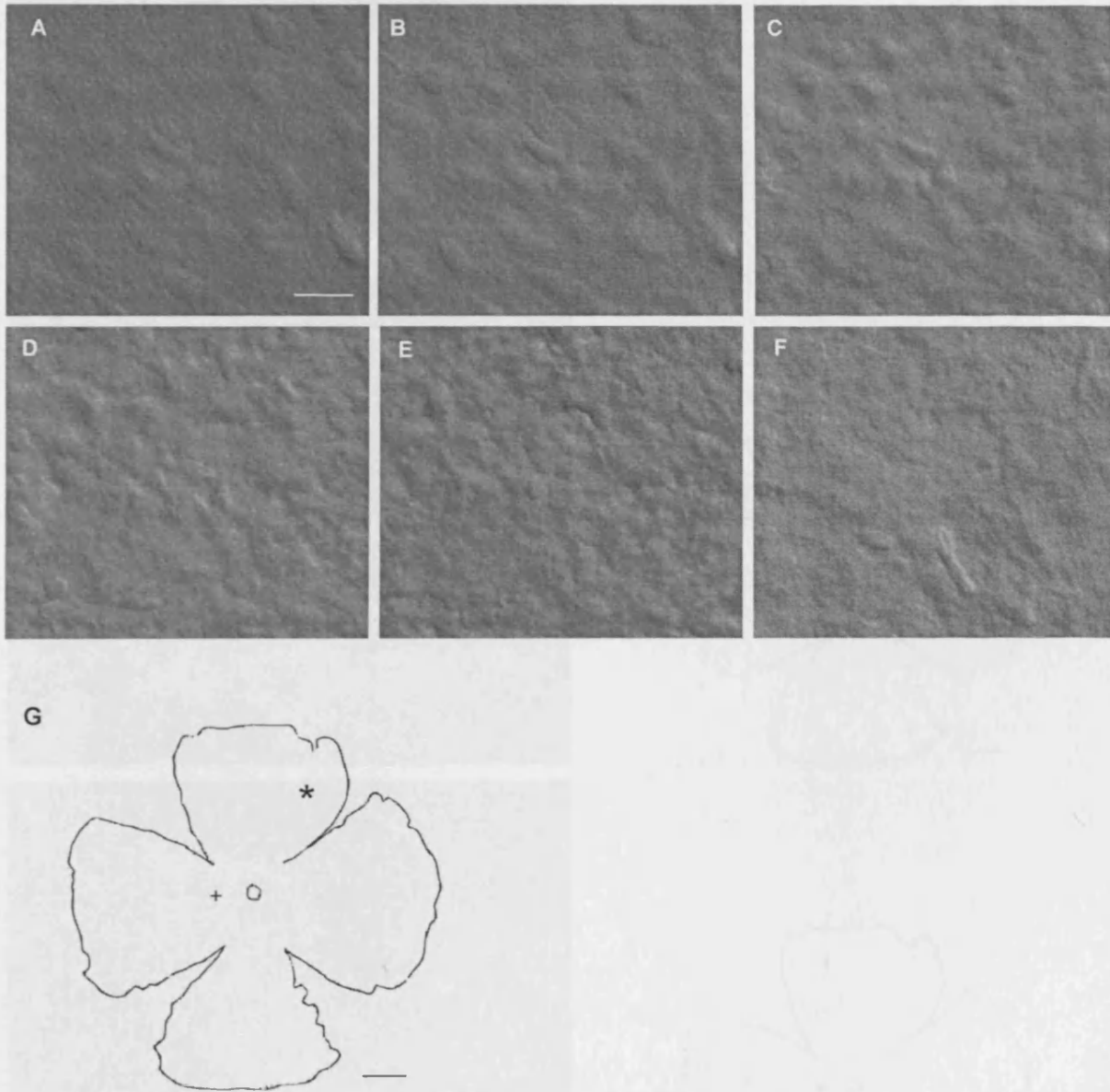


Figure 3-4 NDIC images of the retinal ganglion cell layer. Focusing down meant cells in difference planes of the RGCL gradually appeared in sharp focus (A-E). F is the end of the RGCL and the beginning of inner plexiform layer (IPL), beyond which point no cell body could be observed in sharp focus. The retina is from a normal Caucasian male donor of 63 years old. The sample was taken from the nasal retina (as indicated by *). + represents the position of the fovea, and o is the optic nerve. The scale bar of A-F is 40 μm and G is 5 mm.

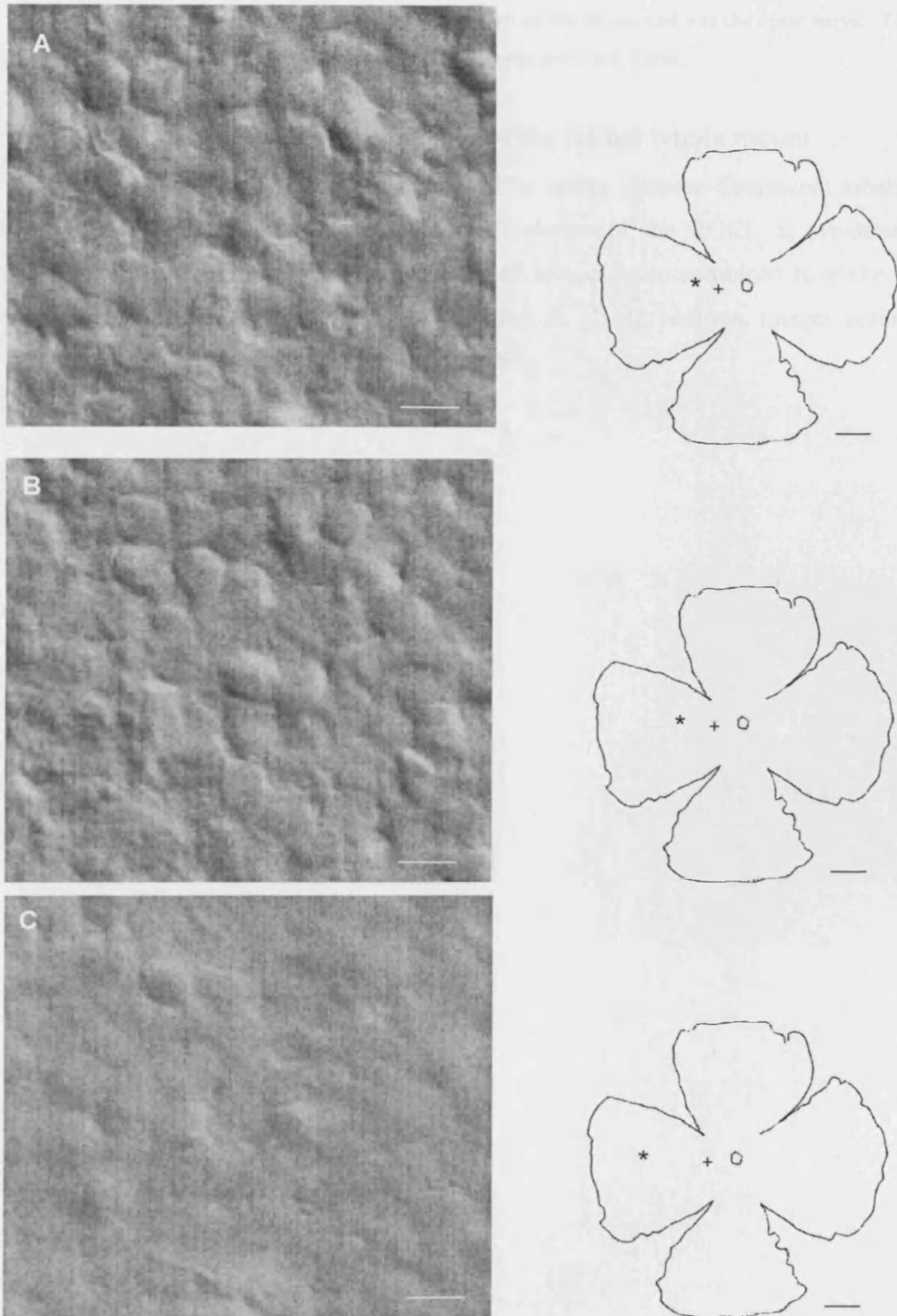
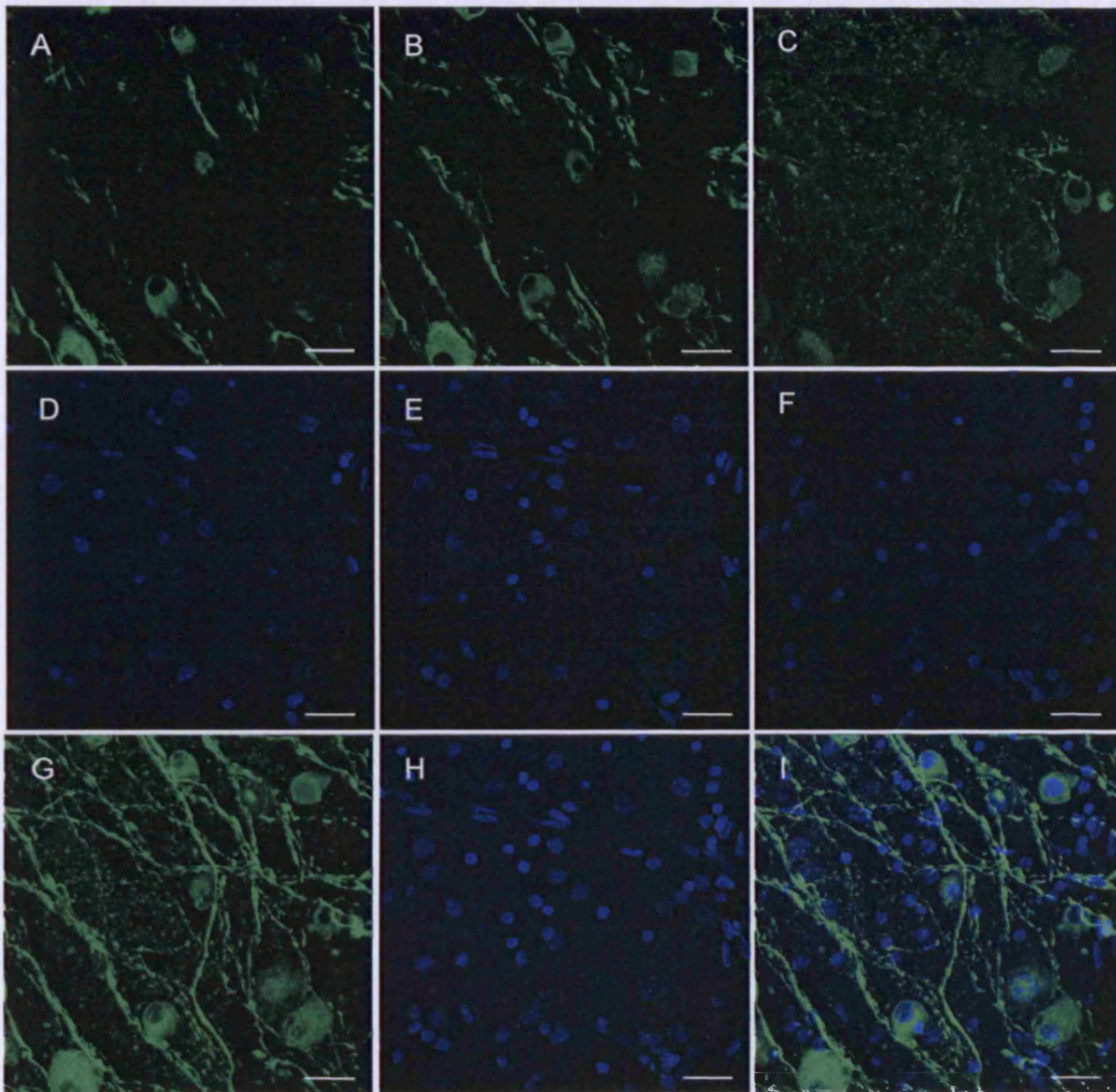


Figure 3-5 Nomarski differential interference contrast microscopy images of cells in the RGCL from central (A) to mid-peripheral (BC) retina. The retina is from a normal Caucasian male donor of 63 years old. The ‘flower petal’ on the right of each image represents the retina whole mount: * indicates

where the sample was taken, + represents the position of the fovea, and o is the optic nerve. The scale bars of the microscopic images are 10 μm and the flower petal are 5 mm.

3.2.3. Single-photon confocal imaging of the retinal whole mount

Single-photon confocal microscopy was used to image immuno-fluorescent labelling of TUJ-1 and DAPI. It scanned through the thickness of the RGCL at pre-determined intervals (Figure 3-6 A-C, D-F). The series of images were combined to make 2D reconstructions, i.e. projection images (Figure 3-6 G, H). In addition, images scanned by different channels could be overlaid (Figure 3-6 I).



J

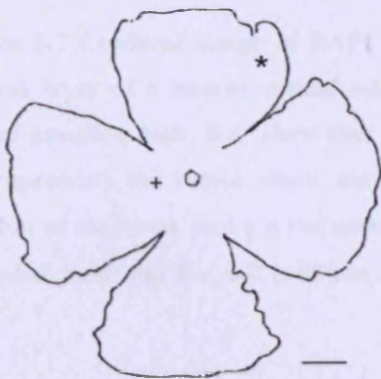


Figure 3-6 A series of confocal images of TUJ-1 labelling (green, A-C) and DAPI labelling (blue, D-F); (G) and (H) are projection images of (A-C) and (D-F) respectively; I is the overlay image of G&H. A-C and D-F are images taken at an z interval of 2 μ m focusing from the retinal ganglion cell layer towards

the inner plexiform layer (C and F are the end of retinal ganglion cells layer and the beginning of the inner plexiform layer). The retina is from a normal Caucasian male donor of 73 years old. The 'flower petal' (J) represents the retina whole mount: * indicates where the sample was taken, + represents the position of the fovea, and o is the optic nerve. Scale bar for A-I is 50 μm and for J is 5 mm.

Furthermore, single-photon confocal microscopy was able to reveal fluorescent labelling of the some of the interior structures of the retina, e.g. the INL (Figure 3-7).

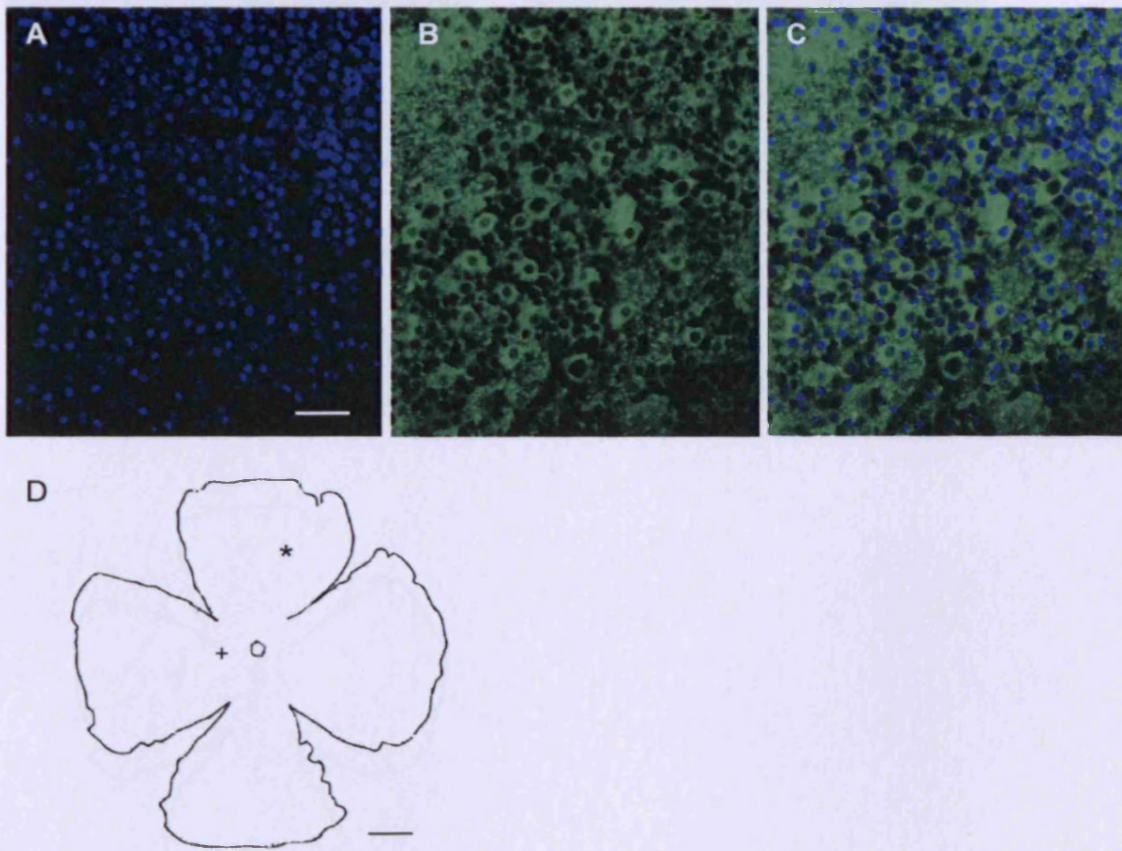


Figure 3-7 Confocal image of DAPI labelling (blue, A) and TUJ-1 labelling (green, B) in the inner nucleus layer of a human retinal whole mount. C is an overlay picture of A and B. In addition to retinal ganglion cells, B-C show that TUJ-1 stains cells in the inner nucleus layer. The 'flower petal' (D) represents the retina whole mount: * indicates where the sample was taken, + represents the position of the fovea, and o is the optic nerve. The retina is from a normal Caucasian male donor of 73 years old. Scale bar for A-C is 50 μm and D is 5 mm.

3.2.4. Multi-photon confocal microscopy

Comparing to single photon confocal microscopy, multi-photon confocal microscopy has a greater depth profiling. The advantage of multi-photon can be appreciated by comparing the two images in Figure 3-8. Typical multiphoton images of neurons in the RGCL, INL and ONL of the retinal whole mounts are shown in Figure 3-9.

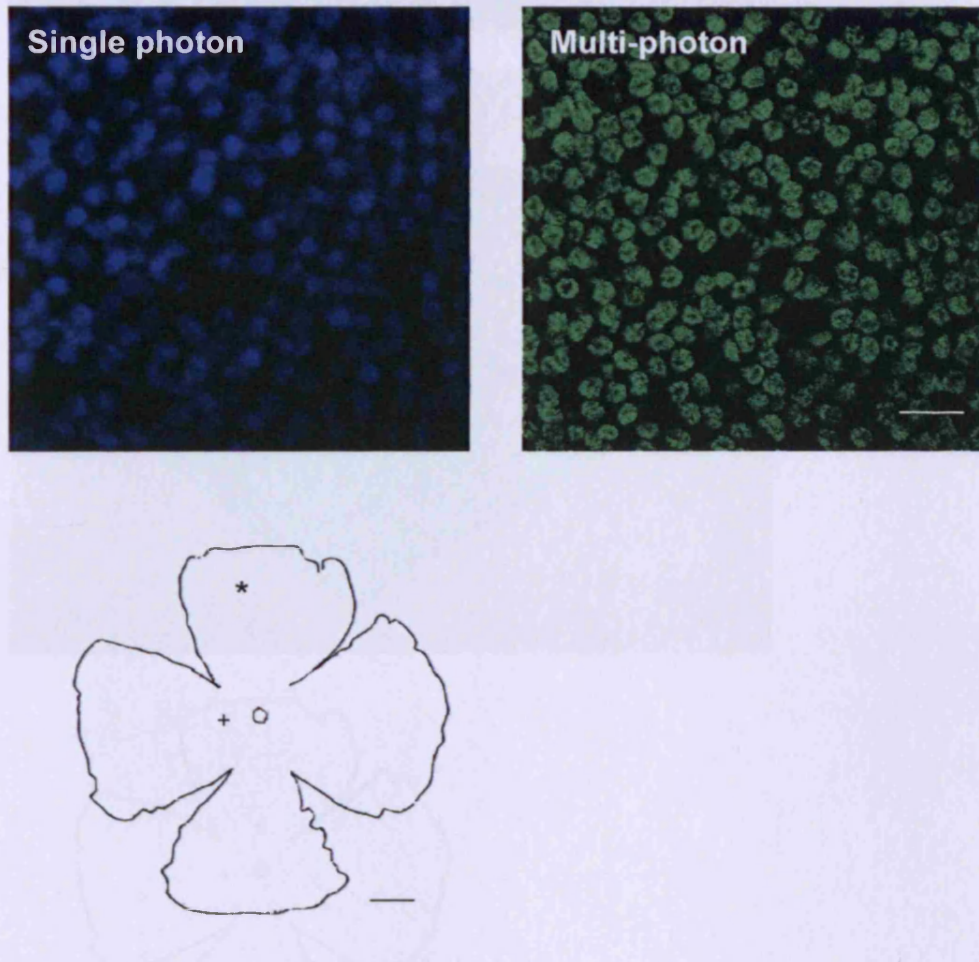


Figure 3-8 Single photon and multi-photon images of cells in the outer nucleus layer which was imaged with the retinal ganglion cell layer upper most. The ‘flower petal’ (D) represents the retina whole mount: * indicates where the sample was taken, + represents the position of the fovea, and o is the optic nerve. The retina is from a normal Caucasian male donor of 73 years old. Scale bar for A-C is 20 μm and D is 5 mm.

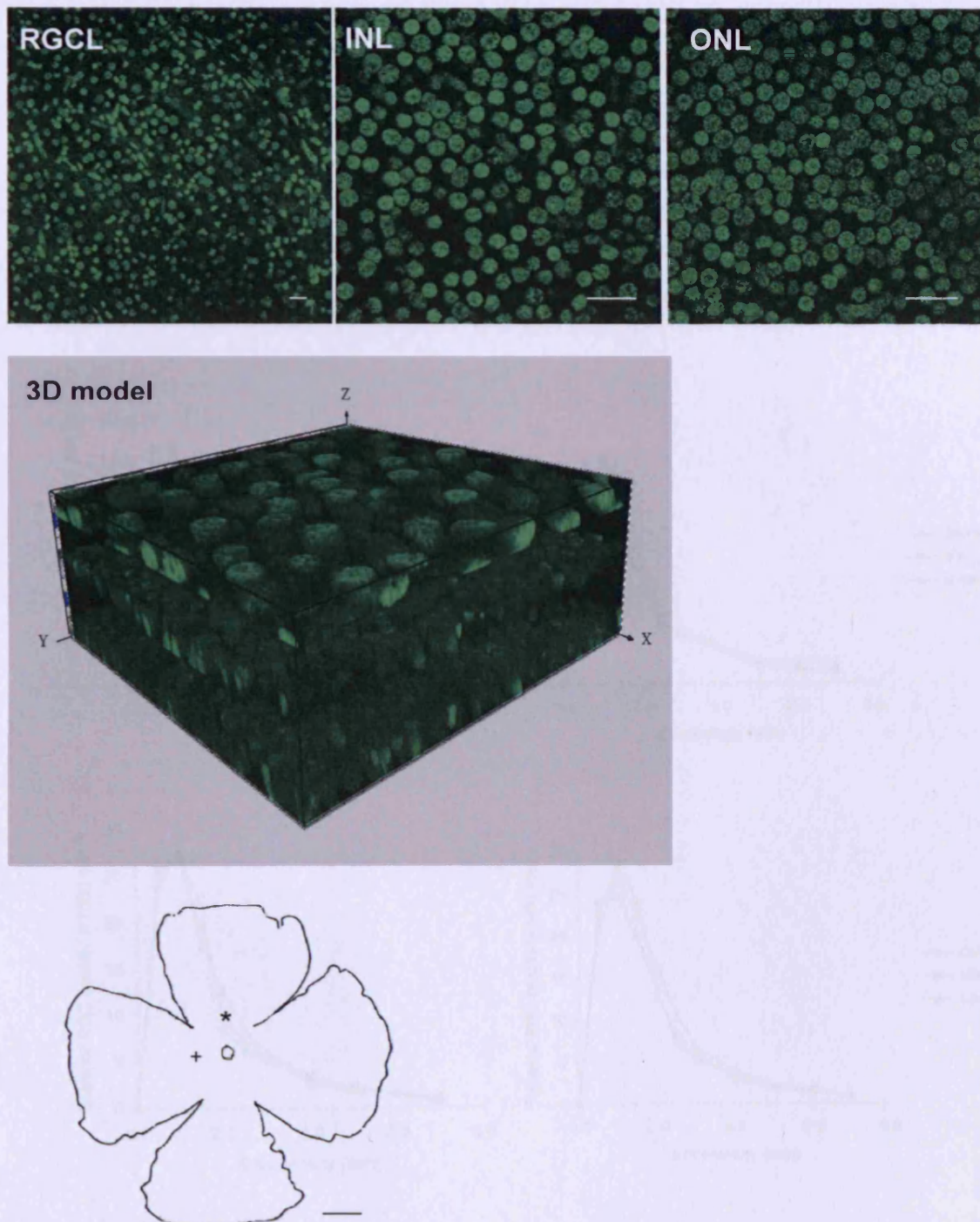


Figure 3-9 Multiphoton images of DAPI stained cell nuclei in the retinal ganglion cell layer (RGCL), inner nucleus layer (INL) and outer nucleus layer (ONL) of the human retinal whole mounts. These were sequentially imaged with the RGCL upper most and focusing from the RGCL to the ONL. An example of 3D models of the layers imaged was built by Imaris software. The ‘flower petal’ represents the retina whole mount: * indicates where the sample was taken, + represents the position of the fovea, and o is the optic nerve. The retina is from a normal Caucasian male donor of 73 years old. Scale bar for RGCL, INL and ONL is 20 μm and ‘flower petal’ is 5 mm.

3.2.5. Method validation

Both NDIC and multiphoton-DAPI methods showed that the density of RGCs peaked around 1mm eccentricity, which reduced with eccentricities from the central to the peripheral retina (Figure 3-10). Among the four retinal quadrants, the highest RGC density was in the nasal region; RGCs in the superior region was more densely packed relative to the inferior retina (Table 3-1).

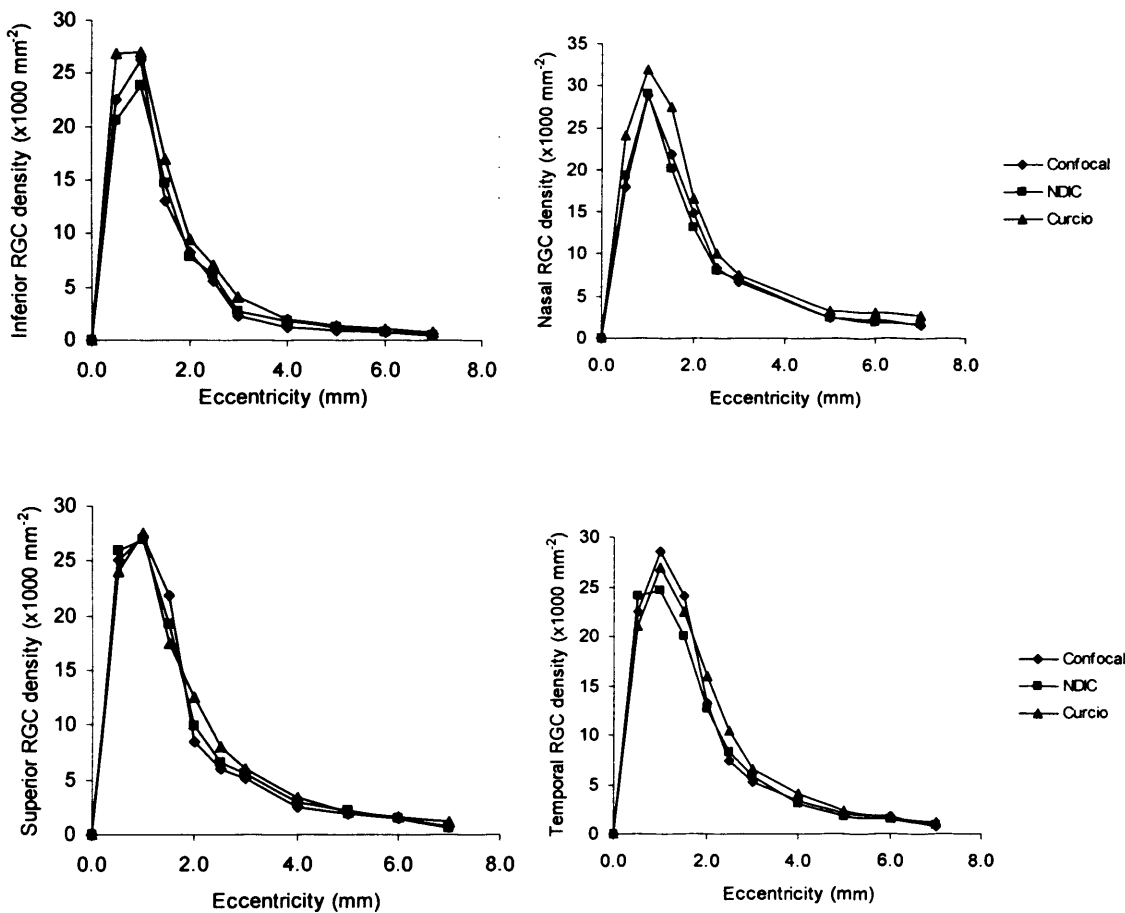


Figure 3-10 The distribution of retinal ganglion cells (RGCs) in the human retinal whole mounts. Samples are taken at the positions of the sampling grid in Figure 2-4. Our results from NDIC (n=3) and multiphoton-DAPI methods (n=6) were comparable to literature values (n=5, Curcio et al, 1990). The direction superior and inferior refer to the appropriate sides of the horizontal meridian, a line that passes through the fovea and the optic disk; nasal and temporal refer to the parts of the vertical meridian that was perpendicular to the horizontal meridian.

Table 3-1 Mean peak densities of RGCs measured by NDIC and multiphoton-DAPI methods.

	Nasal	Temporal	Superior	Inferior
<u>NDIC*</u>				
Peak density (x1000/mm²)	22.97	20.04	19.00	17.80
Standard deviation (x1000/mm²)	1.02	1.60	2.19	1.02
<u>Multiphoton-DAPI*</u>				
Peak density (x1000/mm²)	24.90	19.37	18.93	18.60
Standard deviation (x1000/mm²)	3.06	1.42	1.53	2.12

*n=3

In the multiphoton images, the automatic counts agreed closely with the manual counts (n=3, Figure 3-11, $r^2=0.991$). In the same retinal specimen, there was close agreement between counting results based on NDIC method and multiphoton-DAPI method (n=3, Figure 3-12, $r^2=0.984$). For detailed statistics of false positives and false negatives see Appendix I.

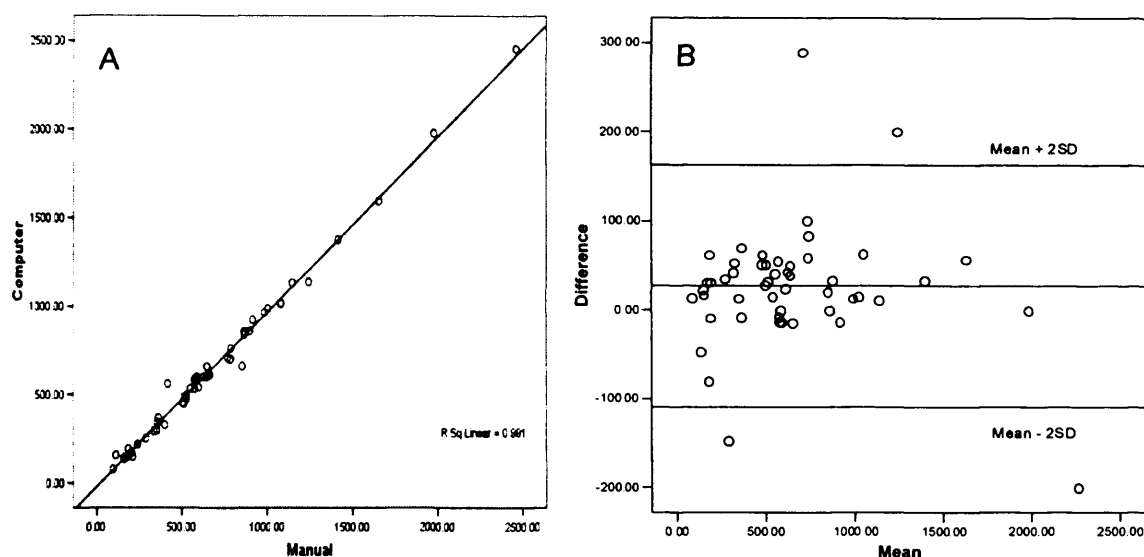


Figure 3-11 Validation of the automated computer counts by manual counts. In multiphoton-DAPI images, the automated counts were compared with manual counts. The results were analysed by linear regression (A, $n=3$, $r^2= 0.991$) and Bland-Altman plot (B, $n=3$, most of the points fall within $\text{mean} \pm 2\text{SD}$), both of which suggest a good correlation of the two counting techniques. SD, standard deviation.

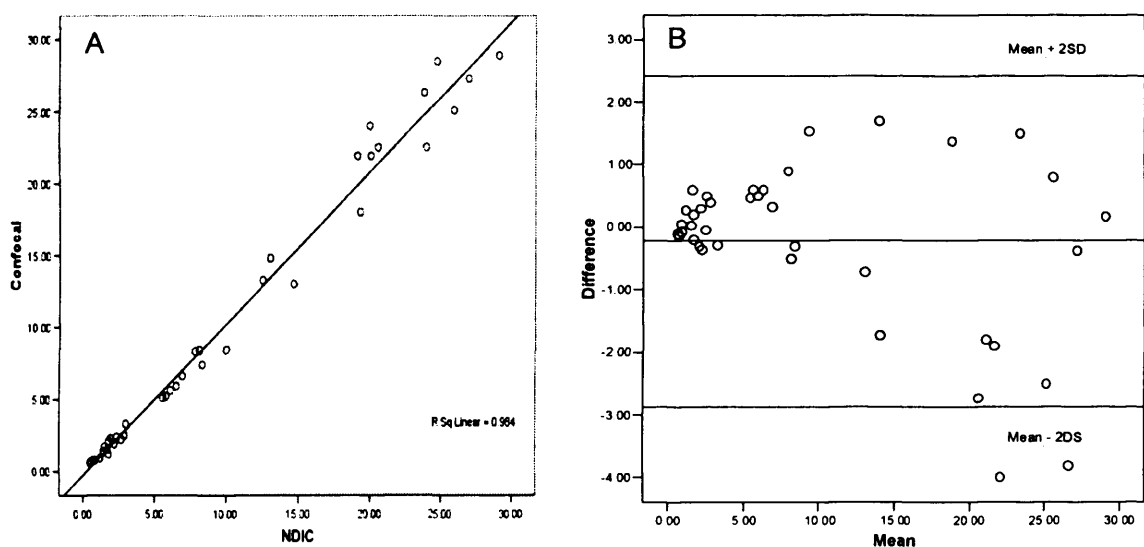


Figure 3-12 Validation of multiphoton-DAPI method by Nomarski differential contrast microscopy (NDIC). Retinal whole mounts were stained by DAPI solution (3 mg/mL) overnight, and imaged by multiphoton microscopy as described in Chapter 2 (2.6.). The same samples were then imaged by NDIC method. The counting results of neurons in the retinal ganglion cell layer were compared with NDIC counts. The results were analysed by linear regression (A, $n=3$, $r^2= 0.984$) and Bland-Altman plot (B, $n=3$, most of the points fall within $\text{mean} \pm 2\text{SD}$), both of which shows good correlations of the counting results measured by multiphoton-DAPI method and NDIC method. SD, standard deviation.

3.3. Discussion

3.3.1. Retinal transverse sections and retinal whole mounts

Retinal transverse sections were used previously to study the distribution of neurons (Van Buren 1963; Vilter 1954). If retinal whole mounts display retinal details in the xy direction, the transverse sections show the third dimension (z direction). Comparing to retinal transverse sections (Figure 3-1), retinal whole mounts (Figure 3-2) had three major advantages in quantifying retinal cells: firstly, it offered a wider field of view of neurons in the xy plane; secondly, the whole mount did not cause the varying degree of tissue shrinkage associated with wax embedding; thirdly, it avoided counting errors introduced by the angle and position of sectioning. Therefore, retinal whole mounts were preferred for quantifying retinal neurons.

3.3.2. DMSO cleared retinal whole mounts

DMSO cleared retinal whole mounts more efficiently with minimum tissue shrinkage compared with the dehydrating tissue in alcohol and xylene. The mechanism of this is not known precisely, however, one could speculate a reasonable explanation considering the chemical properties of DMSO and cell biology. The shrinkage of biological tissue was believed to result when the osmotic pressure exerted by the aqueous environment exceeded the mechanical stability of the cell. For alcohol, its concentration levels were changed in steps during dehydrations, since faster changes usually result in larger osmotic gradients and hence greater degrees of shrinkage. DMSO was highly miscible with water; it can replace total cellular water within cells as well as solubilise the lipid components of membrane. If the osmotic pressure was inversely proportional to the permeation velocity, DMSO crossed cell membranes extremely rapidly and therefore caused little tissue shrinkage.

3.3.3. Immunofluorescent and fast red labelling

Pilot work in our laboratory showed TUJ-1 staining to be a robust technique since it was capable of labelling RGCs in heavily fixed tissue. Both fluorescence (Alexa Fluor 488) and chemical agent (fast red) were experimented with to optimise the staining quality. Our

results indicated that fluorescein labelling was much clearer than fast red (Figure 3-2), and it had the advantage in the application of confocal imaging. TUJ-1 antibody labelled neurons in the RGCL and INL (Figure 3-6 and 3-7), this suggests that TUJ-1 is not specific to RGCs.

3.3.4. Nomarski and confocal microscopy

Although NDIC method generated much better quality images than brightfield illumination, in our study this technique was limited by its depth of field. In order to correlate the quantities of neurons at different levels of the retina, we took an alternative approach: confocal microscopy was used instead of NDIC. As we know that conventional epifluorescence light microscopy illuminates the whole specimen uniformly, thus the contrast and resolution can be degraded by strong scattering (Denk and Svoboda 1997). In contrast, confocal microscopy uses a single point of excitation laser light to scan across the specimen, which overcomes the effects of scattering by means of a detector pinhole. It eliminates the out-of-focus information and is able to reveal the interior details of the specimen. With confocal microscopy, the stepper motor attached to the fine focus enabled the collection of a series of images through a three dimensional object. These images could then be used for a two or three dimensional reconstruction (Figure 3-6). This enabled us to identify objectives that could be easily missed with light microscopy. In addition, double or triple labelling could be collected using sequential scans. Since these images were collected from an optical plane within the sample, overlay images were generated based on the precise co-localisations (Figure 3-6 I).

TUJ-1 antibody was reported to be a specific marker for RGCs (Snow and Robson 1994; Watanabe et al 1991). With confocal microscopy, when focused to the INL, we found TUJ-1 stained cells in the INL (Figure 3-4), which is composed of amacrine cells, bipolar cells, and horizontal cells etc. We conclude therefore that TUJ-1 is not a specific marker for RGC.

3.3.5. Single photon and multi-photon confocal microscopy

The resolution of confocal images decreased as it focused down, and this was particularly apparent in the ONL (Figure 3-8). In some areas, the nuclei could not be distinguished from one another, which made quantification inaccurate. I increased the imaging resolution from 512 x 512 pixels to 1024 x 1024 pixels, but the problem remained. Single photon confocal microscopy is best applied to thin specimens, such as cultured preparations or the most superficial cell layer in a tissue (< 20 μm), because some signal photons are wasted by the confocal pin hole. Therefore, I tried to use multi-photon microscopy to image the retinal specimen instead.

Multiphoton absorption has several advantages over the single photon absorption band (i.e. a photon is a quantum unit of light energy). First, with two photon absorption, the intensity is highest in the vicinity of the focus which drops off quadratically with distance above and below; as a result, fluorophores are excited in a tiny diffraction limited focal volume. Second, the absorption of two photons emits a longer wavelength light which scatters less as it passes through the tissue, resulting in a deeper tissue penetration. Third, because of this, photo bleaching does not occur throughout a significant portion of the specimen. The advantages of multiphoton microscopy made it a perfect tool for quantifying neurons in different layers of the retinal whole mounts.

3.3.6. Automatic quantification

The loss of retinal neurons is an important event in biological development and pathology; counting retinal cells from histological preparations can provide quantitative information central to studying retinal plasticity in ageing and glaucoma. However, to determine the numerical density of cells in retinal whole mounts is difficult indeed. In the past, many nucleus detection methods were developed for automatic analysis, but they are not easily adaptable to immunofluorescence images (Table 3-2). These approaches faced a unique challenge in tissues like the retina, where there are several layers of densely packed cells; furthermore, the intensity of DAPI staining varies between cells from different populations because of the non-uniform DNA distribution inside the nuclei.

Table 3-2 Methods for automated detection and analysis of cell nuclei.

Williams (Williams and Rakic 1988)	Three-dimensional counting.
Malpica (Malpica et al. 1997)	Segment clustered nuclei by a watershed transformation.
Demandolx (Demandolx D 1997)	Segment subcellular structures in Hela cells by applying a grey level thresholding.
Sjostrom (Sjostrom et al. 1999)	The use of an artificial neural network (ANN).
Nedzved (Nedzved A 2000)	Segment cells with sparse density based on morphological characters.
Cullen (Cullen et al. 2005)	Blob detector: quantify spatial relationships between heme-rich deposits and capillaries
Jiyun Byun (Byun et al. 2006)	Blob detector: set a diameter filter that is proportional to the average diameter of nuclei.
Softwares	Image J, Metamorph, Bioquant.

3.3.7. Validation of multiphoton-DAPI method

For every newly developed method, it needs to be validated, either against a gold standard or to compare results with an established method. Based on the multiphoton-DAPI images, we validated the automated computer counts against manual counts (Figure 3-10) and NDIC counts (Figure 3-11); the results were plotted as a linear regression and a Bland-Altman plot. Bland-Altman plot has been frequently used by clinicians to compare a new measurement technique with an established one, and to see whether they agree sufficiently for the new to replace the old. The difference between the two methods (in y axis) was plotted against the mean (in x axis). The accuracy is assessed by looking at how close the data points are to the x axis. Figure 3-10, 11 show that most of the data points fall within 'Mean \pm 2SD', and there is no trend as x value increases. Therefore, we conclude that multiphoton-DAPI method can accurately quantify neurons in the retinal whole mounts.

3.4. Conclusions

Cell counting by Nomarski optic is suitable for imaging single layer of cells located close to the surface of the tissue. However, it does not correlate neuron densities in different layers of retinal whole mounts. With the multiphoton-DAPI method developed, we are able

to accurately quantify and correlate the neuron densities in the inner and outer retina. This is therefore a very useful technique in detecting subtle cellular changes of neurons and to map the spatial and temporal neurodegeneration in the retinal whole mounts.

CHAPTER 4 RETINAL TRANSNEURONAL DEGENERATION IN HUMAN GLAUCOMA

OBJECTIVES

- To quantify neuron densities in different layers of the retina in control and glaucomatous groups
- To determine if transneuronal degeneration occurs in human glaucoma

4.1. Introduction

Glaucoma is a progressive neuropathy with associated vision field loss (Epstein, 1997), but whether the neurodegeneration involves both inner and outer retina remains controversial. In human and experimental glaucoma models, histological evidence support neuron loss in other layers of the retina in addition to the RGCL, including the loss of horizontal cells (Janssen et al., 1996), amacrine cells (May and Mittag, 2004; Moon et al., 2005; Wang et al., 2005) and the associated thinning of the INL (Dkhissi et al., 1996; Osborne et al., 1999). The swelling and loss of photoreceptors was reported in patients with high IOP and end stage glaucoma (Nork et al., 2000; Panda and Jonas, 1992). Consistent with these observations, clinical investigations showed reduction of colour sensitivity (particularly in the blue yellow axis) in human glaucoma (Poinosawmy, Nagasubramanian and Gloster, 1980; Nork, 2000); in the monkey glaucoma model, aberrant multifocal electroretinography (mfERG) responses were seen in both inner and outer retina (Raz et al., 2003); in DBA2 mice (a strain of mice that has

genetic defects in the iris and the obstructed trabecular meshwork), thinning of the outer retinal layers correlated with the decreases in ERG a- and b-wave amplitudes (Bayer et al., 2001). However, it is not clear why these outer retinal degenerations arise.

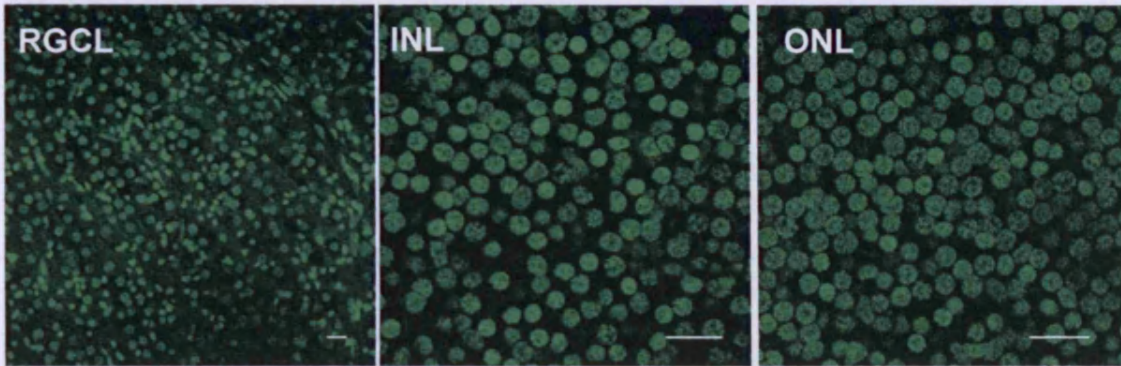
Although significant advances have been made in our understanding of glaucoma pathology, transneuronal damage of the retinas could not be detected by conventional histology. In the present study, multiphoton confocal microscopy was used to image DAPI labelled neurons (Multiphoton-DAPI method, Chapter 2 and 3) at defined levels of the retina. This method allows accurate optical dissection of retinal whole mounts, and provides high resolution images. Therefore, I was able to compare the cellular changes in the RGCL, INL and ONL in normal and glaucomatous human retinas.

4.2. Results

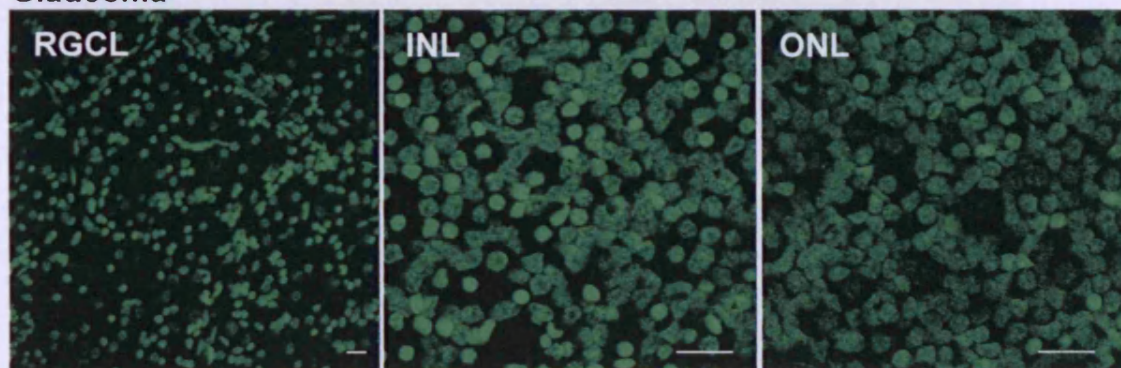
4.2.1. Multiphoton imaging of neurons

At each location on the sampling grid, neurons at the RGCL, INL and ONL were imaged sequentially, the examples of which are shown in Figure 4-1.

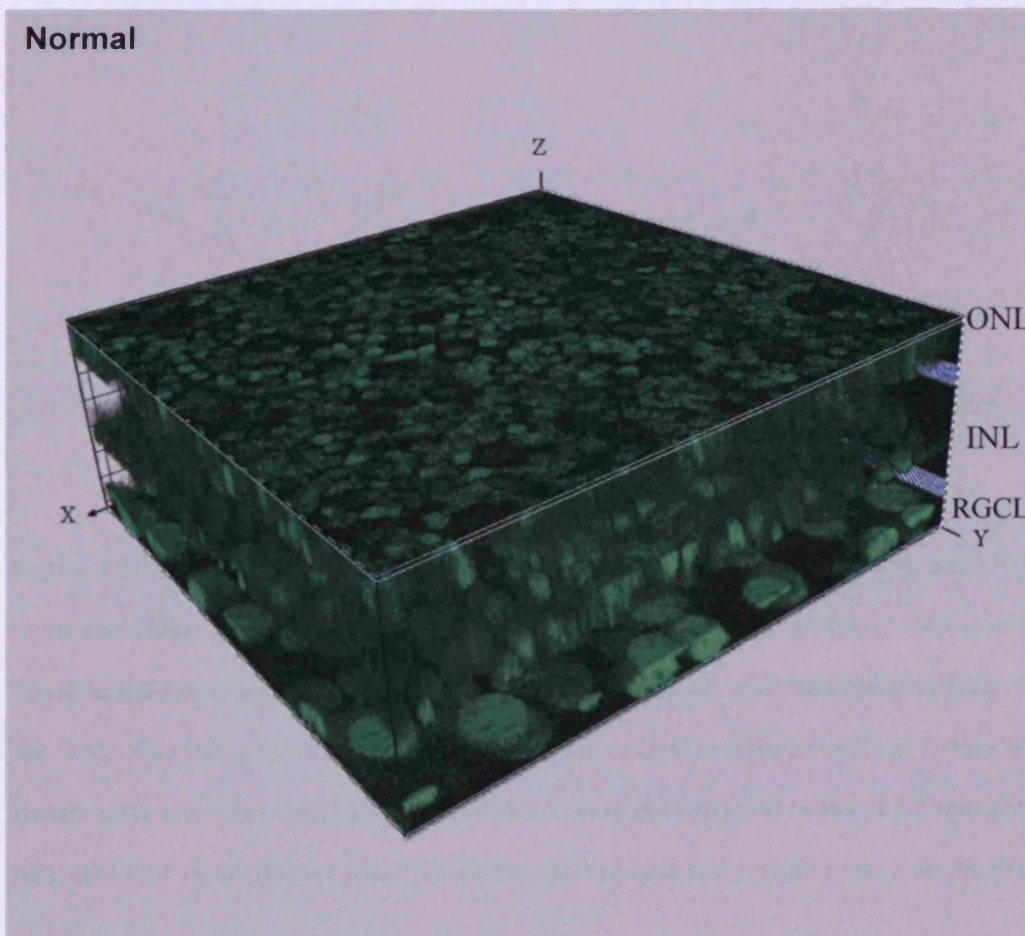
Normal



Glaucoma



Normal



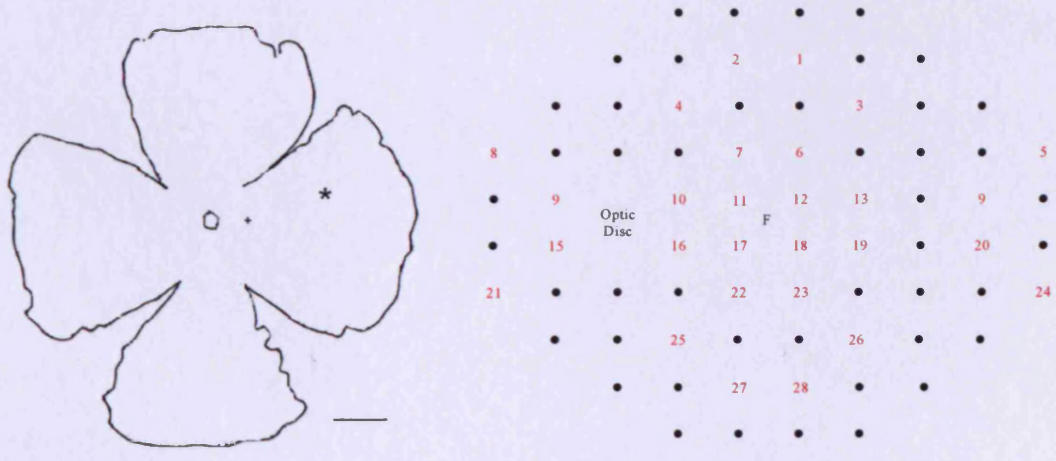
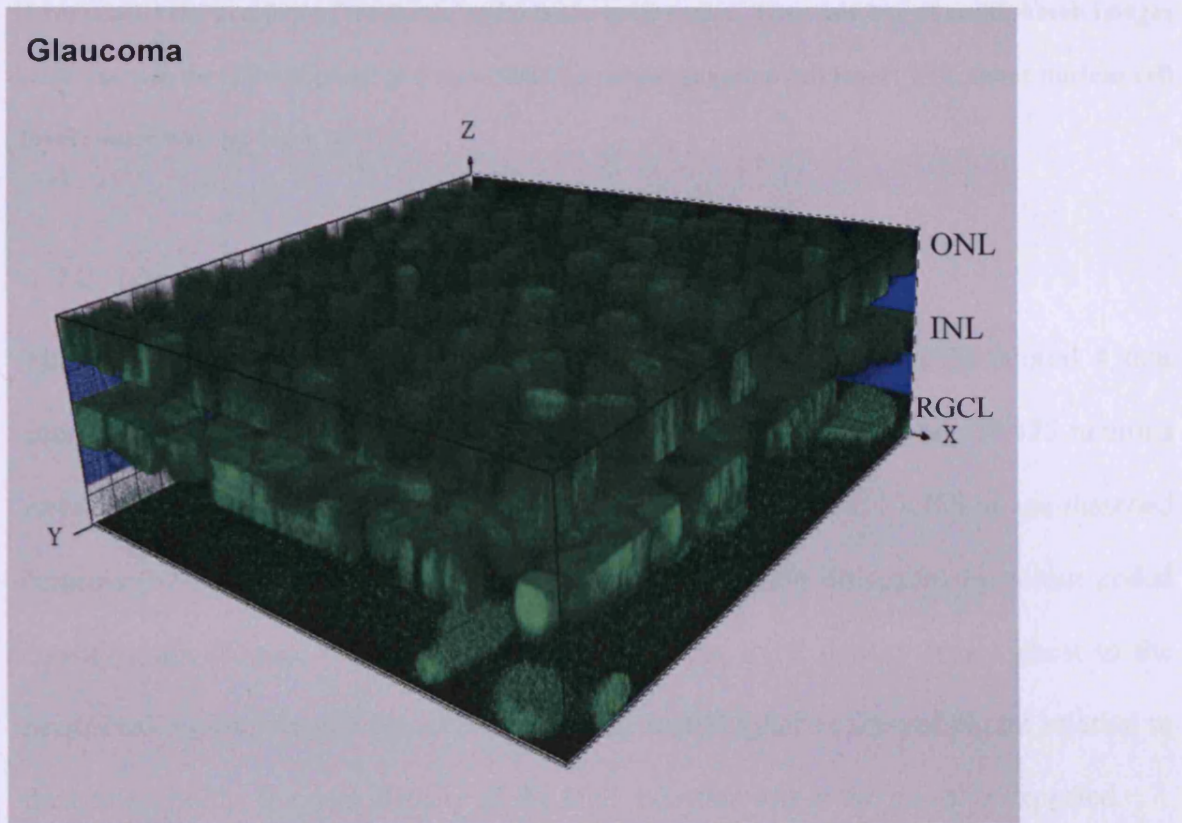


Figure 4-1 Multiphoton images of DAPI stained cell nuclei in the RGCL, INL and ONL in normal (n=6) and glaucomatous (n=6) retinas. Here an example from one retina of each group was given. These images were sequentially taken with the RGCL upper most and focusing from the RGCL to the ONL. Two 3D models of the retinal layers for normal and glaucomatous retinas were built by Imaris software. The images shown were taken from the temporal retina at 2.7 mm eccentricity (as indicated by * in the ‘flower petal’ below the multiphoton images and point 5 on the grid). There is

+ represents the position of the fovea, and o is the optic nerve. The scale bar of multiphoton images is 20 μm and the 'flower petal' is 5 mm. RGCL, retinal ganglion cell layer; INL, inner nucleus cell layer; outer nucleus layer (ONL).

4.2.2. Neuron quantification in the RGCL, INL and ONL

The retinal areas imaged represented 56% of the total area within the central 4 mm eccentricity, and 27% between 4 mm and 7 mm eccentricity. In total, 37,425 neurons were counted in glaucomatous retinas (61-90 years old, n=6) and 57,858 in age-matched controls (67-83 years old, n=6). The neuron densities were illustrated by colour coded density maps (Figure 4-2). Our data confirmed that RGC density was highest in the perifoveal region; neuron densities in the INL were higher in the peripheral relative to the central retina; the peak density of the ONL neurons was at the fovea as expected.

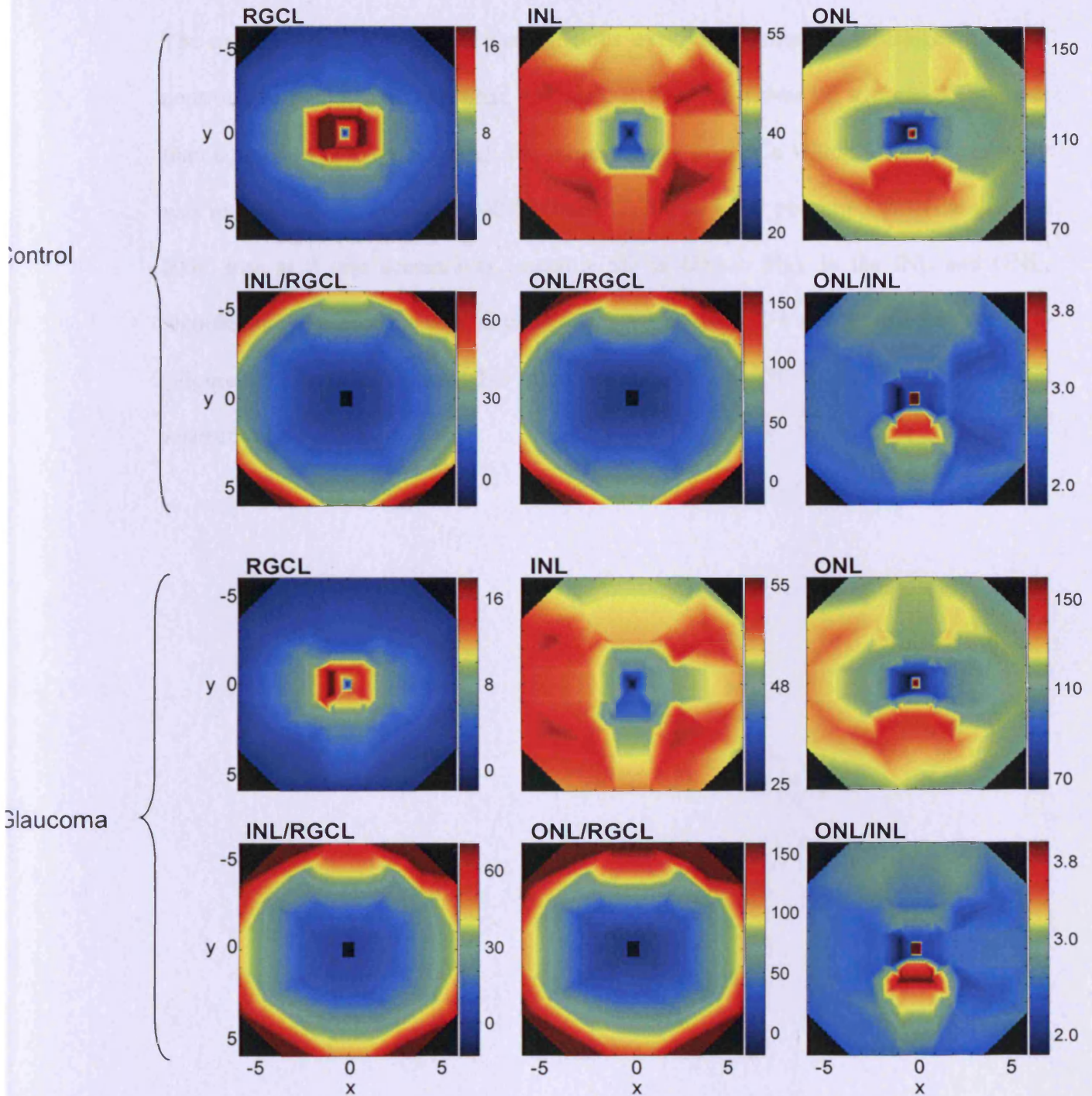


Figure 4-2 Colour coded mean neuron density maps and correlation maps in control (n=6) and glaucomatous (n=6) retinas. Colour gradient was assigned to values of densities, e.g. for RGCL, the colours from red to blue represent densities values range between 0 and 18 (x1000 per mm²), with each colour represents a particular density value. Ratios of neuron densities were shown on the right of each contour plot. The contour map spatially correlates with the sampling grid. xy axis show eccentricities (mm), (0,0) is the fovea. RGCL, retinal ganglion cell layer; INL, inner nucleus cell layer; outer nucleus layer (ONL).

The mean neuron densities in glaucomatous eyes were compared with aged-matched controls. In glaucomatous retinas, the peak RGC density was on average 39% lower than control eyes (Figure 4-3A); the mean density of RGCs within 4 mm eccentricity was reduced by approximately 42 % (from 13,200 to 7,700 per mm²), with the greatest RGC loss at 2 mm eccentricity (mean \pm SD is 48% \pm 5%). In the INL and ONL, significant reductions of neuron densities were between 2-4 mm eccentricity of 10% (Figure 4-3B, $p < 0.05$) and 2-3 mm eccentricity of 7% (Figure 4-3C, $p < 0.05$), respectively.

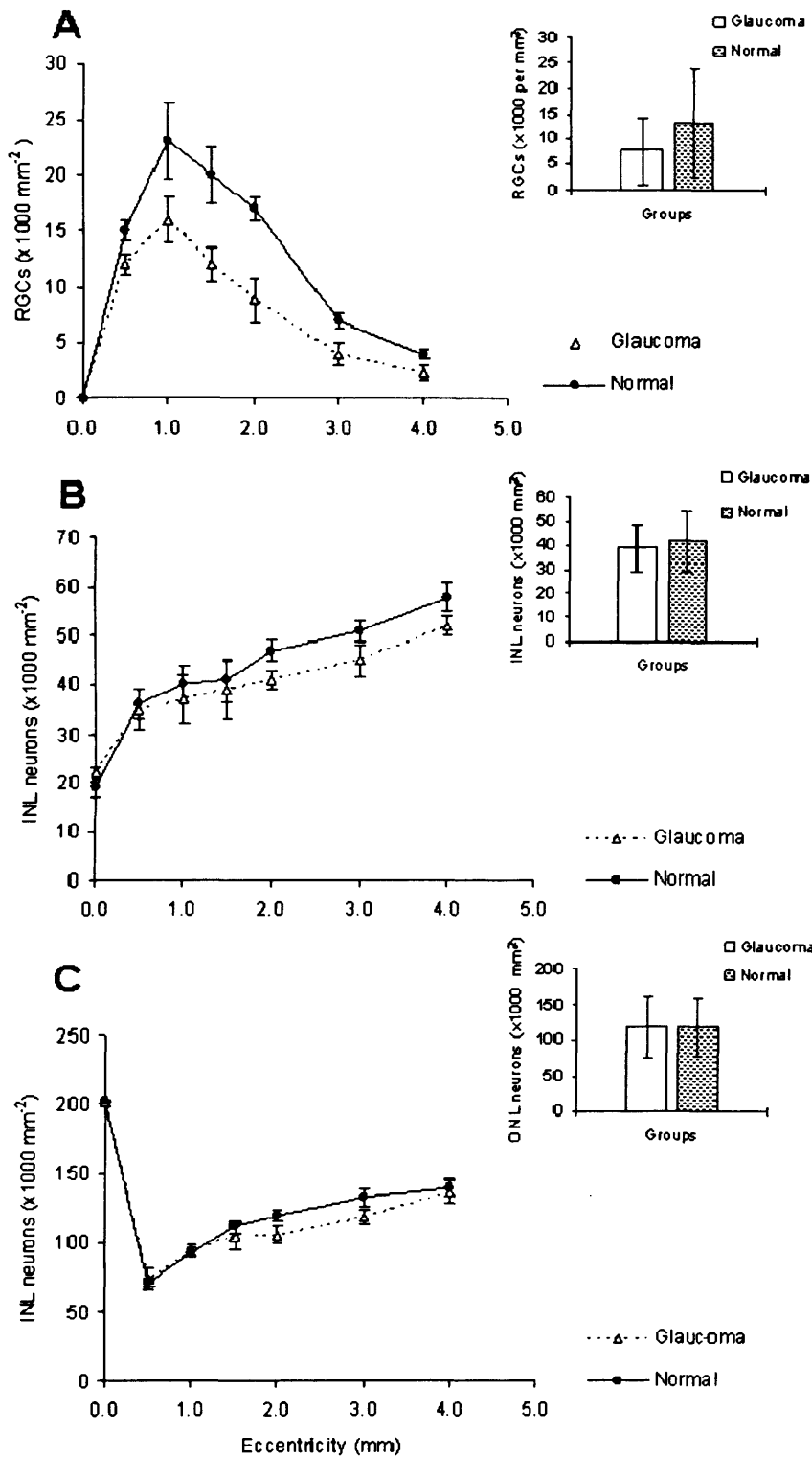


Figure 4-3 Comparisons of neuron densities in the RGCL (A), INL (B) and ONL (C) of glaucomatous ($n=6$) and control ($n=6$) retinas. Lines show means of neuron densities at each eccentricity, and bars show means within 4mm eccentricity. In the RGCL, the neuron density was significantly reduced between 0.5 and 4 mm eccentricity. In the INL and ONL, this was significant between 2-4 and 2-3 mm eccentricity. From the RGCL to ONL, the region of density reductions was narrowed down. Error bars show mean \pm 1 SD. RGCL, retinal ganglion cell layer; INL, inner nucleus cell layer; outer nucleus layer (ONL).

4.2.3. Correlation of neuron densities

In view of the variation of neuron densities between retinas, we expressed the relationship of neuron densities in different layers of the retina as ratios, e.g. at given eccentricity, the INL neurons density divided by RGCL neuron density (INL/RGCL). Within the area examined, the ratios of INL/RGCL and ONL/RGCL in glaucomatous retinas were significantly higher than controls between 3-4 mm eccentricity ($p < 0.05$, Figure 4-4 AB). However, there was no significant difference in ONL/INL in control and glaucomatous groups at any eccentricity tested (Figure 4-4 C); the difference of ONL/INL is minimum between 3-4 mm eccentricity.

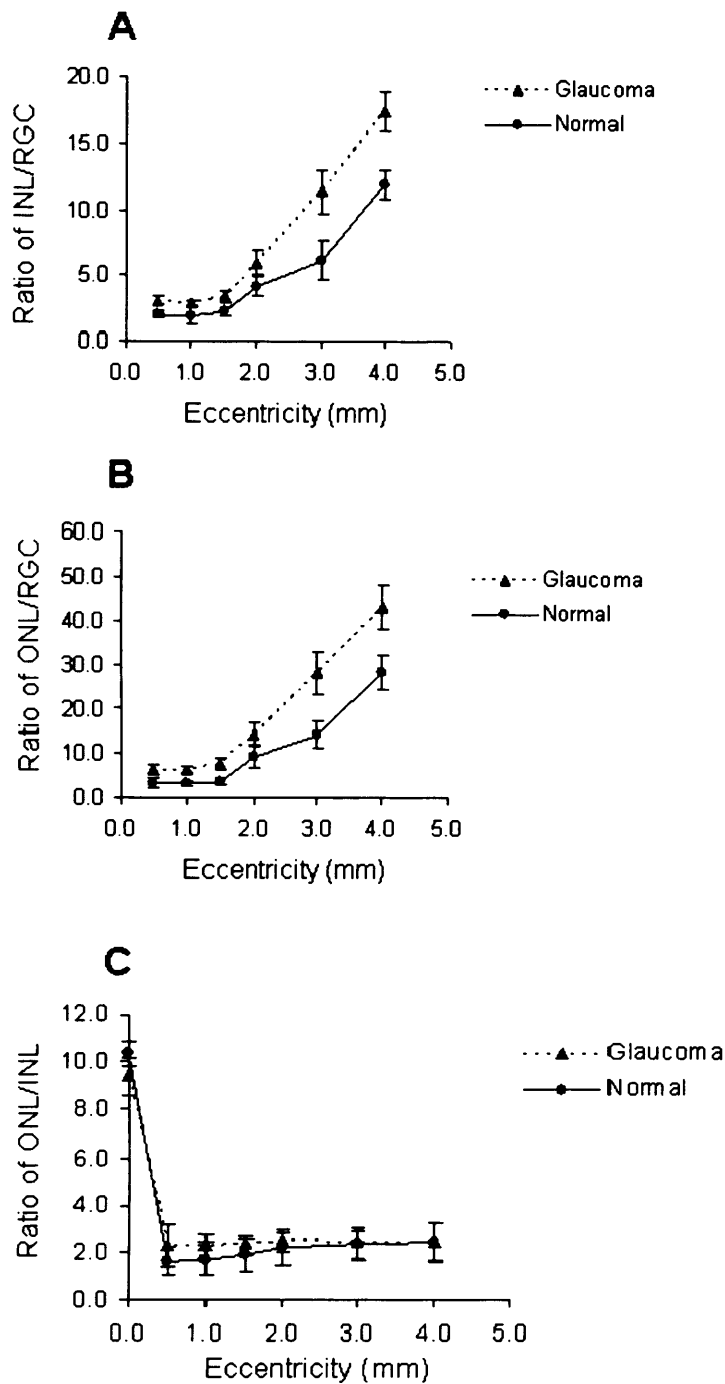


Figure 4-4 The neuron density ratios of INL/RGCL (A), ONL/RGCL (B) and ONL/INL (C) in glaucomatous (n=6) and control (n=6) retinas. Lines show means of neuron density ratios at each eccentricity. In the two groups of comparison, there is significant difference of INL/RGCL and ONL/RGCL between 3 and 4 mm eccentricity, but no significant difference of ONL/INL at any eccentricity tested. Error bars show mean \pm 1 SD. RGCL, retinal ganglion cell layer; INL, inner nucleus cell layer; outer nucleus layer (ONL).

4.3. Discussions

The data are consistent with the hypothesis that glaucoma results in transneuronal degeneration that starts at RGCL. An important finding of the present study is that there was a gradient of neurodegeneration from the RGCL to the ONL. This was manifested in two ways: first, the decreased degree of neuron damage; second, the reduced areas of neuron damage (Figure 4-2,3). With conventional histological techniques, previous studies have not consistently demonstrated glaucomatous neuron loss in the outer retina; however, the multiphoton-DAPI method benefits from greater sensitivity and is able to detect subtle changes in neuron densities. In fact, the outer retinal damage in glaucoma is supported by recent evidence from molecular biology analysis that mRNA levels of red/green and blue cone opsins decreased in monkey experimental glaucoma (Pelzel et al., 2006).

Our observation that the increases in the INL/RGCL and ONL/RGCL ratios in the glaucomatous eyes coincided with the region of the greatest RGC loss (Figures 4-3,4) suggests that RGC loss and outer retinal damage are spatially correlated, and the INL and ONL damages are not simply the result of a non specific retinal damage. Our data cannot confirm that transneuronal effects are responsible for damages in the INL and ONL, but this should be considered as a factor.

The cause of outer retinal damage remains to be clarified. It is possible that it reflects the toxic effect of the release of neurotransmitters such as glutamate. Although it now seems unlikely that this will result in toxic neurotransmitter levels that can be detected in the vitreous (Honkanen et al., 2003), local levels may be elevated to increase the risk

of cell loss (Carter-Dawson et al., 2004). The importance of this in the propagation of further cell loss is controversial since glutamate uptake mechanisms in experimental glaucoma do not appear to be compromised (Hartwick et al., 2005). Other factors that may play a role in propagating neuronal loss outside the RGCL layer include the release of free radicals or alterations in the concentration of extracellular calcium. At the level of the RGCL, there is evidence that partial damage to the optic nerve can increase the risk of loss of other

adjacent cells as a bystander effect (Levkovitch-Verbin et al., 2001; Levkovitch-Verbin et al., 2003).

Transneuronal degeneration has also been noted in many studies in different neuronal systems. There is evidence of extension of glaucomatous injury from the retina and optic nerve to the central visual systems including the lateral geniculate nucleus (LGN) and visual cortex through transneuronal degeneration (Gupta and Yucel, 2001). It was shown in primate glaucoma that atrophy of LGN neurons related to the level of intraocular pressure elevation (Gupta et al., 2007; Weber et al., 2000; Yucel et al., 2000) and correlated with the degree of optic nerve damage (Gupta and Yucel, 2001; Yucel et al., 2001). Transneuronal degeneration was also demonstrated in the substantia nigra (SN) after striatal injury, which has been thought to result from the loss of GABAergic influence (Albin et al., 1990) and transneuronal degeneration of neurons in the substantia nigra reticulata (SNR) occurs after initial ischemic or neurotoxin damage to the striatum because of the imbalance between GABAergic and glutamatergic afferents (Saji et al., 1996).

Our data highlight the importance of trans-retinal degeneration in human glaucoma. Since the outer retinal neurons are lost, some of these changes are irreversible which emphasises the importance of developing methods for the detection of outer retinal damage (Drasdo et al., 2001). Neuroprotection in glaucoma is focused on the prevention of RGC loss in ways that compliment oculohypotensive treatment; consideration should also be given to the prevention of outer retinal damage to maximise the efficacy of this approach.

CHAPTER 5 RETINAL TRANSNEURONAL DEGENERATION IN AGEING

OBJECTIVES

- To quantify neuron densities in the RGCL, INL and ONL of the retina in young and aged eyes
- To determine if transneuronal degeneration occurs in ageing, and if so to compare it with glaucoma

5.1. Introduction

Ageing is ‘the progressive accumulation of changes with time that are associated with or responsible for the ever-increasing susceptibility to disease and death which accompanies advancing age’ (Harman 1981). Most elderly people experience some loss of vision, even in the absence of any identifiable eye disease. Ageing brings a spectrum of functional degenerative or regressive events (Bonnell et al. 2003; Owsley et al. 2001): dark adaptation is delayed in the elderly due to the alteration of the kinetics of rod function (Owsley et al. 2001; Owsley C 1990); standard full-field electrophysiology reveals significant increases in implicit times with a reduction in the amplitudes of a waves (i.e. photoreceptor responses) and b waves (i.e. bipolar and Müller cell responses) (Birch and Anderson 1992; Weleber 1981); the amplitude of multifocal oscillatory potentials, which are thought to reflect inner retinal function and rod-cone interactions, decreases linearly with age whereas their latency increases with age (Kurtenbach and

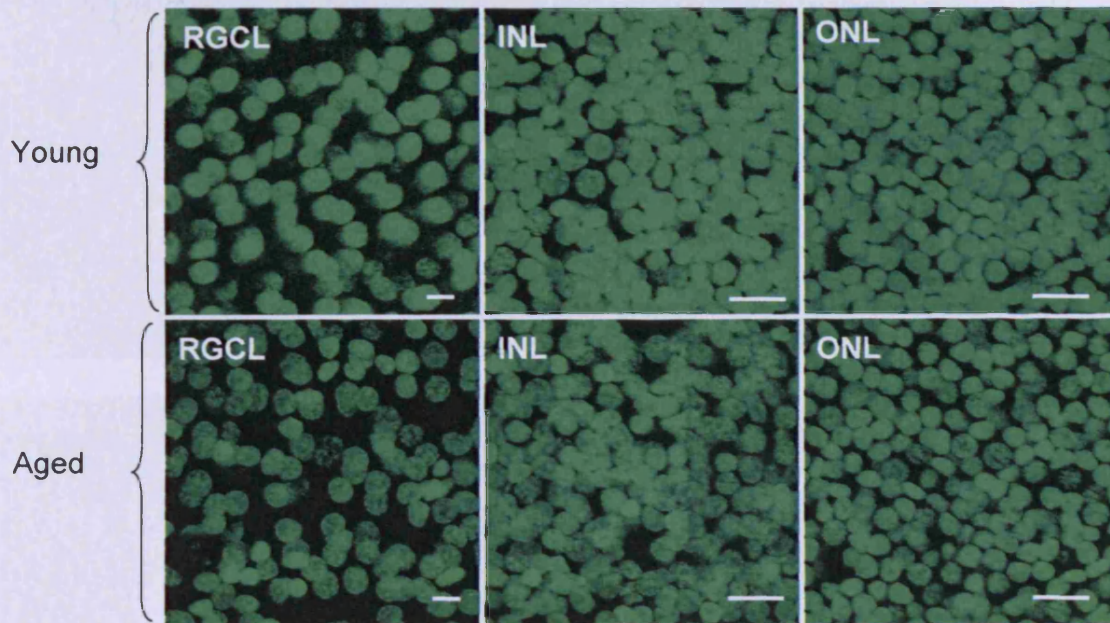
Weiss 2002). These functional changes reflect degeneration in many retinal cell types: histological analysis confirmed the loss of RGCs in the fovea and peripheral retina decrease during ageing (Curcio and Drucker 1993), the rods undergo a significant decrease in density from the fourth decade of life onward (Gao and Hollyfield 1992). Since the rods synapse with the rod bipolar cells in the outer plexiform layer, a decline in rod density (mainly due to death) may ultimately cause an associated decline of other neurones which, like the rod bipolar cells, are connected to them. Age-related morphologic changes (e.g. drusen) also occur at the level of Bruch's membrane (Majji et al. 2000), a basement membrane complex located between the retinal pigment epithelium and the choroid, which may disrupt their supportive role in retinal function. There is evidence that the retina adapts to these ageing changes, for example, the activation of astrocytes may protect neurons from free radicals (Ramirez et al. 2001). Recently, neuronal plasticity was seen in senescent retinas in mice (Liets et al. 2006) and humans (Eliasieh et al. 2007) where the neurons in the INL extended their dendrites to the ONL. However, there was no quantitative data to confirm such plasticity.

In the present study, we used the automated multiphoton-DAPI method developed (Chapter 2,3) to quantify retinal remodelling in human retinas by comparing neuron densities in young and aged groups.

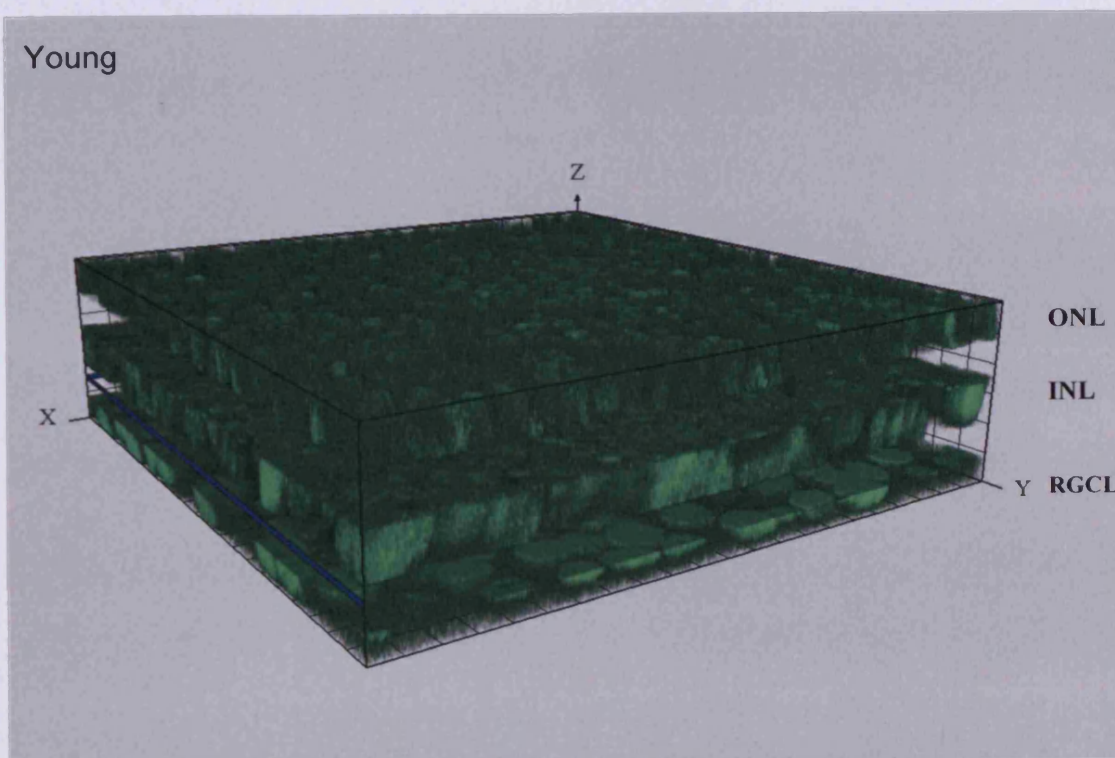
5.2. Results

5.2.1. Multiphoton imaging

Typical multiphoton images of neurons in the RGCL, INL and ONL of young and aged retinas are illustrated in Figure 5-1.



Young



Aged

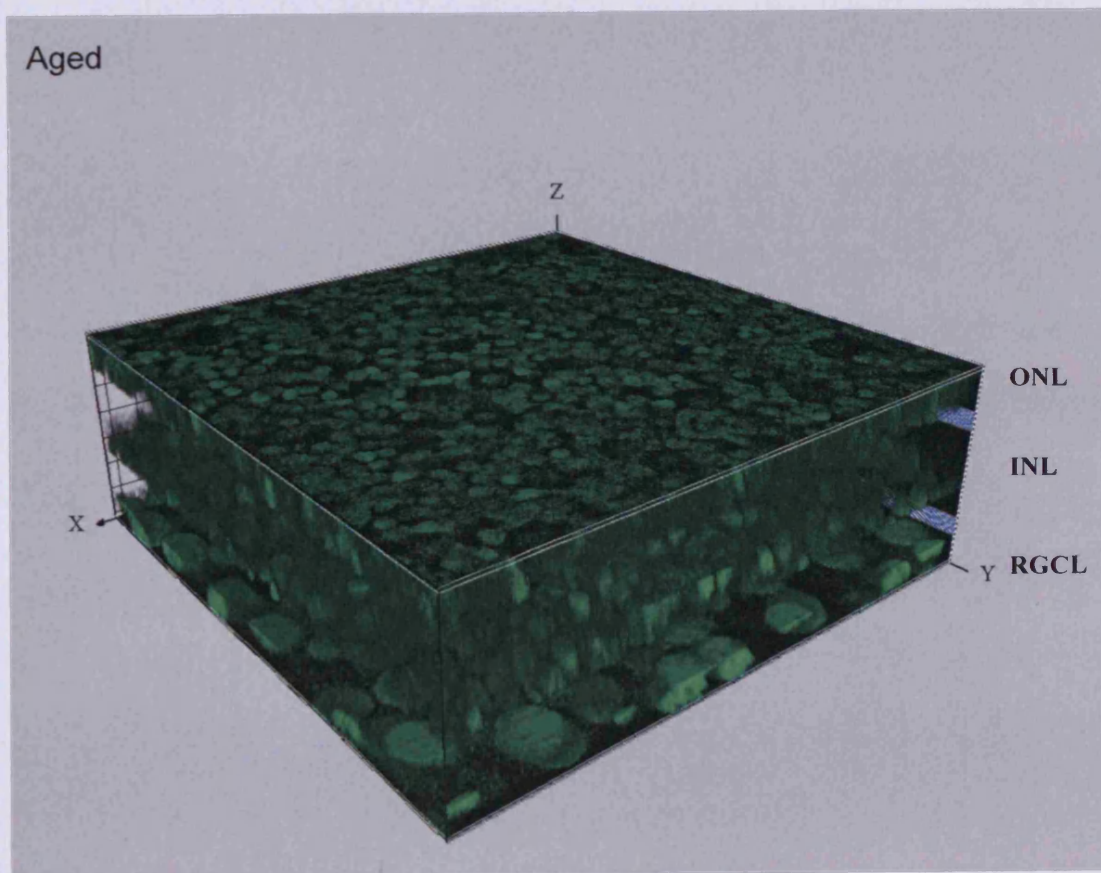


Figure 5-1 Multi-photon images of DAPI stained cell nuclei in RGCL, INL and ONL of young (n=6) and aged (n=6) human retinas. Here an example from one retina of each group is shown. These imaged were sequentially taken with the RGCL upper most and focusing from the RGCL to the ONL. Two 3D models of the retinal layers for young and aged retinas were built by Imaris software. The images shown were taken from the temporal retina at 6 mm eccentricity (as indicated by * in the 'flower petal' below the multiphoton images and point 9 on the grid). There is + represents the position of the fovea, and o is the optic nerve. The scale bar of multiphoton images is 10 μ m and the 'flower petal' is 5 mm. RGCL, retinal ganglion cell layer; INL, inner nucleus cell layer; outer nucleus layer (ONL).

5.2.2. Neuron quantification in the RGCL, INL and ONL

56% of the total area within the central 4 mm eccentricity, and 27% between 4 mm and 7 mm eccentricity was imaged. In total, 262,532 neurons were counted in young (18-33 years old, n=6) and 228,140 in aged human retinas (74-90 years old, n=6). The neuron densities of the RGCL, INL and ONL are illustrated by colour coded density maps (Figure 5-2).

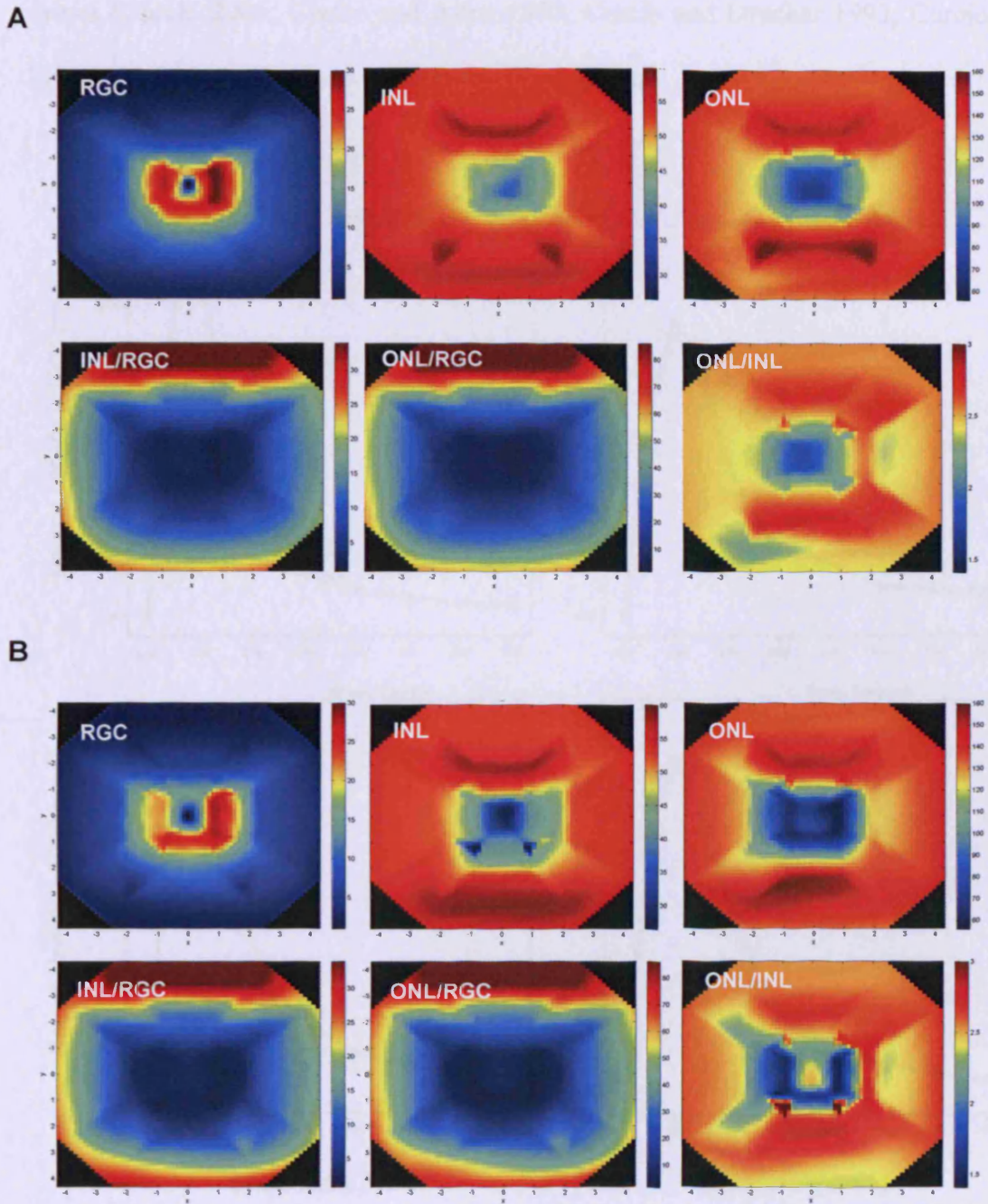


Figure 5-2 Colour coded mean neuron density maps and correlation maps of young (A, n=6) and aged (B, n=6) retinas. Colour gradient was assigned to values of densities, e.g. for RGCL, the colours from red to blue represent densities values range between 0 and 18 ($\times 1000$ per mm^2), with each colour represents a particular density value. Ratios of neuron densities were shown on the right of each contour plot. The contour map spatially correlates with the sampling grid. xy axis show eccentricities (mm), (0,0) is the fovea. RGCL, retinal ganglion cell layer; INL, inner nucleus cell layer; outer nucleus layer (ONL).

To validate our data, the RGC counts in young adults were compared with literature values (Curcio 2001; Curcio and Allen 1990; Curcio and Drucker 1993; Curcio et al. 1990) which showed a good correlation (Figure 5-3).

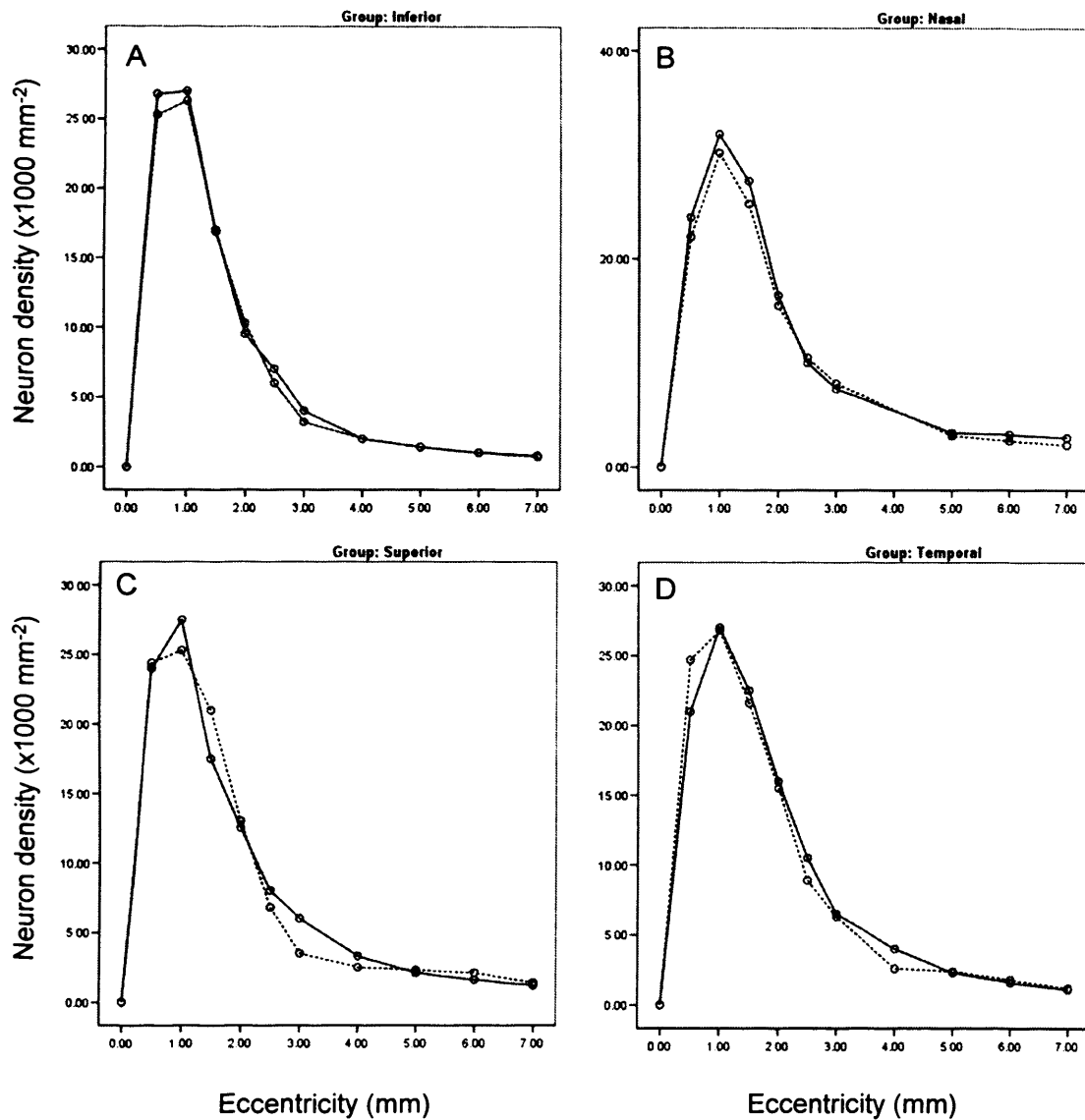


Figure 5-3 Comparisons of RGC quantities measured by multiphoton-DAPI method in young adults (n=6) and literature values (n=5) (Curcio and Allen 1990). The measurements were taken at nasal, temporal, superior and inferior regions of the retina. There was a close correlation between neuron density results from multiphoton-DAPI method and literature values.

The mean neuron densities were compared in aged and young retinas (Figure 5-4). In aged retinas, there were significant reductions of RGCs between 0.5 and 3 mm eccentricity. The mean density of RGCs within 4 mm eccentricity was reduced by approximately 13.8% (from 14,505 to 12,501 per mm^2); the greatest RGC loss was at 1mm eccentricity of 24.7%. In the INL and ONL, significant reductions of neuron densities were between 1-2 mm eccentricity of 8.5% and 0.5-4 mm eccentricity of 15.2%, respectively. The greatest loss of neurons in the INL and ONL was at the same region (1.5 mm eccentricity), but this was different from where the peak neuron loss occurred in the RGCL (1 mm eccentricity).

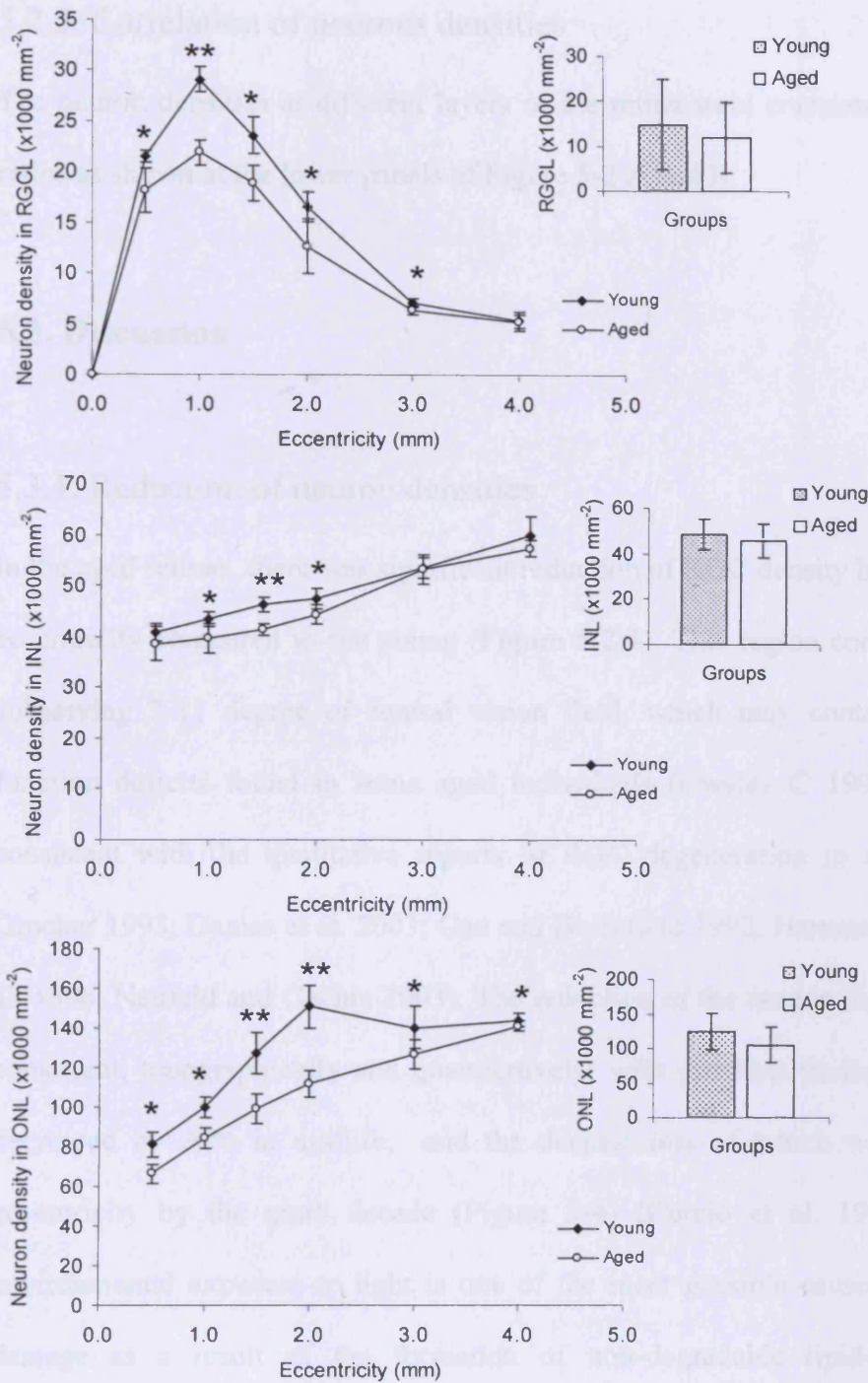


Figure 5-4 Comparisons of neuron densities in the RGCL, INL and ONL of young (n=6) and ageing (n=6) retinas. Lines show means of neuron densities at each eccentricity, and bars show means within 4mm eccentricity. Error bars show mean \pm 1 SD. Compared to young retinas, ageing retinas showed significant reduction of neuron densities in central retina. * $p < 0.05$, ** $p < 0.01$. RGCL, retinal ganglion cell layer; INL, inner nucleus cell layer; outer nucleus layer (ONL).

5.2.3. Correlation of neurons densities

The neuron densities at different layers of the retina were correlated and expressed as ratios as shown at the lower panels of Figure 5-2 A and B.

5.3. Discussion

5.3.1. Reduction of neuron densities

In the aged retinas, there was significant reduction of RGC density between 0.5 to 3 mm eccentricity compared to the young (Figure 5-2,4). This region corresponds to an area subserving 2-11 degree of central vision field, which may contribute to the visual function deficits found in some aged individuals (Owsley C 1990). Our results are consistent with the qualitative reports of RGC degeneration in ageing (Curcio and Drucker 1993; Danias et al. 2003; Gao and Hollyfield 1992; Harman et al. 2000; Kim et al. 1996; Neufeld and Gachie 2003). The reduction of the neuron density in the ONL is consistent, topographically and quantitatively, with previous findings that rod density decreased by 30% in midlife, and the deepest loss of which was at 0.5 to 3 mm eccentricity by the ninth decade (Figure 5-4) (Curcio et al. 1993). Damage from environmental exposure to light is one of the most possible causes for photoreceptor damage as a result of the formation of non-degradable lipid-protein aggregates lipofuscin during lipid peroxidation process.

5.3.2. Correlated neuronal loss

There are three important observations in the present study. First, the reduction of neuron densities in the INL spatially corresponded to the greatest reductions of neurons

in the RGCL and ONL (Figure 5-4); this correlated neuron loss supports a transneuronal mechanism of neurodegeneration in retinal ageing. Second, compared to 2 mm eccentricity, the percentage of neuron loss at 1 mm eccentricity was increased in the RGCL and reduced in the ONL, and this correlated with increased neuron loss in the INL (1.26 fold); this admits of two possible explanations a) there is a closer correlation of neurodegeneration in RGCL&INL than INL&ONL, b) a mechanism other than transneuronal degeneration is responsible for the loss of neurons in the INL. Third, when we compared the locations of the greatest reductions of neuron densities in different layers, interestingly, the greatest loss of INL neurons (1.5 mm eccentricity) was between the greatest loss of RGCL (1mm eccentricity) and ONL neurons (2 mm eccentricity); this confirms the interpretation b) and emphasises the importance of finding other mechanisms responsible for the age related neurodegeneration in the INL.

5.3.3. A complex of age related retinal degenerations

The data of the correlated neuronal loss is consistent with the concept that ageing leads to a complex of degenerative changes which might be the causes or consequences of each other; it is not simply the dying of a particular type of cells or structure. The big picture of retinal ageing is the thinning of the overall retinal thickness (Alamouti and Funk 2003; Lovasik et al. 2003) and the neuroretinal rim. At the cellular level, there are significant reductions of RGCs (Curcio and Drucker 1993; Gao and Hollyfield 1992), optic nerve axons (Balazsi et al. 1984), photoreceptors (Curcio 2001; Curcio et al. 1993; Gao and Hollyfield 1992) and retinal pigmented epithelial cells (Gao and Hollyfield 1992). Moreover, the structural changes correlate with functional neural deterioration (Trick et al. 1992; Willis and Anderson 2000; Wright et al. 1985).

5.3.4. Transneuronal degeneration in ageing and glaucoma

It has been demonstrated here that the retinal transneuronal degeneration in ageing does not occur in the same manner as in glaucoma (Chapter 4), i.e. rather than a cascade of degeneration from RGCL through INL to ONL, in ageing, the neurodegeneration in the RGCL and ONL may together contribute to the damage in the INL (Figure 5-2,4). As mentioned before, transneuronal degeneration occurs in many neurological diseases (Gupta and Yucel 2003; Weber et al. 2000; Yucel et al. 2000; Yucel et al. 2001) although its mechanism is not clear.

The whole chapter focused on investigating the retinal neuronal loss in different levels of the retina under the hypothesis that there is transneuronal degeneration in ageing, i.e. the neuronal loss at different levels are correlated. However, it does not and it is not appropriate to hypothesize that there is neuronal remodelling in ageing. As stated in the introduction in Chapter 5 that ageing is ‘the progressive accumulation of changes with time that are associated with or responsible for the ever-increasing susceptibility to disease and death which accompanies advancing age’. Plasticity involves the transformations of neurons and neural networks as part of their normal functions. It is clearly reversible in many of its manifestations, .e.g. CNS neurons show plasticity in changing the number of dendritic spines in association with learning and memory (Sorra and Harris, 2000). Remodelling, on the other hand, may invoke normal plastic mechanisms, or represent the removal of inhibitory mechanisms that maintain structural homeostasis (Marc et al., 2003). In response to deafferentation, neurons in both retina and CNS display a range of degenerative changes, including apoptosis, reshaping of neurites, revision of synaptic connectivity, modulation of gene expression and glial

transformations, which in turn alter the signal processing in the entire visual pathway (Marc et al. 2003). In the visual system, remodelling can potentially corrupt spatial processing and prevent the retina from providing signals throughout the visual circuits.

5.4. Conclusion

Retinal transneuronal degeneration occurs in ageing, although in a different manner from glaucoma. However, other mechanisms, in addition to transneuronal degeneration, also seem to contribute to the neuronal loss.

CHAPTER 6 TOPOGRAPHY OF NEURONAL LOSS IN THE RETINAL GANGLION CELL LAYER OF HUMAN GLAUCOMA

OBJECTIVES

- To develop a method to delineate the topography of neuronal loss
- To determine the pattern of retinal degeneration in human glaucoma by comparisons with control retinas

6.1. Introduction

In Chapter 4, I have demonstrated a gradient of transneuronal degeneration from the RGCL through the INL to the ONL in human glaucoma. This chapter sought a deeper understanding of the neuronal loss by focusing on the RGCL, which is most vulnerable to glaucomatous damage.

There is a large body of clinical data describing the patterns of visual field defect in glaucoma; however, at the level of the RGC population, comparatively little evidence is available addressing the spatial pattern of damage in human. Knowledge of this is important if we are to understand the relationship between the loss of cells and visual function. In experimental glaucoma, where changes in the RGC population can be directly observed, the patterns of RGC loss are variable between species and the methods used to induce the disease. DBA/2J mice have mutations in two genes (*Gpnmb* and *Tyrp1*) leading to high IOP and subsequent damage; the pattern of RGC loss was found to be focal in the early stages of retinal degeneration (Jakobs et al. 2005), but diffuse in advanced stages (Danias et al. 2003). In rat models of chronic glaucoma, the pattern of RGC apoptosis was focal in some (Mittag et al. 2000; Neufeld et al. 1999)

and more uniform in others (Cordeiro et al. 2004; Laquis et al. 1998). Under conditions of chronic pressure-induced optic nerve damage, Morrison et al reported a focal pattern of axon loss (Morrison et al. 1997). However, it is not known how these glaucoma experimental models compare with human glaucoma.

In order to quantify the changes of neuronal topography in human retinas, we used nearest neighbour analysis (NNA) to map the distribution of the remaining neurons in the RGCL. NNA has a wide range of applications and has been commonly used in studying the topography (Filippopoulos et al. 2006a) and mosaic regularity (Cook and Podugolnikova 2001; Eglén 2006; Rossi et al. 2003) of retinal neurons. The nearest neighbour distance (NND) for each neuron is defined as the distance from its centre point to that of the closest adjacent neuron. NNA explores the spatial randomness of points by comparing NNDs from representative samples with those from related cases, or with theoretically hypothesized models (Bartlett. 1975; Diggle 1983; Oliver Schabenberger 2005). In the current study, we used this method in conjunction with microscopic observations to study the pattern of neuronal loss in the RGCL in glaucomatous retinas by comparisons with age-matched controls.

6.2. Results

6.2.1. Method validation

After morphometric processing of the images, a raster dataset was created, i.e. the position of each neuron was represented by a single point, from which NNDs were

calculated (Chapter 2, Figure 2-8). There were close agreements between NNDs measured by manual and computer counts ($R^2=0.998$, Figure 6-1).

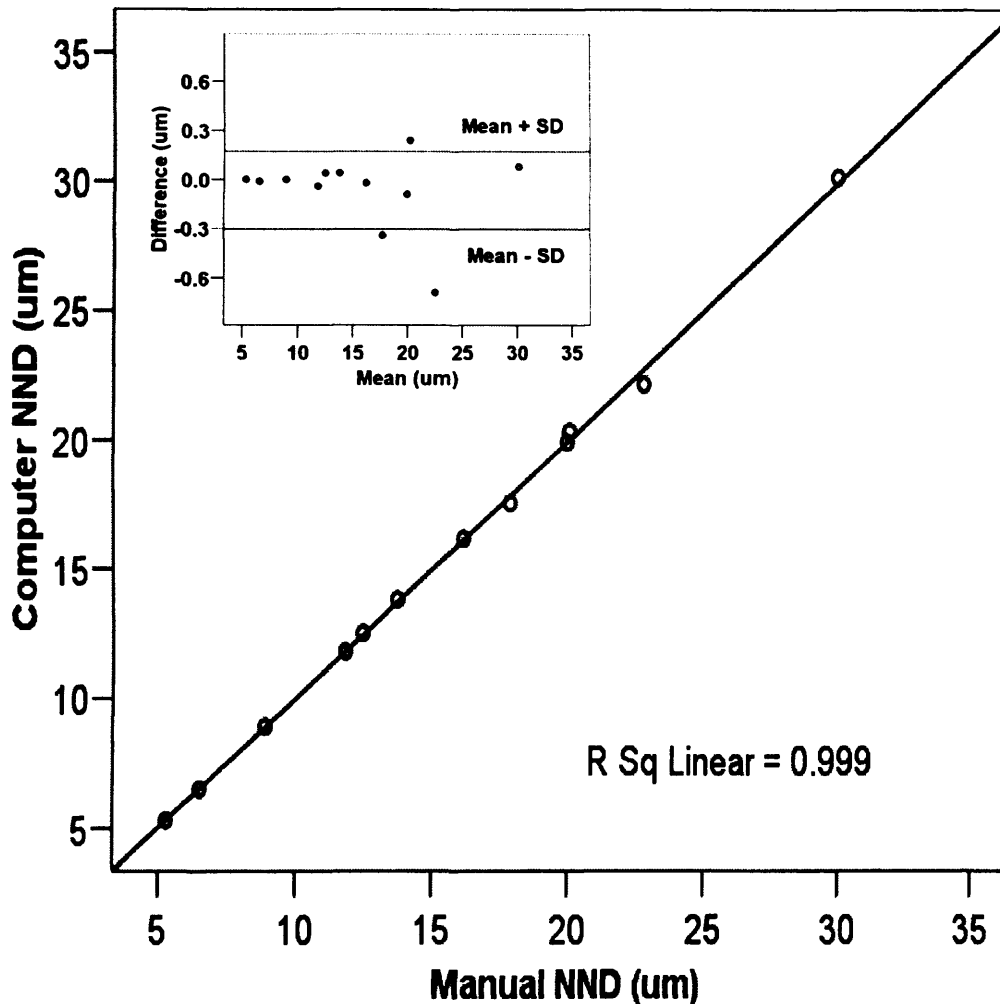


Figure 6-1 Correlation of the nearest neighbour distances (NNDs) counted by manual ($n=6$) and automated method ($n=6$). 20 frames of 0.96 mm^2 each were selected from 12 retinas to cover the full density range. Best-fit linear regression has a correlation coefficient (R^2) of 0.999. This is confirmed by Bland-Altman plot (in the sub-window), i.e. most of the points fall within the range of mean \pm SD, and there is no trend as x value increases.

6.2.2. Neuron densities and nearest neighbour distances (NNDs)

In total, 71,276 nuclei were counted in glaucomatous retinas (67-83 years old, $n=6$) and 120,036 in age-matched control (61-89 years old, $n=6$) retinas. The data confirmed that

neuron density was highest in the perifoveal region; the greatest density reduction in glaucomatous retinas was between 2-3 mm eccentricity of approximately 43%. The neuron density was inversely correlated with the average NNDs ($R^2 = 0.97$, Figure 6-2). On average, the NNDs of glaucomatous retinas were significantly higher than controls (Mann-Witney U test, $p < 0.001$) of 8.9%; this difference was more marked in the peripheral relative to the central retina (Figure 6-3).

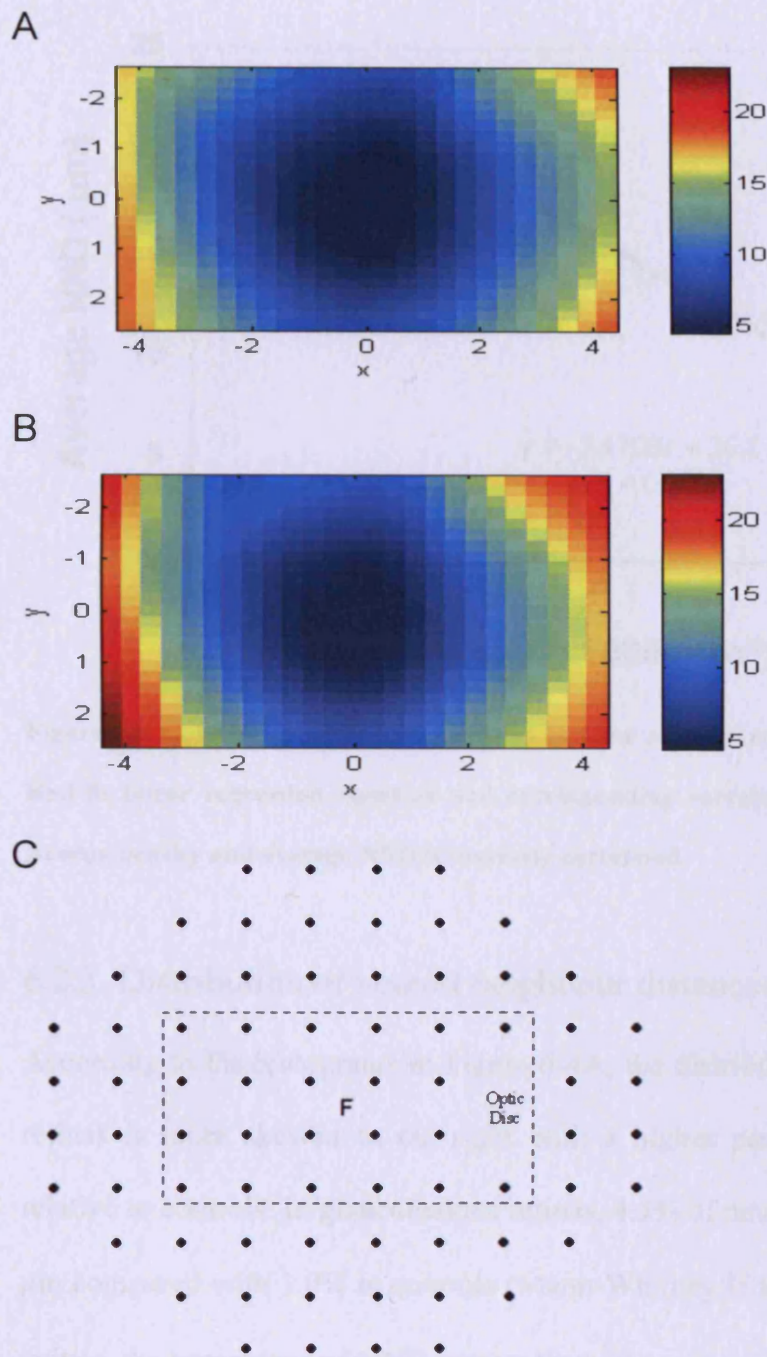


Figure 6-2 Colour coded maps of mean nearest neighbour distances (NNDs) distribution in control (A, n=6) and glaucomatous retinas (B, n=6). Colour gradient is assigned to values of NNDs (μm), e.g. in A the colours from red to blue represent NND values range between 5 and 25 ($\times 1000 \text{ per } \text{mm}^{-2}$), with each colour represents a particular density value. The contour map spatially correlates with the sampling grid in C. xy axis show eccentricities (mm), (0,0) is the fovea.

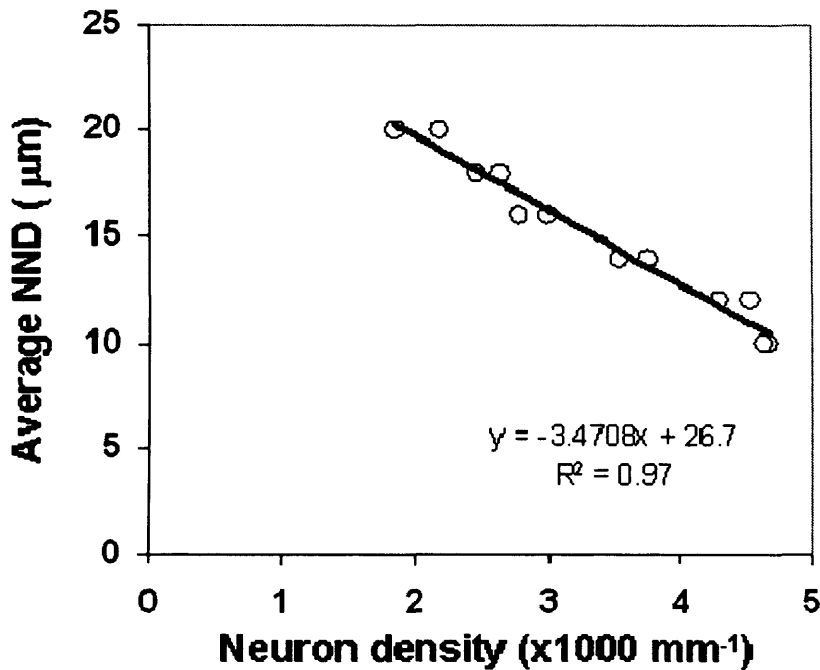


Figure 6-3 Correlation of neuron densities and the average nearest neighbour distances (NNDs). Best-fit linear regression equation and corresponding correlation coefficient (R^2) are indicated. Neuron density and average NND is inversely correlated.

6.2.3. Distribution of nearest neighbour distances (NNDs)

According to the histograms in Figure 6-4A, the distribution of NNDs in glaucomatous retinas is more skewed to the right with a higher positive kurtosis (i.e. heavy tail) relative to controls. In glaucomatous retinas, 4.5% of neurons had NNDs greater than 20 μm compared with 1.0% in controls (Mann-Whitney U test, $P < 0.001$). In glaucomatous retinas, the percentage of NND greater than 40 μm was increased by 8.2 folds compared to controls (Figure 6-4B).

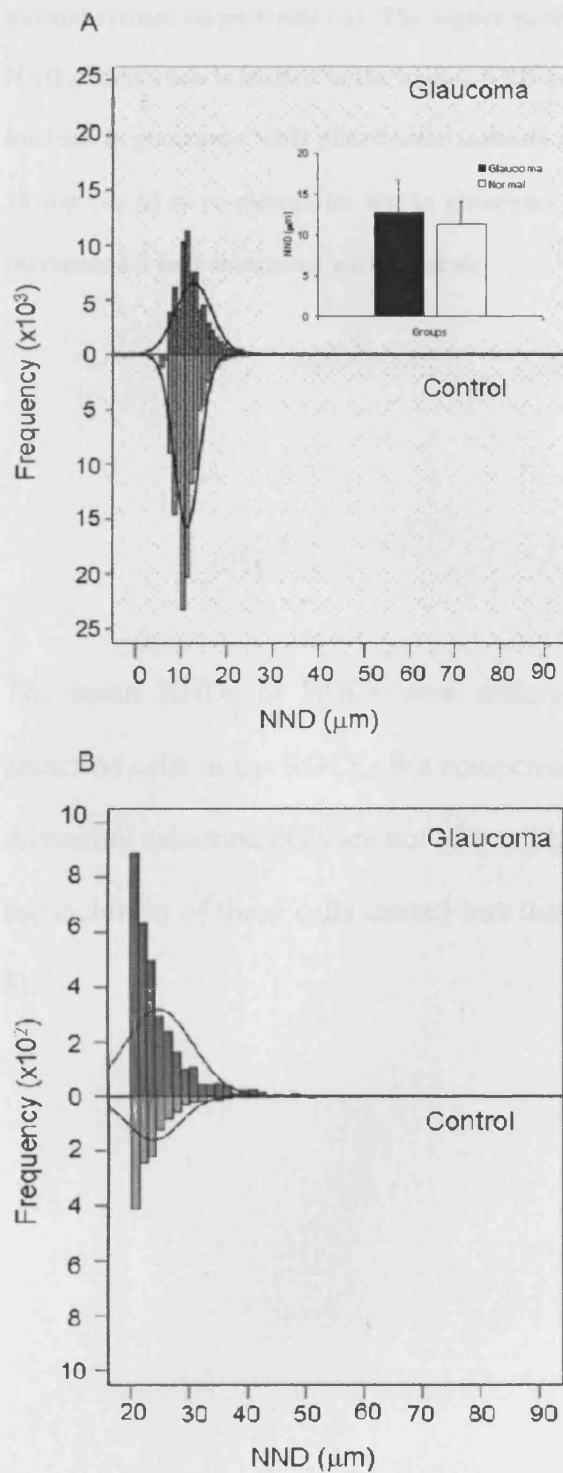


Figure 6-4 Nearest neighbour distances (NNDs) distribution in glaucomatous (n=6) and age-matched control retinas (n=6). Compared with controls, NNDs in glaucomatous retinas are shifted to the right (A), and the densities of neurons reduced (A, bar chart). The skewness and kurtosis of NND distribution in glaucomatous retinas is 2.57 and 16.347, compared with 1.765 10.611 in

normal retinas respectively (A). The higher positive skewness in glaucoma indicate that the peak of NND distribution is shifted to the higher NND values and has a longer tail than control. The higher kurtosis in glaucoma NND distribution indicate that the peak is more flat than control. The NNDs $\geq 20 \mu\text{m}$ (in A) is re-plotted (in B); in glaucoma group, the percentage of NNDs within this range increases 4.5 fold compared with controls.

The mean NNDs of RGCs were underestimated due to the presence of displaced amacrine cells in the RGCL. We compensated for this deviation by a simulation model. Assuming amacrine cells are not affected by glaucomatous damage (Jakobs et al. 2005), the inclusion of these cells caused less than 3% decrease in the mean NNDs (Figure 6-5).

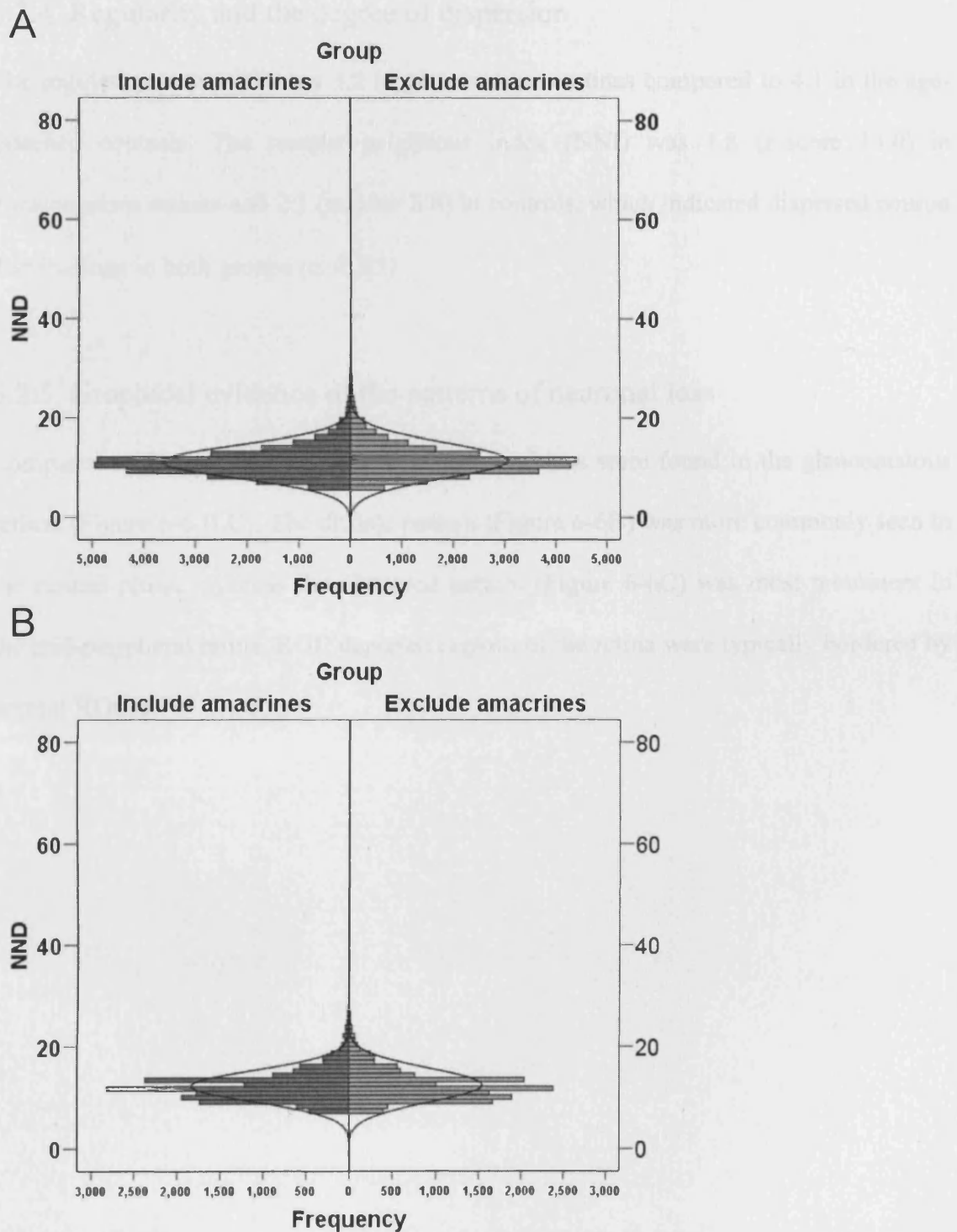


Figure 6-5 Histogram showing the distribution of nearest neighbour distances (NNDs) with and without the correction for the presence of displaced amacrine cells in the RGCL (10%) in normal (A, n=6) and glaucomatous retinas (B, n=6). There is less than 3% difference in the mean NNDs between the inclusion and the exclusion of amacrine cells in both groups.

6.2.4. Regularity and the degree of dispersion

The regularity index (RI) was 3.2 in glaucomatous retinas compared to 4.1 in the age-matched controls. The nearest neighbour index (NNI) was 1.8 (z-score 13.0) in glaucomatous retinas and 2.1 (z-score 8.8) in controls, which indicated dispersed neuron distributions in both groups ($\alpha < 0.05$).

6.2.5. Graphical evidence of the patterns of neuronal loss

Compared with control, two patterns of neuronal loss were found in the glaucomatous retinas (Figure 6-6 B,C). The diffuse pattern (Figure 6-6B) was more commonly seen in the central retina, whereas the clustered pattern (Figure 6-6C) was most prominent in the mid-peripheral retina. RGC depleted regions of the retina were typically bordered by normal RGCs.

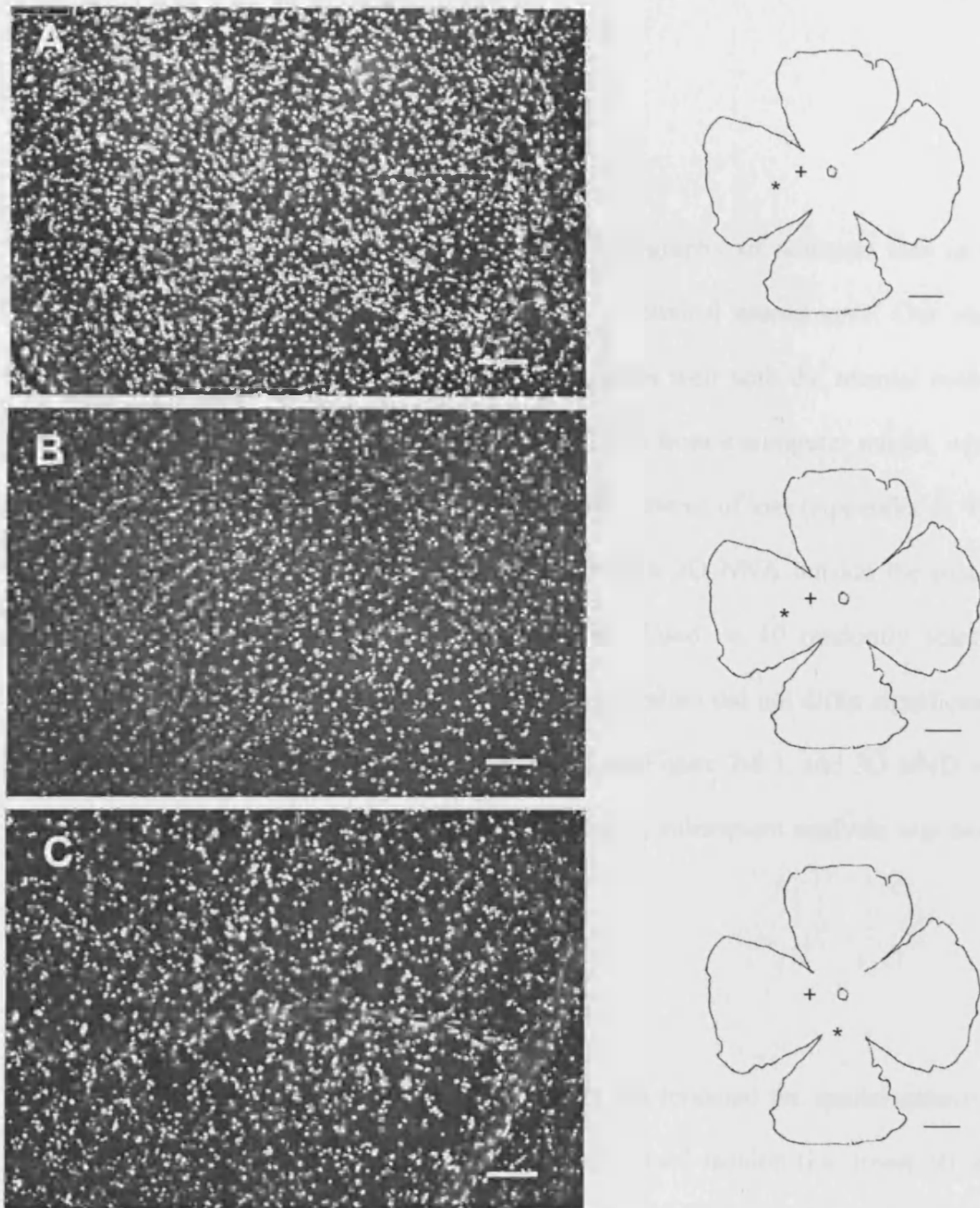


Figure 6-6 Typical images of diffuse pattern (B) and focal pattern (C) of neuronal loss in glaucoma group (n=6) compared with normal (A, n=6). The imaging position is indicated by * in the 'flower petal' on the right of the microscopic images. + represents the position of the fovea, and o is the optic nerve. Arrows in C indicate areas of clustered neuronal loss. The image size is 1600x1200 pixels, i.e. 1.98 pixels/ mm² resolution. The scale bar of microscopic images is 100 μm and the 'flower petal' is 5 mm.

6.3. Discussion

6.3.1. Method validation

The present study was designed to evaluate the topography of neuronal loss in the RGCL at greater resolution than those possible in clinical assessments. Our semi-automated quantification of NNDs is robust and agrees well with the manual method (Figure 6-1). The data can also be related to the results from a computer model, which simulated NND distributions in diffuse and clustered patterns of loss (Appendix I). Two forms of nearest neighbour analysis were performed: a 2D NNA outside the macula region, and a 3D NNA within the macula region. Based on 10 randomly selected regions of the retinal whole mounts, 2D and 3D NND values did not differ significantly (Figure 2-8, where 2D NND was calculated based on Figure 2-8 I, and 3D NND was calculated based on A-J, Mann–Witney U Test, $p > 0.8$), subsequent analysis was based on 2D NND values for consistency.

6.3.2. Altered NNDs in glaucoma

According to the RI and NNI calculated, glaucoma has rendered the spatial pattern of RGCL neurons towards a less regular and more dispersed fashion (i.e. lower RI and lower z-score of NNI in glaucomatous retinas) (Cook 1996; Fei 2003; Hutsler and Chalupa 1994; Rossi et al. 2003; Wassle and Riemann 1978). The higher average NNDs in glaucomatous retinas (Figure 6-2) is consistent with the overall reduction of neuron densities in the RGCL (Figure 6-4A, bar plot), and the inverse correlation of neuron densities and NNDs (Figure 6-3). Within the region sub-serving the central 15 degree of visual field, a substantial component of the pattern of neuronal loss is a diffuse pattern,

which was demonstrated as a right shift of NNDs distribution in glaucomatous retinas relative to controls (Figure 6-4A). The large increase of the percentage of NNDs greater than 20 and 40 μm in the mid-peripheral retina (Figure 6-4B) suggests clustered neuronal loss in this region. We then examined the microscopic images, and they support the results from the mathematical/statistical analysis that there are two different patterns of neuronal loss in the glaucomatous retinas (Figure 6-6).

It is important to stress that the clustered loss to which we refer here occurs at a smaller scale than the focal loss of visual field in the peripheral retina often referred to clinically; in fact, it is part of the focal loss of neurons seen in large sectors of the retinas (Danias et al. 2003; Jakobs et al. 2005). In the present study, the region of examination is within the 15 degree of visual field, whereas the loss of visual field was around 30 degree in these patients. This suggests that neuronal loss proceeds the visual function impairment (Kerrigan-Baumrind et al. 2000). Should the disease continue to progress, the clustered loss of cells seen here would be expected to worsen and be responsible for the loss of central vision.

6.3.3. The underlying mechanism of two patterns of neuronal death

It is likely that the diffuse and clustered pattern of cell loss are caused by two different pathological mechanisms (Danias et al. 2003; Filippopoulos et al. 2006b). Diffuse loss of RGCs could be generated by apoptosis as a result of glaucomatous damage to the distal portions of RGCs, i.e. axons. In addition to apoptosis, further or excessive death of RGCs could result in clustered loss of neurons, which is an indirect negative effect from the degeneration of surrounding RGCs (secondary degeneration). This is

supported by the observation in a partial nerve transection model, where the primary RGC death due to optic nerve injury is accompanied by secondary death of surrounding RGCs that are not directly injured (Levkovitch-Verbin et al. 2001; Levkovitch-Verbin et al. 2003). It is highly likely that the dying neurons exerted a bystander effect on the surviving cells, rendering them more susceptible to death. The mechanism of clustered degeneration of neurons could be attributed to glutamate-induced excitotoxicity, reactive oxygen species released from neighbouring cells etc. The oxidative stress-induced dysfunction of glial cells might also facilitate the secondary degeneration of RGCs (Tezel 2006; Tezel et al. 2004). Therefore, the surrounding RGCs could enter a destructive cascade that can remain active after the initial insult has abated (Yoles and Schwartz 1998).

6.4. Conclusions

In human glaucoma, the pattern of RGC loss is diffuse in the central retina; the clustered neuronal loss in the mid-peripheral retina may reflect a secondary degeneration mechanism.

CHAPTER 7 DENDRITIC MORPHOLOGY OF RETINAL GANGLION CELLS

OBJECTIVES

- To characterise the morphology of RGCs in normal control and glaucomatous retinas
- To determine the cause of the failure in achieving complete dendritic fills in human retinas
- To evaluate the quality of the human tissue used

7.1. Introduction

In previous chapters, I have concentrated on the quantitative changes of the neurons in ageing and glaucoma. In this chapter, I tried to study the branching pattern of neurons, which may represent another important feature of glaucoma pathology; furthermore, the analysis and comparison of dendritic branching patterns in normal and glaucomatous eyes may hold the key to the remodelling of different types of RGCs (i.e. parasol versus midget cells). The diverse and complex morphologies of different classes and subclasses of RGCs were well described by Cajal using Golgi staining technique (Cajal 1893). Subsequent studies with light and electron microscopy led to a further understanding of the morphology and physiology of the vertebrate retina (Boycott and Kolb 1973; Wässle 2004; Kolb 1974; Masland 2001). However, the labelling of the neuronal dendrites has always been technically challenging. Even when some success was achieved, it was not always possible to distinguish the dendrites of an individual cell from those of its neighbours, especially in the central retina where cells were densely packed.

In this chapter, we attempted to stain the individual RGCs using different techniques, including intracellular injection, ballistic delivery of carbocyanine dyes (i.e. gene gun technique) and immunohistochemistry.

7.2. Results

7.2.1. Gene gun technique and intracellular injection

The gene gun technique and the intracellular injection technique were both used to label the dendritic arbour of RGCs. Retinas of different species (e.g. chick, pig, rat human) have been used to develop the technique. Gene gun technique successfully labelled the soma and dendrites of RGCs in live chick retinas (Figure 7-1 A). However, in human retinas neuron dendrites were only partially labelled (Figure 7-1 B). The intracellular injection technique successfully labelled RGCs in live chick retinas and lightly fixed pig retinas (Figure 7-1 C), but not in human retinas.

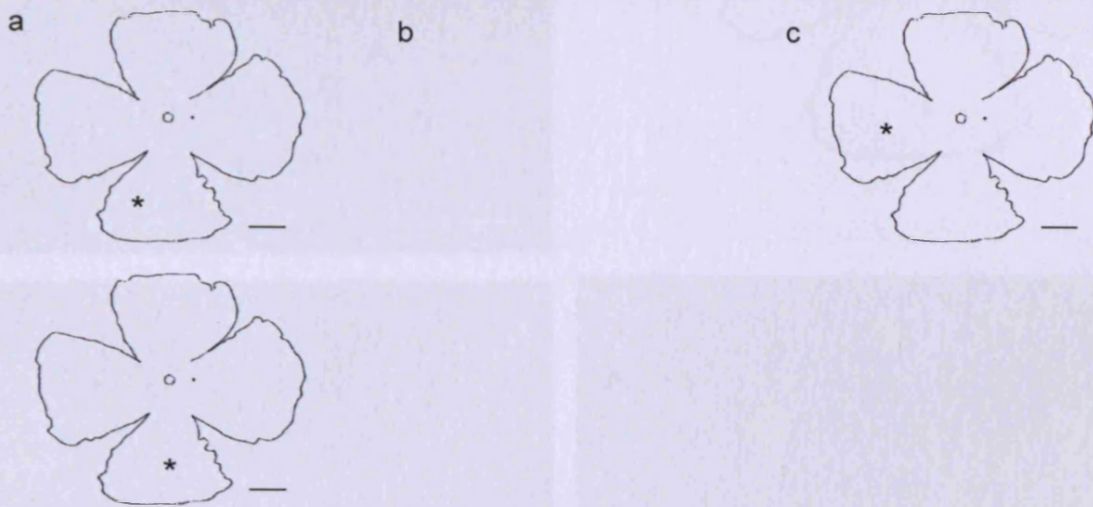
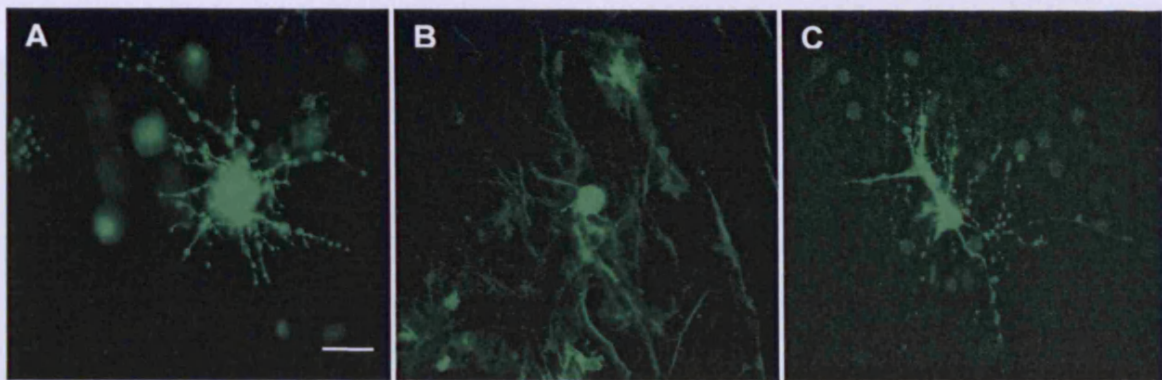


Figure 7-1 Dye labelling of retinal neurons. A and B show DiI labelled RGCs in the fresh chick retina (A) and the fixed human retina (B, Caucasian male of 79 years old) using the gene gun technique, respectively; C shows a lucifer yellow labelled retinal ganglion cell in the porcine retina by intracellular injection. The 'flower petal' a-c corresponds to the sampling position of A-C on the retinal whole mounts. Scale bar of A-C 50 μm . and a-c 5 mm.

7.2.2. Immunofluorescent staining of neuron dendrites

In human retinal whole mounts, immunostaining using SMI 32 antibody also failed to label a complete dendritic arbour of RGCs (Figure 7-2).

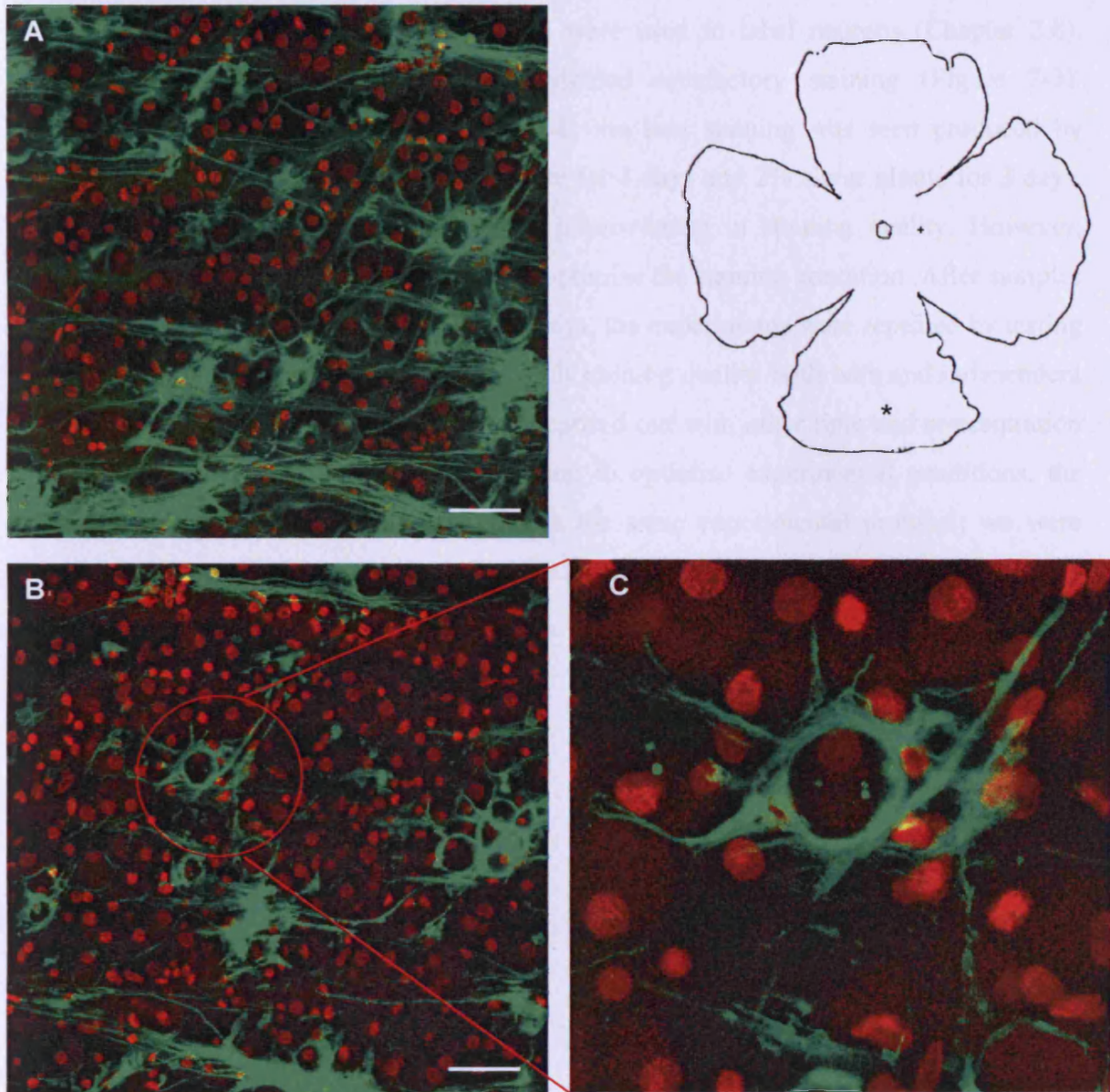


Figure 7-2 Immunofluorescence labelling of retinal ganglion cells (n=3). Green, SMI 32 antibody; red, DAPI staining. Here an example from one retina of each group is shown. SMI32 partially labelled the dendrites of neurons in the retinal ganglion cell layer. The ‘flower petal’ represents the retina whole mount: * indicates where the sample was taken, + represents the position of the fovea, and o is the optic nerve. The retina is from a normal Caucasian male donor of 79 years old. Scale bar for AB is 50 μ m, C is 10 μ m and D is 5 mm.

7.2.3. Golgi impregnation

Several protocols of Golgi impregnation were used to label neurons (Chapter 2.8). However, none of these approaches yielded satisfactory staining (Figure 7-3). According to the procedure in Figure 2-8, the best staining was seen produced by samples being in 1% potassium bichromate for 4 days and 2% silver nitrate for 3 days, beyond which time point there was no improvement in staining quality. However, further modification was still required to optimise the staining condition. After samples being in 1% potassium bichromate for 4 days, the experiments were repeated by testing the effect of silver nitrate concentrations on staining quality both with and independent of time. Similar investigations were also carried out with other time and concentration variables. After time and time again trying to optimise experimental conditions, the staining results were highly variable with the same experimental protocol; we were therefore very reluctant to apply this technique in our valuable glaucoma human tissue.



Figure 7-3 Retinal ganglion cell layer stained by Golgi impregnation in human retinas (n=3). Here an example from one retina of each group is shown. No dendritic structure could be identified. The 'flower petal' on the right of the image shows where the sample is taken on the retina whole mount. * indicates where the sample was taken, + represents the position of the fovea, and o is the optic nerve. The retina is from a normal Caucasian male donor of 74 years old. Scale bar for AB is 50 μ m, C is 10 μ m and D is 5 mm.

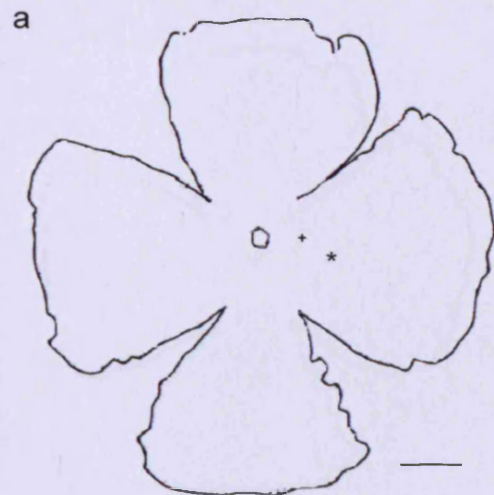
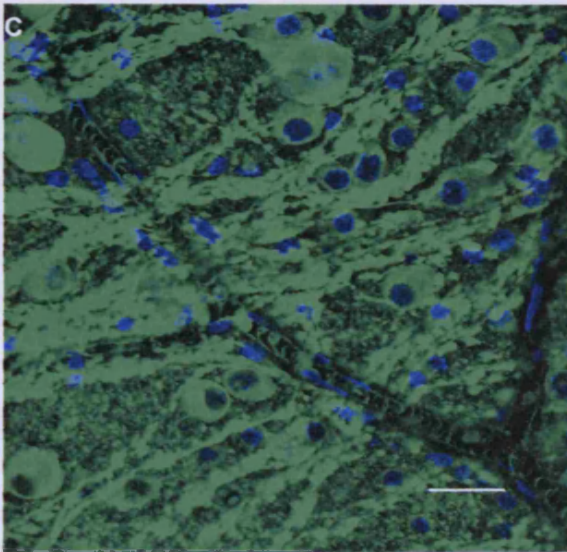
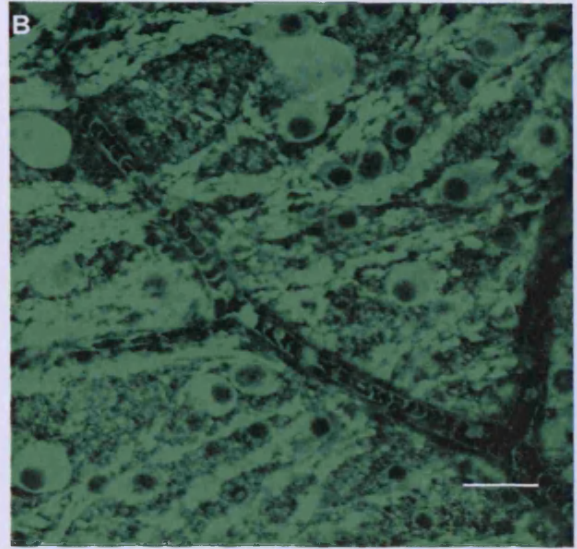
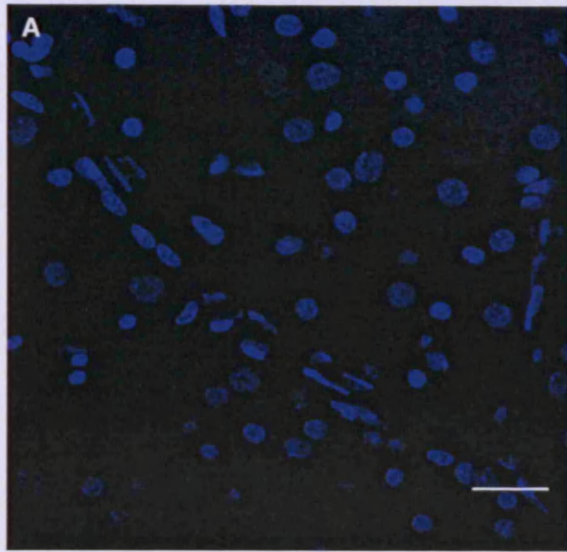
7.2.4. Human tissue quality evaluation

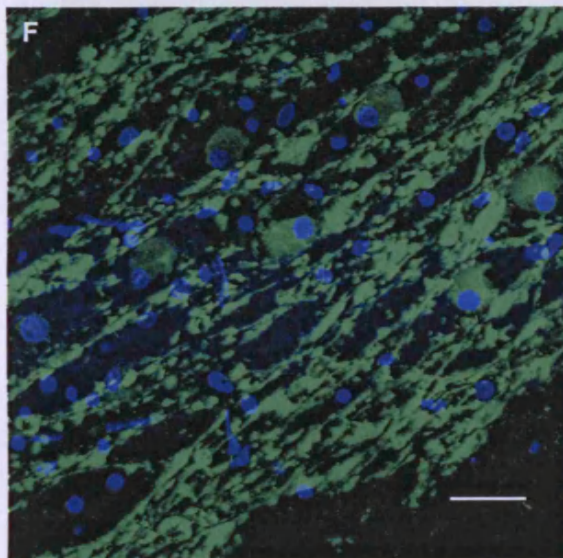
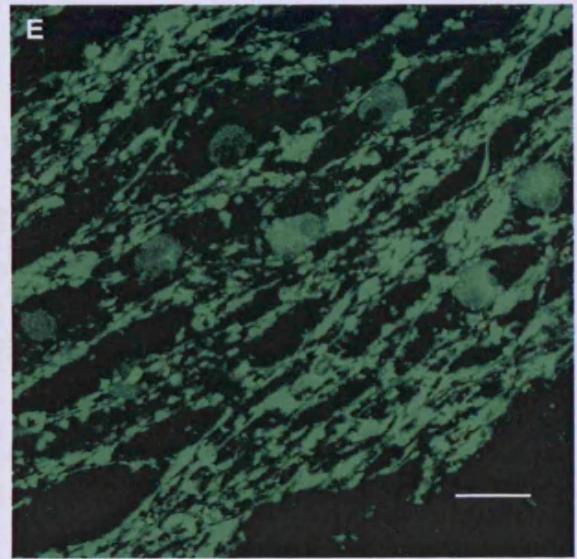
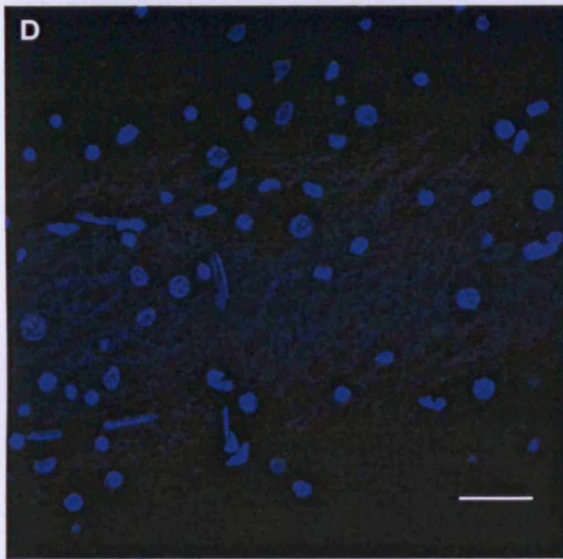
Despite the successful labelling of dendritic arbour in the animal retinas, it was frustrating that all of techniques failed in the human retinas. This led us to consider the quality of the human tissue itself: all the human retinas used here are post-mortem tissue from two sources, which are the Lions Eye Bank at the University of Washington ('US retinas') and the Bristol Eye Bank, UK ('Bristol retinas'). In order to establish the degree of retina degeneration that might have occurred before tissue fixation, experiments were conducted to compare 1) 'Bristol retinas' fixed within 24h versus 48h in PBS at 4°C; 2) 24h 'Bristol retinas' versus 'U.S. retinas'; 3) rat retinas fixed immediately in 4% PFA versus those fixed 48h later in PBS at 4°C.

7.2.4.1. Immunohistochemistry

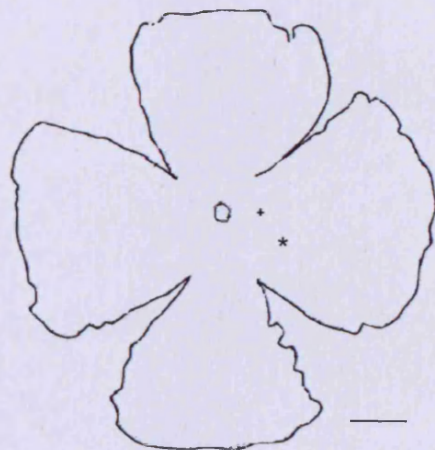
a. Comparisons of human retinas

In human retinas, TUJ-1 labelling was significantly reduced in the 48h group (Figure 7-4 D-F) compared with the 24h group (Mann-Whitney test, $p=0.001$; Figure 7-4 A-C). The percentage of the RGCs labelled in the 24h 'Bristol retina' (Figure 7-4 A-C) was comparable to the normal 'U.S. retina' (Mann-Whitney test, $p>0.7$; Figure 7-4 G-I). Glaucomatous retinas (Figure 7-4 J-L) showed a significantly lower percentage of TUJ-1 labelling than normal retinas from the same source (Figure 7-4 G-I); RGCs were completely depleted in some areas of the retina (Figure 7-4 K). Table 7-1 summarises the ratio of TUJ-1 to DAPI labelling in the three groups of human retinas ($n=3$).





b



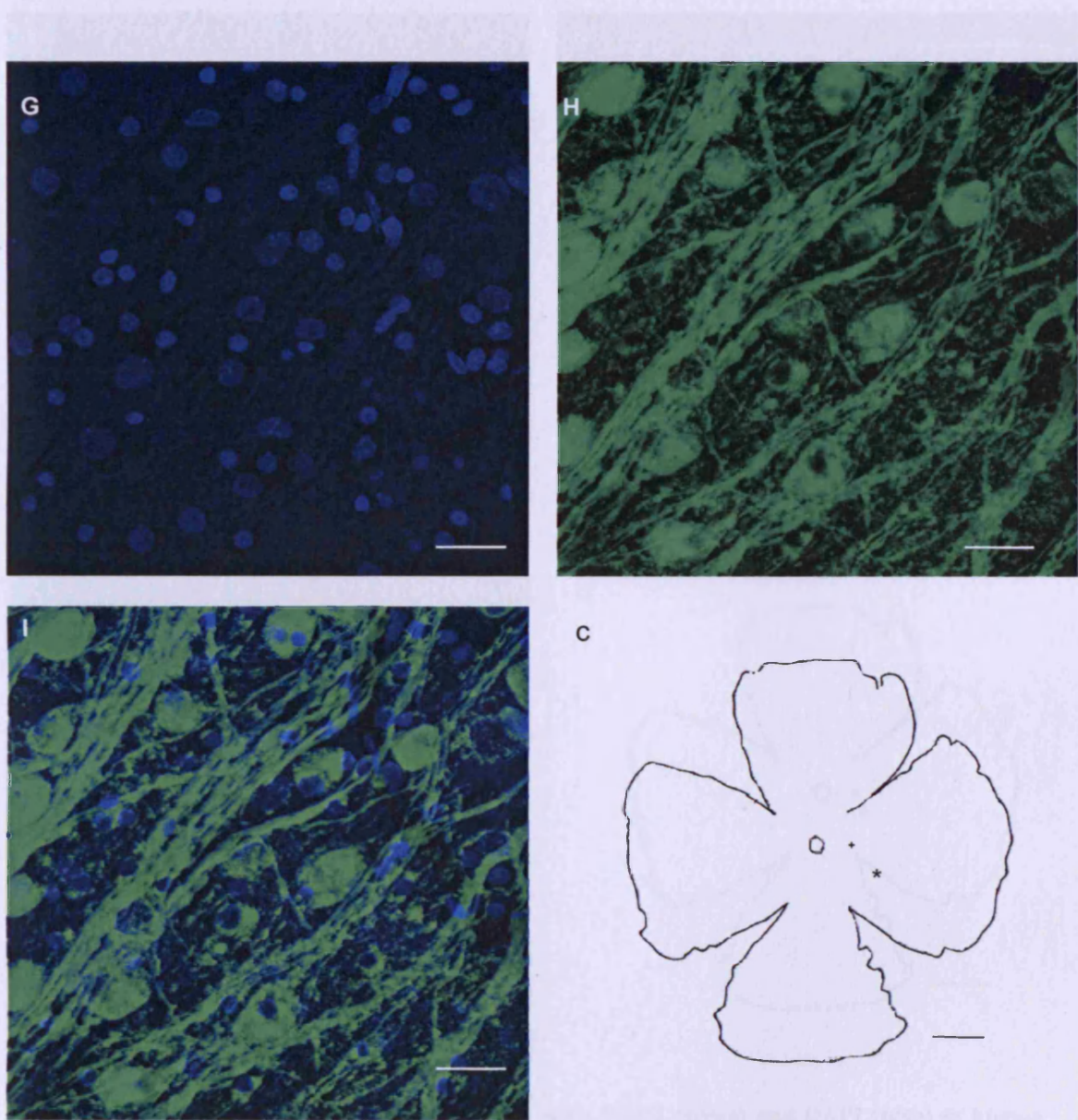


Figure 7.1 Fluorescence microscopy and schematic of RGS dendrites. **G**, DAPI-stained nuclei of RGSs. **H**, Green fluorescent dendrites of RGSs. **I**, Merged image of **G** and **H**. **C**, Schematic of a single RGS dendrite. The central soma is marked with a square, a plus sign, and an asterisk. Scale bars: **G**, **H**, and **I**, 10 μ m; **C**, 5 μ m.

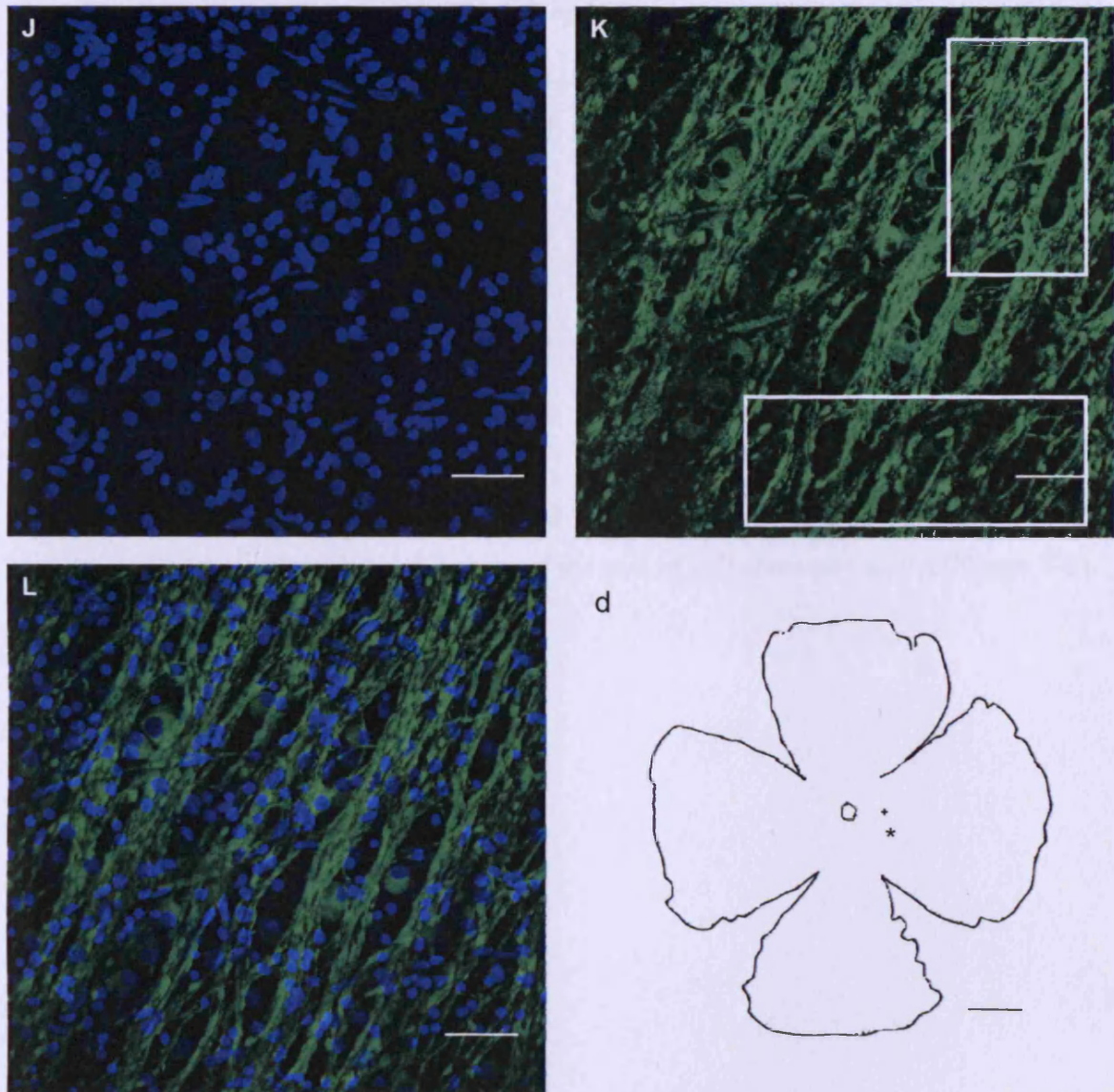


Figure 7-4 Immunofluorescent labelling of RGCs with TUJ-1 (green) and DAPI (blue) in human retinas: A-C, 24h 'Bristol retinas'; D-F, 48h 'Bristol retinas'; G-I, normal 'US retinas'; J-L, glaucomatous 'US retinas'. The 'flower petal' (a-c) represents the retina whole mounts: * indicates where the sample was taken, + represents the position of the fovea, and o is the optic nerve, and a-c corresponds to A-C, D-F, G-I and J-L. TUJ-1 labelling was significantly reduced in the 48h group (D-F) compared with the 24h group (A-C). The percentage of the RGCs labelled in the 24h 'Bristol retina' (A-C) was comparable to the normal 'U.S. retina' (G-I). Glaucomatous retinas (J-L) showed a significantly lower percentage of TUJ-1 labelling than normal retinas from the same source (G-I). RGCs were completely depleted in some areas of the retina (K) which is indicated by the white squares. Scale bar 50 μ m for confocal microscopic images and 5 mm for the 'flower petals'.

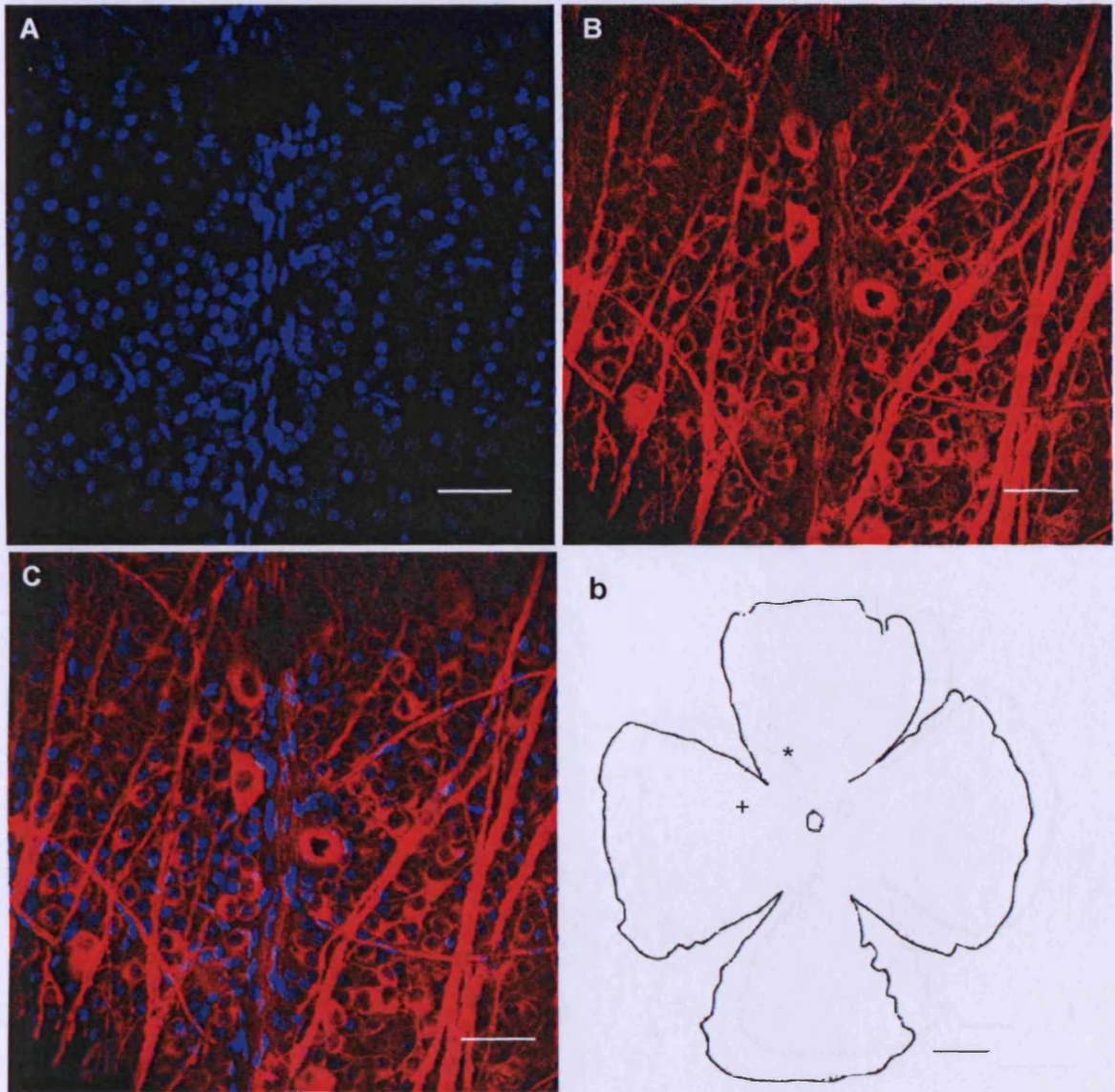
Table 7-1 The ratio of TUJ-1 and DAPI labelling in four groups of human retinas (n=3 in each group).

	Mean	Standard deviation
24h	0.34	0.04
48h	0.12	0.01
US normal	0.37	0.06
Glaucoma	0.05	0.003

b. Comparisons of rat retinas

Rat retinas fixed 48h after death showed a significant lower percentage of TUJ-1 labelling than those fixed immediately, and the loss of cell soma and axons (Figure 7-5).

24 h



48h

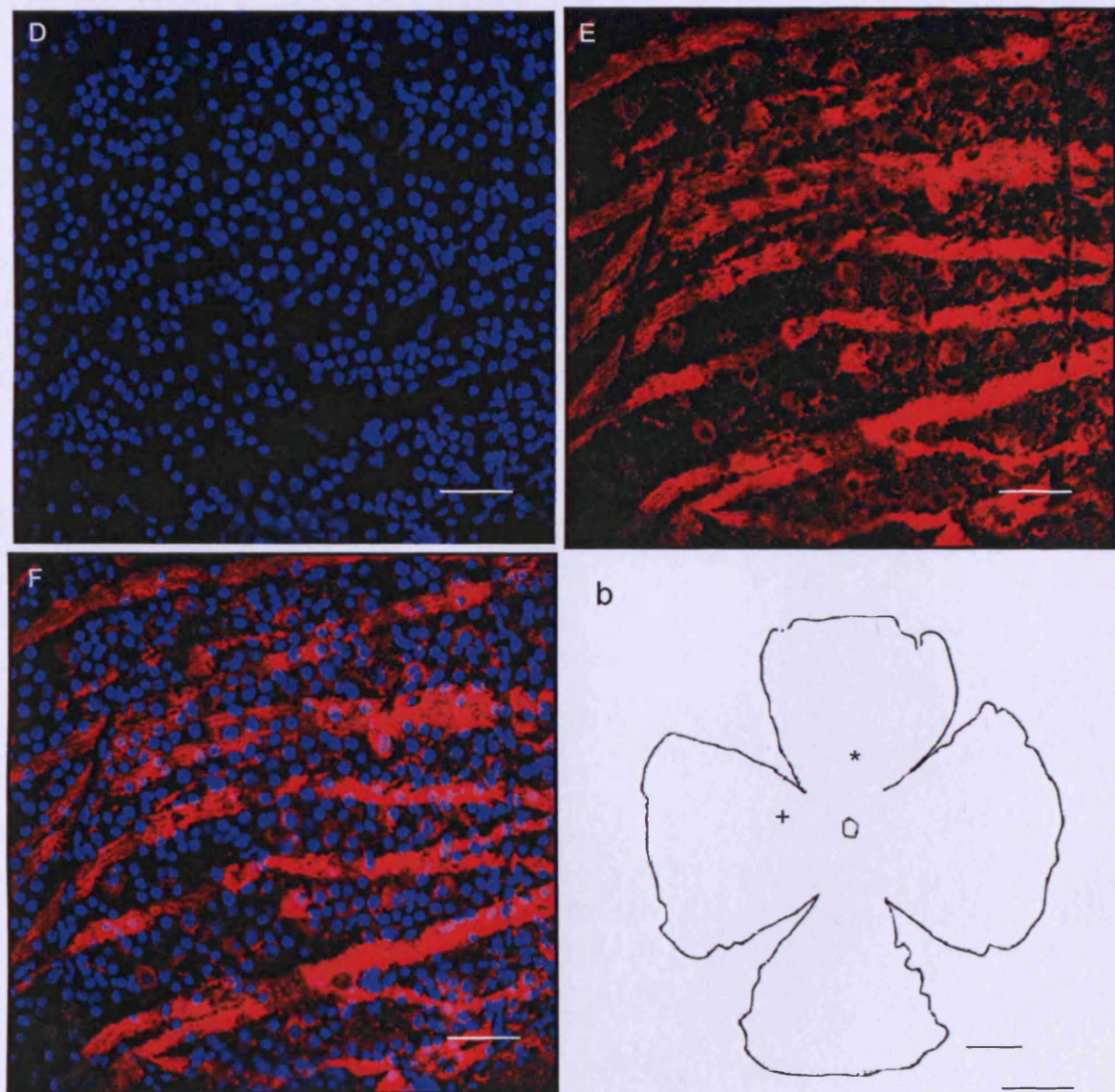


Figure 7-5 Immunofluorescent labelling of neurons in the retinal ganglion cell layers of rat retinas that were immediately fixed (A-C), and after 48h in PBS at 4°C (D-F). C and F are the overlay image of A&B and D&E, respectively. Red, TUJ-1; blue, DAPI. The 'flower petal' a and b represents the retina whole mounts A-C and D-F respectively: * indicates where the sample was taken, + represents the position of the fovea, and o is the optic nerve. Rat retinas fixed 48h after death (D-F) showed a significant lower percentage of TUJ-1 labelling than those fixed immediately (A-C), and the loss of cell soma and axons. Scale bar 50 μ m for confocal images and 5 mm for 'flower petals'.

7.2.4.2. Gene gun and intracellular cell filling

The dendrites of rat retinas fixed immediately were completely labelled using the gene gun technique (Figure 7-6 A), but not those fixed 48h later, i.e. the dendrites severely degenerated (Figure 7-6 B).

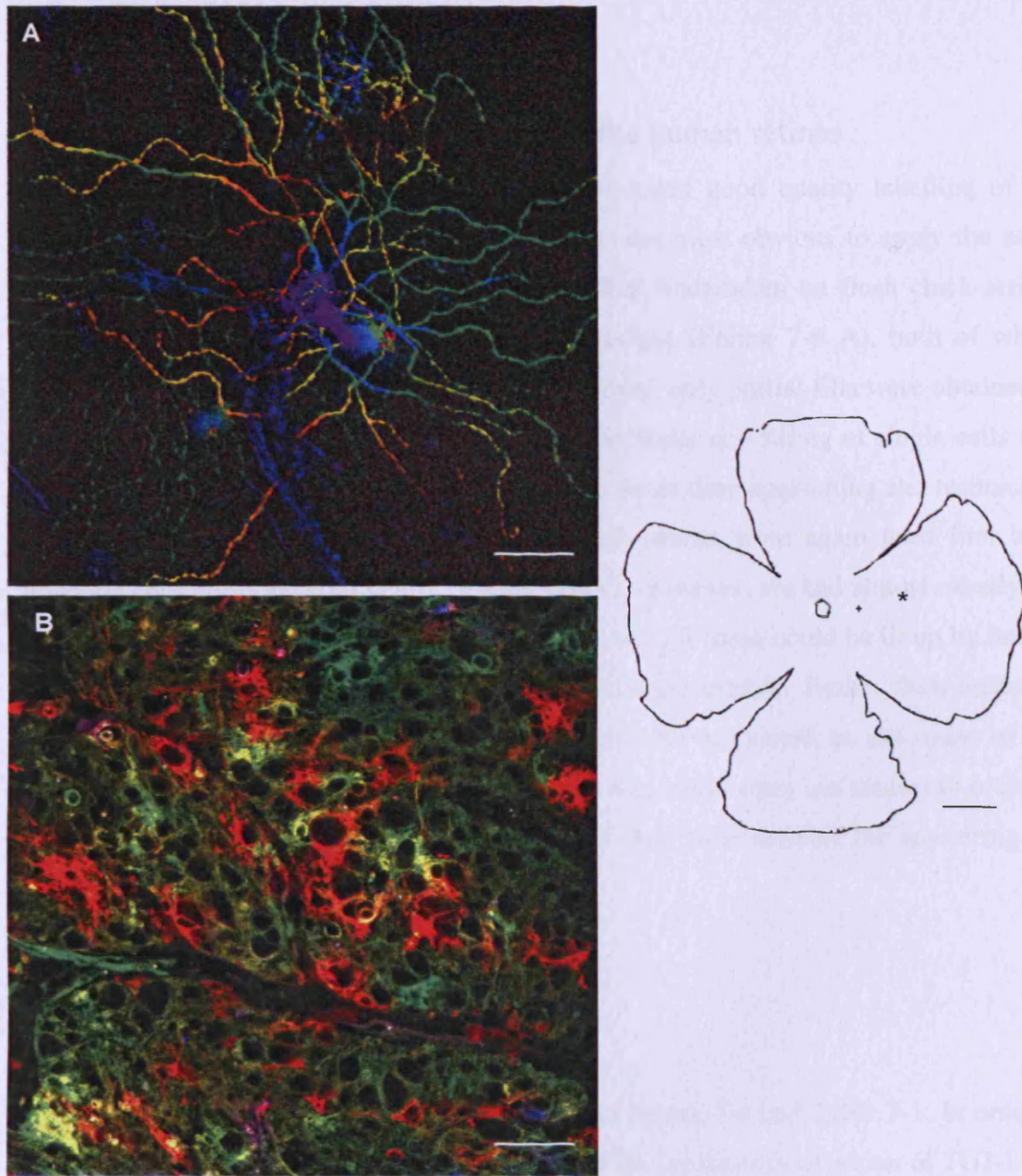


Figure 7-6 Colour coded confocal images of DiI labelled neurons. A) shows a fully labelled retinal ganglion cell in the rat retina fixed immediately in 4% paraformaldehyde; B) shows the same labelling but in a rat retina fixed after 48h from enucleation. The 'flower petal' shows the sampling position on the retina whole mounts A-C and D-F respectively: * indicates where the sample was taken, + represents the position of the fovea, and o is the optic nerve. The dendrites of rat retinas fixed immediately were completely labelled (A), but not those fixed 48h later (B). Scale bar for microscopic images 50 μ m and flower petal 5 mm.

7.3. Discussion

7.3.1. The failure of dendritic labelling in the human retinas

In the pilot studies, the gene gun technique produced good quality labelling of the dendritic arbour of RGCs of fixed rat retinas; it was most obvious to apply the same technique in human tissue. Gene gun test was first undertaken on fresh chick retinas (Figure 7-1 B), and later on freshly fixed rat retinas (Figure 7-6 A), both of which labelled the dendrites of RGCs completely. However, only partial fills were obtained in the human tissue (Figure 7-1 C). Therefore, intracellular cell filling of single cells was sought as an alternative approach. This method is more time-consuming and technically demanding than the gene gun approach. Animal retinas were again used first until injection could be done confidently (Figure 7-1 A). However, we had almost exactly the same problem as before in that although most of the cell soma could be lit up by lucifer yellow injection, the dendritic fillings were often incomplete. Rather than technical deficiency, the degeneration of the human tissue was suspected as the cause of the problem. It therefore became very important that we should carry out studies to evaluate the quality of the tissue in order to determine if they were suitable for answering the research questions proposed.

7.3.2. Tissue quality evaluation

The results of immunostaining are summarised in Figure 7-4 and Table 7-1. In order to interpret our data, it was important to understand the mechanism of action of TUJ-1 and DAPI and the biological implications. TUJ-1 is specific for β -III tubulin, which is one of the earliest neuron-associated cytoskeleton marker proteins expressed in mammalian development (Easter et al. 1993; Lee et al. 1990; Moody et al. 1989). Human h β 4 appeared to be expressed almost exclusively by neurons (Easter et al. 1993; Moody et al. 1989; Sullivan 1988; Sullivan and Cleveland 1986). β -III is expressed in all except cerebella Purkinje neurons, immediately before or during terminal mitosis (Haendel et al. 1996; Katsetos et al. 1993; Moody et al. 1989) and it is regulated by transcription factors necessary for neuronal lineage commitment and early morphological

differentiation (Dennis et al. 2002). In the retina, TUJ-1 labelled RGCs and other neurons in the RGCL. On the hand, DAPI is known to form fluorescent complexes with natural double-stranded DNA, showing fluorescence specificity for AT, AU and GC clusters. Because of this property, DAPI is a useful tool in various cytochemical investigations. When DAPI bound to DNA, its fluorescence was strongly enhanced. There is also evidence that DAPI bound to the minor grooves of DNA, stabilized by hydrogen bonds between DAPI and acceptor groups of AT, AU and GC base pairs. Therefore, DAPI stained all cell nuclei irrespective of cell type.

The ratio of TUJ-1 to DAPI labelling was reduced in the 48h group compared to the 24h group. This admits of two interpretations: 1) both TUJ-1 and DAPI labelling decreased, but TUJ-1 decreased faster; or 2) TUJ-1 labelling decreased, whereas DAPI labelling did not change. Each interpretation has its own implications. Scenario 1) can be explained mathematically: since the absolute number of TUJ-1 labelling was much smaller than DAPI, the same reduction in both would result in a decrease in ratio. Immediately, one would think scenario 2) is impossible, because in the same area, one would expect DAPI labelling to reduce at the same rate as TUJ-1 labelling; however, the reduced TUJ-1 labelling did not necessarily indicate 'the disappearance of the whole cell'; if β -III tubulin degraded prior to nuclei, DAPI labelling could remain the same whereas TUJ-1 reduced. This is supported by the observation that TUJ-1 labelling in the 48h group retinas was much weaker than in the 24h group, whereas the quality of DAPI labelling hardly changed.

7.4. Conclusions

With a combination of the results from intracellular cell filling, gene gun labelling and immunohistochemistry, we have good reason to say that the human retinas have undergone a certain degree of degeneration prior to fixation, and because of this, the dendritic morphology of neurons has been altered. Therefore, the human retinas available to us preclude a reliable and detailed analysis of dendritic changes in human glaucoma.

CHAPTER 8 THE EXPRESSION OF CHONDROITIN SULPHATE GLYCOSAMINOGLYCANS AND AGGREGAN CORE PROTEIN EPITOPES IN YOUNG, AGED, AND GLAUCOMATOUS HUMAN RETINAS

OBJECTIVE

- To characterise the expression of GAG proteins in human retinal transverse sections by immunohistochemistry.

8.1. Introduction

The project is to study the retinal plasticity in ageing and glaucoma. We have quantified the plastic changes in terms of the neuronal density changes in different levels of the retinas in Chapter 4 and 5. Further more, we quantified the pattern of neuronal loss by nearest neighbour analysis in Chapter 6. However, the morphological analysis of the dendritic remodeling, although was reported in experimental glaucoma, can not be confirmed in human (Chapter 7). Here, I approached this question from a different angle: instead of trying to observe dendritic remodeling directly, I investigated if/how the extracellular matrix remodels in glaucoma, which may prevent the neurons from recovery and regenerating. In particular, the expressions of chondroitin sulphate-glycosaminoglycans (CS-GAGs) and aggrecan core protein epitopes in the young, elderly and glaucomatous retinas were compared.

8.2. Results

Retinal transverse sections from 12 human retinas: young (18-33 yr, n=4), old (60-85 yr, n=4) and glaucoma (67-89 yr, n=4) patients were labelled by a range of CS-GAGs and aggrecan core protein mAb and analysed by immunohistochemistry.

8.2.1. Controls

The staining was negative when the primary antibodies were eliminated (Figure 8-1 A). CS-GAG (1B5, 2B6 and 3B3) required chondroitinase ABC digestion of the tissue to expose the 'epitope-stubs' (Figure 8-1 B), whereas the rest of the antibodies tested did not. Wax sections of bovine cartilage served as positive controls (Figure 8-1 C).

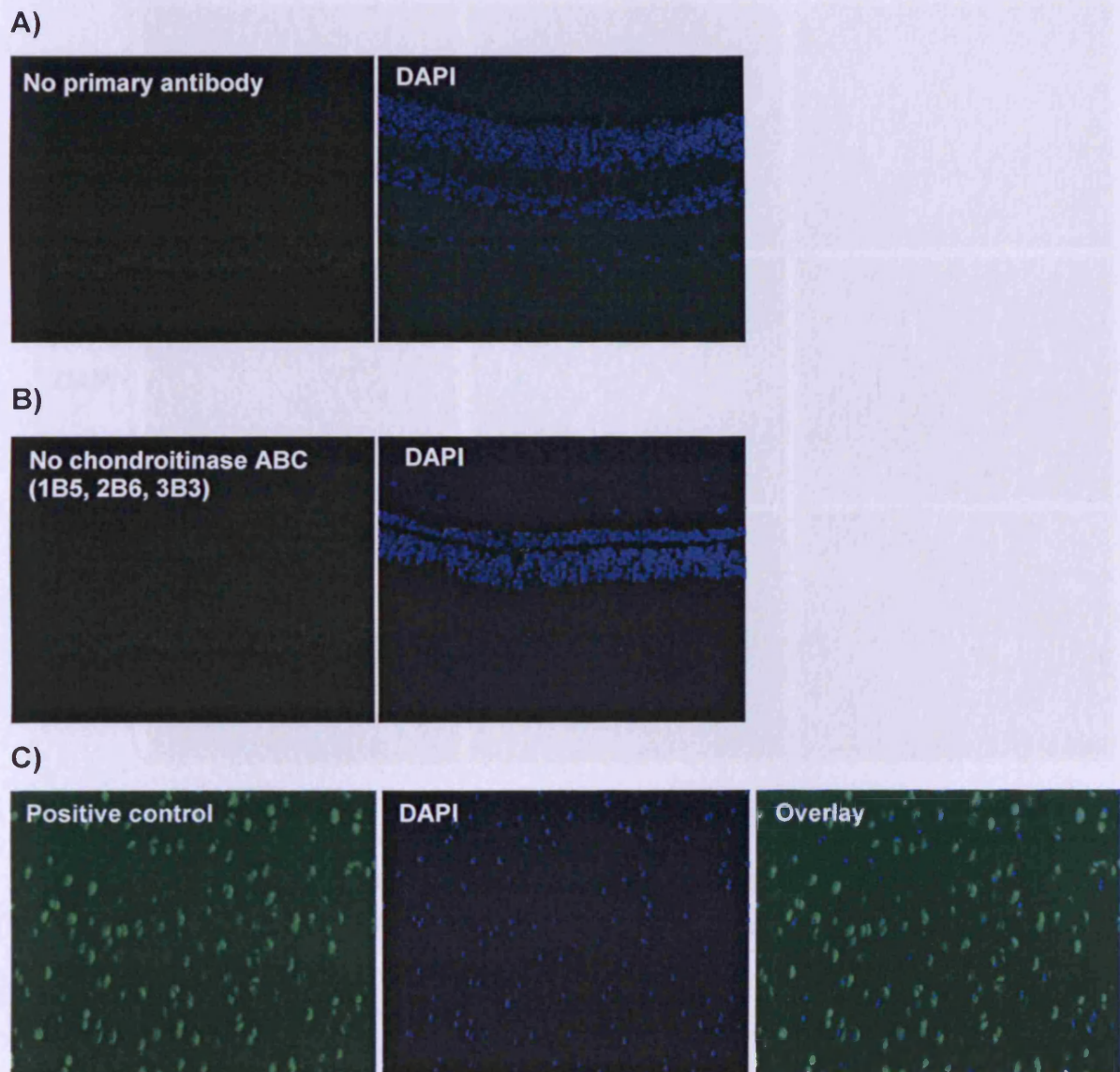


Figure 8-1 The negative and positive controls of different isotopes of GAGs. A) shows the immunostaining when the primary antibodies were eliminated; B) shows the immunostaining of CS-GAG 1B5, 2B6 and 3B3 when the chondroitinase ABC digestion was eliminated; C) shows the positive control staining of bovine cartilage sections.

8.2.2. The expression of CS-GAG 1B5

CS-GAG 1B5 was expressed in the interphotoreceptor matrix in the three groups of the retinas (Figure 8-2), and there was no significant difference in the expression between groups.

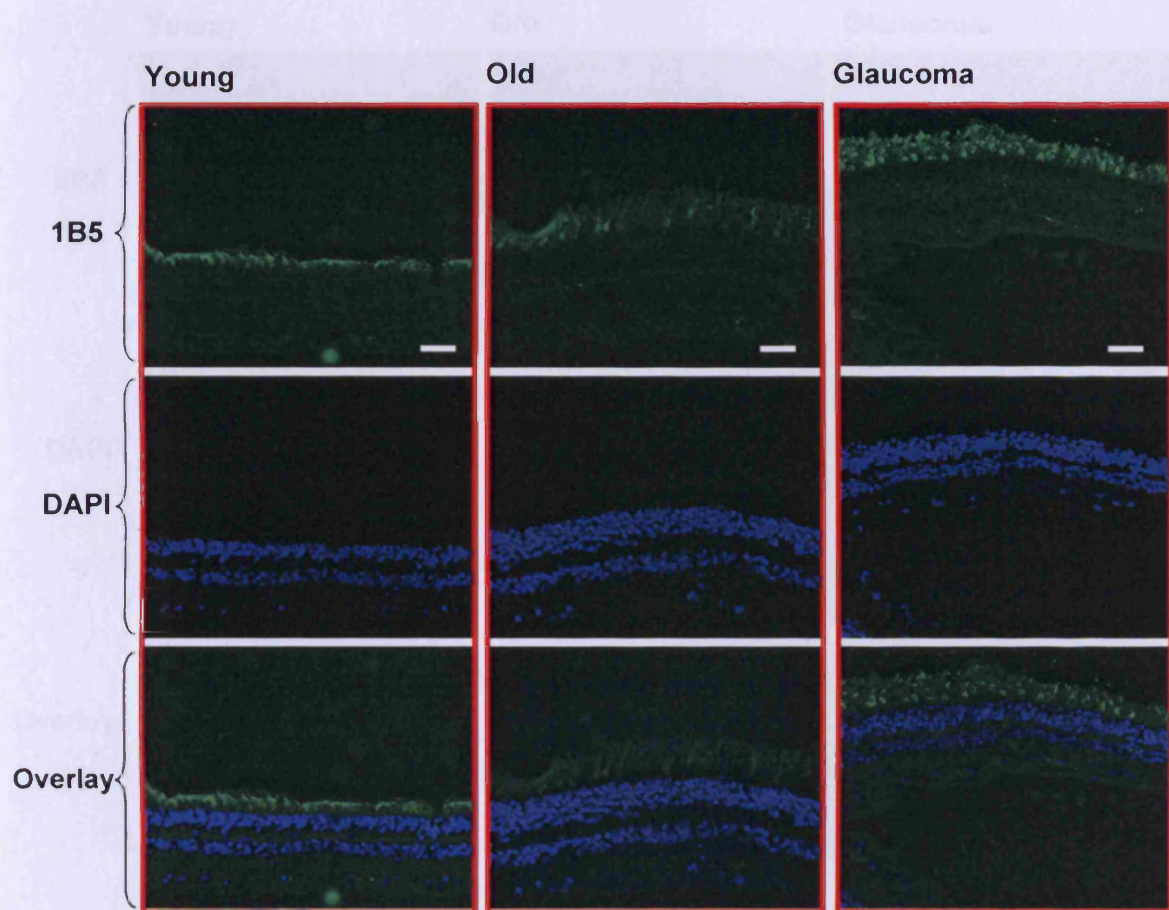


Figure 8-2 1B5 expression in the young (18-33 yr, n=4), aged (58-90 yr, n=4) and glaucomatous (77-89 yr, n=4) retinas. Here an example from one retina of each group is shown. A-C are 1B5, DAPI and overlay images of young retinas; D-F and G-I are those of aged and glaucomatous retinas respectively. Scale bar 50 μ m.

8.2.3. The expression of CS-GAG 2B6

CS-GAG 2B6 was expressed throughout the retina in the three groups of retinas, and it seemed to be up-regulated in the glaucoma group (Figure 8-3).

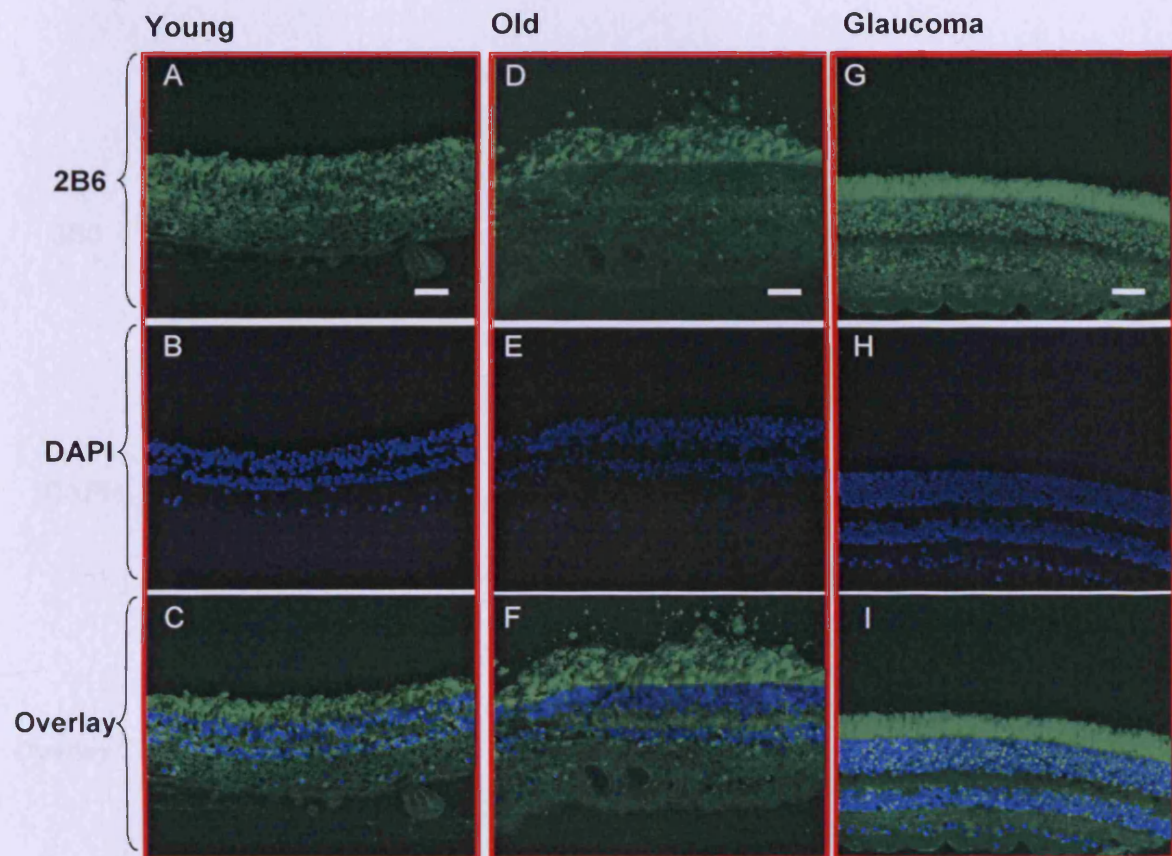


Figure 8-3 2B6 expression in the young (18-33 yr, n=4), aged (58-90 yr, n=4) and glaucomatous (77-89 yr, n=4) retinas. Here an example from one retina of each group is shown. A-C are 2B6, DAPI and overlay images of young retinas; D-F and G-I are those of aged and glaucomatous retinas respectively. Scale bar 50 μ m.

8.2.4. The expression of CS-GAG 3B3

Like CS-GAG 1B5, CS-GAG 3B3 was expressed in the interphotoreceptor matrix in the three groups of retinas (Figure 8-4), and there was no significant difference in the level of expression between groups.

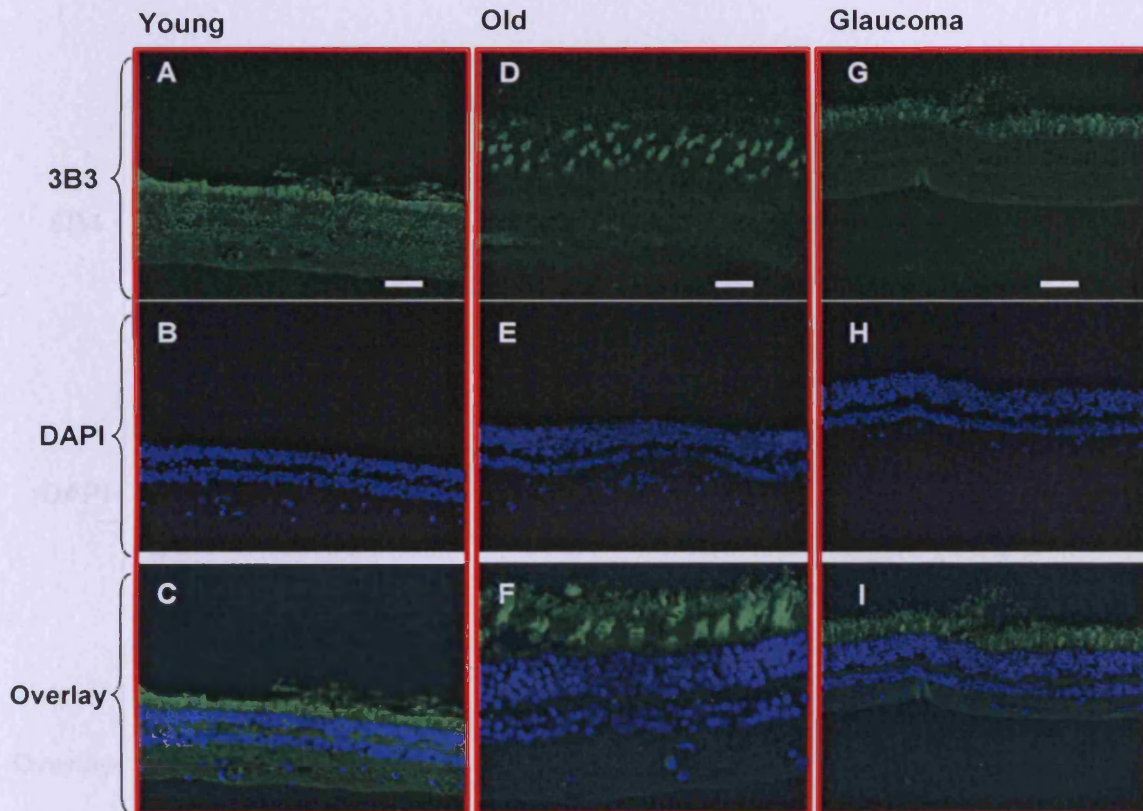


Figure 8-4 3B3 expression in the young (18-33 yr, n=4), aged (58-90 yr, n=4) and glaucomatous (77-89 yr, n=4) retinas. Here an example from one retina of each group is shown. A-C are 3B3, DAPI and overlay images of young retinas; D-F and G-I are those of aged and glaucomatous retinas respectively. Scale bar 50 μ m.

8.2.5. The expression of aggrecan core protein 6B4

Aggrecan core protein 6B4 was expressed throughout the retinas in all the three groups (Figure 8-5), and it appeared to be up-regulated in glaucomatous retinas, especially in the inner retina (i.e. RGCL, INL and IPL). There was no significant difference in the level of expression between the young and aged groups.

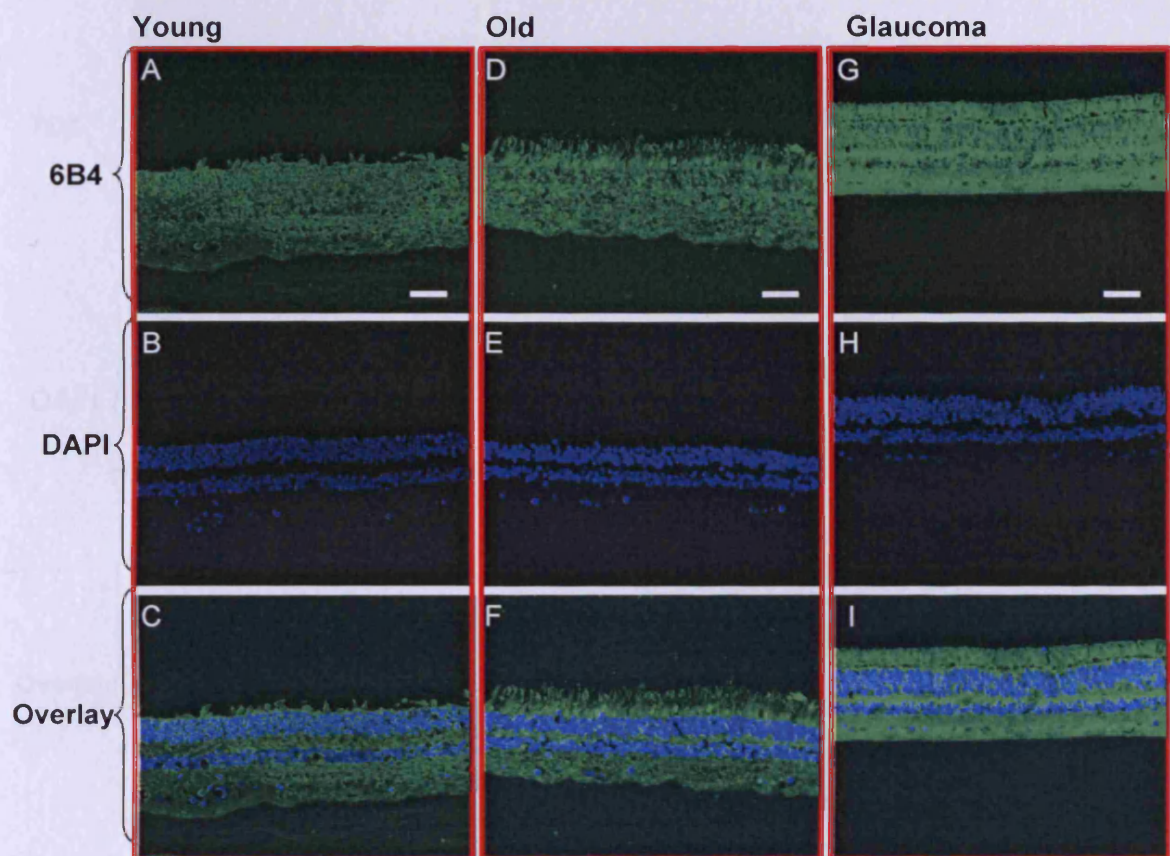


Figure 8-5 6B4 expression in the young (18-33 yr, n=4), aged (58-90 yr, n=4) and glaucomatous (77-89 yr, n=4) retinas. Here an example from one retina of each group is shown. A-C are 6B4, DAPI and overlay images of young retinas; D-F and G-I are those of aged and glaucomatous retinas respectively. Scale bar 50 μ m.

8.2.6. The expression of aggrecan core protein 7D1

Aggrecan core protein 7D1 was expressed throughout the retinas in all the three groups (Figure 8-6), and there was no significant difference in the expression between groups.

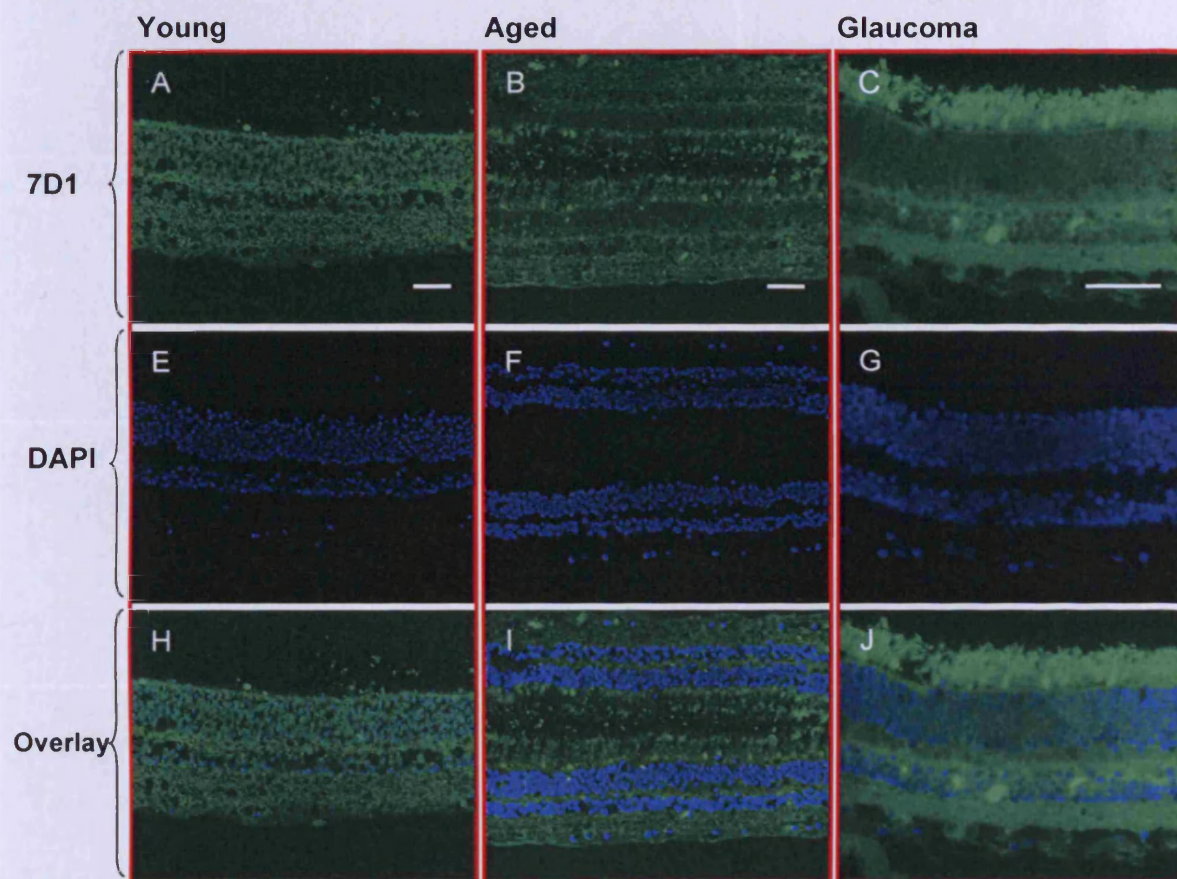


Figure 8-6 7D1 expression in the young (18-33 yr, n=4), aged (58-90 yr, n=4) and glaucomatous (77-89 yr, n=4) retinas. Here an example from one retina of each group is shown. A-C are 6B4, DAPI and overlay images of young retinas; D-F and G-I are those of aged and glaucomatous retinas respectively. Scale bar 50 μ m.

8.2.7. Negative results

No expression of keratocan, lumnican, versican, decorin or 5D4 was found in the human retinas (Figure 8-7).

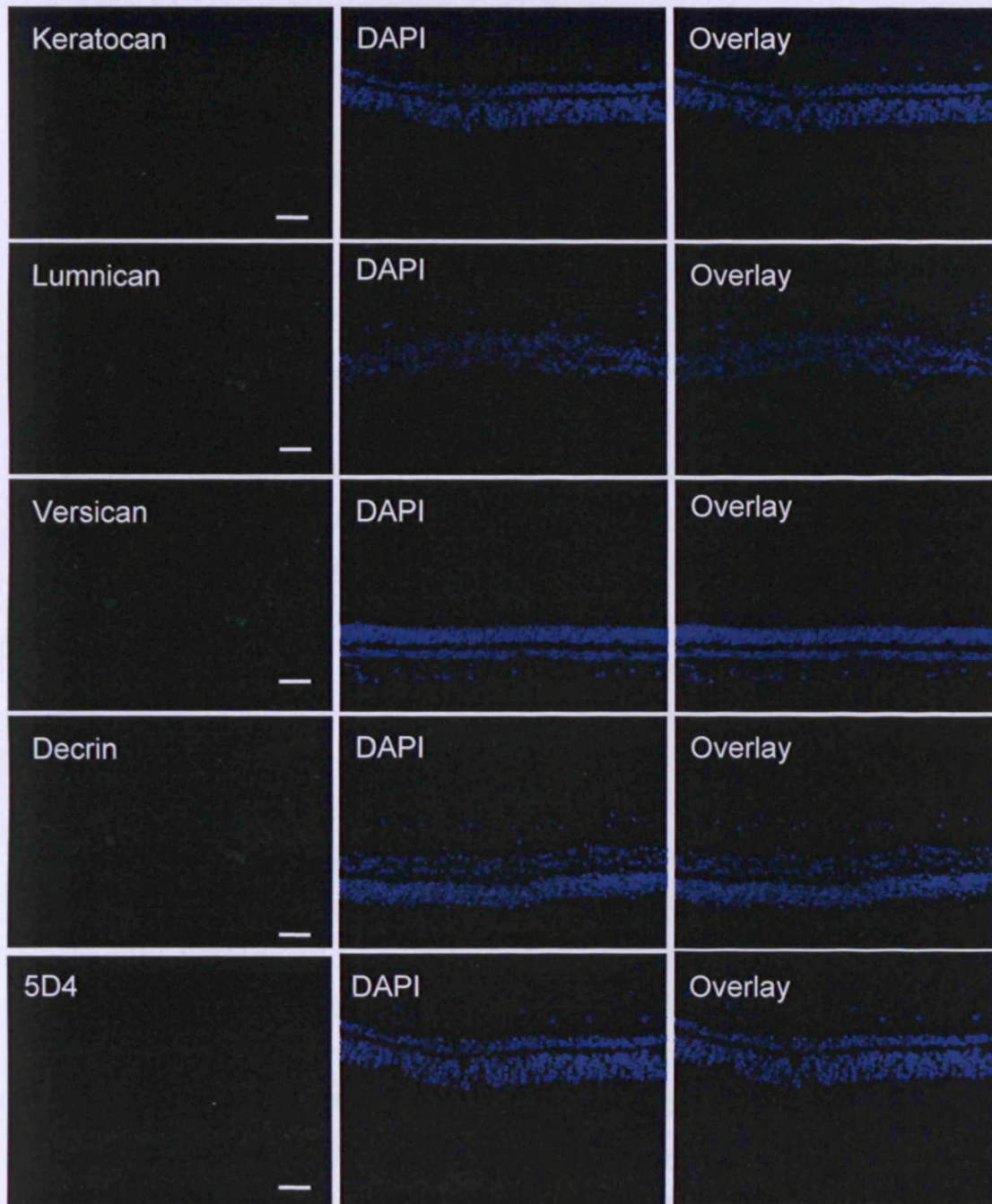


Figure 8-7 There was no expression of keratocan, lumnican, versican, 5D4 or decorin in the human retinas.

8.3. Discussion

One of the major hurdles, which prevents CNS from regeneration and remodelling, is the formation of an astroglial scar in the mature and diseased neural tissue, forming a network of perineuronal nets. In the current study, we have delineated the presence of this structure in the human retinas (Figure 8-2,3,4,5,6,7). CS-GAGs (1B5, 2B6 & 3B3) and aggrecan core protein (6B4 & 7D1) were expressed in three groups of retinas; the expression of 2B6 and 6B4 appeared to be up-regulated in the glaucoma group. Because only negative staining for decorin, biglycan, lumican, keratocan and versican was found, the major source of CS-GAG staining appears to be from aggrecan. Also, negative 5D4 staining suggests that the aggrecan in the retina is not or minimally substituted with KS-GAGs. In the interphotoreceptor matrix, the staining of CS-GAGs was co-localised with aggrecan core protein. Additionally, 6B4 and 7D1 were also expressed in the inner retina, including the INL, the IPL, and the RGCL. This indicates that aggrecan core protein is expressed in these retinal tissue domains. The difference between CS-GAG staining (1B5, 2B6 and 3B3) and the aggrecan core protein (6B4 and 7D1) suggests that in the INL, IPL and RGCL the GAG attachment regions of aggrecan have been removed.

Current treatment of glaucoma has little direct protection on retinal neurons and can not reverse the vision loss in glaucoma. Recently, stem cell transplantation has received considerable media coverage in its therapeutic potential to rescue degenerating retinas, including the experimental transplantation of brain-derived stem cells (Young et al. 2000), bone marrow-derived neural stem cells (Minamino et al. 2005; Otani et al. 2004), retinal specific progenitors (Minamino et al. 2005) and human embryonic stem cell (Banin et al. 2006). In mature animals, the neonatal photoreceptor precursors were shown to have differentiated into the ONL in the degenerating retinas of mature mice (MacLaren et al. 2006). However, the success of transplantation to cure retinal degeneration depends not only on cell differentiation but also interrogation and organization of functional neurons. Chondroitin proteoglycan and aggrecan have been shown to have inhibitory properties towards neurite outgrowth, either via their CS

CHAPTER 8 THE EXPRESSION OF CHONDROITIN SULPHATE GLYCOSAMINOGLYCANS
AND AGGREGAN CORE PROTEIN EPITOPES IN YOUNG, AGED, AND GLAUCOMATOUS
HUMAN RETINAS

chains or their core proteins (Dou and Levine 1997; Dou and Levine 1994; Friedlander et al. 1994). Moreover, aggrecan can also indirectly inhibit neurite outgrowth by high-affinity binding to the cell adhesion molecules N-CAM and Ng-CAM/L1 (Friedlander et al. 1994; Grumet et al. 1993). On the other hand, Pizzorusso has demonstrated that the synaptic plasticity could be restored by digesting the perineuronal net with chondroitinase ABC in mature rat (Pizzorusso et al. 2002). This study confirms the presence of the perineuronal net in the human retinas, and emphasised the importance of this structure in potentially restricting the recovery and regeneration of neurons in the adult retina.

CHAPTER 9 GENERAL DISCUSSION

9.1. Summary

As we know that a human retina is a 3D structure consisting of the nerve fibre layer, three layers of nuclei, two plexiform layers of dendrites, inner- and outer- limit membranes, inner and outer segments of photoreceptors and RPE (Figure 9-1). The multiphoton-DAPI method developed (Chapter 3) is able to image the entire thickness of the retinal whole mount, thereby aiding the 3D reconstruction of the retinal structure (Figure 9-2).

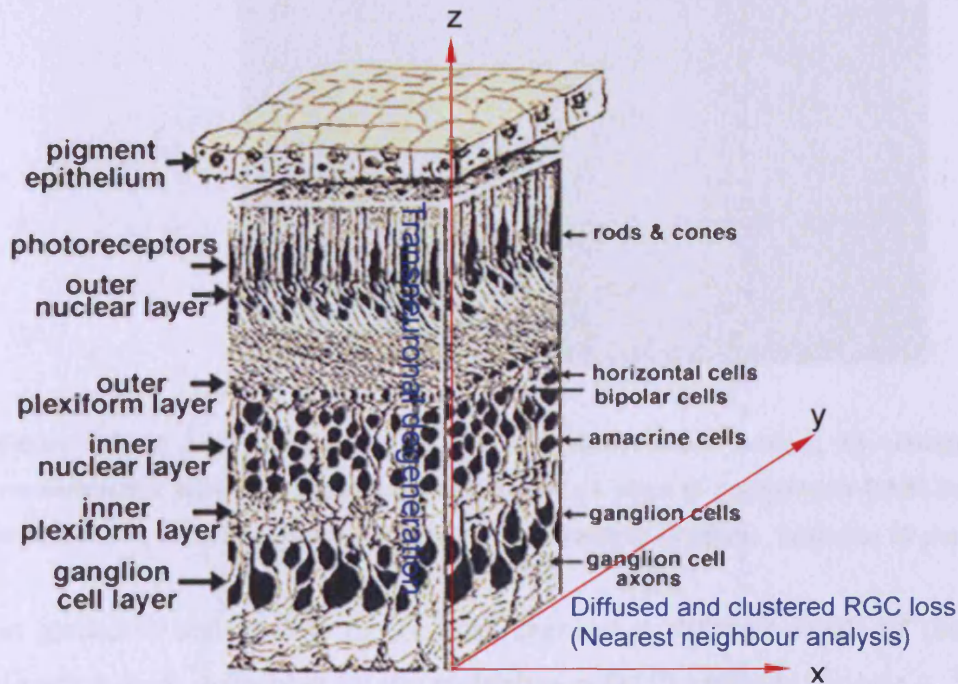


Figure 9-1 An illustration of the 3D structure of the human retina (Adopted from Webvision with permission).

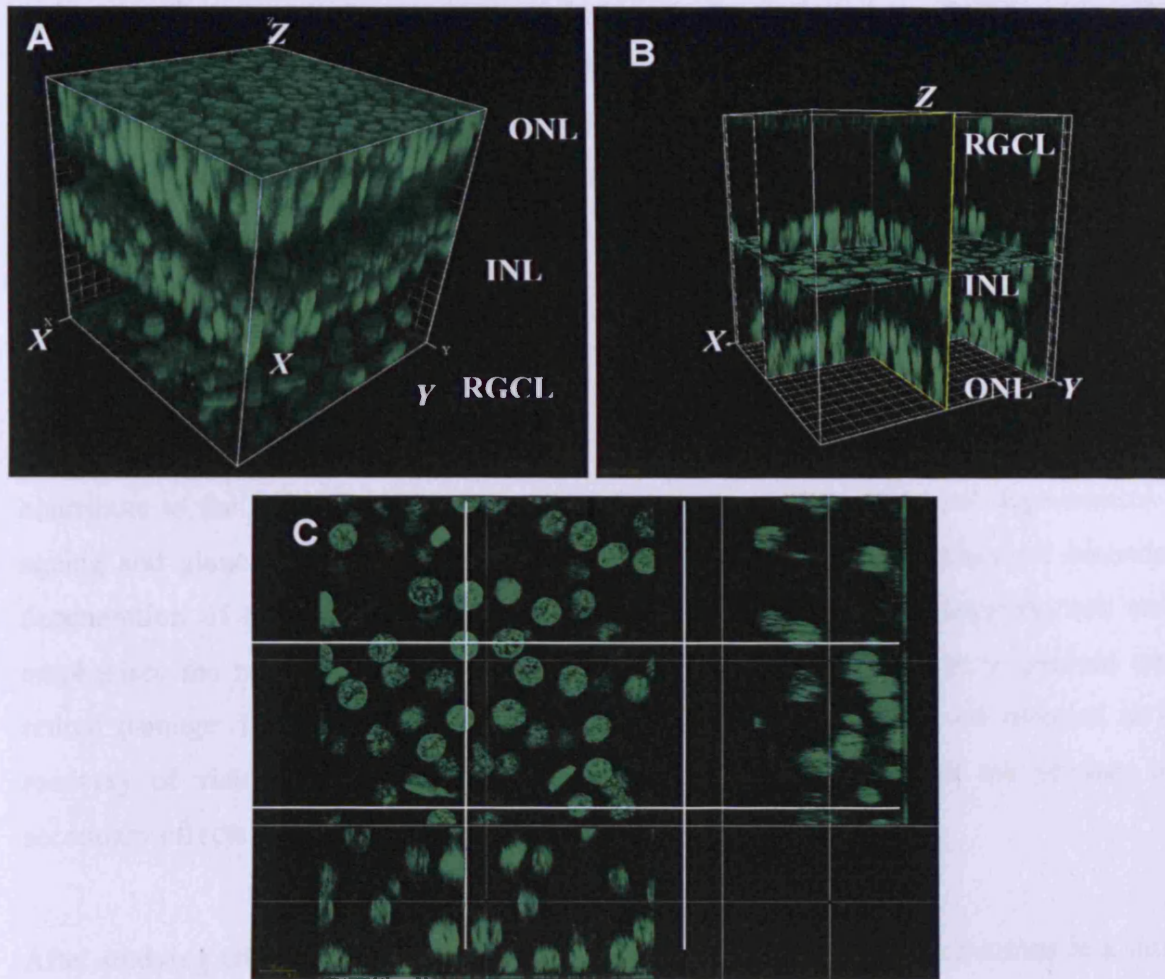


Figure 9-2 A) 3D reconstruction of the multiphoton-DAPI images; B) orthogonal view the 3D reconstruction model; C) a single xy scan within a z stack of multiphoton-DAPI images, in which a z slice is shown vertically (right) and the other horizontally (bottom). Scale bar 20 μm .

In glaucoma and ageing, the cellular changes at different levels of the retina in the z direction were delineated by the multiphoton-DAPI method (Chapter 4, 5). The evidence for RGC loss, taken together with findings of the neuron density reductions in the INL and the ONL, suggests that not all the retinal neurons are equally vulnerable to the disease and ageing. In glaucoma, the neurodegeneration that starts from the RGCL is the result of the optic nerve damage. More importantly, this initiates a cascade of transneuronal degeneration which affects the neurons in the INL and the ONL in the same region where RGCL damage is most severe (Chapter 4). However, the transneuronal degeneration in the aged retinas does not occur in the same manner as in glaucoma. Neurons in both the RGCL and the ONL are markedly affected by ageing (Chapter 5). Spatially, the

neurodegeneration in the INL correlates with both the ONL and the RGCL, although it seems a closer association between INL&RGCL than INL&ONL. In glaucoma, the topographic and quantitative correlations of neuronal loss at different levels of the retina support a transneuronal mechanism of glaucomatous damage rather than a direct retinal damages from the underlying glaucoma pathology; in contrast, in ageing, other mechanisms other than transneuronal degeneration is responsible for the neuronal loss. The mechanism of transneuronal degeneration is not clear, although the loss of neurotrophic support (Levin 2001), the release of excitatory neurotransmitters (Lipton 2005) and oxidative free radicals (Lin and Beal 2006) seen in neurodegenerative diseases may contribute to the transneuronal degeneration in glaucoma. Transneuronal degeneration in ageing and glaucoma highlights the importance of considering the effects of secondary degeneration of neurons. Given the likely disruption of neural connectivity, our study emphasises the need to detect glaucomatous damage at an early stage to prevent outer retinal damage. It also suggests that neuroprotective strategies, or those directed at the recovery of vision loss in ageing and glaucoma, should target both the primary and secondary effects of retinal ganglion cell loss.

After studying all three layers of the retina (Chapter 4, 5), I focused on neurons in a single layer of the retina which is the RGCL (Chapter 6). At the xy plane of the retina, the pattern of the neuron distribution was studied by the NNA. According to the histogram of NNDs, the distribution of NNDs was shifted to the right in glaucomatous retinas relative to the aged-matched controls. This general right shift suggests a diffuse pattern of neuronal loss. In contrast, an 8-fold increase in the large NNDs (greater than 20 μm) implies a clustered loss of neurons in certain areas of the retina. Morphologically, both diffuse and clustered patterns of neuron loss were identified by the microscopic observation, whereby supporting the statistical/mathematical results. Particularly, the diffuse pattern of neuron loss was seen throughout the retinal areas examined; whereas the clustered loss was prominent in the mid-peripheral retina. Provided the above evidence, it is very likely that these two patterns of cell loss results from two different pathological mechanisms leading to RGC depletion, as this is consistent with some of the experimental glaucoma models (Danas et al. 2003; Filippopoulos et al. 2006). Diffused loss of RGCs may be due to apoptosis as a result of glaucomatous damage to the distal portions of the RGCs; further or excessive death of

RGCs (in a clustered pattern) may be indirectly caused by the negative effect from the degeneration of surrounding RGCs, i.e. a secondary degeneration. This is supported by observations in a partial nerve transection model, where the primary RGC death due to optic nerve injury was accompanied by the secondary death of surrounding RGCs that were not directly injured (Levkovitch-Verbin et al. 2001; Levkovitch-Verbin et al. 2003). In glaucomatous retinas, RGC depleted regions of the retina were typically bordered by normal RGCs. This again indicates that the loss of neurons may exert a bystander effect on surviving cells, rendering them more susceptible to death. The mechanism of clustered neuronal degeneration can be attributed to a number of factors, including glutamate induced excitotoxicity, alteration in the ionic concentrations, increased amounts of free radicals, and depletion of growth factors etc. Therefore, the surrounding RGCs can enter a destructive cascade that can remain active after the initial insult is abated (Yoles and Schwartz 1998).

In between the RGCL, INL and ONL, there are the zones for dendritic arbourisation in which the intraretinal signal processing occurs. Although the morphology of the dendrites is altered in experimental glaucoma (Weber et al. 2000; Weber et al. 1998), we are not able to confirm this in human glaucoma due to the degeneration of dendrites before tissue fixation (Chapter 7). However, we are able to characterise the perineuronal net in the human retinas in the young, elderly and glaucomatous retinas (Chapter 8). The GAG proteins have been shown to have inhibitory properties towards neurite outgrowth, either via their CS chains and their core proteins (Dou and Levine 1997; Dou and Levine 1994; Friedlander et al. 1994) or by high-affinity binding to the cell adhesion molecules N-CAM and Ng-CAM/L1 (Friedlander et al. 1994; Grumet et al. 1993). It is therefore important to consider this structure in the therapeutic use of stem cell transplantation or implementation of neurotrophic factors to rescue degenerating retinas. There are differences between the CS-GAG staining (1B5, 2B6 and 3B3) and the aggrecan core protein (6B4 and 7D1). This suggests that in the INL, IPL and RGCL the GAG attachment regions of aggrecan have been removed. The major source of CS-GAG staining appears to be from aggrecan because only negative staining for decorin, biglycan, lumican, keratocan and versican was found. Also, negative 5D4 staining suggests that this aggrecan from the retina is not or minimally substituted with KS-GAGs. While success has been achieved in integrating stem cell

replacement in diseased retinas, it is likely that the manipulation of the perineuronal net is critical to the regeneration retinal neurons.

9.2. Future work

9.2.1. Transneuronal degeneration in ageing and glaucoma

In Chapter 4 and 5, we have demonstrated significant transneuronal degeneration in the glaucomatous and ageing retinas. It will be interesting to see how it correlates with the neurodegeneration in the LGN (Yucel et al. 2000; Yucel et al. 2001; Yucel et al. 2003). Furthermore, in ageing retinas there may be other mechanisms in addition to retinal transneuronal degeneration that account for the death of neurons. These require further investigation.

9.2.2. The topographical changes of RGC distribution in ageing eyes

As we have demonstrated in Chapter 6 that RGCs are lost in a combination of diffuse and clustered patterns in human glaucoma. This opens a door to further investigations into the pattern of cells loss in ageing retinas in comparison to glaucomatous ones.

9.2.3. The expression of proteoglycans in the human retinas

We have characterised the expression of CS-GAGs and aggrecan core proteins in the young, aged and glaucomatous retinas by immunohistochemical analysis (Chapter 8). Further experiments should be conducted to quantify and compare the levels of protein expressions in these groups of retinas.

APPENDIX I STATISTICAL RAW DATA

Chapter 3 Development and validation of a novel multiphoton-DAPI method

Table App I-3.1 Summary of NDIC-Confocal comparisons in RGC counts.

Group			N	Mean Rank	Sum of Ranks
Inferior	NDIC-Confocal	Negative Ranks	3(a)	3.33	10.00
		Positive Ranks	5(b)	5.20	26.00
		Ties	1(c)		
Nasal	NDIC-Confocal	Negative Ranks	3(a)	4.17	12.50
		Positive Ranks	6(b)	5.42	32.50
		Ties	1(c)		
Superior	NDIC-Confocal	Negative Ranks	3(a)	3.83	11.50
		Positive Ranks	5(b)	4.90	24.50
		Ties	1(c)		
Temporal	NDIC-Confocal	Negative Ranks	4(a)	6.00	24.00
		Positive Ranks	4(b)	3.00	12.00
		Ties	1(c)		

a Confocal < NDIC

b Confocal > NDIC

c Confocal = NDIC

Table App I-3.2 Test Statistics (c) of NDIC-Confocal comparisons in RGC counts.

Group		NDIC-Confocal
Inferior	Z	-1.120(a)
	Asymp. Sig. (2-tailed)	.263
Nasal	Z	-1.187(a)
	Asymp. Sig. (2-tailed)	.235
Superior	Z	-.916(a)
	Asymp. Sig. (2-tailed)	.360
Temporal	Z	-.840(b)
	Asymp. Sig. (2-tailed)	.401

a Based on negative ranks.

b Based on positive ranks.

c Wilcoxon Signed Ranks Test

Table App I-3.3 Ranks of NDIC-Confocal comparisons in RGC counts.

		N	Mean Rank	Sum of Ranks
Confocal – NDIC	Negative Ranks	13(a)	19.77	257.00
	Positive Ranks	22(b)	16.95	373.00
	Ties	1(c)		
	Total	36		

a Confocal < NDIC

b Confocal > NDIC

c Confocal = NDIC

Table App I-3.4 Test Statistics(b) of NDIC-Confocal comparisons in RGC counts.

	Confocal – NDIC
Z	-.951(a)
Asymp. Sig. (2-tailed)	.342

a Based on negative ranks.

b Wilcoxon Signed Ranks Test

Chapter 4 Retinal transneuronal degeneration in human glaucoma

Table App I-4.1 Estimates of numbers of RGCL, INL and ONL of the control compared to glaucomatous human retina (*group 1=glaucoma group, 2= control group, n=6 in each group).

Dependent Variable	Eccentricity (mm)	Group*	Mean density (x1000 mm ⁻²)	Std. Error	95% Confidence Interval		
					Lower Bound	Upper Bound	
RGCL	.0	1	.000	.914	-1.855	1.855	
		2	.000	1.055	-2.142	2.142	
	.5	1	11.804	.914	9.949	13.659	
		2	16.733	1.055	14.592	18.875	
	1.0	1	13.638	.914	11.783	15.493	
		2	22.433	1.055	20.292	24.575	
	1.5	1	11.953	.914	10.098	13.807	
		2	21.533	1.055	19.392	23.675	
	2.0	1	7.135	.914	5.280	8.989	
		2	18.233	1.055	16.092	20.375	
	3.0	1	3.947	.914	2.092	5.801	
		2	9.300	1.055	7.158	11.442	
	4.0	1	2.672	.914	.817	4.527	
		2	5.967	1.055	3.825	8.108	
	INL	.0	1	23.725	2.849	17.942	29.508
			2	22.000	3.289	15.323	28.677
.5		1	35.584	2.849	29.801	41.367	
		2	36.200	3.289	29.523	42.877	
1.0		1	37.568	2.849	31.785	43.351	
		2	42.600	3.289	35.923	49.277	
1.5		1	39.040	2.849	33.257	44.823	
		2	45.567	3.289	38.889	52.244	
2.0		1	39.616	2.849	33.833	45.399	
		2	51.167	3.289	44.489	57.844	
3.0		1	43.712	2.849	37.929	49.495	
		2	54.800	3.289	48.123	61.477	
4.0		1	45.376	2.849	39.593	51.159	
		2	59.833	3.289	53.156	66.511	

Continued

Dependent Variable	Eccentricity (mm)	Group*	Mean density (x1000 mm ⁻²)	Std. Error	95% Confidence Interval	
					Lower Bound	Upper Bound
ONL	.0	1	200.000	6.013	187.793	212.207
		2	200.000	6.943	185.904	214.096
	.5	1	74.688	6.013	62.481	86.895
		2	56.967	6.943	42.871	71.062
	1.0	1	86.272	6.013	74.065	98.479
		2	71.133	6.943	57.038	85.229
	1.5	1	90.880	6.013	78.673	103.087
		2	83.900	6.943	69.804	97.996
	2.0	1	97.088	6.013	84.881	109.295
		2	109.933	6.943	95.838	124.029
	3.0	1	105.152	6.013	92.945	117.359
		2	128.333	6.943	114.238	142.429
	4.0	1	110.272	6.013	98.065	122.479
		2	143.967	6.943	129.871	158.062

Table App I-4.2 Pairwise comparisons of cells numbers at matched eccentricities in control and glaucomatous human retinas (*group 1=glaucoma group, 2= control group, n=6 in each group). The matched values of significant difference were high lighted in red.

Dependent Variable	Eccentricity	Group*		Sig.(a)	95% Confidence Interval for Difference(a)	
					Lower Bound	Upper Bound
RGCL	.0	1	2	-	-	-
	.5	1	2	.001	-7.762	-2.096
	1.0	1	2	.000	-11.628	-5.962
	1.5	1	2	.000	-12.414	-6.748
	2.0	1	2	.000	-13.932	-8.266
	3.0	1	2	.001	-8.186	-2.520
	4.0	1	2	.024	-6.128	-.461
INL	.0	1	2	.694	-7.108	10.558
	.5	1	2	.888	-9.449	8.217
	1.0	1	2	.255	-13.865	3.801
	1.5	1	2	.143	-15.360	2.307
	2.0	1	2	.012	-20.384	-2.717
	3.0	1	2	.015	-19.921	-2.255
	4.0	1	2	0.002	-23.291	-5.624
ONL	.0	1	2	-	-	-
	.5	1	2	.062	-.926	36.368
	1.0	1	2	.108	-3.508	33.786
	1.5	1	2	.452	-11.667	-25.627
	2.0	1	2	.171	-31.492	5.802
	3.0	1	2	.016	-41.828	-4.534
	4.0	1	2	0.001	-52.342	-15.048

Based on estimated marginal means

* The mean difference is significant at the .05 level.

a Adjustment for multiple comparisons: Bonferroni.

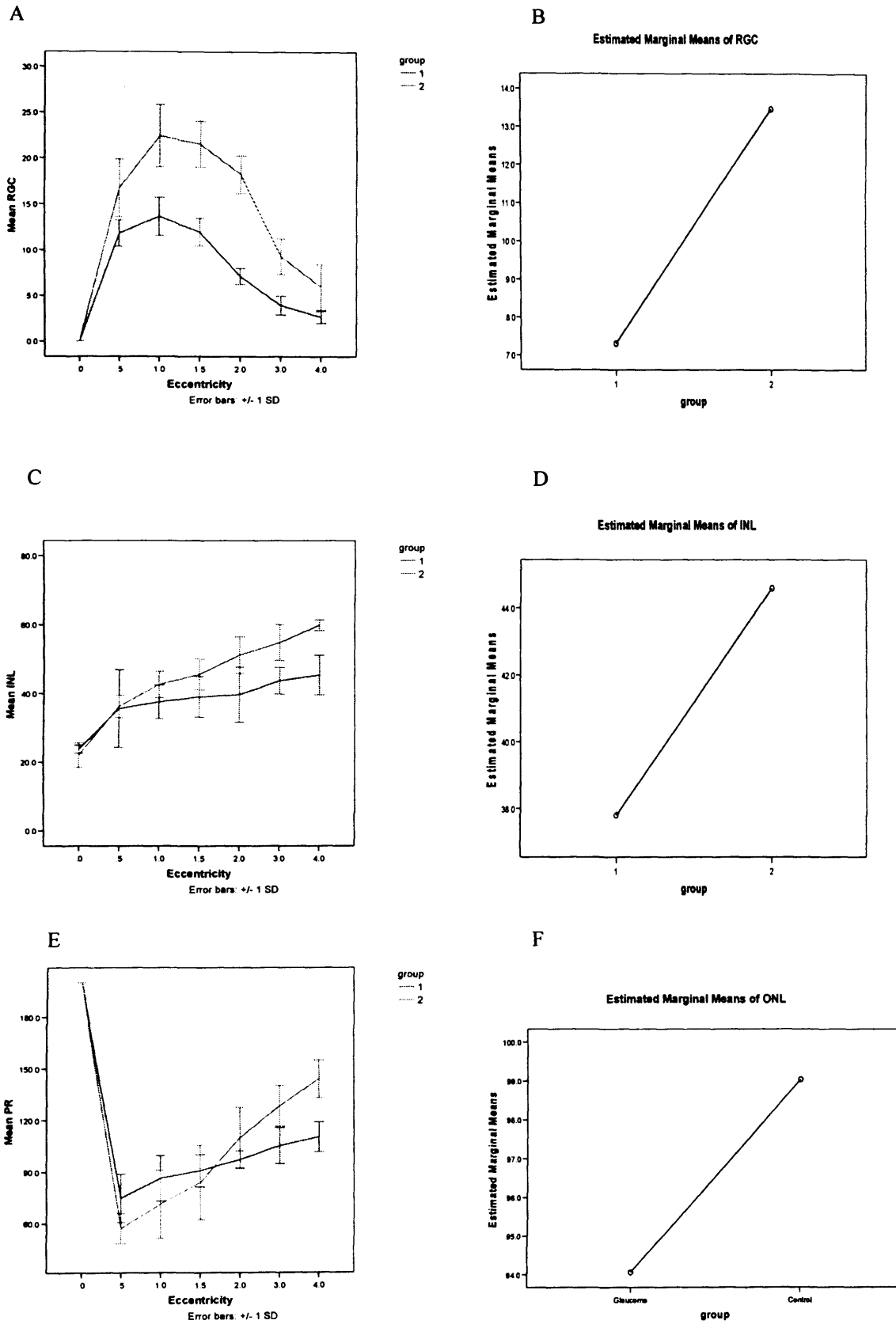


Figure App I-4.1 Distribution of RGCs (A), cells in INL (C) and ONL (E) of the retina and their estimated margin means (B, D, F). n=6.

Table App I-4.3 Estimates of cells ratios in control and glaucomatous human retinas (*group 1=glaucoma group, 2= control group, n=6 in each group).

Dependent Variable	Eccentricity	group	Mean	Std. Error	95% Confidence Interval		
					Lower Bound	Upper Bound	
ONL/RGC	.5	1	6.295	2.861	.453	12.138	
		2	3.428	3.303	-3.318	10.174	
	1.0	1	6.359	2.861	.517	12.202	
		2	3.159	3.303	-3.588	9.905	
	1.5	1	7.623	2.861	1.780	13.465	
		2	3.856	3.303	-2.890	10.602	
	2.0	1	13.800	2.861	7.957	19.642	
		2	6.019	3.303	-.727	12.766	
	3.0	1	27.974	2.861	22.131	33.816	
		2	14.083	3.303	7.336	20.829	
	4.0	1	43.147	2.861	37.304	48.989	
		2	28.109	3.303	21.363	34.856	
	INL/RGC	.5	1	3.003	1.068	.821	5.185
			2	2.188	1.234	-.331	4.708
1.0		1	2.769	1.068	.587	4.951	
		2	1.944	1.234	-.575	4.464	
1.5		1	3.260	1.068	1.078	5.442	
		2	2.150	1.234	-.370	4.669	
2.0		1	5.613	1.068	3.431	7.794	
		2	2.847	1.234	.328	5.367	
3.0		1	11.418	1.068	9.236	13.600	
		2	6.141	1.234	3.622	8.661	
4.0		1	17.372	1.068	15.190	19.554	
		2	11.915	1.234	9.395	14.434	

Continued

Dependent Variable	Eccentricity	group	Mean	Std. Error	95% Confidence Interval	
					Lower Bound	Upper Bound
ONL/INL	.5	1	2.283	.240	1.793	2.773
		2	1.571	.277	1.005	2.136
	1.0	1	2.298	.240	1.809	2.788
		2	1.707	.277	1.142	2.272
	1.5	1	2.342	.240	1.853	2.832
		2	1.887	.277	1.322	2.453
	2.0	1	2.524	.240	2.035	3.014
		2	2.190	.277	1.625	2.755
	3.0	1	2.418	.240	1.929	2.908
		2	2.371	.277	1.806	2.937
	4.0	1	2.464	.240	1.974	2.953
		2	2.410	.277	1.845	2.975

Table App I-4.4 Pairwise Comparisons of cell number ratios in control and glaucomatous human retinas (*group 1=glaucoma group, 2= control group, n=6 in each group).

Dependent Variable	Eccentricity	*Group		Sig.(a)	95% Confidence Interval for Difference(a)	
					Lower Bound	Upper Bound
ONL/RGC	.5	1	2	.517	-6.057	11.792
	1.0	1	2	.470	-5.724	12.125
	1.5	1	2	.396	-5.158	12.691
	2.0	1	2	.085	-1.144	16.705
	3.0	1	2	.003	4.967	22.816
	4.0	1	2	.002	6.113	23.962
INL/RGC	.5	1	2	.621	-2.518	4.148
	1.0	1	2	.617	-2.508	4.157
	1.5	1	2	.502	-2.223	4.443
	2.0	1	2	.101	-.568	6.098
	3.0	1	2	.003	1.944	8.610
	4.0	1	2	.002	2.124	8.790

ONL/INL	.5	1	2	.061	-.035	1.460
	1.0	1	2	.117	-.157	1.339
	1.5	1	2	.224	-.293	1.203
	2.0	1	2	.369	-.414	1.082
	3.0	1	2	.899	-.701	.795
	4.0	1	2	.884	-.694	.802

Based on estimated marginal means

* The mean difference is significant at the .05 level.

a Adjustment for multiple comparisons: Bonferroni.

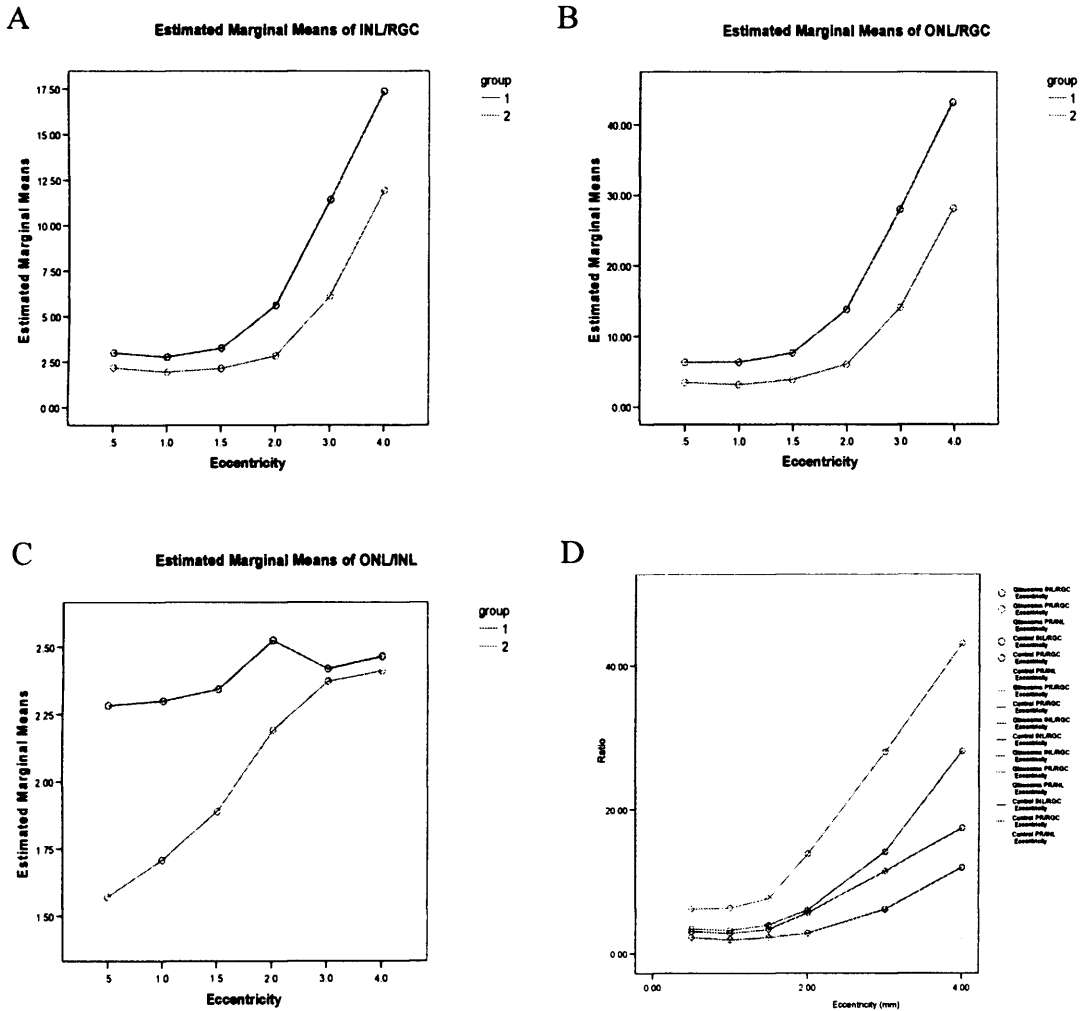


Figure App I-4.2 The ratio of cell numbers in INL/RGC (A), ONL/RGC (B) and ONL/INL (C). D compares these ratios between control and glaucomatous retinas. n=6 in both control and glaucomatous groups.

Chapter 6 the topography of neuron loss in the retinal ganglion cell layer in human glaucoma

5000 random distributed points were generated by Image Pro Plus software (MediaCybernetics, UK). Different percentages of point were removed either randomly, or in a defined area (clustered removal). The size of the area was 20% larger than the percentage of points contained to ensure the removal of a sufficient number of points, e.g. if we were to remove 10% of the points in a clustered fashion, an area of 12% of the total size of the image was randomly selected. The tests results were summarised in the following figures.

Changes in nearest neighbour distances (NNDs) distribution

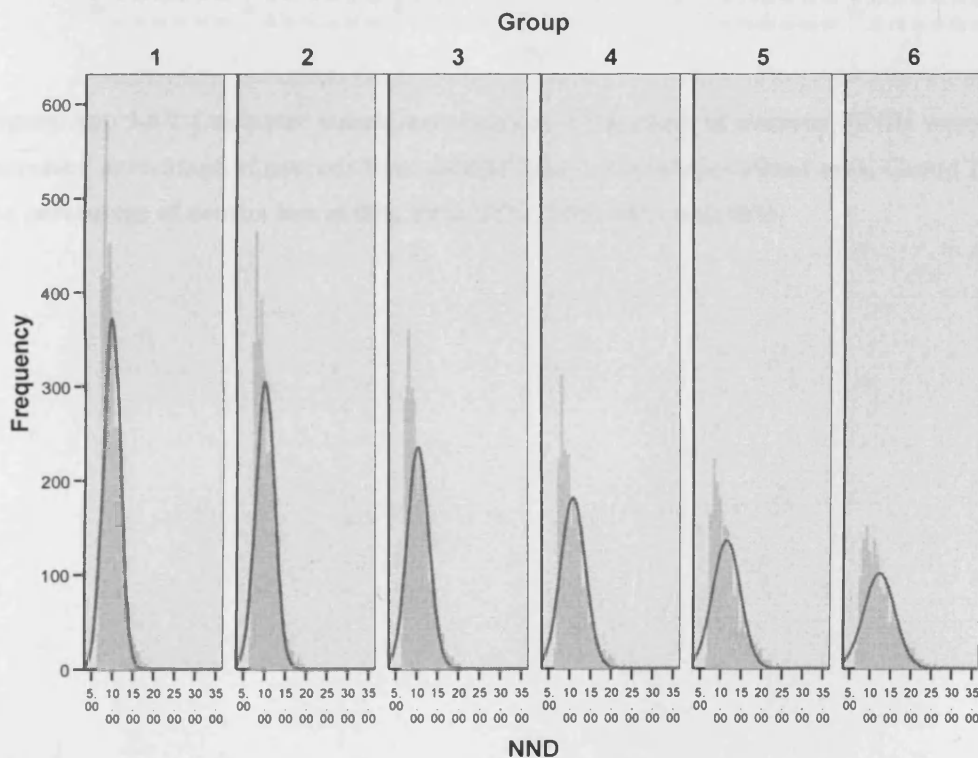


Figure App I-6.1 Computer simulation model of diffused loss of neurons. NNDs were measured when increased percentage of neurons were randomly deleted from a population of 5000 neurons. Group 1-5 correspond to the percentage of neuron loss of 10%, 20%, 30%, 40% and 50%.

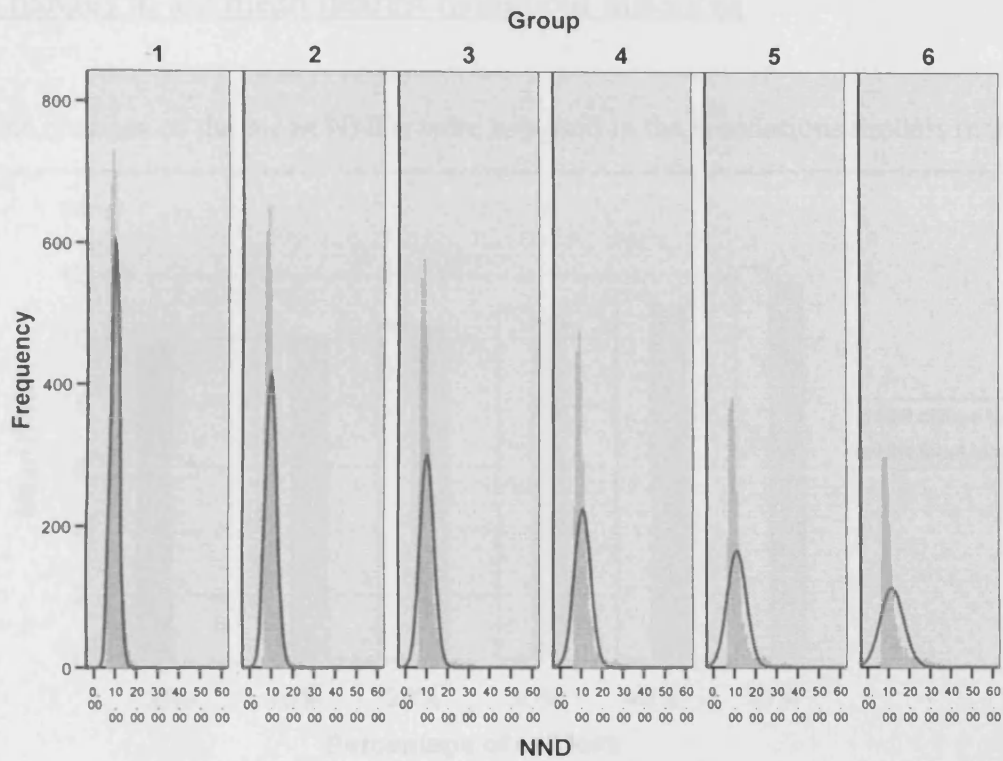


Figure App I-6.2 Computer simulation model of cluster loss of neurons. NNDs were measured when increased percentage of neurons were deleted from a randomly defined area. Group 1-6 correspond to the percentage of neuron loss of 0%, 10%, 20%, 30%, 40% and 50%.

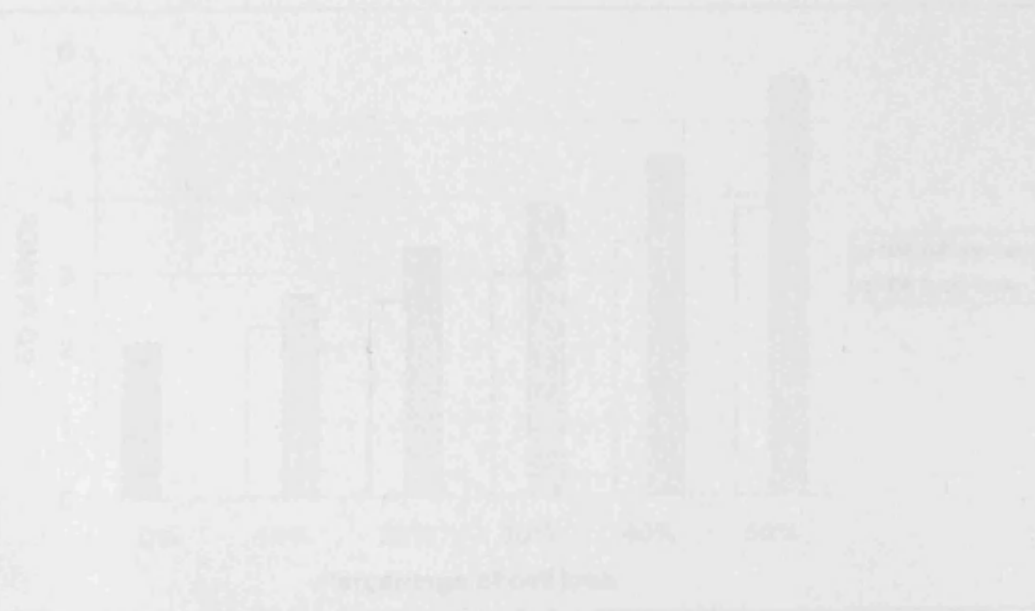


Figure App I-6.3 The distribution of mean NNDs with the percentage of neuron loss. Cluster Neuron Nearest Neighbor Distances (NNDs).

Changes in the mean nearest neighbour distances

The changes of the mean NNDs were assessed in the simulations models mentioned above.

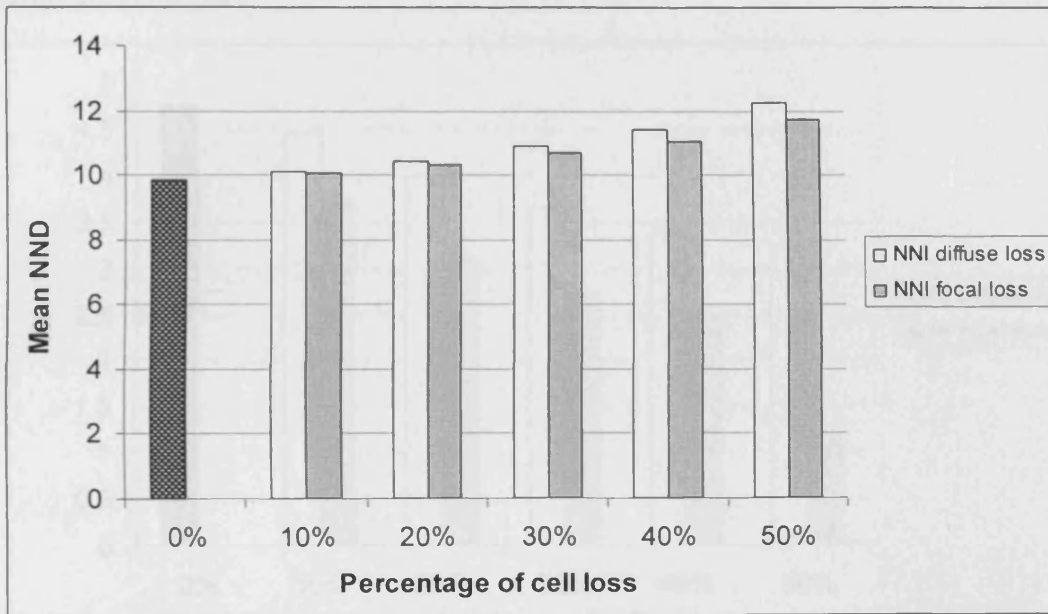


Figure App I-6.3 Mean nearest neighbour distance (NND) increases when a higher percentage of neuron is lost. This is more marked in diffused pattern of neuron loss than cluster pattern.

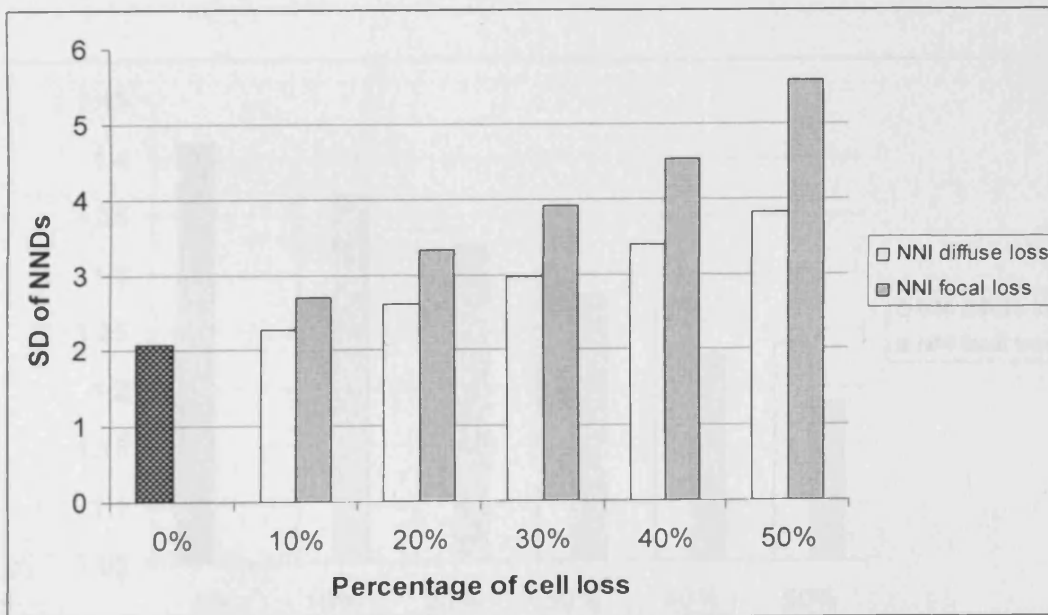


Figure App I-6.2 The correlated increase of mean NNDs with the percentages of neuron loss. Cluster loss causes a more variable distribution of NNDs.

Changes in nearest neighbour indexes

The changes of the nearest neighbour indexes (RI and NNI) were assessed based on the simulation models.

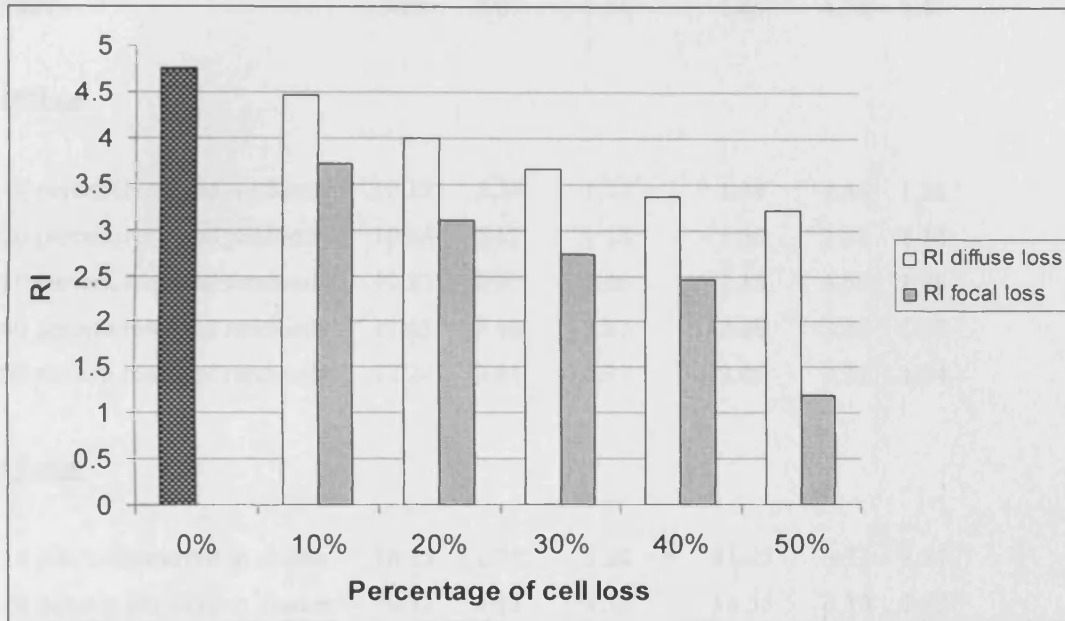


Figure App I-6.3 The reduction of regularity index (RI) with increased percentage of cell loss. Cluster loss causes greater reduction of RI, and renders the cell distribution to a less regular pattern.

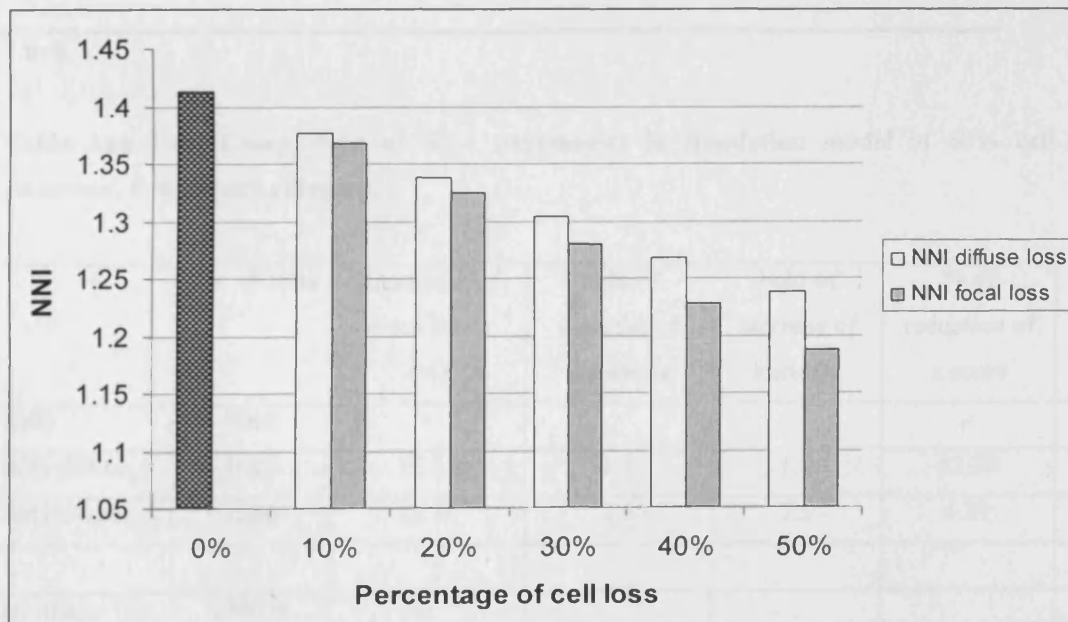


Figure App I-6.4 The reduction of nearest neighbour index (NNI) in increased percentage of cell loss. The effect of cluster loss of cells causes a greater reduction in NNI in higher percentage of cell loss than diffused loss, e.g. 40-50%.

Table App-6.1 Change of NNA parameters with increased percentage of cell loss in a simulation model.

	Mean*	SD	Skewness	Kurtosis	RI	NNI
5000	9.85	2.07	1.14	1.46	4.76	1.41
<u>Diffuse</u>						
10 percent removed randomly	10.12	2.27	1.13	1.38	4.46	1.38
20 percent removed randomly	10.44	2.62	1.18	1.55	3.98	1.34
30 percent removed randomly	10.87	2.97	1.26	2.13	3.66	1.30
40 percent removed randomly	11.43	3.40	1.27	2.08	3.36	1.27
50 percent removed randomly	12.24	3.81	0.97	0.66	3.21	1.24
<u>Cluster</u>						
10 percent removed in cluster	10.05	2.71	3.20	21.25	3.71	1.37
20 percent removed in cluster	10.33	3.33	3.33	16.55	3.10	1.32
30 percent removed in cluster	10.68	3.91	3.18	14.16	2.73	1.28
40 percent removed in cluster	11.07	4.52	2.94	10.98	2.45	1.23
50 percent removed in cluster	11.74	5.57	2.73	9.20	2.11	1.19

* n=6

Table App I-6.2 Comparison of NNA parameters in simulation model of 40% cell loss and in glaucoma. n=6 in each category.

	No. of cells	Reduction of mean NND (%)	Fold of increase of skewness	Fold of increase of kurtosis	% of reduction of z score	% of NNDs>40
5000	5000	-			-	-
40% diffuse	3000	16.04	1.1	1.4	32.89	0
40% clustered	3000	12.39	2.6	7.5	4.89	0.10
Normal	120036	-				0.01
Glaucoma	71276	12.69	1.4	1.5	32.31	0.12

APPENDIX II Constituents and preparation of buffer solutions

Phosphate Buffer

Phosphate Buffer (0.2M PB, pH 7.4):

Na₂HPO₄ (anhydrous) ----- 21.8 g

NaH₂PO₄ (anhydrous) ----- 6.4 g

Distilled water ----- 1000 ml

Mix to dissolve and adjust pH to 7.4

Store this solution at room temperature.

Phosphate Buffer (0.1M PB, pH 7.4):

Na₂HPO₄ (anhydrous) ----- 10.9 g

NaH₂PO₄ (anhydrous) ----- 3.2 g

Distilled water ----- 1000 ml

Mix to dissolve and adjust pH to 7.4

Store this solution at room temperature.

Phosphate buffered saline (PBS)

10X PBS (0.1M PBS, pH 7.2):

Na₂HPO₄ (anhydrous) ----- 10.9 g

NaH₂PO₄ (anhydrous) ----- 3.2 g

NaCl ----- 90 g

Distilled water ----- 1000 ml

Mix to dissolve and adjust pH to 7.2

Store this solution at room temperature. Dilute 1:10 with distilled water before use and adjust pH if necessary.

Tris Buffered Saline (TBS)

10X TBS (0.5M Tris Base, 9% NaCl, pH 7.6):

Trizma base ----- 61 g
NaCl ----- 90 g
Sodium Azide-----2 g
Distilled water ----- 1000 ml

Mix to dissolve and adjust pH to 7.6 using concentrated HCl.

Store this solution at room temperature. Dilute 1:10 with distilled water before use and adjust pH if necessary.

4% Paraformaldehyde in 0.1M Phosphate Buffer

0.2M Phosphate Buffer (PB), pH7.4:

Na₂HPO₄ ----- 21.8 g
NaH₂PO₄ ----- 6.4 g
Distilled water ----- 1000 ml

4% Paraformaldehyde in 0.1M Phosphate Buffer:

Paraformaldehyde ----- 40 g add into
Distilled water -----500 mL

Heat to 60-65 °C while stirring. Add a few drops of 1M NaOH until solution clear.

Continue to stir to dissolve.

Add 0.2 M Phosphate buffer ----- 500 mL

Cool the solution and filter.

1% Acid Alcohol Solution

Hydrochloric acid ----- 10 ml
70% ethanol ----- 1000 ml

Mix well and store at room temperature.

Differentiate 30 second to 2 minutes after haematoxylin over-stain.

50 um paraffin sections require 2 minutes differentiation.

Normal Goat Serum Blocking Solution

- 2% goat serum (blocking)
- 1%BSA (stabilizer)
- 0.1% Triton X-100 (penetration enhancer)
- 0.01M PBS, pH 7.2

Mix well and store at 4 °C.

Normal BSA blocking solution

- 5%BSA (stabilizer)
- 0.01M PBS, pH 7.2

Mix well and store at 4 °C.

Cupric Sulfate

After immunocytochemistry, the sections were removed from the PBS wash, dipped briefly in distilled water, and treated with CuSO₄ (Fisher Scientific, UK) in ammonium acetate buffer (50 mM CH₃COONH₄, pH 5.0) for 30 min, dipped briefly in distilled water, and returned to PBS.

ABComplex/Alkaline Phosphatase Kit

Mix a drop of avidin and one drop of biotin with 5 mL of distilled water, vortex and leave for 30 min before use.

Substrate solution for fact red staining

Dissolve one fast red tablet in 10 mL of TBS solution and filter through a 0.2 µm filter.

For the reference of some of the protocols see

http://www.ihcworld.com/protocol_database.htm

References

2000. The Advanced Glaucoma Intervention Study (AGIS): 7. The relationship between control of intraocular pressure and visual field deterioration. The AGIS Investigators. *Am J Ophthalmol* 130(4), pp. 429-440.
- Alamouti, B. and Funk, J. 2003. Retinal thickness decreases with age: an OCT study. *Br J Ophthalmol* 87(7), pp. 899-901.
- Albin, R.L., et al. 1990. Abnormalities of striatal projection neurons and N-methyl-D-aspartate receptors in presymptomatic Huntington's disease. *The New England journal of medicine* 322, pp. 1293-1298.
- Albon, J., et al. 1995. Changes in the collagenous matrix of the aging human lamina cribrosa. *Br J ophthalmology* 79, pp. 368-375.
- Anderson, D.R. 1969. Ultrastructure of human and monkey lamina cribrosa and optic nerve head. *Arch Ophthalmol* 82, pp. 800-814.
- Balazsi, A. G. et al. 1984. The effect of age on the nerve fiber population of the human optic nerve. *Am J Ophthalmol* 97(6), pp. 760-766.
- Bandtlow, C. E. and Zimmermann, D. R. 2000. Proteoglycans in the developing brain: new conceptual insights for old proteins. *Physiol Rev* 80(4), pp. 1267-1290.
- Banin, E. et al. 2006. Retinal incorporation and differentiation of neural precursors derived from human embryonic stem cells. *Stem Cells* 24(2), pp. 246-257.
- Bansal, A. et al. 2000. Mice lacking specific nicotinic acetylcholine receptor subunits exhibit dramatically altered spontaneous activity patterns and reveal a limited role for retinal waves in forming ON and OFF circuits in the inner retina. *J Neurosci* 20(20), pp. 7672-7681.
- Bartlett., M. S. 1975. *The statistical analysis of spatial pattern*. London: Chapman and Hall.
- Bayer A U, et al. 2001 Retinal morphology and ERG response in the DBA/2NNia mouse model of angle-closure glaucoma. *Invest Ophthalmol Vis Sci* 42(6), pp. 1258-1265.
- Birch, D. G. and Anderson, J. L. 1992. Standardized full-field electroretinography. Normal values and their variation with age. *Arch Ophthalmol* 110(11), pp. 1571-1576.
- Bonnel, S. et al. 2003. The aging of the retina. *Exp Gerontol* 38(8), pp. 825-831.
- Boycott, B. B. and Kolb, H. 1973. The connections between bipolar cells and photoreceptors in the retina of the domestic cat. *The Journal Of Comparative Neurology* 148(1), pp. 91-114.

- Brivanlou, I. H. et al. 1998. Mechanisms of concerted firing among retinal ganglion cells. *Neuron* 20(3), pp. 527-539.
- Byun, J. et al. 2006. Automated tool for the detection of cell nuclei in digital microscopic images: application to retinal images. *Mol Vis* 12, pp. 949-960.
- Cajal, S. R. 1893. La retine des vertebrales. *La Cellule* 9, pp. 17-257.
- Caparas, V.L. et al. 1991. Immunohistochemistry of proteoglycans in human lamina cribrosa. *American journal of ophthalmology* 112, pp. 489-495.
- Choplin, N. T. et al. 1998. Differentiating patients with glaucoma from glaucoma suspects and normal subjects by nerve fiber layer assessment with scanning laser polarimetry. *Ophthalmology* 105(11), pp. 2068-2076.
- Coblentz, F. E. et al. 2003. Evidence that ganglion cells react to retinal detachment. *Experimental Eye Research* 76(3), pp. 333-342.
- Conti A.C. et al. Experimental brain injury induces regionally distinct apoptosis during the acute and delayed post-traumatic period. *Journal of Neuroscience*. 1998. 18(15), pp. 5663-5672.
- Cook, J. E. 1996. Spatial properties of retinal mosaics: an empirical evaluation of some existing measures. *Vis Neurosci* 13(1), pp. 15-30.
- Cook, J. E. and Podugolnikova, T. A. 2001. Evidence for spatial regularity among retinal ganglion cells that project to the accessory optic system in a frog, a reptile, a bird, and a mammal. *Vis Neurosci* 18(2), pp. 289-297.
- Cook, W. H. et al. 1951. A cytological study of transneuronal atrophy in the cat and rabbit. *J Comp Neurol* 94(2), pp. 267-291.
- Cordeiro, M. F. et al. 2004. Real-time imaging of single nerve cell apoptosis in retinal neurodegeneration. *PNAS* 101(36), pp. 13352-13356.
- Crawford, M. L. et al. 2001. Experimental glaucoma in primates: changes in cytochrome oxidase blobs in V1 cortex. *Invest Ophthalmol Vis Sci* 42(2), pp. 358-364.
- Cullen, K. M. et al. 2005. Pericapillary haem-rich deposits: evidence for microhaemorrhages in aging human cerebral cortex. *J Cereb Blood Flow Metab* 25(12), pp. 1656-1667.
- Curcio C A, and Allen K A 1990. Topography of ganglion cells in human retina. *J Comp Neurol* 300(1), pp. 5-25.
- Curcio C A, and Drucker D N 1993. Retinal ganglion cells in Alzheimer's disease and aging. *Ann Neurol* 33(3), pp. 248-257.

- Curcio, C. A. 2001. Photoreceptor topography in ageing and age-related maculopathy. *Eye* 15(Pt 3), pp. 376-383.
- Curcio, C. A. et al. 1987. A whole mount method for sequential analysis of photoreceptor and ganglion cell topography in a single retina. *Vision Res* 27(1), pp. 9-15.
- Curcio, C. A. et al. 1990. Human photoreceptor topography. *J Comp Neurol* 292(4), pp. 497-523.
- Curcio, C. A. et al. 1993. Aging of the human photoreceptor mosaic: evidence for selective vulnerability of rods in central retina. *Invest Ophthalmol Vis Sci* 34(12), pp. 3278-3296.
- Dacey, D. M. 1994. Physiology, morphology and spatial densities of identified ganglion cell types in primate retina. *Ciba Found Symp* 184, pp. 12-28; discussion 28-34, 63-70.
- Dacey, D. M. 1996. Circuitry for color coding in the primate retina. *Proceedings of the National Academy of Sciences of the United States of America* 93(2), pp. 582-588.
- Dacey, D. M. and Petersen, M. R. 1992. Dendritic field size and morphology of midget and parasol ganglion cells of the human retina. *Proc Natl Acad Sci U S A* 89(20), pp. 9666-9670.
- Danias, J. et al. 2003. Quantitative analysis of retinal ganglion cell (RGC) loss in aging DBA/2NNia glaucomatous mice: comparison with RGC loss in aging C57/BL6 mice. *Invest Ophthalmol Vis Sci* 44(12), pp. 5151-5162.
- DeBello, W. M. et al. 2001. Adaptive axonal remodeling in the midbrain auditory space map. *Journal of Neuroscience* 21(9), pp. 3161-3174.
- Demandolx D, D. J. 1997. Multiparameter image cytometry: from confocal micrographs to major subcellular structures in fluorescence microscope images of hela cells. *Bioimaging* 5, pp. 159-169.
- Denk, W. and Svoboda, K. 1997. Photon upmanship: why multiphoton imaging is more than a gimmick. *Neuron* 18(3), pp. 351-357.
- Dennis, K. et al. 2002. Cloning and characterization of the 5'-flanking region of the rat neuron-specific Class III beta-tubulin gene. *Gene* 294(1-2), pp. 269-277.
- Diggle, P. J. 1983. *Statistical analysis of spatial point patterns*. London : Academic.
- Dkhissi O, et al. 1996. Changes in retinal dopaminergic cells and dopamine rhythmic metabolism during the development of a glaucoma-like disorder in quails. *Invest Ophthalmol Vis Sci* 37, pp. 2335-2344.
- Donnerlly, K. P. 1978. Stimulations to determine the variance and edge effect of total nearest neighbour distance. Hodder, I. ed. Cambridge University Press, Cambridge, pp. 91-95.

- Dou, C.-L. and Levine, J. M. 1997. Identification of a Neuronal Cell Surface Receptor for a Growth Inhibitory Chondroitin Sulfate Proteoglycan (NG2). *Journal of Neurochemistry* 68(3), pp. 1021-1030.
- Dou, C. L. and Levine, J. M. 1994. Inhibition of neurite growth by the NG2 chondroitin sulfate proteoglycan. *J. Neurosci.* 14(12), pp. 7616-7628.
- Drance, S. et al. 2001. Risk factors for progression of visual field abnormalities in normal-tension glaucoma. *Am J Ophthalmol* 131(6), pp. 699-708.
- Drasdo, N., et al. 2001. The s-cone PHNR and pattern ERG in primary open angle glaucoma. *Inves Ophthalmol Vis Sci* 42, pp. 1266-1272.
- Drasdo, N. and Fowler, C. W. 1974. Non-linear projection of the retinal image in a wide-angle schematic eye. *Br J Ophthalmol* 58(8), pp. 709-714.
- Dubin, A. R. a. M. W. 1977. Development of receptive field properties of retinal ganglion cells in kittens. *J. Neurophysiol.* 40, pp. 1188–1199.
- Eglen, S. J. 2006. Development of regular cellular spacing in the retina: theoretical models. *Math Med Biol* 23(2), pp. 79-99.
- Eliasieh, K. et al. 2007. Cellular reorganization in the human retina during normal aging. *Invest Ophthalmol Vis Sci* 48(6), pp. 2824-2830.
- Enroth-Cugell, C., and Robson, J.G. 1966. The contrast sensitivity of retinal ganglion cells of the cat. *J Physio* 187, pp. 517-552.
- Epstein D. 1997. Primary open-angle glaucoma. In: Epstein DL A R, Schuman JS [ed.] *Chandler and Grant's Glaucoma*. (4th edn.) Baltimore, Md: Williams&Wilkins, pp. 183-198.
- Easter, S. S., Jr. et al. 1993. Initial tract formation in the mouse brain. *J Neurosci* 13(1), pp. 285-299.
- Evans, J. 1991. *Causes of blindness and partial sight in England and Wales*. HMSO (Studies on Medical and Population Subjects).
- Eysel, U. T. and Wolfhard, U. 1984. The effects of partial retinal lesions on activity and size of cells in the dorsal lateral geniculate nucleus. *J Comp Neurol* 229(2), pp. 301-309.
- Fei, Y. 2003. Development of the cone photoreceptor mosaic in the mouse retina revealed by fluorescent cones in transgenic mice. *Mol Vis* 9, pp. 31-42.
- Filippopoulos, T. et al. 2006a. Topographic and Morphologic Analyses of Retinal Ganglion Cell Loss in Old DBA/2NNia Mice. *Invest. Ophthalmol. Vis. Sci.* 47(5), pp. 1968-1974.

Filippopoulos, T. et al. 2006b. Topographic and morphologic analyses of retinal ganglion cell loss in old DBA/2NNia mice. *Invest Ophthalmol Vis Sci* 47(5), pp. 1968-1974.

Fisher, S. K. and Lewis, G. P. 2003. Muller cell and neuronal remodeling in retinal detachment and reattachment and their potential consequences for visual recovery: a review and reconsideration of recent data. *Vision Research* 43(8), pp. 887-897.

Fisher S K, et al. 2005. Cellular remodeling in mammalian retina: results from studies of experimental retinal detachment. *Prog Retin Eye Res* 24, pp. 395-431.

Flammer, J. et al. 2002. The impact of ocular blood flow in glaucoma. *Prog Retin Eye Res* 21(4), pp. 359-393.

Foster, P.J., Buhrmann, R., Quigley, H.A., and Johnson, G.J. (2002). The definition and classification of glaucoma in prevalence surveys. *The British journal of ophthalmology* 86, pp. 238-242.

Fox, K. and Caterson, B. 2002. Neuroscience. Freeing the brain from the perineuronal net. *Science* 298(5596), pp. 1187-1189.

Friedlander, D. R. et al. 1994. The neuronal chondroitin sulfate proteoglycan neurocan binds to the neural cell adhesion molecules Ng-CAM/L1/NILE and N-CAM, and inhibits neuronal adhesion and neurite outgrowth. *J. Cell Biol.* 125(3), pp. 669-680.

Friedman, D. S. 2004. Prevalence of Open-Angle Glaucoma among Adults in the United States. *Archives of Ophthalmology* 122(4), pp. 532-538.

Gabelt, B. T. and Kaufman, P. L. 2005. Changes in aqueous humor dynamics with age and glaucoma. *Prog Retin Eye Res* 24(5), pp. 612-637.

Gao, H. and Hollyfield, J. G. 1992. Aging of the human retina. Differential loss of neurons and retinal pigment epithelial cells. *Invest Ophthalmol Vis Sci* 33(1), pp. 1-17.

Getis, D. C. a. A. 1998. Point pattern analysis [Online].

Goldbaum, M.H., et al. 1989. The extracellular matrix of the human optic nerve. *Archives of ophthalmology* 107(8), pp. 1225-1231.

Gordon, M. O. et al. 2002. The Ocular Hypertension Treatment Study: baseline factors that predict the onset of primary open-angle glaucoma. *Arch Ophthalmol* 120(6), pp. 714-720.

Gottanka, J. et al. 1997. Severity of optic nerve damage in eyes with POAG is correlated with changes in the trabecular meshwork. *J Glaucoma* 6(2), pp. 123-132.

Grumet, M. et al. 1993. Functional characterization of chondroitin sulfate proteoglycans of brain: interactions with neurons and neural cell adhesion molecules. *J. Cell Biol.* 120(3), pp. 815-824.

- Grutzendler, J. et al. 2003. Rapid labeling of neuronal populations by ballistic delivery of fluorescent dyes. *Methods* 30(1), pp. 79-85.
- Gupta, N., et al. 2007. Chronic ocular hypertension induces dendrite pathology in the lateral geniculate nucleus of the brain. *Exp Eye Research* 84(1), pp. 176-184.
- Gupta, N. and Yucel, Y. H. 2001. Glaucoma and the brain. *J Glaucoma* 10(5 Suppl 1), pp. S28-29.
- Gupta, N. and Yucel, Y. H. 2003. Brain changes in glaucoma. *Eur J Ophthalmol* 13 Suppl 3, pp. S32-35.
- Haendel, M. A. et al. 1996. Cytoskeletal changes during neurogenesis in cultures of avian neural crest cells. *J Neurocytol* 25(4), pp. 289-301.
- Harman, A. et al. 2000. Neuronal density in the human retinal ganglion cell layer from 16-77 years. *Anat Rec* 260(2), pp. 124-131.
- Harman, D. 1981. The aging process. *Proc Natl Acad Sci U S A* 78(11), pp. 7124-7128.
- Hartwick, A.T., Zhang, X., Chauhan, B.C., and Baldrige, W.H. (2005). Functional assessment of glutamate clearance mechanisms in a chronic rat glaucoma model using retinal ganglion cell calcium imaging. *Journal of neurochemistry* 94, pp. 794-807.
- Hendry, S. H. C. and Calkins, D. J. 1998. Neuronal chemistry and functional organization in the primate visual system. *Trends in Neurosciences* 21(8), pp. 344-349.
- Hernandez, M.R. 2000. The optic nerve head in glaucoma: role of astrocytes in tissue remodeling. *Progress in retinal and eye research* 19(3), pp. 297-321.
- Hernandez, M. R. et al. 2002. Differential gene expression in astrocytes from human normal and glaucomatous optic nerve head analyzed by cDNA microarray. *Glia* 38(1), pp. 45-64.
- Hernandez, M.R., et al. 1988. Cell culture of the human lamina cribrosa. *Investigative ophthalmology & visual science* 29(1), 78-89.
- Hernandez, M.R. et al. 1987. Extracellular matrix of the human lamina cribrosa. *Am J Ophthalmol* 104, pp. 567-576.
- Hewitt, A.W., et al. 2006. Complex genetics of complex traits: the case of primary open-angle glaucoma. *Clinical & Exp Ophthalmol* 34(5), pp. 472-484.
- Honig, M. G. H., R. I. 1989. Carbocyanine dyes. Novel markers for labelling neurons. *Trends Neurosci* 12(9), pp. 336-338.

- Honkanen, R.A., et al. 2003. Vitreous amino acid concentrations in patients with glaucoma undergoing vitrectomy. *Arch Ophthalmol* 121(2), pp. 183-188.
- Hutsler, J. J. and Chalupa, L. M. 1994. Neuropeptide Y immunoreactivity identifies a regularly arrayed group of amacrine cells within the cat retina. *J Comp Neurol* 346(4), pp. 481-489.
- Jakobs, T. C. et al. 2005. Retinal ganglion cell degeneration is topological but not cell type specific in DBA/2J mice. *J. Cell Biol.* 171(2), pp. 313-325.
- Janssen P, et al. 1996. Evidence for glaucoma-induced horizontal cell alterations in the human retina. *German Journal of Ophthalmology* 5(6), pp. 378-385.
- John, S. W. et al. 1998. Essential iris atrophy, pigment dispersion, and glaucoma in DBA/2J mice. *Invest Ophthalmol Vis Sci* 39(6), pp. 951-962.
- Johnson, H. and Cowey, A. 2000. Transneuronal retrograde degeneration of retinal ganglion cells following restricted lesions of striate cortex in the monkey. *Exp Brain Res* 132(2), pp. 269-275.
- Jonas, J. B. et al. 1990. Histomorphometry of the human optic nerve. *Invest Ophthalmol Vis Sci* 31(4), pp. 736-744.
- Kerrigan-Baumrind, L. A. et al. 2000. Number of ganglion cells in glaucoma eyes compared with threshold visual field tests in the same persons. *Invest Ophthalmol Vis Sci* 41(3), pp. 741-748.
- Katsetos, C. D. et al. 1993. Differential localization of class III, beta-tubulin isotype and calbindin-D28k defines distinct neuronal types in the developing human cerebellar cortex. *J Neuropathol Exp Neurol* 52(6), pp. 655-666.
- Kaushik, S. et al. 2003. Neuroprotection in glaucoma. *J Postgrad Med* 49(1), pp. 90-95.
- Kiernan, J. A. and Hudson, A. J. 1991. Changes in sizes of cortical and lower motor neurons in amyotrophic lateral sclerosis. *Brain* 114(2), pp. 843-853.
- Kim, C. B. et al. 1996. Effects of aging on the densities, numbers, and sizes of retinal ganglion cells in rhesus monkey. *Neurobiol Aging* 17(3), pp. 431-438.
- Kolb, H. 1974. The connections between horizontal cells and photoreceptors in the retina of the cat: electron microscopy of Golgi preparations. *J Comp Neurol* 155(1), pp. 1-14.
- Kolb, H. et al. 1992. Neurons of the human retina: a Golgi study. *J Comp Neurol* 318(2), pp. 147-187.
- Kornzweig, A.L et al. 1968. Selective atrophy of the radial peripapillary capillaries in chronic glaucoma. *Arch Ophthalmol* 80(6), pp. 696-702.

- Kurtenbach, A. and Weiss, M. 2002. Effect of aging on multifocal oscillatory potentials. *J Opt Soc Am A Opt Image Sci Vis* 19(1), pp. 190-196.
- Laquis, S. et al. 1998. The patterns of retinal ganglion cell death in hypertensive eyes. *Brain Res* 784(1-2), pp. 100-104.
- Lee, M. K. et al. 1990. The expression and posttranslational modification of a neuron-specific beta-tubulin isotype during chick embryogenesis. *Cell Motil Cytoskeleton* 17(2), pp. 118-132.
- Leske, M. C. et al. 1994. The Barbados Eye Study. Prevalence of open angle glaucoma. *Arch Ophthalmol* 112(6), pp. 821-829.
- Leske, M. C. et al. 2003. Factors for glaucoma progression and the effect of treatment: the early manifest glaucoma trial. *Arch Ophthalmol* 121(1), pp. 48-56.
- Levin L A 2001. Relevance of the site of injury of glaucoma to neuroprotective strategies. *Surv Ophthalmol* 45 Suppl 3, pp. S243-249; discussion S273-246.
- Levkovitch-Verbin, H. et al. 2001. Optic Nerve Transection in Monkeys May Result in Secondary Degeneration of Retinal Ganglion Cells. *Invest. Ophthalmol. Vis. Sci.* 42(5), pp. 975-982.
- Levkovitch-Verbin, H. et al. 2003. A Model to Study Differences between Primary and Secondary Degeneration of Retinal Ganglion Cells in Rats by Partial Optic Nerve Transection. *Invest. Ophthalmol. Vis. Sci.* 44(8), pp. 3388-3393.
- Lewis, G. P. et al. 1998. Neurite outgrowth from bipolar and horizontal cells after experimental retinal detachment. *Investigative Ophthalmology and Visual Science* 39(2), pp. 424-434.
- Libby, R. T. et al. 2005. Inherited glaucoma in DBA/2J mice: pertinent disease features for studying the neurodegeneration. *Vis Neurosci* 22(5), pp. 637-648.
- Liesegang, T. J. 1996. Glaucoma: changing concepts and future directions. *Mayo Clin Proc* 71(7), pp. 689-694.
- Liets, L. C. et al. 2006. Dendrites of rod bipolar cells sprout in normal aging retina. *Proc Natl Acad Sci U S A* 103(32), pp. 12156-12160.
- Lin M T, and Beal M F 2006. Mitochondrial dysfunction and oxidative stress in neurodegenerative diseases. *Nature* 443, pp. 787-795.
- Lin, B. et al. 2004. Retinal Ganglion Cell Type, Size, and Spacing Can Be Specified Independent of Homotypic Dendritic Contacts. *Neuron* 43(4), pp. 475-485.
- Linden, R. and Perry, V. H. 1982. Ganglion cell death within the developing retina: a regulatory role for retinal dendrites? *Neuroscience* 7(11), pp. 2813-2827.

- Lipton S. A. 2005. The molecular basis of memantine action in Alzheimer's disease and other neurologic disorders: low-affinity, uncompetitive antagonism. *Curr Alzheimer Res* 2 (2), pp. 155-165.
- Lovasik, J. V. et al. 2003. Neuroretinal basis of visual impairment in the very elderly. *Graefes Arch Clin Exp Ophthalmol* 241(1), pp. 48-55.
- Lutjen-Drecoll, E. et al. 1986. Quantitative analysis of 'plaque material' between ciliary muscle tips in normal- and glaucomatous eyes. *Exp Eye Res* 42(5), pp. 457-465.
- Marc, R. E. et al. 2003. Neural remodeling in retinal degeneration. *Prog Retin Eye Res* 22(5), pp. 607-655.
- MacLaren, R. E. et al. 2006. Retinal repair by transplantation of photoreceptor precursors. *Nature* 444(7116), pp. 203-207.
- Majji, A. B. et al. 2000. Age-Related Retinal Pigment Epithelium and Bruch's Membrane Degeneration in Senescence-Accelerated Mouse. *Invest. Ophthalmol. Vis. Sci.* 41(12), pp. 3936-3942.
- Malpica, N. et al. 1997. Applying watershed algorithms to the segmentation of clustered nuclei. *Cytometry* 28(4), pp. 289-297.
- Masland, R. H. 2001. Neuronal diversity in the retina. *Curr Opin Neurobiol* 11(4), pp. 431-436.
- Masland, R. H. 2001. The fundamental plan of the retina. *Nature Neuroscience* 4(9), pp. 877-886.
- Mason, R. P. et al. 1989. National survey of the prevalence and risk factors of glaucoma in St. Lucia, West Indies. Part I. Prevalence findings. *Ophthalmology* 96(9), pp. 1363-1368.
- May C A, and Mittag T 2004. Neuronal nitric oxide synthase (nNOS) positive retinal amacrine cells are altered in the DBA/2N^{Nia} mouse, a murine model for angle-closure glaucoma. *J Glaucoma* 13(6), pp. 496-499.
- Mikelberg, F. S. et al. 1989. The normal human optic nerve. Axon count and axon diameter distribution. *Ophthalmology* 96(9), pp. 1325-1328.
- Minamino, K. et al. 2005. Long-term survival of bone marrow-derived retinal nerve cells in the retina. *Neuroreport* 16(12), pp. 1255-1259.
- Mittag, T. W. et al. 2000. Retinal damage after 3 to 4 months of elevated intraocular pressure in a rat glaucoma model. *Invest Ophthalmol Vis Sci* 41(11), pp. 3451-3459.

- Moody, S. A. et al. 1989. Development of the peripheral trigeminal system in the chick revealed by an isotype-specific anti-beta-tubulin monoclonal antibody. *J Comp Neurol* 279(4), pp. 567-580.
- Moon J. I. et al. 2005. Changes in retinal neuronal populations in the DBA/2J mouse. *Cell Tissue Res* 320, pp. 51-59.
- Morgan, J. E. et al. 2000. Retinal ganglion cell death in experimental glaucoma. *Br J Ophthalmol* 84(3), pp. 303-310.
- Morgenstern, D. A. et al. 2002. Chondroitin sulphate proteoglycans in the CNS injury response. *Prog Brain Res* 137, pp. 313-332.
- Morrison, J. C. et al. 1997. A rat model of chronic pressure-induced optic nerve damage. *Exp Eye Res* 64(1), pp. 85-96.
- Morrison, J. C. et al. 2005. Understanding mechanisms of pressure-induced optic nerve damage. *Progress in Retinal and Eye Research* 24(2), pp. 217-240.
- Morrison, J.C. et al. 1994. Chondroitin sulfate proteoglycan distribution in the primate optic nerve head. *Investigative ophthalmology & visual science* 35, pp. 838-845.
- Nada J. Lingel, and Smith, D.L. 2006. Evaluating the Optic Nerve Head in Glaucoma. (Pacific University College of Optometry).
- Nedzved A, A. S., Pitas I. 2000. Morphological segmentation of histology cell images. *Proceedings of 15th International Conference on Pattern Recognition, Barcelona, Spain.* 1, pp. 500-503.
- Nelson, P. et al. 2003. Quality of life in glaucoma and its relationship with visual function. *J Glaucoma* 12(2), pp. 139-150.
- Neufeld, A.H. 1999. Nitric oxide: a potential mediator of retinal ganglion cell damage in glaucoma. *Survey of ophthalmology* 43 Suppl 1, pp. S129-135.
- Neufeld, A. H. et al. 1999. Inhibition of nitric-oxide synthase 2 by aminoguanidine provides neuroprotection of retinal ganglion cells in a rat model of chronic glaucoma. *Proc Natl Acad Sci U S A* 96(17), pp. 9944-9948.
- Neufeld, A. H. and Gachie, E. N. 2003. The inherent, age-dependent loss of retinal ganglion cells is related to the lifespan of the species. *Neurobiol Aging* 24(1), pp. 167-172.
- Nickells R. W. 2007. From ocular hypertension to ganglion cell death: a theoretical sequence of events leading to glaucoma. *Can J Ophthalmol* 42(2), pp. 278-287.
- Noe, G. et al. 2003. Associations between glaucomatous visual field loss and participation in activities of daily living. *Clin Experiment Ophthalmol* 31(6), pp. 482-486.

- Nork T. M. 2000. Acquired color vision loss and a possible mechanism of ganglion cell death in glaucoma. *Trans Am Ophthalmol Soc* 98, pp. 331-363.
- Nork T. M. et al. 2000 Swelling and Loss of Photoreceptors in Chronic Human and Experimental Glaucomas. *Arch Ophthalmol* 118(2), pp. 235-245.
- Nork, T. M. et al. 2000a. Swelling and Loss of Photoreceptors in Chronic Human and Experimental Glaucomas. *Arch Ophthalmol* 118(2), pp. 235-245.
- Nork, T. M. et al. 2000b. Swelling and loss of photoreceptors in chronic human and experimental glaucomas. *Arch Ophthalmol* 118(2), pp. 235-245.
- Ogden, T. E. 1978. Nerve fiber layer astrocytes of the primate retina: morphology, distribution, and density. *Invest Ophthalmol Vis Sci* 17(6), pp. 499-510.
- Oliver Schabenberger, C. A. G. 2005. Statistical methods for spatial data analysis. Boca Raton, FL : Chapman & Hall/CRC.
- Osborne N. N. et al. 1999. Neuroprotection in relation to retinal ischemia and relevance to glaucoma. *Surv Ophthalmol* 43 Suppl 1, pp. S102-128.
- Osborne, N. N. et al. 2004. Retinal ischemia: mechanisms of damage and potential therapeutic strategies. *Progress in Retinal and Eye Research* 23(1), pp. 91-147.
- Otani, A. et al. 2004. Rescue of retinal degeneration by intravitreally injected adult bone marrow-derived lineage-negative hematopoietic stem cells. *J Clin Invest* 114(6), pp. 765-774.
- Owsley C, S. M. 1990. Vision and aging. . In: Boller F, Grafman J, eds. *Handbook of neuropsychology.* , pp. 229-249.
- Owsley, C. et al. 2001. Delays in rod-mediated dark adaptation in early age-related maculopathy. *Ophthalmology* 108(7), pp. 1196-1202.
- Page-McCaw, P. S. et al. 2004. Retinal network adaptation to bright light requires tyrosinase. *Nat Neurosci* 7(12), pp. 1329-1336.
- Panda S, and Jonas J B 1992. Decreased photoreceptor count in human eyes with secondary angle-closure glaucoma. *Invest Ophthalmol Vis Sci* 33, pp. 2532-2536.
- Panda, S. and Jonas, J. B. 1992. Decreased photoreceptor count in human eyes with secondary angle-closure glaucoma. *Invest Ophthalmol Vis Sci* 33(8), pp. 2532-2536.
- Pavlidis, M. et al. 2003. Retinal ganglion cells resistant to advanced glaucoma: a postmortem study of human retinas with the carbocyanine dye DiI. *Invest Ophthalmol Vis Sci* 44(12), pp. 5196-5205.

- Peichl, L. and Bolz, J. 1984. Kainic acid induces sprouting of retinal neurons. *Science* 223(4635), pp. 503-504.
- Pelzel H. R. et al. 2006. Decrease of cone opsin mRNA in experimental ocular hypertension. *Mol Vis* 12, pp. 1272-1282.
- Perry, V. H. et al. 1984. Retinal ganglion cells that project to the dorsal lateral geniculate nucleus in the macaque monkey. *Neuroscience* 12(4), pp. 1101-1123.
- Perry, V. H. and Linden, R. 1982. Evidence for dendritic competition in the developing retina. *Nature London* 297(5868), pp. 683-685.
- Pizzorusso, T. et al. 2002. Reactivation of Ocular Dominance Plasticity in the Adult Visual Cortex. *Science* 298(5596), pp. 1248-1251.
- Poinosawmy D. et al. 1980. Colour vision in patients with chronic simple glaucoma and ocular hypertension. *Br J Ophthalmol* 64(11), pp. 852-857.
- Polyak, S. 1957. *The Vertebrate Visual System*. Univ. Chicago Press, Chicago.
- Quigley H A, and Addicks E M 1981 Regional differences in the structure of the lamina cribrosa and their relation to glaucomatous optic nerve damage. *Arch Ophthalmol* 99(1), pp. 137-143.
- Quigley, H. A. 1993. Open-angle glaucoma. *N Engl J Med* 328(15), pp. 1097-1106.
- Quigley, H. A. 1996. Number of people with glaucoma worldwide. *Br J Ophthalmol* 80(5), pp. 389-393.
- Quigley, H. A. 2001. Selective citation of evidence regarding photoreceptor loss in glaucoma. *Arch Ophthalmol* 119(9), pp. 1390-1391.
- Raff, M. C. et al. 2002. Axonal self-destruction and neurodegeneration. *Science* 296(5569), pp. 868-871.
- Ramirez, J. M. et al. 1996. Structural specializations of human retinal glial cells. *Vision Res* 36(14), pp. 2029-2036.
- Ramirez, J. M. et al. 2001. Changes of astrocytes in retinal ageing and age-related macular degeneration. *Exp Eye Res* 73(5), pp. 601-615.
- Ramo, A. S. et al. 1987. Transient morphological features of identified ganglion cells in living fetal and neonatal retina. *Science* 237(4814), pp. 522-525.
- Raz D, et al. 2003. Functional damage to inner and outer retinal cells in experimental glaucoma. *Invest Ophthalmol Vis Sci* 44(8), pp. 3675-3684.

- Redmond, L. et al. 2002. Calcium regulation of dendritic growth via CaM kinase IV and CREB-mediated transcription. *Neuron* 34(6), pp. 999-1010.
- Repka, M. X. and Quigley, H. A. 1989. The effect of age on normal human optic nerve fiber number and diameter. *Ophthalmology* 96(1), pp. 26-32.
- Rockhill, R. L. et al. 2000. Spatial order within but not between types of retinal neurons. *Proceedings of the National Academy of Sciences* 97(5), pp. 2303-2307.
- Rohen, J. W. and Witmer, R. 1972. Electron microscopic studies on the trabecular meshwork in glaucoma simplex. *Albrecht Von Graefe's Archive For Clinical And Experimental Ophthalmology* 183(4), pp. 251-266.
- Rossi, C. et al. 2003. The spatial order of horizontal cells is not affected by massive alterations in the organization of other retinal cells. *J Neurosci* 23(30), pp. 9924-9928.
- Rusoff, A. C. and Dubin, M. W. 1978. Kitten ganglion cells: Dendritic field size at 3 weeks of age and correlation with receptive field size. *Invest Ophthalmol Vis Sci* 17(8), pp. 819-821.
- Saji, M., et al. 1996. Prevention of transneuronal degeneration of neurons in the substantia nigra reticulata by ablation of the subthalamic nucleus. *Exp Neurol* 141(1), pp. 120-129.
- Sanchez, R.M. et al. 1986. The number and diameter distribution of axons in the monkey optic nerve. *Invest Ophthalmol Vis Sci* 27(9), pp. 1342-1350.
- Schlamp C. et al. 2006. Progressive ganglion cell loss and optic nerve degeneration in DBA/2J mice is variable and asymmetric. *BMC Neuroscience* 7, pp. 66.
- Schlamp, C. L. et al. 2001. Changes in Thy1 gene expression associated with damaged retinal ganglion cells. *Mol Vis* 7, pp. 192-201.
- Schnell, S. A. et al. 1999. Reduction of lipofuscin-like autofluorescence in fluorescently labeled tissue. *J Histochem Cytochem* 47(6), pp. 719-730.
- Sernagor, E. et al. 2001. Development of retinal ganglion cell structure and function. *Prog Retin Eye Res* 20(2), pp. 139-174.
- Shieh, P. B. et al. 1998. Identification of a Signaling Pathway Involved in Calcium Regulation of BDNF Expression. *Neuron* 20(4), pp. 727-740.
- Sjostrom, P. J. et al. 1999. Artificial neural network-aided image analysis system for cell counting. *Cytometry* 36(1), pp. 18-26.
- Sorra, K. E. and Harris, K. M. 2000. Overview on the structure, composition, function, development, and plasticity of hippocampal dendritic spines. *Hippocampus* 10(5), pp. 501-511.

- Stacy, R. C. et al. 2005. Disruption and Recovery of Patterned Retinal Activity in the Absence of Acetylcholine. *J. Neurosci.* 25(41), pp. 9347-9357.
- Stone, E. M. et al. 1997. Identification of a Gene That Causes Primary Open Angle Glaucoma. *Science* 275(5300), pp. 668-670.
- Su, J. H. et al. 1997. Transneuronal Degeneration in the Spread of Alzheimer's Disease Pathology: Immunohistochemical Evidence for the Transmission of Tau Hyperphosphorylation. *Neurobiology of Disease* 4(5), pp. 365-375.
- Sullivan, K. F. 1988. Structure and utilization of tubulin isotypes. *Annu Rev Cell Biol* 4, pp. 687-716.
- Sullivan, K. F. and Cleveland, D. W. 1986. Identification of conserved isotype-defining variable region sequences for four vertebrate beta tubulin polypeptide classes. *Proc Natl Acad Sci U S A* 83(12), pp. 4327-4331.
- Sullivan R. K. P, et al. 2007. Dendritic and Synaptic Plasticity of Neurons in the Human Age-Related Macular Degeneration Retina. *Invest. Ophthalmol Vis Sci* 48(6), pp. 2782-2791.
- Svoboda, K. and Yasuda, R. 2006. Principles of Two-Photon Excitation Microscopy and Its Applications to Neuroscience. *Neuron* 50(6), pp. 823-839.
- Tengroth, B. et al. 1985. A comparative analysis of the collagen type and distribution in the trabecular meshwork, sclera, lamina cribrosa and the optic nerve in the human eye. *Acta ophthalmologica* 173, pp. 91-93.
- Tezel, G. and Wax, M. B. 2000. Increased production of tumor necrosis factor-alpha by glial cells exposed to simulated ischemia or elevated hydrostatic pressure induces apoptosis in cocultured retinal ganglion cells. *J Neurosci* 20(23), pp. 8693-8700.
- Tezel, G. 2006. Oxidative stress in glaucomatous neurodegeneration: mechanisms and consequences. *Prog Retin Eye Res* 25(5), pp. 490-513.
- Tezel, G. et al. 1996. Comparative optic disc analysis in normal pressure glaucoma, primary open-angle glaucoma, and ocular hypertension. *Ophthalmology* 103(12), pp. 2105-2113.
- Tezel, G. et al. 2004. Role of tumor necrosis factor receptor-1 in the death of retinal ganglion cells following optic nerve crush injury in mice. *Brain Res* 996(2), pp. 202-212.
- Tielsch, J. M. et al. 1991. Racial variations in the prevalence of primary open-angle glaucoma: The Baltimore eye survey. *J. AM. MED. ASSOC.* 266(3), pp. 369-374.
- Trick, G. L. et al. 1992. The human pattern ERG: alteration of response properties with aging. *Optom Vis Sci* 69(2), pp. 122-128.

- Troilo, D. et al. 1996. Factors controlling the dendritic arborization of retinal ganglion cells. *Visual Neuroscience* 13, pp. 721-733
- Tuulonen, A. and Airaksinen, P. J. 1991. Initial glaucomatous optic disk and retinal nerve fiber layer abnormalities and their progression. *Am J Ophthalmol* 111(4), pp. 485-490.
- Vaquero, C. F. et al. 2001. A dopamine- and protein kinase A-dependent mechanism for network adaptation in retinal ganglion cells. *Journal of Neuroscience* 21(21), pp. 8624-8635.
- Van Buren, A. 1963. *The retinal ganglion cell layer*. Springfield: Thomas. Springfield: Thomas.
- Vilter, V. 1954. *Asymetrie cyto-architectonique de la Fovea retinienne de*
- Wang X. et al. 2005. Factors contributing to neuronal degeneration in retinas of experimental glaucomatous rats. *J Neurosci Res* 82(5), pp. 674-689.
- Wall, J. T. et al. 2002. Human brain plasticity: an emerging view of the multiple substrates and mechanisms that cause cortical changes and related sensory dysfunctions after injuries of sensory inputs from the body. *Brain Research Reviews* 39(2-3), pp. 181-215.
- Wässle, H. 2004. Parallel processing in the mammalian retina. *Nat. Rev. Neurosci.* 5, pp. 747-757.
- Wassle, H. and Riemann, H. J. 1978. The mosaic of nerve cells in the mammalian retina. *Proc R Soc Lond B Biol Sci* 200(1141), pp. 441-461.
- Watanabe, M. and Rodieck, R. W. 1989. Parasol and midget ganglion cells of the primate retina. *J Comp Neurol* 289(3), pp. 434-454.
- Wax, M. B. et al. 1998. Clinical and ocular histopathological findings in a patient with normal-pressure glaucoma. *Arch Ophthalmol* 116(8), pp. 993-1001.
- Weber, A. J. et al. 1998. Morphology of single ganglion cells in the glaucomatous primate retina. *Invest Ophthalmol Vis Sci* 39(12), pp. 2304-2320.
- Weber, A. J. et al. 2000. Experimental glaucoma and cell size, density, and number in the primate lateral geniculate nucleus. *Investigative Ophthalmology and Visual Science* 41(6), pp. 1370-1379.
- Weiler, R. et al. 2000. Modulation of coupling between retinal horizontal cells by retinoic acid and endogenous dopamine. *Brain Research Reviews* 32(1), pp. 121-129.
- Weinreb, R. N. and Khaw, P. T. 2004. Primary open-angle glaucoma. *Lancet* 363(9422), pp. 1711-1720.

- Weleber, R. G. 1981. The effect of age on human cone and rod ganzfeld electroretinograms. *Invest Ophthalmol Vis Sci* 20(3), pp. 392-399.
- Wensor, M. D. et al. 1998. The prevalence of glaucoma in the Melbourne Visual Impairment Project. *Ophthalmology* 105(4), pp. 733-739.
- Whitmore, A. V. et al. 2003. The proapoptotic proteins Bax and Bak are not involved in Wallerian degeneration. *Cell Death Differ* 10(2), pp. 260-261.
- Whitmore, A. V. et al. 2005. Glaucoma: Thinking in new ways--a role for autonomous axonal self-destruction and other compartmentalised processes? *Progress in Retinal and Eye Research* 24(6), pp. 639-662.
- Williams, R.W., and Chalupa, L.M. 1983. An analysis of axon caliber within the optic nerve of the cat: evidence of size groupings and regional organization. *J Neurosci* 3(8), pp. 1554-1564.
- Williams, R. W. and Rakic, P. 1988. Three-dimensional counting: an accurate and direct method to estimate numbers of cells in sectioned material. *J Comp Neurol* 278(3), pp. 344-352.
- Willis, A. and Anderson, S. J. 2000. Effects of glaucoma and aging on photopic and scotopic motion perception. *Invest Ophthalmol Vis Sci* 41(1), pp. 325-335.
- Wong, R. O. L. and Ghosh, A. 2002. Activity-dependent regulation of dendritic growth and patterning. *Nat Rev Neurosci* 3(10), pp. 803-812.
- Wright, C. E. et al. 1985. The influence of age on the electroretinogram and visual evoked potential. *Doc Ophthalmol* 59(4), pp. 365-384.
- Yang, P. 2004. DNA microarray analysis of gene expression in human optic nerve head astrocytes in response to hydrostatic pressure. *Physiological genomics* 17(2), pp. 157-169.
- Yoles, E. and Schwartz, M. 1998. Potential neuroprotective therapy for glaucomatous optic neuropathy. *Surv Ophthalmol* 42(4), pp. 367-372.
- Young, M. J. et al. 2000. Neuronal differentiation and morphological integration of hippocampal progenitor cells transplanted to the retina of immature and mature dystrophic rats. *Mol Cell Neurosci* 16(3), pp. 197-205.
- Yucel, Y. H. et al. 2000. Loss of neurons in magnocellular and parvocellular layers of the lateral geniculate nucleus in glaucoma. *Archives of Ophthalmology* 118(3), pp. 378-384.
- Yucel, Y. H. et al. 2001. Atrophy of relay neurons in magno- and parvocellular layers in the lateral geniculate nucleus in experimental glaucoma. *Investigative Ophthalmology & Visual Science* 42(13), pp. 3216-3222.

Yucel, Y. H. et al. 2001. Atrophy of relay neurons in magno- and parvocellular layers in the lateral geniculate nucleus in experimental glaucoma. *Investigative Ophthalmology & Visual Science* 42(13), pp. 3216-3222.

Yucel, Y. H. et al. 2003. Effects of retinal ganglion cell loss on magno-, parvo-, koniocellular pathways in the lateral geniculate nucleus and visual cortex in glaucoma. *Progress in Retinal and Eye Research* 22(4), pp. 465-481.

